Phase contrast imaging with a laboratory-based microfocus X-ray source

Kathryn L. Kelly

Phase contrast imaging with a laboratory-based microfocus X-ray source

Kathryn L. Kelly

A thesis presented for the degree of
Doctor of Philosophy

Department of Physics
Durham University
England

May 2007

Dedicated to:

My family, Andrew and Tally

Phase contrast imaging with a laboratory-based microfocus X-ray source

Kathryn Kelly

Submitted for the degree of Doctor of Philosophy
May 2007

Abstract

This project looks at the design of an in-line X-ray phase contrast imaging system, based around the Bede Microsource®, on a suitable scale for imaging small pathological samples. The system is applied to two test objects to assess feasibility of its use in practice. The system comprises: microfocus X-ray source, copper and rhodium targets, phase object and detector. By altering sample position, phase contrast is seen to vary proportionally with propagation distance. By increasing source size, phase contrast is seen to degrade with increasing source dimensions. It is furthermore determined that transverse coherence in the direction perpendicular to a sample boundary dominates the result. Using different operating voltages with an image manipulation approach, the importance of monochromaticity is investigated. It is determined that less polychromatic X-rays provide better phase contrast. However, applying a filter method of monochromation reduces phase contrast due to beam hardening, so this method is unsuitable for phase imaging with this system. By increasing sample thickness, phase contrast is seen to plateau at a certain thickness, dependant on X-ray energy, revealing a practical limitation of the system. Introduction of water and glass to the system is seen to be detrimental to phase contrast, due to beam hardening. However phase contrast is not destroyed by the presence of water. When imaging a mammographic test object comprising low-contrast details and breast tissue morphology, the system detects all low-contrast details extremely well. Furthermore, using a phase object together with breast tissue morphology, with the harder rhodium X-rays, the system detects an anomaly of ~500μm through the noise of simulated breast tissue. Finally, we see the difference in two scorpion sting images: an absorption image taken at the beginning of the project and a phase image taken after the system has been improved.

Declaration

All of the work contained within this thesis is based on research carried out at the X-Ray Scattering and Magnetism Group, Department of Physics, Durham University, England. No part of this thesis has been submitted for any degree or other qualification either at the University of Durham or any other institution, and it is all my own work.

Selected material from chapters 1, 4, 5 and 6 of this thesis has been published in the following paper:

Kelly, K. L. & Tanner, B. K., "Factors affecting in-line phase-contrast imaging with a laboratory micro-focus x-ray source". *Advances in X-ray Analysis* **49**: 31-36 (2006)

Acknowledgements

In order to complete this project I have had support from many quarters. I am grateful for financial support provided for this project by the Engineering and Physical Sciences Research Council and Bede Scientific Instruments Ltd. My supervisor, Brian Tanner, has been a good source of information, support and useful contacts. The support I have received from Tamzin Lafford and Richard Bytheway, both from Bede Scientific Instruments Ltd, has been invaluable, not least because they brought an industrial perspective to the project and helped me to focus on practical application of phase contrast imaging. Their loan of equipment really helped to expand the project.

John Dobson made some major contributions to this project in the form of equipment design and production. He has also been my first port of call when the Microsource® developed problems or became temperamental! For other equipment production, the workshop has always done a great job for me, so my thanks go to: Phil Armstrong, Steve Lishman and George Teasdale. A number of staff from other research groups have allowed me access to their equipment, including: Andy Monkman, Naveed Zaidi, Ken Durose, David Patterson and Pauline Russell. I am especially grateful to Wayne Dobby and Ian Manfren for allowing me access to the Level 2 & 3 teaching laboratory facilities, and for loaning me a lot of equipment over the duration of the project. John Kotre at the Regional Medical Physics group, based at Newcastle General Hospital, has become a really valuable contact: the loan of a mammographic test object and his input during my results analysis has really helped to shape the direction of this project.

As an experimental physicist, I sought advice on the best way to go about the computing work on the theory side of the project. To this end I am grateful for pointers given to me by Gordon Love, Richard Wilson, Chris Saunter and Mark Swinbank. Thanks are also due to Antony Hill and James Buchanan for helping me to find my way around Matlab.

The members of the X-ray scattering team have all had an impact on this project, either by sharing equipment, giving me their opinion on results or simply putting a new idea in

my head during a discussion of my work. Over the course of this project, these have included: Tom Beale, James Buchanan, Sean Giblin, Tom Hase, Peter Hatton, Neil Parkinson, Alex Pym, Amir Rozatian, Phil Spencer, Brian Tanner, Ian Terry and Stuart Wilkins.

Norman Thompson and Clive Doloughon have been involved in issues relating to my hearing loss, and between them they have organized everything necessary to make sure that my hearing loss has never been a problem. This covered health and safety issues and communication, and I'm grateful to them both for their help in this matter.

A number of people have supported this project in a less direct way. These include my friends and contemporaries from undergraduate years. We have taken many opportunities to get together to take out our frustration during difficult parts of our respective postgraduate degrees, and this has provided one of my largest support bases.

My partner has provided support both intentionally and unintentionally. He has put up with tantrums and yelling when things have gone slowly in the lab, with no reproach, and has been pleased for me when things have gone well. He has never lost his ability to make me laugh even after the most difficult day in the lab, and has made me relax on weekends by taking me up hills to keep some perspective!

My brother has always been an inspiration, and his encouragement and the example of his undergraduate and postgraduate achievements have helped me to aim for my goals with that little bit more determination. And last but by no means least, my parents have never wavered in their support of my choices, and their encouragement and pride in my achievements has always boosted my work more than they realize. Their support during my PhD has been the biggest factor in my completing it.

Contents

List of Figures

List of Tables

1. Introduction

This project looks at the design of an in-line X-ray phase contrast imaging system, based around the Bede Microsource®, on a laboratory scale which is suited to imaging small pathological samples. The starting point for the project is to consider some background information on absorption and phase contrast imaging in the X-ray regime.

1.1 Absorption imaging with X-rays

W. C. Röntgen's discovery of X-rays in 1895 [1] paved the way for a huge branch of research and excellent medical diagnostic tools. For more than a century X-rays have been exploited for their ability to pass through matter to a greater or lesser extent. X-ray diffraction provides one of the main techniques for determining crystal structure of new materials while hospitals have benefited from the use of radiology equipment for detecting broken and fractured bones using X-ray images.

The type of X-ray image used by a radiology department is an absorption contrast image: the variation of intensity in this type of image shows the locations where X-rays have been absorbed to different extents in the object of interest. The first documented X-ray image shows a hand belonging to W. C. Röntgen's wife (Figure 1.1). The bones in her hand appear less intense than the rest of the tissue because they provide locations of higher density for the X-rays to travel through and hence more X-rays are absorbed. When a broken bone is imaged using radiological equipment in a hospital, the location of the break is seen in the image as a section of higher intensity because fewer X-rays are absorbed on propagating through this gap than by the sections of bone on either side.

Figure 1.1: An X-ray image of Frau Röntgen's hand, taken from [2]

In an absorption-contrast X-ray image, the boundaries can be unclear and weakly-absorbing materials or sections of similar densities are not resolved well, so while the images are very useful, they do not reveal all of the detail. In order to build up a detailed image with strong contrast, an unfeasibly long exposure time would be required. In the context of imaging pathological samples, this problem is partly reduced by staining the unresolved sections within the objects of interest with additional contrast media, usually iodine or barium compounds [6]. Due to the high atomic masses of iodine and barium, the stained tissues absorb X-rays more strongly than their unstained counterparts and the resulting absorption images display some additional detail. However, this adds substantial cost and preparation time to the imaging method and is inconvenient for the subject: it would be much more preferable to eliminate the need for contrast media altogether.

1.2 Optical phase-contrast imaging

Phase contrast was first discovered by Frits Zernike during his work with diffraction gratings, dating from 1920 [3]. He noticed that small flaws in the groove spacings affected the diffractive property of the grating, particularly if the flaw was repeated periodically along the length of the grating. The effect of this periodic flaw on the image gave the impression that a coarser grating was superimposed on the fine grating, leading to weak lines on each side of the strong spectral line. He referred to these as 'Rowland ghosts'. When he looked down at the grating along the line-of-sight of a spectral line, he saw that it was striped, rather than uniformly illuminated as he had expected. In

addition, when he used a small telescope to view the grating, the stripes disappeared when he focused on the grating surface. His interpretation of this was that the ghosts and principal line differed in phase.

Zernike introduced a reference surface to determine by how much these phases differed. He used a glass plate with a thin metallic surface which transmitted only a small amount of light, and scratched a fine slit in the metallic layer. This was then placed in the centre of the principal spectral line to broaden out the light in order to provide a coherent background with which the diffraction pattern could interfere. Using this set-up he determined that the ghosts and the principal line were out of phase by 90^{o}. In order to remove this phase difference, he then placed a glass plate in the spectrum, with a groove of $\lambda/2$ depth coinciding with the principal spectral line and the ghosts falling on the plain glass at either side of the groove. With the addition of this phase plate, the spectral line and ghosts all reached the telescope with equal phase and the stripes on the surface of the grating could be seen.

Zernike then extended this work to a microscope. An image of the light source is formed in the back focal plane of the microscope objective, made up of a central direct image and diffracted images on each side. This is analogous to the spectral line and Rowland ghosts of his previous experiment. The addition of his phase plate in the focal plane of the microscope objective brought the diffracted images and the direct image into phase with each other and the resultant image showed black and white contrast. Zernike suggested that this method should be named "phase-strip method for observing phase objects in good contrast" but eventually shortened it to "phase contrast method". This work earned Zernike a Nobel Prize in physics in 1953.

Ultimately, by using the phase contrast method, phase changes in the light, caused by transmission through a phase object, are transformed into intensity changes. Thus the intensity map of the image represents the changes in phase at each respective point in the phase object [4].

1.3 X-ray phase-contrast imaging

When an X-ray beam passes through a medium with variations in refractive index, phase gradients develop in the transmitted beam [5]. Techniques need to be developed to exploit this phenomenon and to extend the use of phase-contrast imaging to X-ray and other non-visible wavelengths. This would provide images displaying edge contrast at the boundaries between even weakly-absorbing materials in the X-ray regime, rather than relying solely on their poor absorption contrast property. An example of a phase contrast image is shown in Figure 1.2, together with an absorption image of the same object for comparison. Both of these images were taken during the course of this project.

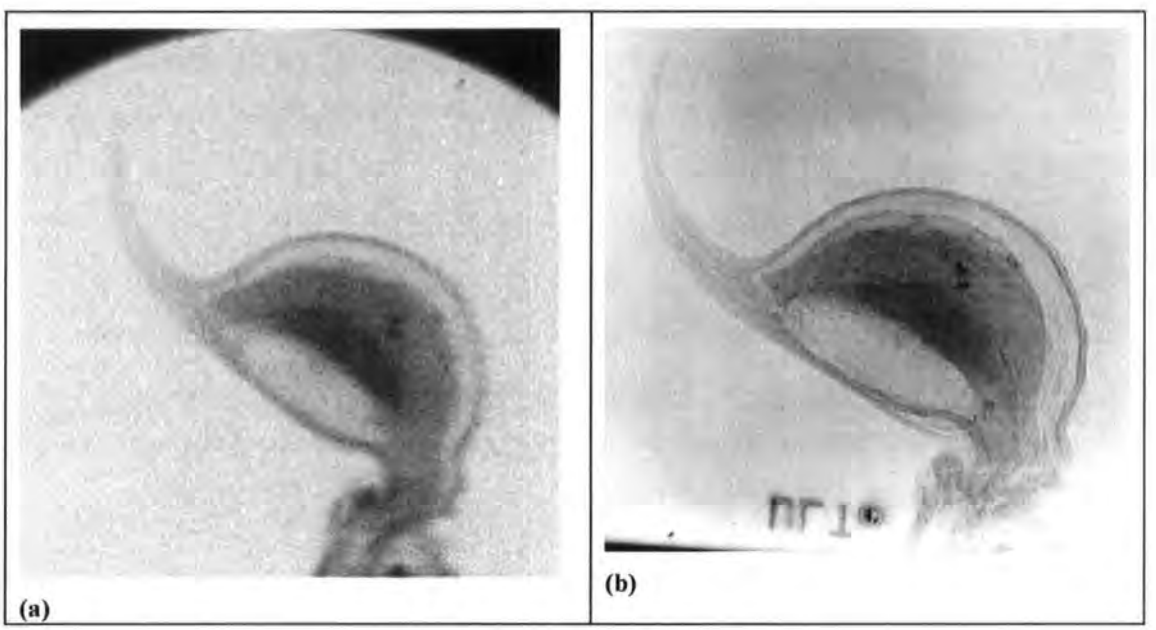

Figure 1.2: X-ray images of a scorpion sting:
(a) Absorption contrast, (b) Phase contrast.

The absorption image (figure 1.2(a)) shows the shape of the sting and the hinge attaching the sting to the tail, and it is seen that there is a crescent-shaped mass inside. The phase contrast image (figure 1.2(b)) goes further: the outline of the sting, the mass within, the connection between the sting and tail, and even the shaft through which the poison is injected into the prey, all show well-resolved edge contrast. The scorpion example will be revisited in chapter 6.

The scorpion comparison is a good example of the advantage of a phase contrast imaging system over traditional absorption imaging methods for an object containing weakly-absorbing sections. The advantages are not limited to the additional detail recorded within the images, however. In the context of pathological sample images, X-ray phase contrast imaging will eliminate the requirement for absorption-contrast-enhancing methods, ie 'staining' of samples with iodine or barium [6]. In addition, in the context of *in-vivo* imaging, phase contrast images of weakly-absorbing materials in the X-ray regime would require a lower dose than their absorption contrast counterparts, [47] due to the technique not requiring a long exposure time in order to build up sufficient differences in image intensity between sections of similar density.

Unfortunately, X-ray phase contrast images can be difficult to achieve because the small scale of X-ray wavelengths corresponds to very slight variations in the X-ray refractive indices of materials and so extremely sensitive detectors are required.

1.3.1 X-ray Interferometer

The first known attempt to achieve phase contrast images using X-rays was by Bonse and Hart [7] in 1965. This method uses a Mach-Zehnder-type X-ray interferometer (Figure 1.3) comprising a beamsplitter, two transmission mirrors and an analyser crystal, all made by carving two wide grooves into a single-crystal block.

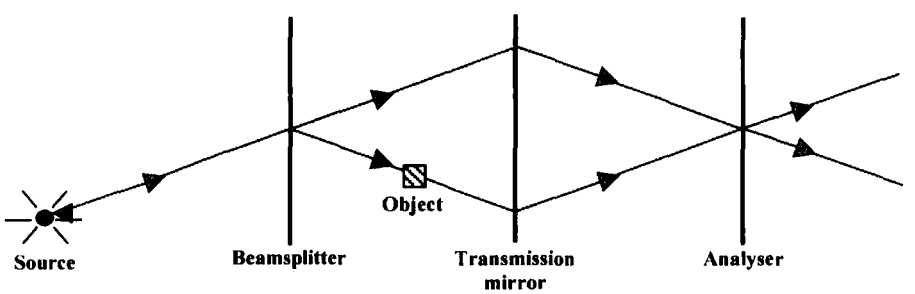

Figure 1.3: Schematic of X-ray interferometer technique

The beamsplitter uses Laue diffraction in order to split the incident beam into two coherent beams [7]. Objects of interest are placed in the path of one of these two beams

between the beamsplitter and the mirrors, thus the final image displays the interference fringes from the two beams after recombination. The object is often immersed in an index-matching liquid to suppress the refraction [6, 18-19]. Exposure of a uniform object yields equally-spaced fringes while local electron density (and hence refractive index) variations in an object are represented by a phase contrast topograph (6, 9-18, 20-38).

Using the X-ray interferometer on its own does not yield an image of the object itself, but it is the manipulation of the phase contrast topograph which gives the useful information. X-ray interferometers have since been combined with X-ray computed tomography methods [6, 9, 10-18, 20, 25-31, 35, 38-43]. The reference beam contains a wedge-shaped phase-shifter, which results in straight fringes with regularly-spaced intervals called carrier fringes. When a sample is added to the set-up, the carrier fringes are displaced due to the phase shift from the sample. The Fourier transform (FT) [6] of the interference fringes is taken, although the spatial resolution of the resulting image is limited by the carrier fringe interval. A fringe-scanning (FS) method [6] can also be used, which takes into account many images with varying phase shift by moving the wedge-shaped phase-shifter for each image. The images from both the FT and FS manipulations are then reconstructed using a computer tomography algorithm, and both methods extract a phase-contrast image from the interference patterns.

An alternative type of interferometer has also been used for phase-contrast imaging: the shearing interferometer [36, 38, 39, 44-46] (Figure 1.4). This shears the X-ray beams by only a small angle so they travel through different sections of the sample while remaining close together.

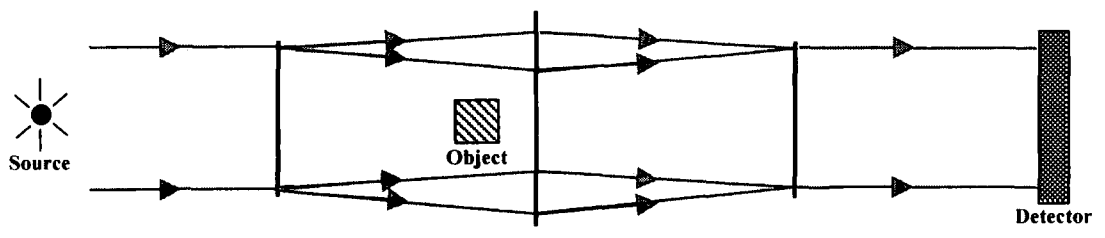

Figure 1.4: Schematic of shearing interferometer technique

Referring to Figure 1.4, the shearing interferometer comprises three transmission gratings and a detector: the first transmission grating diffracts the incident wave into $\pm 1^{st}$ orders; the second transmission grating recombines the split rays, and the third is an amplitude grating in the region of interference. This set-up provides differential phase contrast micrographs. Alternatively the first grating may be replaced with a prism [38, 45, 46], or the third may be replaced with an analyser crystal to deflect those X-rays propagating at a specific angle to the optical axis [44]. Again, this method may be teamed with computed tomography methods in order to yield a useful image.

Because the interferometer is usually cut from a single crystal block, the main drawback to the interferometer method is in the dimensions of the set-up. A typical length scale for the beamsplitter-transmission mirror or transmission mirror-analyser distance is ~34mm [6]. This has been increased to ~ 70mm for the standard shearing interferometer set-up [44] illustrated in Figure 1.4. This does limit the size of the samples, especially if the set-up includes the addition of a cell containing an index-matching liquid. Unless these dimensions are scaled up, the applications available to the single crystal interferometry method for phase-contrast imaging will remain severely limited. Less conventional interferometers, for example the shearing interferometer with a prism, allow for a larger space for samples, even of the order of several metres [45]. These dimensions are much more realistic, making the less conventional interferometry methods feasible for more applications. Of all phase contrast imaging techniques, interferometry comprises the most complex set-up due to the precisely-cut crystals required to form the beamsplitter, transmitter and interference planes. In addition, interferometry methods require the high spatial coherence and high-intensity monochromatic beams which are only achieved at synchrotron sources: thus interferometry methods are not available to a laboratory environment. However, once the system is calibrated with a reference beam, phase changes can be determined directly from the resulting phase maps which is a huge advantage.

1.3.2 In-line

Phase contrast images have also been achieved without using an interferometer. The simplest set-up is to use an X-ray source, object and detector, as shown in Figure 1.5.

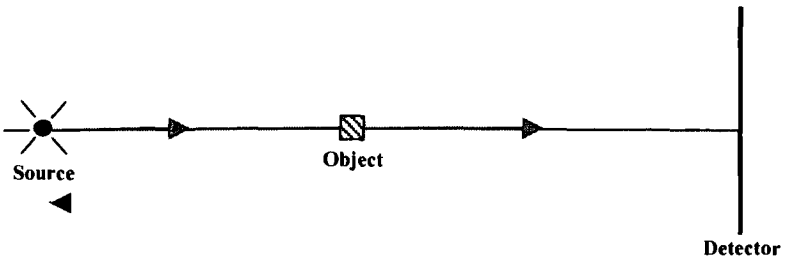

Figure 1.5: Schematic of simplest set-up for achievement of phase contrast

The transverse coherence length of the X-ray beam is inversely proportional to the source size:

$$d = \frac{\lambda l}{\sigma} \qquad (1\text{-}1) \qquad [48]$$

where λ is the wavelength, l is the source-sample distance and σ is the source size. So *ideally,* in order to provide spatially coherent radiation, the source size must be as small as possible, emulating a point source. While this simple method has been set up using synchrotron radiation [49], it has been demonstrated using a polychromatic laboratory source with a diameter of less than 20μm [48]. This provides a spatially coherent source but not a chromatically coherent one. Using an object comprising a combination of glass fibres and air bubbles confined in a polymer glue, Wilkins *et al* [48] captured images with the detector in two locations. When the detector was only 1mm from the object, absorption images were obtained which retained only a fraction of the detail, as expected. With the detector 1200mm from the object, the refracted X-rays were projected sufficiently to yield a detailed phase-contrast image.

Other methods used to achieve phase contrast are variations on the simple set-up described above. The majority of the documented experiments use monochromatic X-ray beams from synchrotron radiation sources [6, 9-18, 20-46, 49-147]. Synchrotron beamlines provide very intense, coherent X-ray beams which keep exposure times short.

The synchrotron radiation is usually monochromated because monochromation of the X-ray beam increases the contrast sensitivity (by elimination of the broadening effect caused by polychromatic radiation), and decreases the dose to the sample [151]. Some experiments have used laboratory sources [5, 7, 47, 48, 52, 64, 66, 74, 97, 146, 152 - 187]: copper is the most common target used in laboratory X-ray sources, but tungsten [160, 164], molybdenum [169] and silver [97, 180] tubes have also been used. Molybdenum tubes are commonly used for medical radiography and so it is useful to conduct research with the same X-ray characteristic energy. Again, for the reasons mentioned above, these sources are often partially monochromated.

1.3.3 Diffraction-Enhanced Imaging (DEI)

Provided the optical system is sensitive to the propagation direction of the X-rays, it should be capable of resolving phase gradients and so will be suitable for phase-contrast imaging [47]. This idea leads to a further useful modification to the simple set-up: the addition of an analyser crystal after the object [5, 47, 65, 95-147, 178-187]. This type of modified system is referred to as 'diffraction enhanced imaging', or DEI. A typical layout is shown in Figure 1.6.

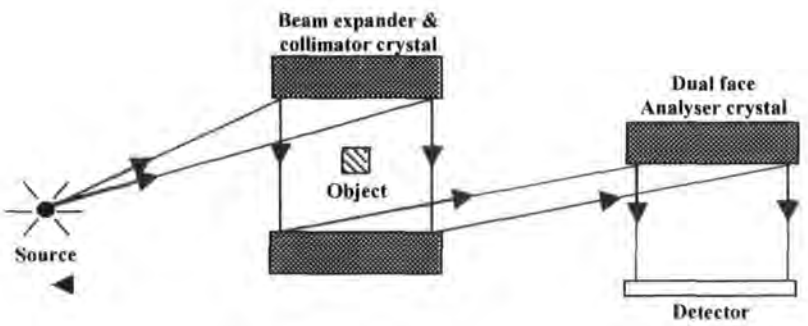

Figure 1.6: Schematic of diffraction-enhanced imaging technique

The beam expander and collimator crystal broadens out the X-ray beam to provide a plane wavefront. The plane wavefront is then distorted as it travels through the regions of varying refractive index in the object, and the addition of an analyser crystal to the set-up provides an angular filter for these distortions [47, 98]. The analyser crystal diffracts directly to the detector only those X-rays propagating in a chosen direction. By

changing the angle of the analyser, a number of images can be built up, each with different contrast for the features of the object. A further development of the DEI set-up includes a double monochromator with a prism between the two monochromator crystals in order to select different harmonic orders of the monochromated X-rays [103]. The introduction of an analyser crystal or prism to the set-up adds a distinct advantage because it is capable of obtaining a number of images of the same object, each with an emphasis on a different feature. However, because the analyser allows only a very narrow bandwidth to pass through, only a fraction of the source intensity reaches the detector, and so very high intensity sources are required. Much of the DEI work to date has been based at synchrotron facilities.

A recently developed method for phase contrast imaging exploits the Talbot effect [35]. This is a self-imaging phenomenon seen when a periodic object is illuminated by spatially coherent radiation. Examples of suitable objects include a grating or a mesh. This phenomenon is seen as a detector is moved along the optical axis, during which the self-image of the periodic object appears and disappears periodically. Talbot interferometry makes use of a second grating, placed at one of these self-image locations along the optical axis, at a slight angle to the vertical (typically 1 degree). The gratings generally have the same period. Illumination by plane waves generates a fringe pattern representing the superposition of the first grating's self-image with the periodic pattern of the second grating. On illumination by a curved wavefront, the fringe pattern is displaced. By placing a phase object in front of the first object, the fringe displacement can be used for phase information retrieval. To date, this method has been employed using synchrotron radiation and has been used to image a plastic sphere [35].

1.4 Current applications

Although X-rays are still most commonly used for absorption contrast imaging in research and in medical diagnostic applications, phase contrast imaging methods are becoming more widely used in research and are improving rapidly. Phase contrast imaging techniques can detect more detail than absorption contrast images in many objects including non-living biological specimens. To date, the phase-contrast imaging

techniques described above have been used to provide detailed images of a wide range of objects. The most common objects imaged by the above methods are some combination of fibres, bubbles or polymer spheres [5, 6, 8, 27, 32, 35, 37, 44, 47-51, 54, 57, 58, 61, 63, 69-71, 75, 80, 83-85, 90, 91, 104, 110, 112, 116, 117, 130, 134, 158, 163-166, 168, 169, 171, 173, 175-177, 182, 185, 186, 188 189, 208 - 210] because the edges of each of these objects are simple step-functions, making it easy to distinguish between absorption and phase contrast. Other non-biological objects imaged using these methods include bread [77], cochlear implant components [157], crystals [29, 36, 78, 98, 100, 102], crystal fibres [190, 191], diamond [60], electronic components [76, 171], graphite filters [149], laser-heated air [184], metallic objects [46, 53, 59, 82, 84, 88, 89, 107, 127, 177, 211], paper [49, 66, 163, 168, 192], hand phantoms [164], mammographic phantoms [28, 56, 65, 70, 81, 93, 96, 98-100, 108, 111, 113, 115, 121, 123, 140, 145, 155, 159, 160, 163, 167, 169, 73, 181, 193, 212], plastic objects [36, 111, 139, 164, 171], polymer/plastic sheets [160, 172, 174-176], photonic crystals [225], radioactive fuel particles [226], semiconductor devices [163, 168] and thin films and foils [5, 45, 47, 49, 59, 60, 68, 70, 168, 179, 181, 213]. Particularly sensitive systems have even achieved images of beryllium windows [149].

Some phase-contrast imaging techniques have been used on natural objects and substances, such as flowers [93], leaves [34, 47, 70, 120], plant roots [55, 80, 156], salt crystals [187], soil [156], water [134, 214], wood [70, 163] and Chinese medicines [215, 216].

Phase-contrast imaging is now moving towards medical applications, with the use of the techniques discussed above for the imaging of some pathological specimens. These include parts of bats [146], birds [74, 111, 175, 176], cows [147], dogs [87, 207], small fish [48, 154, 180, 182, 194], frogs [180], horses [207], various insects [47, 64, 79, 114, 128, 132, 133, 144, 154, 163, 168, 194, 217], marsupials [146], mice [16, 39, 41, 43, 63, 74, 83, 86, 94, 98, 100, 105, 111, 122, 140, 145, 151, 181, 195, 218, 219], rabbits [9, 15, 17, 18, 20, 26, 37, 69, 83, 207, 218, 220], rats [10, 15-18, 20, 37-38, 41-43, 58, 69, 73, 80, 138, 143, 221], oxen [222], shrimp [174] and wallabies [86]. Individual pathological

samples of interest have thus far included the following: blood [14, 22, 74], bones [62, 63, 74, 79, 147, 194, 195, 221, 223], brain tissue [138, 222], breast tissue [43, 56, 64, 65, 74, 92, 93, 97, 98, 101, 104, 105, 109, 126, 134, 135, 175, 176, 193, 224], cartilage [11, 74, 105, 106, 118, 119, 124, 125, 127, 130, 137, 142, 145, 148, 223], cancerous colon tissues [12, 43], eyes [87, 207], feathers [70], a foetal inner-ear [52], heart tissue [42], kidneys [16, 37, 43, 64, 143], legs [140, 145, 219], liver [12, 13, 21, 30, 37, 129, 152, 154], lungs [69, 74, 83, 86, 94, 120, 145, 154, 218, 220], thyroid glands [28, 141], teeth [72, 120] and uterus tissues [120, 136].

Many of the results gained from experiments with phase contrast imaging are qualitative images, showing contrast at boundaries between sections of different refractive index and comparing these to absorption images of the same object. Algorithms are currently being tested to reconstruct sample thicknesses [173] via computed tomography, although these are mainly limited to spherical objects. The ultimate limitation in resolution of phase contrast images is pixel size [50].

1.5 Toward shorter wavelengths

Further work in phase contrast imaging has recently begun at neutron wavelengths [196]. Phase contrast images have been achieved using both polychromatic [197-201] and monochromatic [199, 201, 203] neutrons from fusion [200] and spallation [198, 204] sources. Thermal neutrons [198-201, 203, 205] and cold neutrons [199, 204, 205] have both demonstrated their compatibility with phase contrast methods. The majority of work at these short wavelengths has involved an in-line set-up [197-200, 206], however interferometry has also proved successful [196, 202].

Samples imaged using neutron phase contrast methods to date include cog wheels [198], crystals [197], metal foams [198, 201, 205], meshes [198] and screws [203], polymer and ceramic materials [200], sulphur and water isotopes[202], syringe needles [198, 205] and a wasp [199]. Other than the wasp, biological samples have not yet been imaged using neutron phase contrast imaging according to published literature.

For the foreseeable future, phase contrast imaging with neutrons will be limited to major spallation and fusion sources because suitable laboratory sources are not yet available. Thus X-ray phase contrast imaging will become available to more applications, sooner, although there is much development work yet to be completed within both regimes. Much further work is required to develop reliable phase contrast methods within the laboratory, in order to move the field forward.

1.6 Overview of this project

Although synchrotron beamlines are available for phase contrast imaging techniques, the real way forward for commercial exploitation of phase contrast imaging is to develop laboratory-scale systems. With this in mind, this project investigates the effect of several factors within a laboratory-based imaging system which are expected to influence the phase contrast content of the images. The in-line method shows the most promise at the laboratory scale because the interferometry and DEI methods waste a significant amount of the incident intensity while the in-line method makes use of it all. For this reason, the in-line method is used in this project. A very simple object is used in the experiments, which has just one boundary, which allows for easy quantification of the phase contrast in the images.

One of the key differences between the in-line and absorption imaging set-ups is the propagation distance between the sample and the detector. So this project investigates the relationship between the propagation distance and phase contrast in order to determine the limiting propagation distance below which the system cannot achieve phase contrast images.

According to equation (1-1), the transverse coherence length is inversely proportional to the source size, and so it follows that the source size should be as small as possible. However while synchrotrons can achieve miniscule source sizes, laboratory-based sources generally achieve source dimensions of the order of tens of microns or larger. This project maps the relationship between source dimensions and phase contrast, with the aim of looking at how source size limits the phase contrast in practice.

Monochromatic X-rays are suitable for phase contrast imaging because the narrower the bandwidth, the smaller the spread in diffraction at a sample boundary. The high intensities of synchrotron sources allow for excellent monochromation of the X-rays while retaining more than sufficient intensity for imaging purposes. However, perfect monochromaticity is impossible to achieve with a laboratory source without removing a huge proportion of the intensity, so the options available are partially monochromated or fully polychromatic X-ray spectra. Both of these options are used in this project in order to check the system's capability in each case and to determine which option produces the better phase contrast.

Most samples used in phase contrast imaging to date have been very thin: small fibres, films or bubbles, slices of biological tissues. It is expected that as the thickness of a sample is increased, the absorption property of the material would provide more and more of the image contrast. So this project looks for practical limits on the achievable phase contrast as sample thickness is increased.

Although a number of pathological samples have been imaged in phase contrast systems (as detailed earlier in this chapter), according to the published literature no work has been done to investigate the effect of water on phase contrast imaging systems. Most pathological specimens contain huge amounts of water (human tissue being a prime example), so this is a gap in knowledge in the field which does need to be addressed. To this end, this project investigates the effects of increasing path lengths of water in the system and explains the results using a model of the system. A similar experiment is completed using glass in the system, with a view to finding out whether glass-mounted pathological specimens can be imaged.

After looking at the effects of the above factors on the imaging set-up and applying the lessons learned, the system is applied to a test object and a pathological sample in order to find out its capability of achieving phase contrast images of increasingly complex samples.

The layout of this thesis is as follows:

- Chapter 2 discusses the theory behind X-ray phase contrast imaging and reports on a simulation of an in-line set-up, which generates the phase contrast image expected for the single-boundary object used in most of the experiments.
- Chapter 3 discusses the experimental issues which were overcome before images could be recorded and analysed for this project.
- Chapter 4 reports on the experiments investigating the effects of sample position, source size, monochromaticity and sample thickness.
- Chapter 5 reports on the introduction of water and glass to the set-up
- Chapter 6 shows the images achieved for a mammographic test object and a scorpion sting.
- Chapter 7 concludes with a summary of the project's findings and a discussion of laboratory-based phase contrast imaging systems of the future.

References

[1] Bragg, *X-rays and crystal structure (4th Edn)*, G. Bell & Sons Ltd (1924)

[2] Rontgen W., Nature **52** pp.274

[3] Zernike F., *Science*, **121**, pp.345-349 (1955)

[4] Born & Wolf, *Principles of Optics: electromagnetic theory of propagation,*

[5] *interference and diffraction of light (7th Edn)*, Cambridge University Press (1999)

[6] Gao D. et al, *Aust. J. Phys.* **48** pp.103-111 (1995)

[7] Momose A., *Nucl. Instr. Meth A* **352** pp.622-628 (1995)

[8] Bonse U. & Hart M., *Appl. Phys. Lett.* **6** (8) pp.155-156 (1965)

[9] Momose A. et al., *Rev. Sci. Intrs.* **66** (2) pp.1434-1436 (1995)

[10] Momose A. et al., *Nature Medicine* **2** (4) pp.473-475 (1996)

[11] Beckmann F. et al., *J. Computer Assisted Tomography* **21** (4) pp.539-553 (1997)

[12] Momose A. et al., *J. Synchrotron Rad.* **5** pp.309-314 (1998)

[13] Takeda T. et al., *Radiology* **214** pp.298-301 (2000)

[14] Takeda T. et al., *J. Synchrotron. Rad.* **7** pp.280-282 (2000)

[15] Momose A. et al., *Radiology* **217** pp.593-596 (2000)

[16] Takeda T. et al., *Nucl. Instr. Meth A* **467-468** pp.1322-1325 (2001)

[17] Momose A, *J. Synchrotron Rad.* **9** pp.136-142 (2002)

[18] Yoneyama A. et al., *J. Synchrotron Rad.* **9** pp.277-281 (2002)

[19] Takeda T. et al., *Circulation* **105** pp.1708-1712 (2002)

[20] Sasaki I. et al., *Applied Optics* **21** (23) pp.4246-4252 (1982)

[21] Momose A. et al., *Rev. Sci. Intrs.* **66** (2) pp.1434-1436 (1995)

[22] Takeda T. et al., *Acad. Radiol.* **2** pp.799-803 (1995)

[23] Momose A. et al., *Acad. Radiol.* **2** pp.883-887 (1995)

[24] Momose A. et al., *Nature Medicine* **2** (5) pp.596 (1996)

[25] Hirano K. & Momose A, *Phys. Rev. Lett.* **76** (20) pp.3735-3737 (1996)

[26] Momose A. et al., *J. Synchrotron Rad.* **4** pp.311-312 (1997)

[27] Yoneyama A. et al., *Rev. Sci. Instr.* **70** (12) pp.4582-4586 (1999)

[28] Hirano K. et al., *Jpn. J. Appl. Phys* **38** pp.L1556-L1558 (1999)

[29] Takeda T. et al., *Cellular and Molecular Biology* **46** (6) pp.1077-1088 (2000)

[30] Bergamin A. et al., *J. Phys. D* **33** pp.2678-2682 (2000)

[31] Momose A. et al., *Nucl. Instr. Meth. A* **467-468** pp.917-920 (2001)

[32] Momose A. et al., *Analytical Sciences* **17** pp.i527 (2001)

[33] Yoneyama A. et al., *Jpn. J. Appl. Phys.* **41** pp.L161-L163 (2002)

[34] Koyama I. & Momose A., *Nucl. Instr. Meth. B* **199** pp.446-450 (2003)

[35] Koyama I. et al., *Jpn. J. Appl. Phys.* **42** pp.L80-L82 (2003)

[36] Momose A. et al., *Jpn. J. Appl. Phys.* **42** pp.L866-L868 (2003)

[37] David C, et al., J. Phys. IV **104** pp.595-598 (2003)

[38] Momose A. et al., J. Phys. IV **104** pp.599-602 (2003)

[39] Yoneyama A. et al., *Nucl. Instr. Meth. A* **523** pp.217-222 (2004)

[40] Momose A., *Optics Express* **11** (9) pp.2303-2314 (2003)

[41] Kohmura Y. et al., *J. Appl. Phys.* **96** (4) pp.1781-1784 (2004)

[42] Takeda T. et al., *Jap. J. Appl. Phys.*, **43** (9A) pp.L1144-L1146 (2004)

[43] Yoneyama A. et al., *J. Synchrotron Rad.*, **12** pp.534-536 (2005)

[44] Takeda T., *Nucl. Instr. Meth. A.*, **548** pp.38-46 (2005)

[45] David C. et al., *Appl. Phys. Lett.* **81** (17) pp.3287-3289 (2002)

[46] Kohmura Y. et al., *J. Appl. Phys.* **93** (4) pp.2283-2285 (2003)

[47] Kohmura Y. et al., J. Phys. IV **104** pp.571-574 (2003)

[48] Davis T. J. et al., *Nature* **373** pp.595-598 (1995)

[49] Wilkins S. W. et al., *Nature* **384**, pp.335-338 (1996)

[50] Snigirev A. et al., *Rev. Sci. Instr.*, **66** (12) pp.5486-5492 (1995)

[51] Raven C. et al., *Rev. Sci. Instr.*, **67** (9), 3359-3363 (1996)

[52] Raven C. et al., *Appl. Phys. Lett.*, **69** (13), pp.1826-1828 (1996)

[53] Momose A. & Takeda T., *Nature Medicine* **2** (8) pp.852-853 (1996)

[54] Snigirev A. et al., *Opt. Comms.* **135**, pp.378-384 (1997)

[55] Lagomarsino S. et al., *Appl. Phys. Lett.* **71** (18) pp.2557-2559 (1997)

[56] Yun W. et al., *J. Synchrotron Rad.* **5** pp.1390-1395 (1998)

[57] Arfelli F. et al., *Phys. Med. Biol* **43** pp.2845-2852 (1998)

[58] Jark W. et al., *Journal of Alloys and Compounds,* **286** pp.9-13 (1999)

[59] Beckmann F. et al., *Biophysical Journal*, **76** pp. 98-102 (1999)

[60] Cloetens P. et al., *J. Phys. D.* **32** pp.A145-A151 (1999)

[61] Kowalski G. et al., *J. Phys. D.* **32** pp.A166-A171 (1999)

[62] Gureyev T. E. et al., *J. Phys. D.* **32** pp.563-567 (1999)

[63] Mori K. Et al., *Jpn. J. Appl. Phys.* **38** pp.L1339-L1341 (1999)

[64] Gureyev T. E., *J. Digital Imaging,* **13** (2) Suppl 1 pp.121-126 (2000)

[65] Fitzgerald R., *Physics Today*, **53** (7) pp.23-26 (2000)

[66] Arfelli F. et al., *Radiology* **215** pp.286-293 (2000)

[67] Gureyev T. E. et al., *Tappi Journal* Feb 2001, p.52 (2001)

[68] Kagoshima Y. Et al., *Jpn. J. Appl. Phys.* **40** pp.L1190-L1192 (2001)

[69] Gureyev T. E. et al., *J. Synchrotron Rad.* **9** pp.148-153 (2002)

[70] Suzuki Y. et al., *J, Synchrotron Rad.* **9** pp.160-165 (2002)

[71] Stevenson A. W., *Nucl. Instr. Meth. Phys. B* **199** pp427-435 (2003)

[72] Kagoshima Y. et al., *J. Phys IV France* **104** pp.49-52 (2003)

[73] Stock S. R. et al., *J. Synchrotron Rad.* **10** pp.393-397 (2003)

[74] Rao D. V., *Nucl. Instr. Meth. A* **523** pp.206-216 (2004)

[75] Lewis R. A., *Phys. Med. Biol.* **49** pp.3573-3583 (2004)

[76] Yokosuka H. et al., J. Phys. IV **104** pp.591-594 (2004)

[77] Neuhäusler U. et al, J. Phys. IV **104** pp.567-570 (2004)

[78] Falcone P. M. et al., J. Food Science **69** (1) pp.38-43 (2004)

[79] Hu Z. W., Acta Crystallographica D **60** pp.621-629 (2004)

[80] Paganin D. et al., J. Microscopy **214** (3) pp.315-327 (2004)

[81] Kocsis M. & Snigirev A., *Nucl. Instr. Meth. A*, **525** pp.79-84 (2004)

[82] Pagot E. et al., *Phys. Med. Biol.*, **50** pp.709-724 (2004)

[83] Peele A. G. & Nugent K. A., *Rev. Sci. Instr.*, **75** (10) pp.3382-3386 (2004)

[84] Kitchen M. J. et al., *Phys. Med. Biol.*, **49** pp.4335-4348 (2004)

[85] Monin P. et al., *Med. Phys.*, **31** (6) pp.1372-1383 (2004)

[86] Coan P. et al., *J. Synchrotron Rad.*, **12** pp.241-245 (2005)

[87] Lewis R. A., *Nucl. Instr. Meth. A.*, **548** pp.23-29 (2005)

[88] Antunes A. et al., *J. Phys. D.*, **38** pp.A85-A88 (2005)

[89] Agliozzo S. et al, *J. Cryst. Growth,* **281** pp.623-638 (2005)

[90] Brunello E. et al., *J. Cryst. Growth,* **282** pp.228-235 (2005)

[91] Xiao T. Q. et al., *Nucl. Instr. Meth. A.*, **548** pp.155-162 (2005)

[92] Hirano M. et al., *Nucl. Instr. Meth. A.*, **548** pp.187-193 (2005)

[93] Olivo A. et al., *Nucl. Meth. Phys. A.*, **548** pp.194-199 (2005)

[94] Abrami A. et al., *Nucl. Instr. Meth. A.*, **548** pp.221-227 (2005)

[95] Kitchen M. J. et al., *Nucl. Instr. Meth. A.*, **548** pp.240-246 (2005)

[96] Gureyev T. E. & Wilkins S. W., *Il Nuovo Cimento* **19D** (2-4) pp.545-552 (1997)

[97] Chapman D. et al., *Phys. Med. Biol.* **42** pp.2015-2025 (1997)

[98] Ingal V. N. et al., Phys. Med. Biol. **43** pp.2555-2567 (1998)

[99] Menk R. H., *Nucl. Phys. B (Proc. Suppl.)* **78** pp.604-609 (1999)

[100] Dilmanian F. A. et al., *Phys. Med. Biol.* **45** pp.933-946 (2000)

[101] Zhong Z. et al., *Nucl. Instr. Meth. A* **450** pp.556-567 (2000)

[102] Pisano E. D. et al., *Radiology* **214** pp.895-901 (2000)

[103] Kobayashi K., *Appl. Phys. Lett.* **78** (1) pp.132-134 (2001)

[104] Zhong Z. et al., *Rev. Sci. Instr.* **73** (3) pp.1614 (2002)

[105] Hasnah M. et al., *Rev. Sci. Instr.* **73** (3) pp.1657-1659 (2002)

[106] Zhong Z. et al., *Synchrotron Radiation News* **15** (6) pp.27-34 (2002)

[107] Mollenhauer J. et al., *Osteoarthritis and Cartilage* **10** pp.163-171 (2002)

[108] Kagoshima Y. et al., *J. Synchrotron Rad.* **9** pp.132-135 (2002)

[109] Kiss M. Z. et al., *Nucl. Instr. Meth. A* **491** pp.280-290 (2002)

[110] Hasnah M. O. et al., *Med. Phys.* **29** (10) pp.2216-2221 (2002)

[111] Hasnah M. et al., *Nucl. Instr. Meth A* **492** pp.236-240 (2002)

[112] Lewis R. A., *Medical Imaging 2002: Physics of medical imaging, Proceedings of SPIE* Vol 4682 pp.286-297(2002)

[113] Cheung K.-C. et al., *Nucl. Instr. Meth. A* **513** pp.32-35 (2003)

[114] Bravin A., *J. Phys. D* **36** pp.A24-A29 (2003)

[115] Hirano K., *J. Phys. D* **36** pp.1469-1472 (2003)

[116] Pagot E. et al., *Appl. Phys. Lett.* **82** (20) pp.3421-3423 (2003)

[117] Kiss M. Z. et al., *Phys. Med. Biol.* **48** pp.325-340 (2003)

[118] Oltulu O. et al., *J. Phys. D* **36** pp.2152-2156 (2003)

[119] Muehleman C. et al., *The Anatomical Record A* **272** (A) pp.392-397 (2003)

[120] Li J. et al., *J. Anat.* **202** pp.463-470 (2003)

[121] Giles C. et al., *J. Synchrotron Rad.* **10** pp.421-423 (2003)

[122] Rigon L. et al., *J. Phys. D* **36** pp.A107-A112 (2003)

[123] Lewis R. A. et al., *British Journal of Radiology* **76** pp.301-308 (2003)

[124] Dendy P. & Harrison R., *British Journal of Radiology* **76** pp.289 (2003)

[125] Bravin A. et al., *Nucl. Instr. Meth A* **510** pp.35-40 (2003)

[126] Muehleman C. et al., *Osteoarthritis and Cartilage* **12** pp.97-105 (2004)

[127] Fiedler S. et al., *Phys. Med. Biol.* **49** pp.175-188 (2004)

[128] Levine L. E. & Long G. G., J. Appl. Crystallography **37** pp.757-765 (2004)

[129] Li G., *Chinese Science Bulletin* **49** (20) pp.2120-2125 (2004)

[130] Jiang X. M. et al., *High Energy Physics and Nuclear Physics*, **28** (12) pp.1282-1290 (2004)

[131] Li J. et al., *Osteoarthritis and Cartilage* **13** pp.187-197 (2005)

[132] Yeo A. et al., *J. Membrane Sci.*, **250** pp.189-193 (2005)

[133] Zhu P.-P., *Acta Physica Sinica*, **54** (1) pp.58-63 (2005)

[134] Huang W.-X., *Acta Physica Sinica*, **54** (2) pp.677-681 (2005)

[135] Hasnah M. O. et al., *Med. Phys.*, **32** (2) pp.549-552 (2005)

[136] Keyriläinen J. et al., *European J. Radiology* **53** pp.226-237 (2005)

[137] Liu C. et al., *Med. Sci. Monit.*, **11** (5) pp.MT33-MT38 (2005)

[138] Wagner A. et al., *Nucl. Instr. Meth. A.*, **548** pp.47-53 (2005)

[139] Mannan K. A. et al., *Nucl. Instr. Meth. A.*, **548** pp.106-110 (2005)

[140] Pavlov K. M. et al., *Nucl. Instr. Meth. A.*, **548** pp.163-168 (2005)

[141] Siu K. K. W. et al., *Nucl. Instr. Meth. A.*, **548** pp.169-174 (2005)

[142] Rocha H. S. et al., *Nucl. Instr. Meth. A.*, **548** pp.175-180 (2005)

[143] Ibison M. et al., *Nucl. Instr. Meth. A.*, **548** pp.181-186 (2005)

[144] Gang L. et al., *Nucl. Instr. Meth. A.*, **548** pp.200-206 (2005)

[145] Hönnicke M. G. et al., *Nucl. Instr. Meth. A.*, **548** pp.207-212 (2005)

[146] Menk R.-H. et al., *Nucl. Instr. Meth. A.*, **548** pp.213-220 (2005)

[147] Rocha H. S. et al., *Nucl. Instr. Meth. A.*, **548** pp.228-233 (2005)

[148] Connor D. M. et al., *Nucl. Instr. Meth. A.*, **548** pp.234-239 (2005)

[149] Takeda T. et al., *Jap. J. Appl. Phys.*, **43** (8A) pp.5652-5656 (2004)

[150] Yabashi M. et al., *J. Phys. D: Appl. Phys.*, **38** pp.A11-A16 (2005)

[151] Chang S.-L. et al., *Phys. Rev. Lett.*, **94** pp.174801/1-174801/4 (2005)

[152] Ingal, V. N. & Beliaevskaya E. A., *Phys. Med.* **12** (2) pp.75-81 (1996)

[153] Pogany A. et al., *Rev. Sci. Instr.* **68** (7) pp.2774-2782 (1997)

[154] Gureyev T. E. et al., *J. Opt. Soc. Am. A* **15** (3) pp.579-585 (1998)

[155] Gao D. et al., *Radiographics* **18** (5) pp.1257-1267 (1998)

[156] Kotre C. J. & Birch I. P., *Phys. Med. Biol.* **44** pp. 2853-2866 (1999)

[157] Moran C. J. et al., *Plant and Soil,* **223** pp99-115 (2000)

[158] Xu J. et al., *Otology & Neurotology"* **22** pp.862-868 (2001)

[159] Gureyev T. E., *Phys. Rev. Lett.* **86** (25) pp.5827-5830 (2001)

[160] Kotre C. J. et al., *British Journal of Radiology,* **75** pp.170-173 (2002)

[161] Donnelly E. F., Med. Phys. **29** (6) pp.999-1002 (2002)

[162] Bushuev V. A. et al., *Metallofiz. Noveish. Tekhnol.* **24** (4) pp.559-569 (2002)

[163] Paganin D. et al., *J. Microscopy* **206** (1) pp.33-40 (2002)

[164] Mayo S. C. et al., *J. Microscopy* **207** (2) pp.79-96 (2002)

[165] Ohara H. et al., *Medical imaging 2002: Physics of medical imaging, Proceedings of SPIE* Vol 4682 pp.713-723 (2002)

[166] Donnelly E. F., *Med. Phys.* **30** (9) pp.2292-2296 (2003)

[167] Hong Y. U. et al., *Chin. Phys. Lett.* **20** (2) pp220-222 (2003)

[168] Wu X. & Liu H., *Med. Phys.* **30** (8) pp.2169-2179 (2003)

[169] Mayo S. C. et al., *Opt. Express* **11** (19) pp.2289-2302 (2003)

[170] Freedman M. T. et al., *Medical Imaging 2003: Physics of medical Imaging, Proceedings of SPIE* Vol.5030 pp.533-540 (2003)

[171] Faulkner H.M.L. & Rodenburg J. M., *Phys. Rev. Lett.* **93** (2) pp.023903-1-4 (2004)

[172] Mayo S. C. et al., J. Phys. IV **104** pp.543-546 (2004)

[173] Gureyev T. E. et al., *Opt. Comm.*, **240** pp.81-88 (2004)

[174] Gureyev T. E. et al., *Phys. Rev. Lett.*, **93** (6) pp.068103/1-068103/4 (2004)

[175] Han S. et al., *Rev. Sci. Instr.***75** (10) pp.3146-3151 (2004)

[176] Bailat C. J. et al., *Appl. Phys. Lett.*, **85** (19) pp.4517-4519 (2004)

[177] Hamilton T. J. et al., *Phys. Med. Biol.*, **49** pp.4985-4996 (2004)

[178] Krimmel S. et al., *Nucl. Instr. Meth. A.*, **542** pp.399-407 (2005)

[179] Davis T. J. ET AL., *Phys. Rev. Lett.* **74** (16) pp.3173-3177 (1995)

[180] Davis T. J. et al., *J. Opt. Soc. Am. A* **13** (6) pp.1193-1198 (1996)

[181] Ingal, V. N. & Beliaevskaya E. A., *Phys. Med.* **12** (2) pp.75-81 (1996)

[182] Ingal V. N. & Beliaevskaya E. A., *Zh. Tekh. Fiz.* **67** (1) pp.68-77 (1997)

[183] Ingal, V. N. & Belyaevskaya E. A., *Tech. Phys.* **42** (1) (1997)

[184] Bushuev V. A. et al., *Il Nuovo Cimento* **19D** (2-4) pp.513-520 (1997)

[185] Bushuev V A, Petrakov A P, "X-ray phase contrast of laser-heated air space", *Cryst. Rep.* **46** (2) pp.171-175 (2001)

[186] Keyriläinen J. et al., *Nucl. Instr. Meth. A* **488** pp.419-427 (2002)

[187] Petrakov A. P., *Tech. Phys.* **48** (5) pp.607-611 (2003)

[188] Petrakov A. P. & Kryazhev A. A., *Tech. Phys.*, **49** (10) pp.1381-1383 (2004)

[189] Gureyev T. E. et al., *Appl. Opt.* **43** (12) pp.2418-2430 (2004)

[190] Pavlov K. M. et al., *J. Phys. D: Appl. Phys.* **37** pp.2746-2750 (2004)

[191] Barbosa L. B. et al., *J. Crystal Grow.* **235** pp.327-332 (2002)

[192] De Almeida Silva R. et al., *J. Cryst. Growth* **262** pp.246-250 (2004)

[193] Homstad R. et al., *Pulp & Paper Canada* **104** (7) pp.T186-T189 (2003)

[194] Wu X. & Liu H., *Med. Phys.* **31** (5) pp.997-1002 (2004)

[195] Pogany A. et al., *Acta Physica Sinica* **49** (12) pp.2357-2368 (2000)

[196] Van der Veen F. & Pfeiffer F., *J. Phys.: Condens. Matter* **16** pp.5003-5030 (2004)

[197] Becker P. et al., Cryst. Res. Technol. **36** pp.589-600 (2001)

[198] McMahon P. J. et al., *Phys. Rev. Lett.* **91** (14) pp.145502.1-145502.4 (2003)

[199] Kardjilov N. et al., *Nucl. Instr. Meth A* **527** pp.519-530 (2004)

[200] Jacobson D. L., Applied *Radiation and Isotopes* **61** pp.547-550 (2004)

[201] Bastürk M. et al., *Nucl. Instr. Meth. A.*, **542** pp.106-115 (2005)

[202] Lehmann E. et al., *Nucl. Instr. Meth. A.*, **542** pp.95-99 (2005)

[203] Zawisky M. et al., *Europhysics Letters* **68** (3) pp.337-343 (2004)

[204] Dubus F. et al., *IEEE Transactions on Nuclear Science*, **52** (1) pp.364-370 (2005)

[205] Kühne G. et al., *Nucl. Instr. Meth. A.*, **542** pp.264-270 (2005)

[206] Kardijilov N. et al., *Nucl. Instr. Meth. A.*, **542** pp.100-105 (2005)

[207] Chen J. W. et al., *Acta Physica Sinica*, **54** (3) pp.1132-1135 (2005)

[208] Antunes A. et al., *Nucl. Instr. Meth. B.*, **238** pp.28-31 (2005)

[209] Chen J. W. et al., *Acta Physica Sinica*, **54** (3) pp.1132-1135 (2005)

[210] Antunes A. et al., *Nucl. Instr. Meth. B.*, **238** pp.28-31 (2005)

[211] Hönnicke M. G. et al, *Rev. Sci. Instr.*, **76** (9) pp.093703 (2005)

[212] Peele A. G. et al., *Rev. Sci. Instr.* **76** (8) pp.083707

[213] Momose A. et al., *Macromolecules*, **38** (16) pp.7179-7200 (2005)

[214] Ignatiev K. I. et al., *Philosophical Magazine*, **85** (28) pp.3273-3300 (2005)

[215] Briedis D. et al., Phys. Med. Biol., **50** (15) pp.3599-3611 (2005)

[216] Vogt U. et al., *Opt. Lett.*, **30** (16) pp.2167-2169 (2005)

[217] Otten A. et al, *J. Synchrotron Rad.*, **12** pp.745-750 (2005)

[218] Wei X. et al., *Phys. Med. Biol.*, **50** (18) pp.4277-4286 (2005)

[219] Wei X. et al., *Chinese Phys. Lett.*, **22** (9) pp.2255-2258 (2005)

[220] Peele A. G. et al., *Rev. Sci. Instr.* **76** (8) pp.083707

[221] Kitchen M. J. et al., *Brit. J. Radiol.*, **78** (935) pp.1018-1027 (2005)

[222] Yoneyama A. et al., *Appl. Opt.*, **44** (16) pp.3258-3261 (2005)

[223] Lewis R. A. et al., *Phys. Med. Biol.*, **50** (21) pp.5031-5040 (2005)

[224] Yu Y. Q. et al., *Skeletal radiology*, **35** (3) pp.156-164 (2006)

[225] Hönnicke M. G. et al., *J. Synchrotron. Rad.*, **12** pp.701-706 (2005)

[226] Koyama I. et al., *Jap. J. Appl. Phys*, **44** (11) pp.8219-8221 (2005)

[227] Liu C. L. et al., *High Energy Physics and Nuclear Physics*, **29** pp.130-132 (2005)

[228] Petukhov A. V. et al, *J. Appl. Cryst,*, **39** pp.137-144 (2006)

[229] Snigireva I. et al., *J. Environmental Monitoring*, **8** (1) pp.33-42 (2006)

2. Theory of X-ray phase contrast imaging

An essential part of any project's initiation is to look at the underlying theory. This chapter includes an introduction to X-ray phase contrast imaging theory and discusses why some materials are more suited to phase contrast imaging than absorption contrast imaging and vice versa.

It is helpful to model an imaging system in order to gain some idea of the images that can be expected, in fact some of the published literature in the field discusses simulations of phase contrast images. Examples of samples used in these simulations include cylinders [1] and a photograph of a woman's face [2]. Later in this chapter, a simulation of an in-line phase contrast imaging system is discussed, with a simple single-boundary sample in place. This simulation provides an idea of how the corresponding phase contrast images should look, in advance of obtaining phase contrast images of a similar sample in practice.

2.1 Index of refraction

In order to discuss the behaviour of an X-ray wavefront as it travels through a sample, it is necessary to begin with the index of refraction. Both phase and absorption imaging rely on the refractive index of the material of a given sample. This is given by the following:

$$n = 1 - \delta + i\beta \qquad (2\text{-}1) \qquad [3]$$

The absorption of radiation intensity is governed by the complex part of the refractive index, the refractive index increment, given by:

$$\beta = \frac{n_a r_e \lambda^2}{2\pi} f_c \qquad (2\text{-}2) \qquad [4]$$

where n_a represents the concentration of atoms per unit volume, r_e the classical electron radius, λ the wavelength of incident radiation and f_c the complex part of the atomic

scattering factor. This refractive index increment contributes to the absorption coefficient as follows:

$$\mu = -\frac{2\pi}{\lambda}\int_{-\infty}^{0}\beta dz \quad \text{(2-3).} \qquad [5]$$

The absorption coefficient, μ, determines the X-ray absorbance of the material. As a wavefront propagates through a given material, the intensity is absorbed exponentially according to the following:

$$I = I_0 \exp(-\mu z) \quad \text{(2-4)} \qquad [6]$$

where I_0 and I are the incident and transmitted intensities respectively, and z the thickness of the material.

The prominent X-ray interaction mechanisms which contribute to a material's X-ray absorbance are the following:

- Photoelectric absorption;
- Compton scattering [7].

When an X-ray photon collides with an electron in the material, if the X-ray energy is higher than the binding energy of the shell, the electron is ejected from the shell. The initial energy of the X-ray photon is partly used in ejecting the electron and the rest provides the kinetic energy for the ejected electron. The hole created by the photoelectron is filled by an electron falling from a higher energy (shell), with the release of a photon of energy equal to the difference in the two shell energies. This photon can then be absorbed further with the ejection of lower energy Auger electrons. So all of the original photon energy has been converted and photoelectric absorption has occurred.

X-ray photons can also 'bounce off' free electrons in a material. This causes the electron to recoil, using part of the photon energy as kinetic energy, while the photon is scattered on a different path, at a lower energy. The photon can scatter in any direction, and in

imaging, the net result of this interaction is that photons can potentially be scattered into sections of an image which should show a low photon count. These photons do not contribute helpful information, behaving like a 'veil' across the image, so some methods are used to eliminate the scattering effect in X-ray imaging. One option is to make use of an anti-scatter grid [8], which consists of very thin, parallel strips of lead held together by a material with a low atomic number. The lead absorbs incident photons which propagate at an angle to the optic axis, reducing the scattered radiation incident on the detector. An alternative option is simply to use an 'air gap' [9] between the sample and the detector, which allows most of the scattered X-rays to miss the detector altogether. This 'air gap' is in fact an intrinsic part of the set-up for in-line phase contrast imaging, with a significant propagation distance required between the sample and the detector. So Compton scattering should not be present to a significant extent in most of the images in this project, except where the sample and detector are placed adjacent to one another.

The probability that photoelectric absorption occurs is proportional to the atomic number of the sample material and inversely proportional to the cube of the photon energy. The probability that Compton scattering will occur is independent of atomic number and varies very slowly with photon energy [7]. So for light materials, to which phase contrast imaging is mainly applied, photoelectric absorption would occur less at high energies (e.g. rhodium X-rays) than at low energies (e.g. copper X-rays), and the Compton effect would be more significant than photoelectric absorption (in the absence of an air gap or other anti-scatter technique) at all energies [7].

The phase of the wavefront is governed by the real part of the refractive index, the refractive index decrement, δ, given by:

$$\delta = \frac{n_a r_e \lambda^2}{2\pi} f_r \quad (2\text{-}5). \qquad [5]$$

The variables represented are the same as those in equation (2-2), with f_r the real part of the atomic scattering factor. As a wavefront propagates through a given material, the phase is modified as follows:

$$\Delta\phi = -\frac{2\pi}{\lambda}\int_{-\infty}^{0}\delta dz \quad (2\text{-}6), \qquad [10]$$

where z is the material thickness.

To provide examples of the behaviour of the refractive index increment and decrement with X-ray energy, both of these variables are generated using XOP software (provided by the ESRF) for polymethylmethacrylate (PMMA) and lead. PMMA is a weakly-absorbing polymer while lead is a very strongly absorbing metal. The refractive index increment and decrement for lead are shown in figure 2.1.

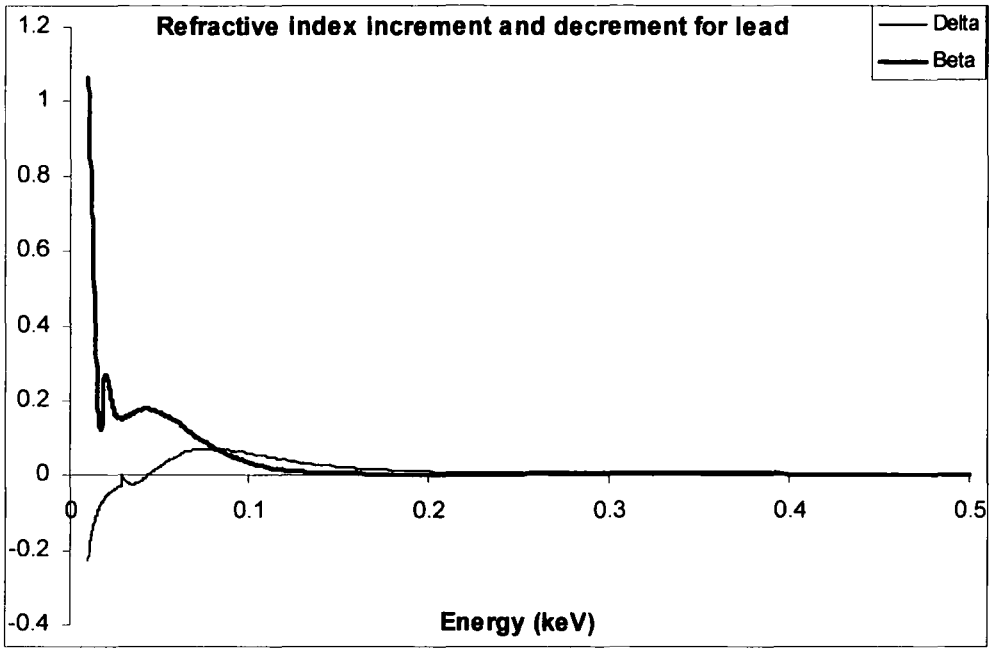

(a)

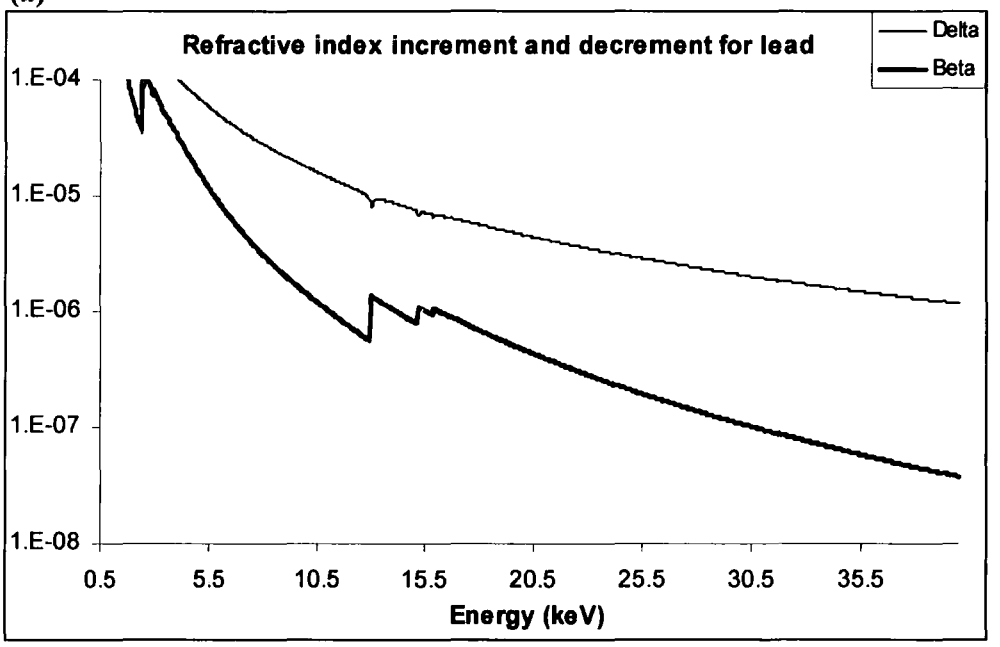

(b)

Figure 2.1: Refractive index increment and decrement for lead, (a) 0–0.5keV, (b) 0.5keV–40keV

The information in figure 2.1 is split into a high-energy chart and a low-energy chart in order to show the behaviour in detail at both ends of the scale. At very low energies (less than 0.1keV), it is seen that for a typical strongly-absorbing material, the absorption

component of the refractive index has very high values. At commonly-used X-ray energies (1keV – 40keV), however, it is seen that the phase component of the refractive index is comparable to the absorption component (within a factor of 10^2). Thus for strongly-absorbing materials, exploitation of the absorption properties at X-ray wavelengths will yield as much information as the refractive index allows.

The refractive index increment and decrement for PMMA are shown in figure 2.2 for 0.5-40keV.

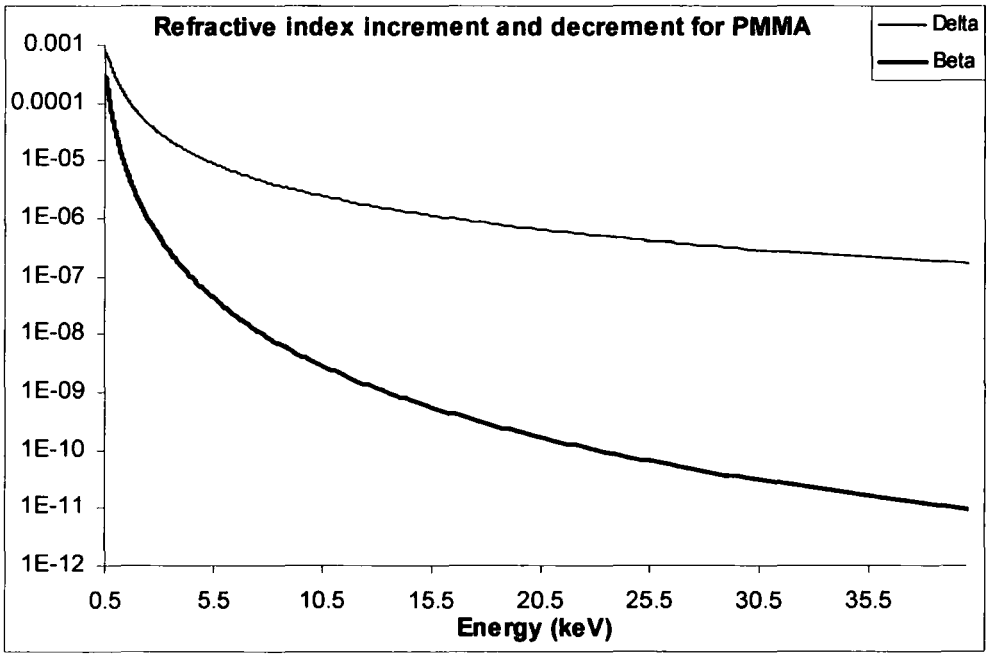

Figure 2.2: Refractive index increment and decrement for PMMA, 0.5keV–40keV

At commonly-used X-ray energies (1keV – 40keV), it is seen that for a typical weakly-absorbing material, the phase component of the refractive index is several orders of magnitude higher than the absorption component. Thus for weakly-absorbing materials, exploitation of the phase properties at X-ray wavelengths will yield far more information than exploitation of the absorption properties.

2.2 Models of a flat wavefront through an in-line set-up

In order to model a wavefront through a phase object in an in-line set-up, it is necessary to determine whether Fresnel or Fraunhofer diffraction will occur. This is done by determining the Rayleigh length, R, as follows:

$$R = \frac{a^2}{\lambda} \quad (2\text{-}7) \qquad [11]$$

where a is the aperture or obstacle size, and λ the wavelength. The Rayleigh length is compared to the sample-detector distance within the set-up, over which the transmitted X-rays propagate to the image plane. A propagation distance longer than the Rayleigh length results in Fraunhofer diffraction, while a propagation distance shorter than the Rayleigh length results in Fresnel diffraction. Consider an initial source size of the order ~10μm in diameter, using copper X-rays with an energy of 8.048keV (wavelength 1.54Å). The Rayleigh length in this situation, calculated using equation 2-7, is 0.649m. Consider the same source size, using rhodium X-rays with an energy of 20.216keV (wavelength 0.61 Å). The Rayleigh length in this situation, calculated using equation 2-7, is 1.64m. Assuming a source – detector distance of less than 0.60m, Fresnel diffraction occurs in both cases.

The in-line set-up is modelled using Matlab, and the corresponding programs are included in Appendix A.

A flat wavefront is simulated in this model. It is assumed that the sample is far from the source, so the radius of curvature of the diverging wavefront is large enough to allow approximation to a flat wavefront. Initially, the following flat wavefront, Ψ, is generated with phase, ϕ, set to zero.

$$\Psi = 1000\exp(i\phi) \qquad (2\text{-}8)$$

The wave amplitude is represented by a constant factor of 1000 across the wavefront. The phase component, with a value of 0i, also remains constant across the wavefront.

The amplitude and phase components of Ψ, as generated by the program, are plotted separately in figure 2.3.

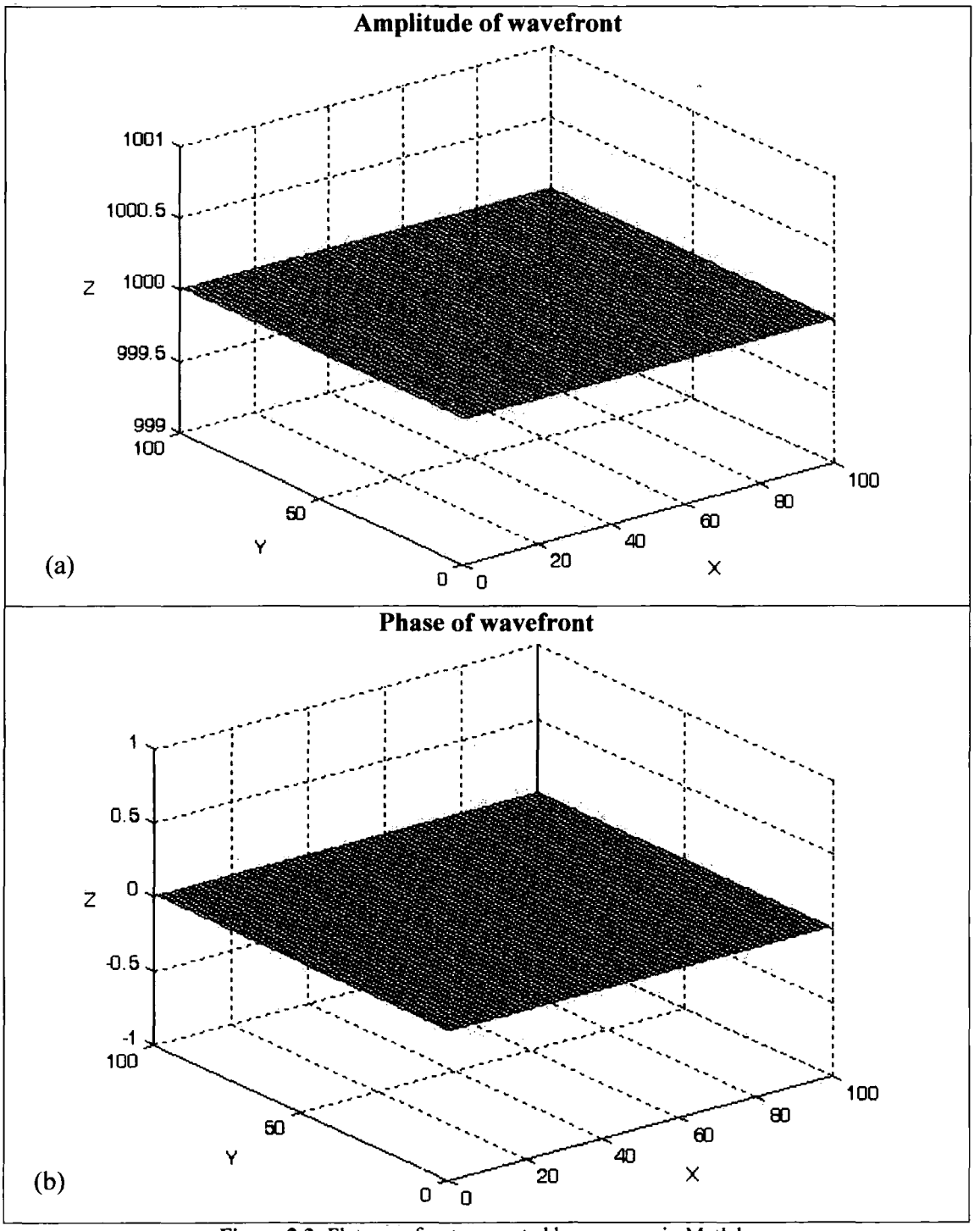

Figure 2.3: Flat wavefront generated by program in Matlab.

(a) Amplitude and (b) Phase of wavefront.

In order to provide a phase object which can be easily reproduced in practice, a step function is applied such that:

$$x < 0 \text{ or } x = 0: \qquad \Delta\phi = \frac{-2\pi}{\lambda}\delta z \qquad (2\text{-}9)$$

$$x > 0: \qquad \Delta\phi = \frac{-2\pi}{\lambda}2\delta z \qquad (2\text{-}10)$$

This represents the X-rays passing through an object made of the same material throughout, but of different thickness on either side of a central boundary. In reality, this will introduce an absorption component, and so an additional absorption step function is simulated such that:

$$x < 0 \text{ or } x = 0: \qquad I = I_0 \exp(-\mu z) \qquad (2\text{-}11)$$

$$x > 0: \qquad I = I_0 \exp(-2\mu z) \qquad (2\text{-}12)$$

The program simulates the transmission of the flat wavefront through such a step-function phase object via the following calculation:

$$x < 0 \text{ or } x = 0: \qquad \Psi_{Step} = \Psi_0 \exp(-\mu z)\exp\left(-\frac{2\pi i}{\lambda}\delta z\right) \qquad (2\text{-}13)$$

$$x > 0: \qquad \Psi_{Step} = \Psi_0 \exp(-2\mu z)\exp\left(-\frac{4\pi i}{\lambda}\delta z\right) \qquad (2\text{-}14)$$

The values inserted into the calculations include:

- $\lambda = 1.54$Å, i.e. copper X-rays
- $z = 100\mu$m, so thicknesses on each side of the boundary are 100μm and 200μm
- $\delta = 4.74517 \times 10^{-7}$ (Value for mylar at copper K_α energy)
- $\mu = 8.96278$ (Value for mylar at copper K_α energy)

The real and imaginary components of the wavefront immediately after transmission by the phase object are plotted separately in figure 2.4.

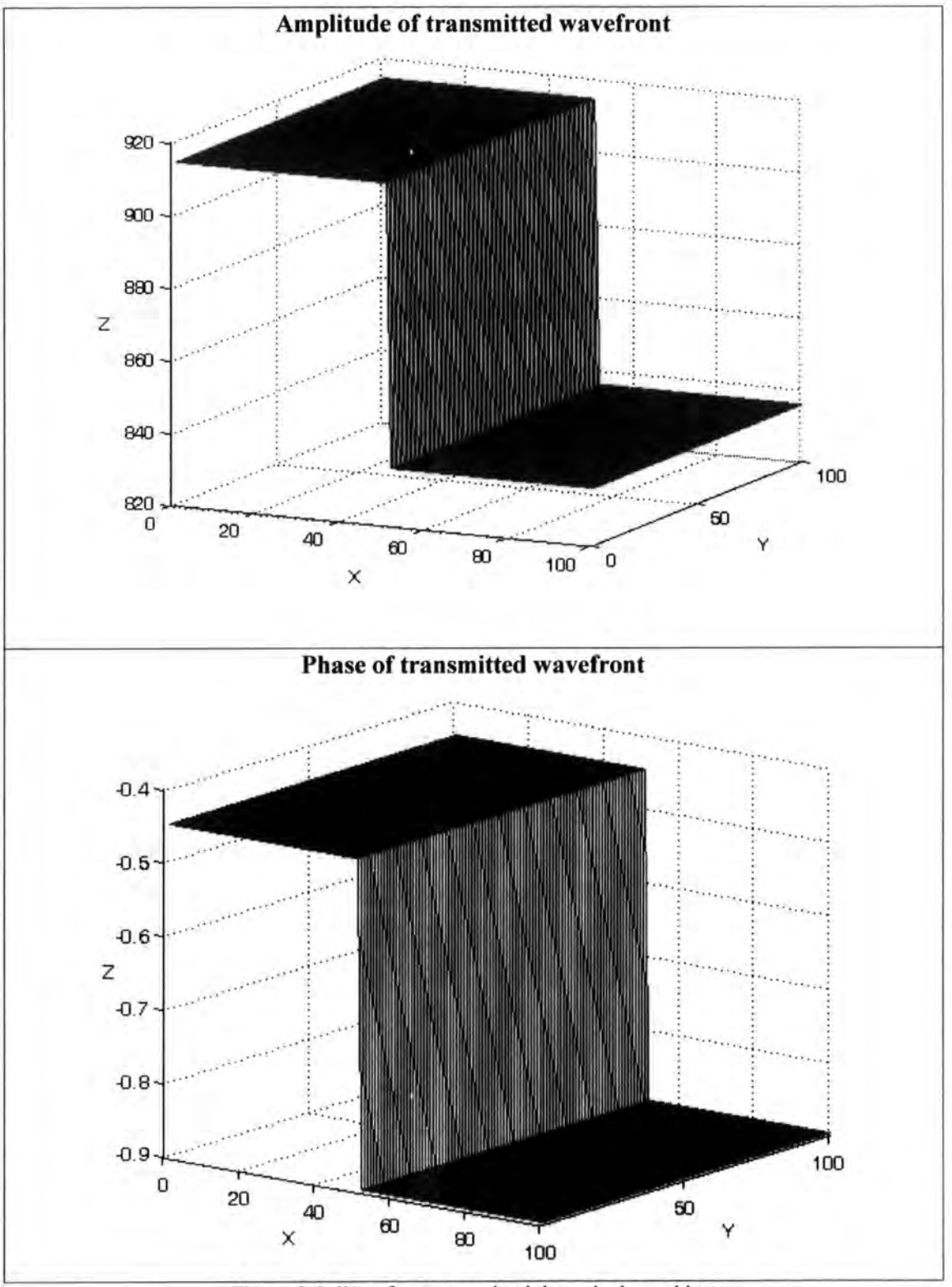

Figure 2.4: Wavefront transmitted through phase object

(a) Amplitude and (b) Phase of wavefront

It is seen from figure 2.4 (a) that the amplitude of the wavefront forms a step-function, as expected. An absorption image would be recorded with the detector plane at this position, and so by squaring this amplitude, the absorption image of this object is simulated. Figure 2.5 shows the absorption image of this object to be a simple step in intensity.

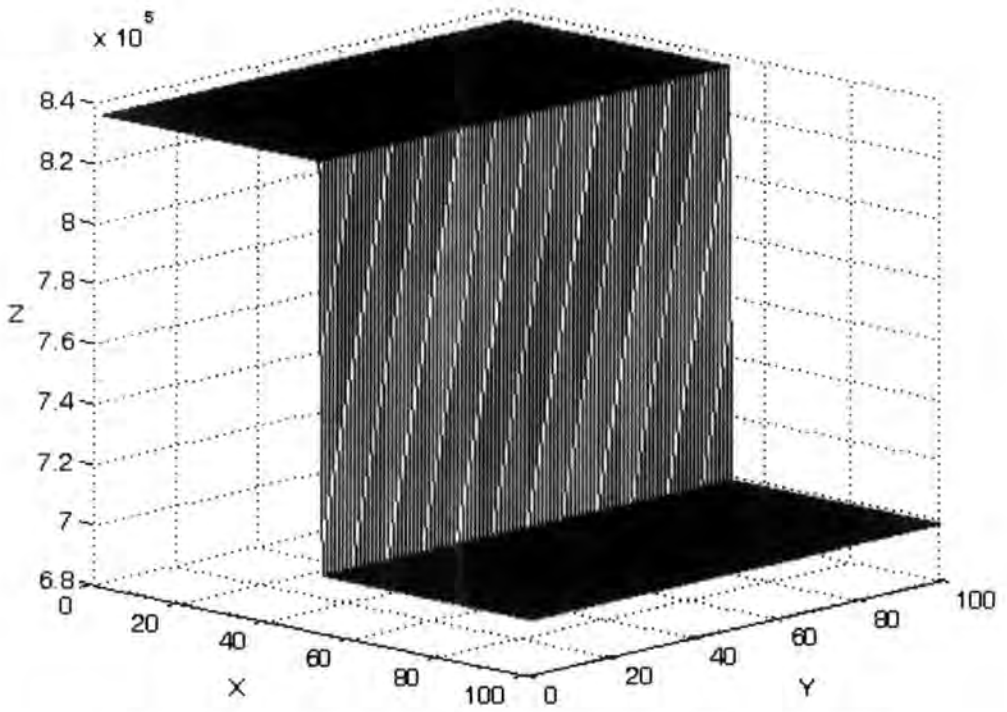

Figure 2.5: Simulated intensity of absorption image of step function object

Continuing the phase contrast simulation, the wavefront transmitted by the step-function phase object is then propagated to a detector. This involves further absorption and phase-shifting by the air, since it is not assumed that the system is set up in a vacuum. This is simulated by the application of equation 2-13 over the whole wavefront, using the following values:

- $\lambda = 1.54$Å
- $\delta = 3.87519$ x 10-9 (Value for air at copper K_α energy)
- $\mu = 0.0111423$ (Value for air at copper K_α energy)

Every matrix element at the sample plane is assumed to contribute to every matrix element at the image plane. This follows Huygen's Principle that every point along a wavefront acts as a secondary transmitter [11]. The distance over which each individual element of the transmitted wavefront propagates is determined by considering the wavefront matrix at the sample plane to cover an area of size 2mm x 2mm, and the final wavefront at the detector plane to cover an area of size 10mm x 10mm. The distance covered by each element of the wavefront matrix is determined within a series of loops via the following series of calculations:

Vertical position on detector: $$Y_{image} = \frac{s \times 10^{-3}}{y} \quad (2\text{-}15)$$

Horizontal position on detector: $$X_{image} = \frac{t \times 10^{-3}}{x} \quad (2\text{-}16)$$

Vertical position at sample plane: $$Y_{Object} = \frac{tmpy \times 2 \times 10^{-3}}{y} \quad (2\text{-}17)$$

Horizontal position at sample plane: $$X_{Object} = \frac{tmpx \times 2 \times 10^{-3}}{x} \quad (2\text{-}18)$$

Here, s refers to a loop variable representing the vertical detector pixels, t refers to a loop variable representing the horizontal detector pixels, and tmpy and tmpx refer to loop variables representing the vertical and horizontal wavefront matrix elements respectively at the sample plane. The variables x and y are the total number of steps in each horizontal and vertical loop respectively. All matrices used are of dimension (x,y). Angle θ, subtended by the wavefront matrix element in the sample plane at the detector plane in the vertical direction, over a propagation distance D is given by:

$$\theta = \arctan\left(\frac{\left|Y_{\mathrm{Im}age} - Y_{Object}\right|}{D}\right) \quad (2\text{-}19)$$

Angle ϕ, subtended by the wavefront matrix element in the sample plane at the detector plane in the horizontal direction is given by:

$$\phi = \arctan\left(\frac{\left|X_{Image} - X_{Object}\right|}{D}\right) \qquad (2\text{-}20)$$

The propagation distance for each individual matrix element is then calculated to be:

$$Distance = \frac{D}{\cos(\theta)\cos(\phi)} \qquad (2\text{-}21)$$

In this way, every matrix element is propagated to every point on the detector. The value for D used in the simulation is 0.3m. The intensity of each matrix element is calculated via the following:

$$I_n = \Psi^2 \qquad (2\text{-}22)$$

At every pixel, the sum of all the intensities propagated to that point is taken:

$$I = \sum_{1}^{n} I_n \qquad (2\text{-}23)$$

The simulation of the final image projected onto the detector is plotted in figure 2.6.

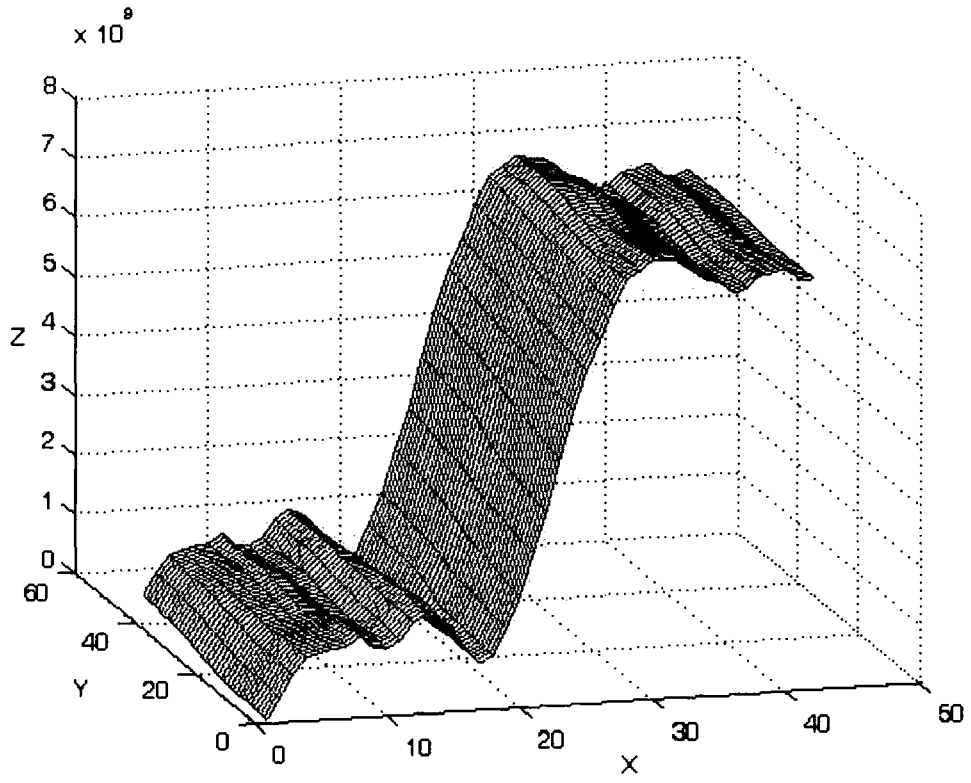

Figure 2.6: Final intensity map of propagation phase contrast image of step function object

It is seen in figure 2.6 that when the phase-shifted wavefront is propagated a distance from the object, the step in phase causes a peak and trough in the final image intensity. This is the main indicator of the presence of phase contrast in an image of an edge or boundary.

A similar simulation is completed with the application of a graded function to the object such that:

$x < -10$ or $x = -10$: $$\Delta\phi = \frac{-2\pi}{\lambda}\delta z \qquad (2\text{-}24)$$

$-10 < x < 10$: $$\Delta\phi = \frac{-2\pi}{\lambda}\delta z\left(1 + \frac{(x+11)}{20}\right) \qquad (2\text{-}25)$$

$x > 10$ or $x = 10$: $$\Delta\phi = \frac{-2\pi}{\lambda}2\delta z \qquad (2\text{-}26)$$

This represents the X-rays passing through an object made of the same material throughout, but of different thickness on either side of a central graded boundary. This leads to an additional graded absorption function such that:

$x < -10$ or $x = -10$: $$I = I_0 \exp(-\mu z) \quad (2\text{-}27)$$

$-10 < x < 10$: $$I = I_0 \exp\left(-\mu z\left(1 + \frac{(x+11)}{20}\right)\right) \quad (2\text{-}28)$$

$x > 10$ or $x = 10$: $$I = I_0 \exp(-2\mu z) \quad (2\text{-}29)$$

The program simulates the transmission of the original flat wavefront (shown earlier in figure 2.3) through such a graded-function object via the following calculation:

$x < -10$ or $x = -10$: $$\Psi_{Graded} = \Psi_0 \exp(-\mu z)\exp\left(-\frac{2\pi i}{\lambda}\delta z\right) \quad (2\text{-}30)$$

$-10 < x < 10$:

$$\Psi_{Graded} = \Psi_0 \exp\left(-\mu z\left(1 + \frac{(x+11)}{20}\right)\right)\exp\left(-\frac{2\pi i}{\lambda}\delta z\left(1 + \frac{(x+11)}{20}\right)\right) \quad (2\text{-}31)$$

$x > 10$ or $x = 10$: $$\Psi_{Graded} = \Psi_0 \exp(-2\mu z)\exp\left(-\frac{4\pi i}{\lambda}\delta z\right) \quad (2\text{-}32)$$

The same values are inserted into the calculations for the variables λ, z, δ and μ as before. The amplitude and phase of the wavefront immediately after transmission by the phase object are plotted separately in figure 2.7.

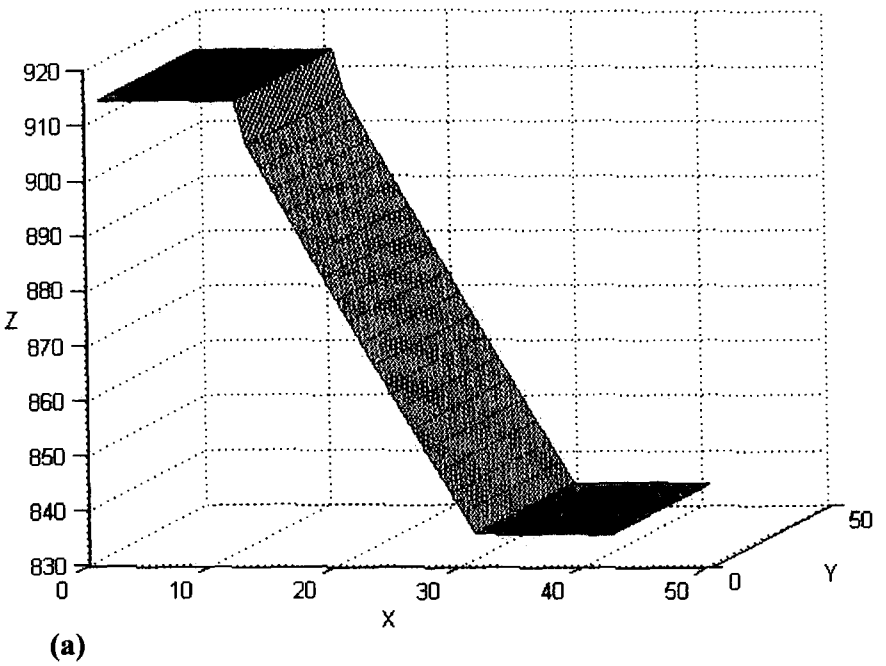

(a)

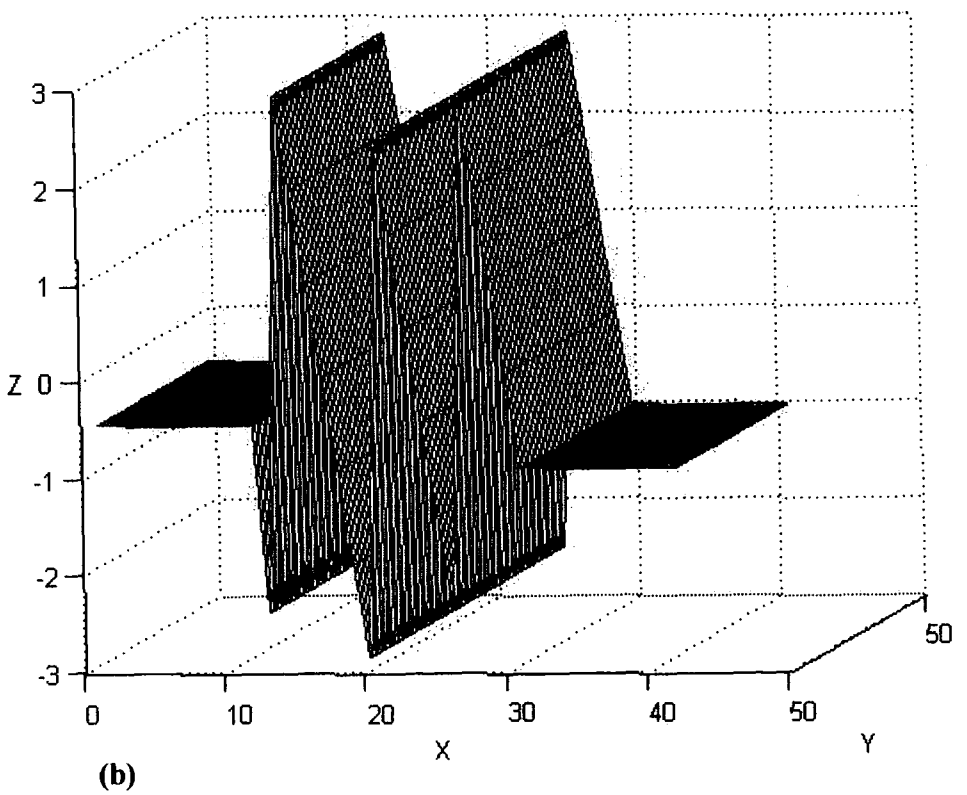

(b)

Figure 2.7: Wavefront transmitted through graded function.

(a) Amplitude and (b) Phase of wavefront

It is seen from figure 2.7 that the amplitude of the wavefront forms a graded function, as expected. The phase, however, oscillates across the x-axis as the thickness of the object increases. This is because the power of the phase exponential in the wavefront calculation reaches a multiple of -2π three times along the graded function.

Again, by squaring this amplitude, the absorption image of the graded object is simulated. Figure 2.8 shows the absorption image of this object to be a simple graded intensity function.

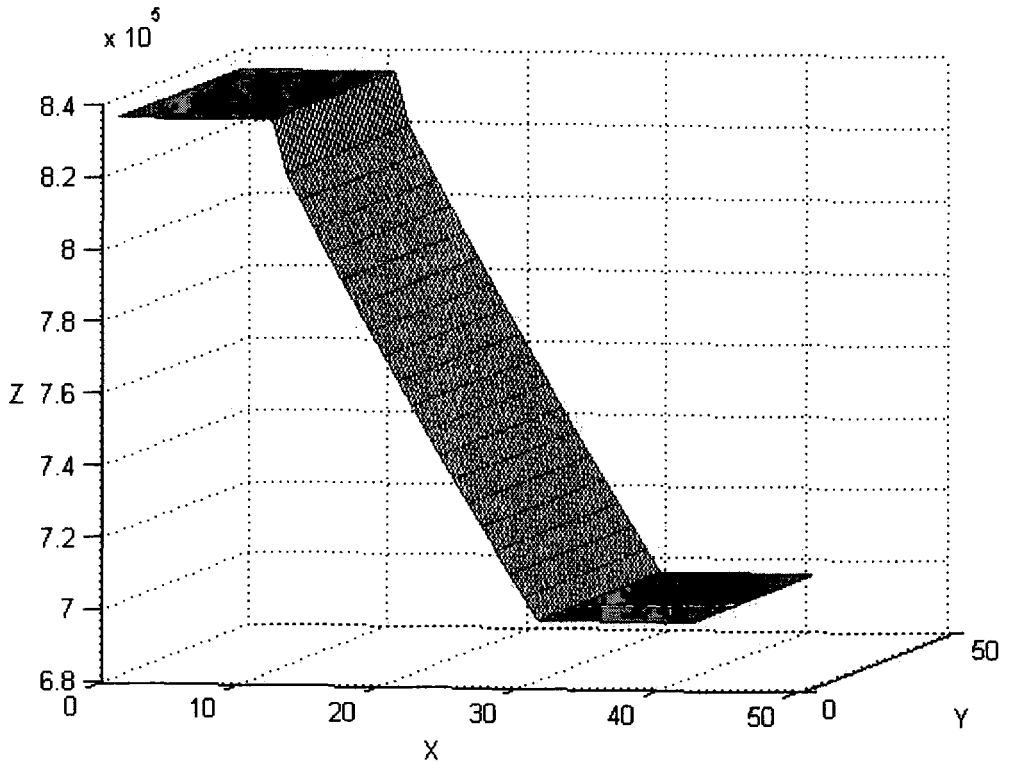

Figure 2.8: Simulated intensity of absorption image of graded function object

The transmitted wavefront is propagated in the same way as before, and the sum of all propagated intensities is taken at every pixel of the detector via equation 2-23. The simulated final image of the graded function, after propagation, is shown in figure 2.9.

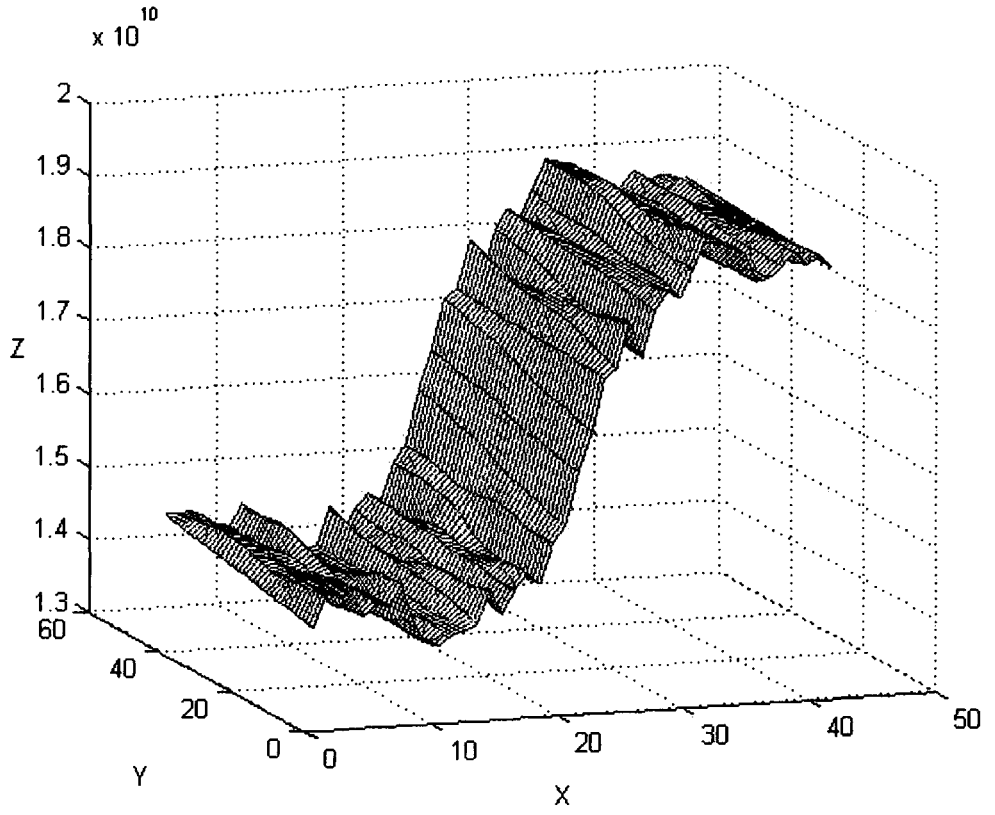

Figure 2.9: Final intensity map of propagation image of graded function object

It is seen in figure 2.9 that the propagation image of an object with a more graded function does not display the strong peak and trough seen in the image of the step function phase object. The gradual increase in thickness across the object does not bring about the sharp phase contrast feature of a step function, as seen earlier in figure 2.6. Rather, the oscillating phase component makes the slope less smooth, with 'noisy' flatter sections on each side of the slope, representing the sections of constant thickness within the object. The absorption component contributes to the overall shape of the final image, with a longer, shallower slope due to the gradual change in absorption across the graded section of the object.

These simulations give an idea of the propagation images obtained for a step function object providing a steep phase gradient, and a graded function object providing several shallower phase gradients. The phase effects are not easily discernible in a graded function object, while the steep phase gradient of a step function object provides an

ideal phase object with a strong peak and trough in the final image intensity map. Most of the experiments in this project will make use of an object approximating to the step function sample simulated in this chapter, so the simulation work shows the type of image that can be expected.

It is necessary to note here that these simulations cannot be applied to propagation distances of more than the Rayleigh length: that would require a Fourier treatment because the detector would then lie in the Fraunhofer regime.

References

[1] Pavlov K. M. et al., *J. Phys. D: Appl. Phys.* **37** pp.2746-2750 (2004)

[2] Gureyev T. E. et al., *Phys. Rev. Lett.* **86** (25) pp.5827-5830 (2001)

[3] Arfelli F et al, *Phys. Med. Biol.* **43** (1998)

[4] Montgomery D. et al.,*Rev. Sci. Instr.*, **75** (10) pp.3986-3988 (2004)

[5] Attwood D. T., *Soft X-rays and extreme ultraviolet radiation : principles and applications*, Cambridge University Press (1999)

[6] International Tables for X-ray crystallography Vol. III, Kynoch Press (1974)

[7] Farr R. F., *Physics for Medical Imaging,* W. B. Saunders (1997)

[8] Dendy P. P. et al., *Physics for Diagnostic Radiology (2nd Edn),* Institute of Physics Publishing (1999)

[9] Webb S., *The Physics of Medical Imaging, Institute of Physics Publishing (1998)*

[10] Kagoshima Y. et al., *Jpn. J. Appl. Phys.* **40** pp.L1190-L1192 (2001)

[11] Hecht E., *Optics (3rd Edn)*, Addison-Wesley (1998)

3. In-line set-up

This project used an in-line set-up for phase contrast imaging, as discussed in chapter 1. This set-up comprised simply of an X-ray source, sample and detector, as shown in figure 3.1.

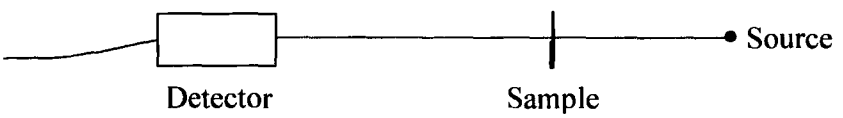

Figure 3.1: Schematic diagram of in-line set-up

This chapter discusses each of these aspects of the set-up.

The source used for the duration of this project was a Bede Microsource®, a laboratory-based microfocus X-ray source, with rhodium and copper targets in place. An obvious and important first step for the project was to look at the source and to examine the spectra and beam characteristics with each target in place.

All aspects of the data acquisition method are important in a project such as this. An important issue to address early on was how to compare phase contrast as aspects of the imaging system were gradually changed. The vast majority of published work in this field discusses phase contrast qualitatively, by comparing images side by side (e.g. [1]). One approach to quantification of phase contrast has been to grade images according to the visibility of particular details, and to compare the numerical scores [2]. Another approach has been to apply a common fringe visibility function to the line profile across the image of a boundary [3, 4, 5, 6, 7]. This is the method favoured for this project, but it is actually taken further such that the absorption contrast is quantified and the absorption effects are eliminated by the phase contrast calculation. This is important since most objects exhibit some absorption effects.

The influence of noise on the images is considered, by looking at the dark background of the detector, checking for a bias, and quantifying the improvement to the noise levels

when integrating images over increasing numbers of frames and taking thicker line profiles for calculation of image contrast. A suitable method for error measurement is also discussed. These steps are important in setting up a system, because noise effects must be minimised and potential errors quantified in a project which relies predominantly on image analysis.

The repeatability of the system is considered by taking consecutive images of a sample, with all settings remaining consistent, and comparing these using the quantitative method developed for this project. This is done with each target in place in turn. This is an important step because it is necessary to verify that any changes seen between images during this project are due to the factor under investigation at the time and not due to random fluctuations in the system.

Finally, a mount has been designed and made for the purpose of this project, which prevents movement or vibration while samples are imaged. This is outlined later on in this chapter.

3.1 Bede Microsource®

This project made use of a Bede Microsource® [8,9]. This is a compact, laboratory-based microfocus X-ray source which provides a high-intensity X-ray beam with a small size (of the order of tens of micrometres), at a low operating power of up to 80W. Thus the source produces X-rays of high brilliance (defined as the flux per unit area of source per unit solid angle).

3.1.1 X-ray production method

The microfocus X-ray source produces X-rays by directing an electron beam onto a metal target. The electron beam is positioned, shaped and focused onto the target by magnetic coils, using the same principle as a scanning electron microscope.

The X-ray generator comprises a sealed, evacuated X-ray tube. This houses an electron gun, provided by a dispenser cathode. As the electrons travel along the X-ray tube, they

are focused down to a line focus by a magnetic electron lens. They are aligned using an electron mask with a small aperture, and the stigmation of the beam is controlled by a quadropole magnet. The electron beam is ultimately focused onto a target of metal foil, which is usually copper, molybdenum or rhodium. The electron beam can be deflected over the surface area of the target, which is a useful property for maximising the lifetime of the target and avoiding areas sustaining target damage. All of these properties are controlled electronically by the operator. The target is cooled by a continuous jet of water directed onto the opposite side to that bombarded by the electron beam. The tube exit window is composed of beryllium. A diagram of the X-ray production method is shown in figure 3.2.

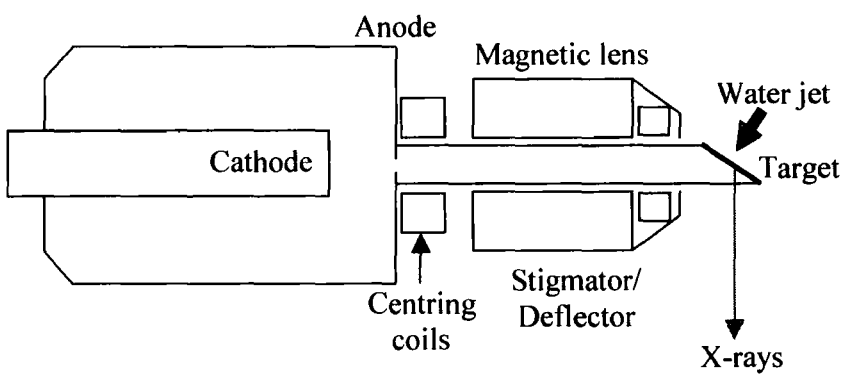

Figure 3.2: Diagram of Microsource® X-ray production method

The resulting X-ray beam produced may be varied, using the electronic and magnetic controls mentioned above, between a spot of small diameter and a line of narrow width. For the majority of work on this project, the X-ray beam size was kept to a minimum.

3.1.2 Copper and rhodium targets

This project made use of copper and rhodium targets. Copper X-rays are the softer of the two, with a characteristic K_α energy of 8.048 keV and K_β energy of 8.905 keV. The copper spectrum emitted for an excitation voltage of 40kV is shown in figure 3.3.

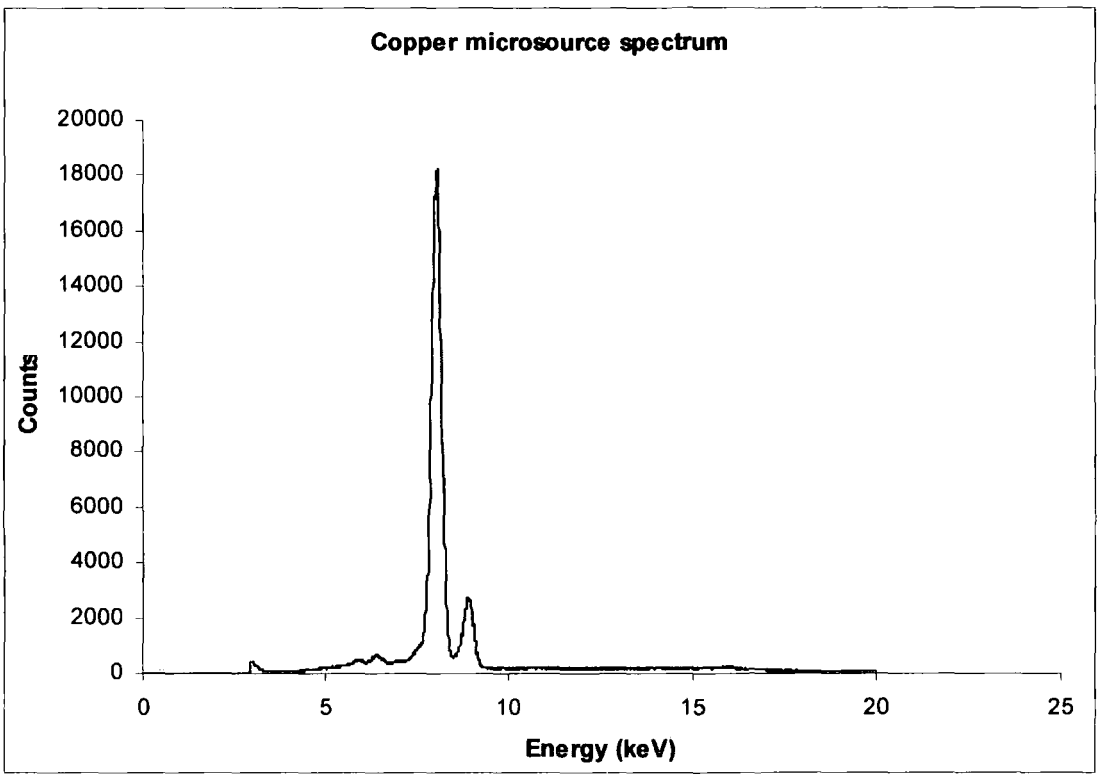

Figure 3.3: Microsource® X-ray spectrum with copper target.

With the copper target in place, the source was run at a voltage of 40kV and a current of 0.05mA (unless otherwise stated). These settings allowed a minimum source size of 12μm width x 17μm height. By analysing the area under the spectrum in figure 3.3, the dominance of the K_α line over the Bremsstrahlung could be calculated. The K_α-to-Bremsstrahlung ratio for the copper target at the above setting is 1.60.

Rhodium X-rays are harder, with a characteristic K_α energy of 20.216 keV and K_β energy of 22.723 keV. The rhodium spectrum emitted at 50kV and 0.05mA is shown in figure 3.4.

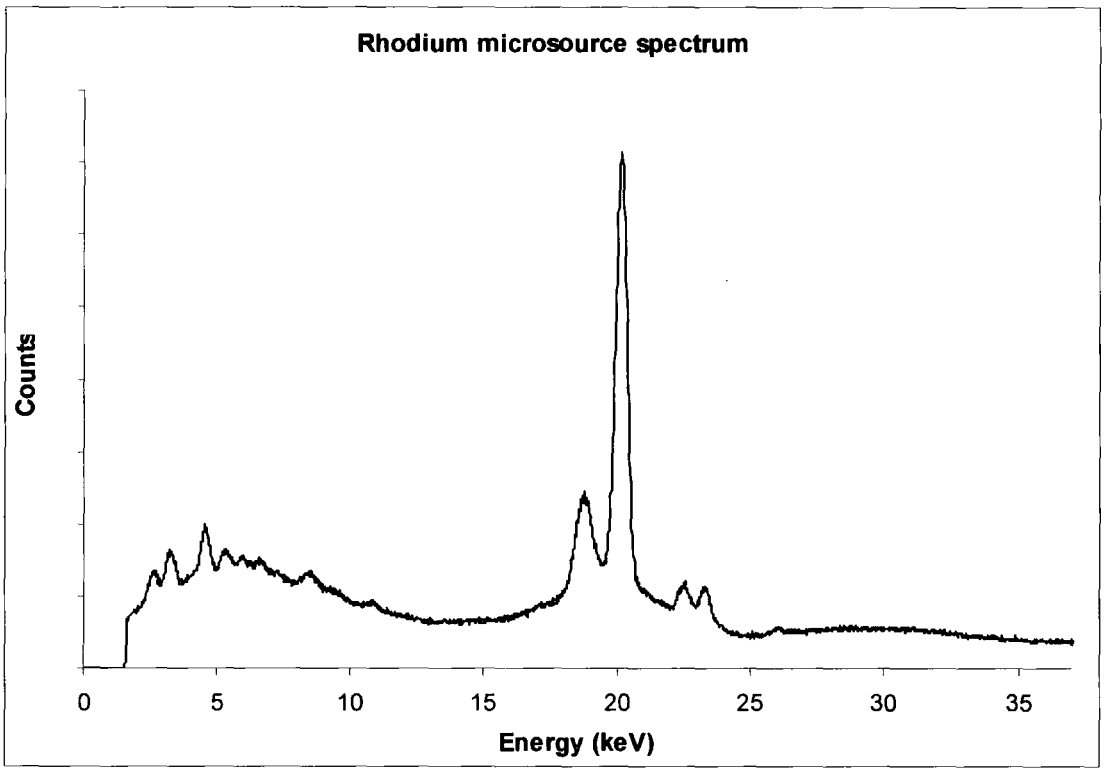

Figure 3.4: Microsource® X-ray spectrum with rhodium target

With the rhodium target in place, the source was run at a voltage of 50kV and a current of 0.05mA (unless otherwise stated) because a higher operating voltage is required in order to excite the harder K_α line to a significant intensity. This allowed a minimum spot size of 19μm width x 18μm height. Bremsstrahlung radiation is much stronger here, with a K_α-to-Bremsstrahlung ratio of just 0.25 at the above settings.

3.2 Data acquisition

Given that this project investigated the phase contrast content of X-ray images, the results of the experimental work relied heavily on image analysis. So it was important to ascertain that the images acquired for the purpose of this project were of a high standard and were suitable for the individual analyses. To this end a variety of detection methods were utilised, and the contributions of noise were investigated. In addition, a method for quantifying the phase contrast content of the images is discussed.

3.2.1 Detection methods

The Microsource® spectra were recorded using an Amptek X-ray detector, which counts incident X-ray photons of all energies. This was connected to a computer running Ortec Maestro-32 spectral analysis software. The system was calibrated using spectra from a variable X-ray source, building up several characteristic line energies to calibrate the energy channels in the recorded spectra.

Dental X-ray film is a well-established X-ray image acquisition method: images are formed by reduction of the emulsion layers on the base film, followed by development. Intraoral dental X-ray film has a useful detection area of 41mm x 31mm and occlusal dental X-ray film has a larger field of view of 50mm x 70mm. Both have a resolution of 25μm. However, the X-ray film required a significant exposure time of 6 minutes in order to pick up sample details. Film images were recorded digitally using a microscope and CCD camera, but by focusing on each image individually there were always inconsistencies in the microscope intensity and focus settings and so the final digital images were unsuitable for quantitative comparison. X-ray films were used for much of the image acquisition for the experiments discussed in chapter 6, where qualitative image comparisons were sufficient for the majority of the experiments.

A more convenient method of image acquisition uses an X-ray CCD camera, which allows digital image acquisition direct to a computer. The camera used for most of the image acquisition for this project was a Photonic Science X-ray Eye i2i CCD camera. Images were acquired directly to a computer running Media Cybernetics image Pro Plus software. The field of view was 10mm in diameter with a pixel size of 11.6μm x 11.2μm, and this required an exposure time of 40 seconds. With the camera and software settings fixed throughout the duration of an experiment, the digital images can be compared quantitatively. This is particularly important for the quantitative analysis of images as discussed in Chapters 4 and 5.

3.2.2 Quantification of phase contrast

Much of the work reported in the X-ray phase-contrast imaging literature relies on qualitative comparisons between absorption and phase contrast images of the same objects. This is a logical and useful way of highlighting the differences between images acquired by the two methods. However, in order to investigate fully the influence of a factor on the phase contrast content of images, it is required that a quantitative comparison is drawn between many images. To this end, all experiments for this project requiring a quantitative analysis were conducted using a sample approximating to a Heaviside function [11]. This was achieved by overlapping two or more layers of a material and using the boundary between the single layer and the multiple layer as the sample, as shown in figure 3.5.

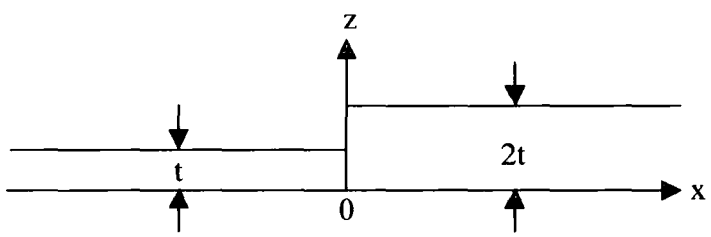

Figure 3.5: Sample approximating to a Heaviside function

In figure 3.5, t represents the thickness of the material, thus in this example the Heaviside-like function is the following:

$$\begin{aligned} z &= t \quad x < 0 \\ z &= 2t \quad x > 0 \end{aligned} \qquad (3\text{-}1)$$

This sample was placed in the X-ray beam such that the z-axis was in the direction of propagation of the X-rays. Figure 3.6 shows a typical phase contrast image achieved using a Heaviside function sample, together with its intensity profile in figure 3.7.

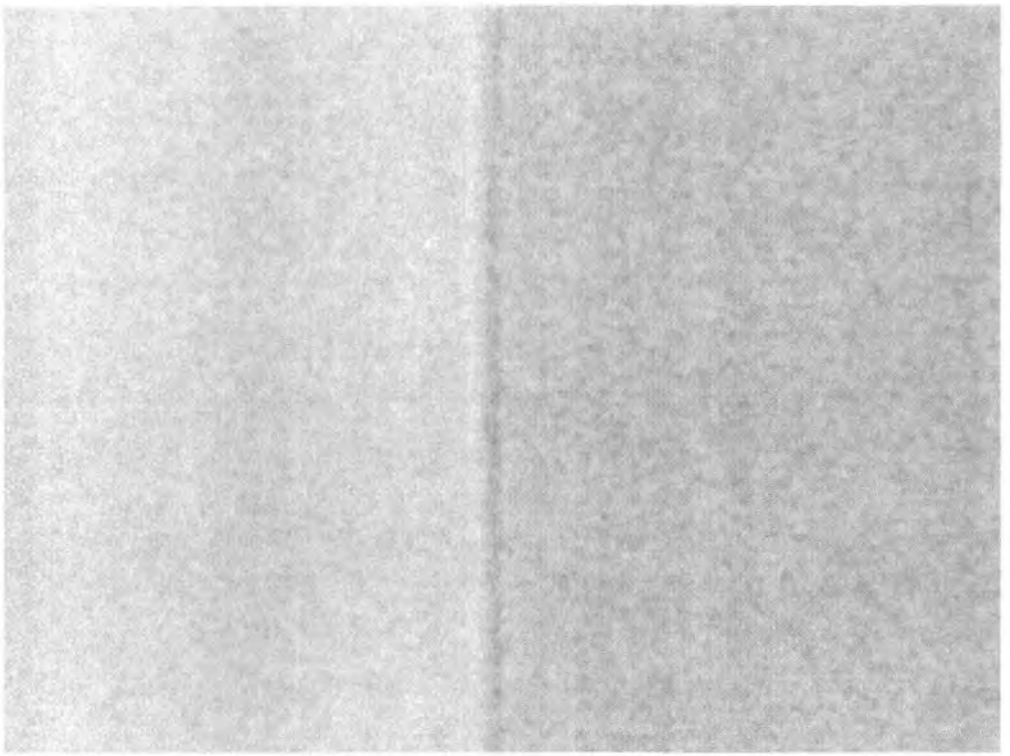

Figure 3.6: Typical Heaviside function phase contrast image

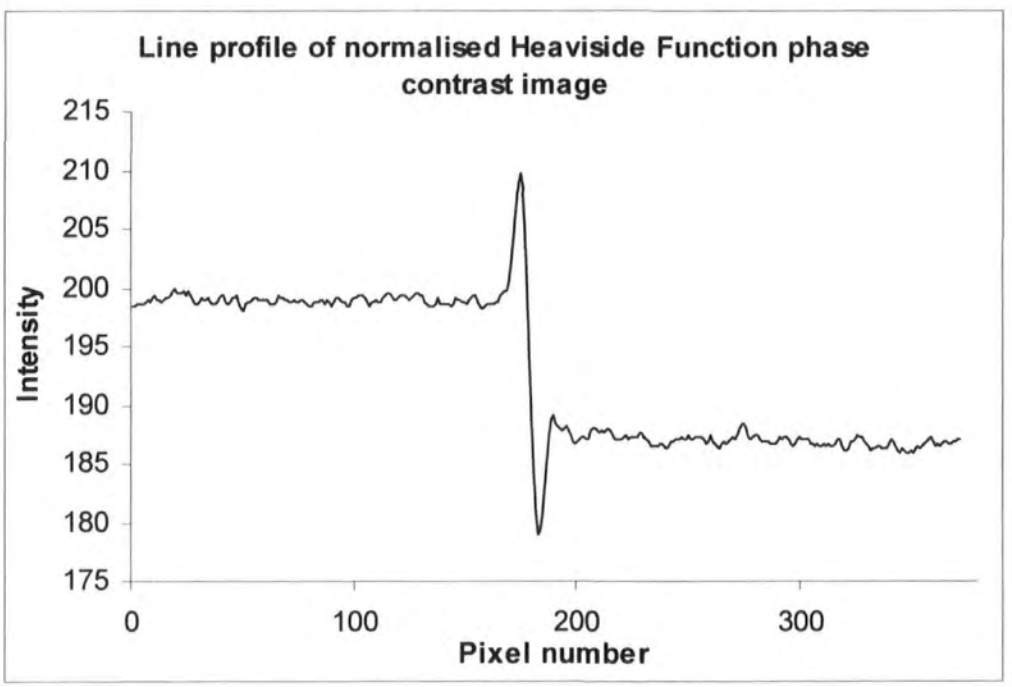

Figure 3.7: Intensity profile across a typical Heaviside function phase contrast image

The intensity is fairly constant where the X-rays have passed through the sections of material of uniform thickness. The peak and trough suggest the 'creation' and 'destruction' respectively of photons in the parts of the image adjacent to the boundary. Since photons cannot simply be 'created' in these circumstances, the peak and trough actually show where some of the X-rays have been refracted from one side of the boundary to the other, and so phase contrast is present in the image.

For the purpose of quantification of the phase contrast recorded by each image, the maximum and minimum intensities are read off the image line profile as shown in figure 3.8:

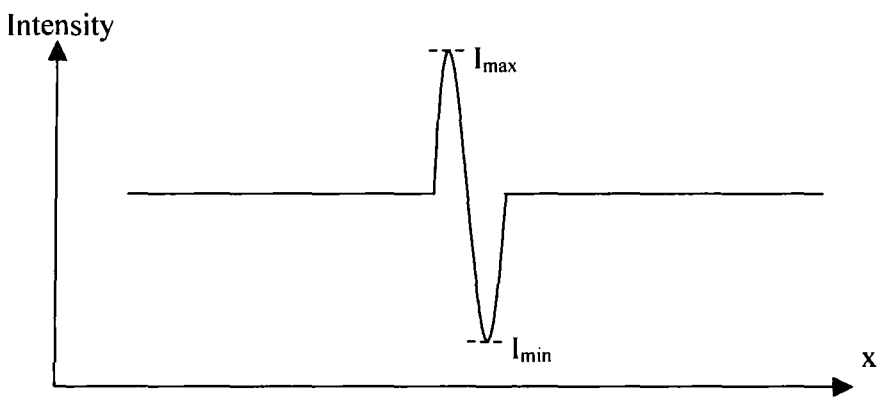

Figure 3.8: Intensity profile across a typical phase-contrast image of a sample approximating to a Heaviside function

In order to make use of this image for quantitative analysis of the phase contrast, a standard fringe visibility function is used. This is given by:

$$C = \frac{I_{max} - I_{min}}{I_{max} + I_{min}} \qquad (3\text{-}2) \qquad [12]$$

The fringe visibility equation has been used in a similar fashion with in-line phase contrast images produced using synchrotron X-rays [3, 4, 5], diffraction enhanced images produced using synchrotron X-rays [3], phase sensitive images produced using

an interferometer with synchrotron X-rays [6], and with phase contrast images produced using neutrons [7].

In reality, the image will show some absorption contrast due to the abrupt change in thickness across the sample, as shown in figure 3.9, and so the absorption contrast must be taken into account when calculating the phase contrast.

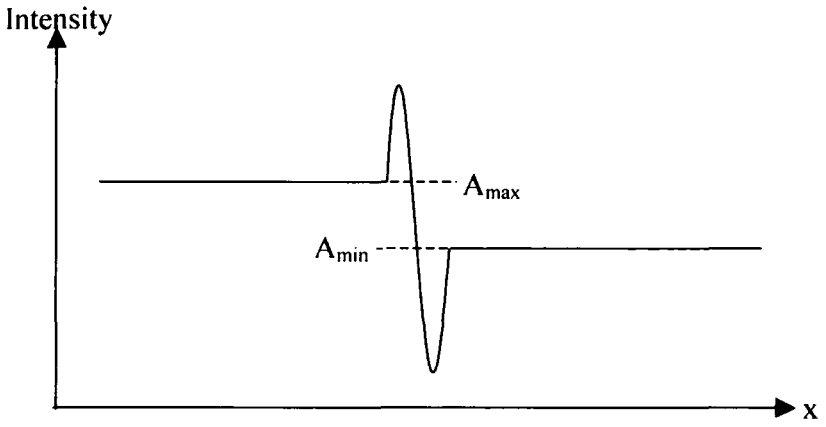

Figure 3.9: Intensity profile across a typical phase-contrast image of a sample approximating to a Heaviside function, including some absorption contrast

The absorption maximum and minimum intensities are determined by taking the average value along the section of higher intensity and the average value along the section of lower intensity respectively. Again, A_{max} and A_{min} are inserted into the visibility function (equation 3-2) in order to determine the level of absorption contrast present in the image.

With absorption contrast present in the image, applying the visibility function (equation 3-2) to the maximum and minimum intensities I_{max} and $I_{min,}$ will extract both the phase and absorption components of the image. Thus the absorption property of the sample will distort the phase visibility when calculated as described above. In order to extract only the phase component, an adjustment is required before applying the visibility function. This adjustment is determined by considering the effect of a sample of uniform

thickness, with a change in phase factor halfway across it. This would produce an image with the phase effect but not the absorption effect. The side of the image in figure 3.9 with the higher intensity represents the thinner section of the sample. In order to remove the absorption component from the image and adjust it correctly to show only the phase factor, the thicker (lower intensity) section must be 'thinned', to the same absorption level as the thinner section. This is done by determining the difference in intensity between the higher and lower intensity sections, as follows:

$$Absorption = A_{max} - A_{min} \qquad (3\text{-}3)$$

This difference is then added to the minimum intensity of the phase component, I_{min}, in order to increase it to the intensity level it would reach if there were no change in absorption across the sample. The modified phase visibility function is now given by:

$$PhaseContrast = \frac{I_{max} - (I_{min} + (A_{max} - A_{min}))}{I_{max} + I_{min} + (A_{max} - A_{min})} \qquad (3\text{-}4)$$

Using these visibility methods, a pure phase contrast value and an absorption contrast value were assigned to each image, allowing many images to be compared in a graphical format. This quantification of image contrast was particularly important for displaying the changing phase contrast achieved as an individual factor in the imaging process was gradually changed.

3.2.3 Noise contributions and errors

While digital image acquisition was the most convenient method of acquiring the phase-contrast images, there were some issues which needed to be taken into consideration when analysing the images. The camera itself provided some small additional intensity due to electrons permanently trapped in the potential wells which form the pixels, and noise in the electronics. In addition, the length of time over which the camera was exposed was important, as was the line profile used for phase contrast quantification. These factors were taken into consideration as discussed here.

3.2.3.1 Dark background

An X-ray camera makes an unwanted contribution to the images which must be taken into consideration. The act of applying a voltage to the camera allows some electrons to rest in the pixels, forming a bias. The bias remains constant regardless of the exposure time. In addition, during exposure, a number of electrons are randomly forced down the potential wells of the detector without the help of X-ray photons. These provide a dark background and build up during the exposure. Both of these effects will contribute to the intensity variation of the image. By recording an image without any X-rays incident on the camera, a 'dark' background can be determined.

In this way, a dark background of the X-ray camera was accumulated over 256 frames and averaged. The intensity profile across this image showed the level of the camera's contribution to a given image. This intensity profile is shown in figure 3.10.

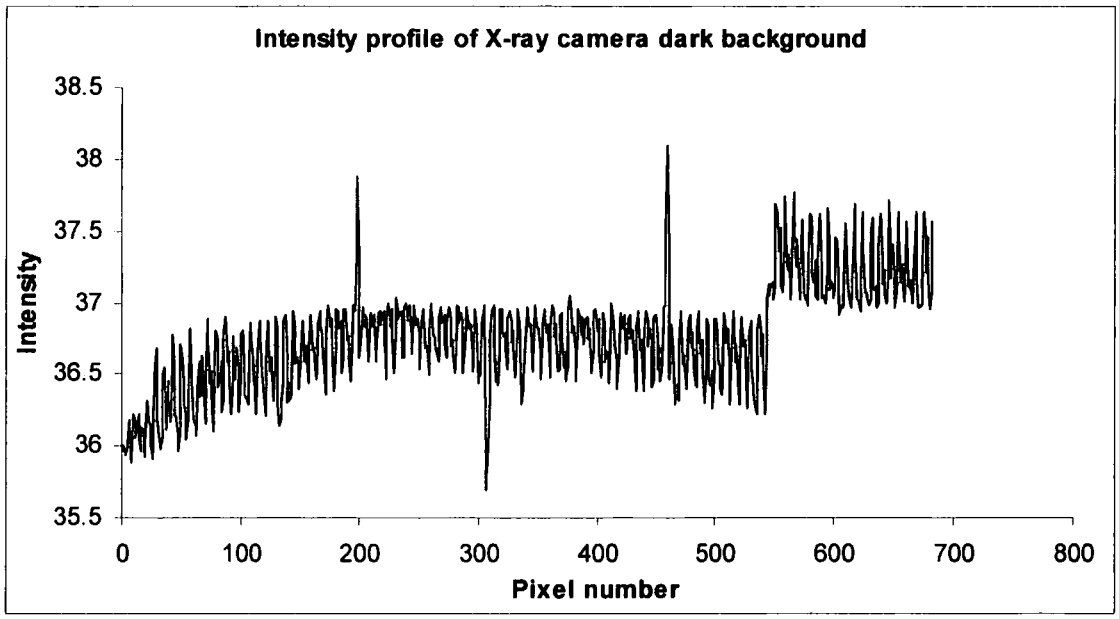

Figure 3.10: Intensity profile of X-ray camera dark background

The dark background had a mean intensity level of ~36 counts, with peaks reaching a maximum of 38 counts. The 'step' in intensity at approximately 550 pixels may be due to a non-uniform thickness of the exclusion layer: the material to the right of the step

may be thinner than that to the left. This background intensity contribution would become significant for very low-intensity exposures and needs to be subtracted from the final images.

In order to determine the levels of bias and dark background, a number of images were accumulated without exposing the camera to X-rays. The images were accumulated over 1 frame, 2, 3, 4, 5 and 6 frames. The mean intensity of each dark background was calculated and plotted against the number of frames, as shown in figure 3.11:

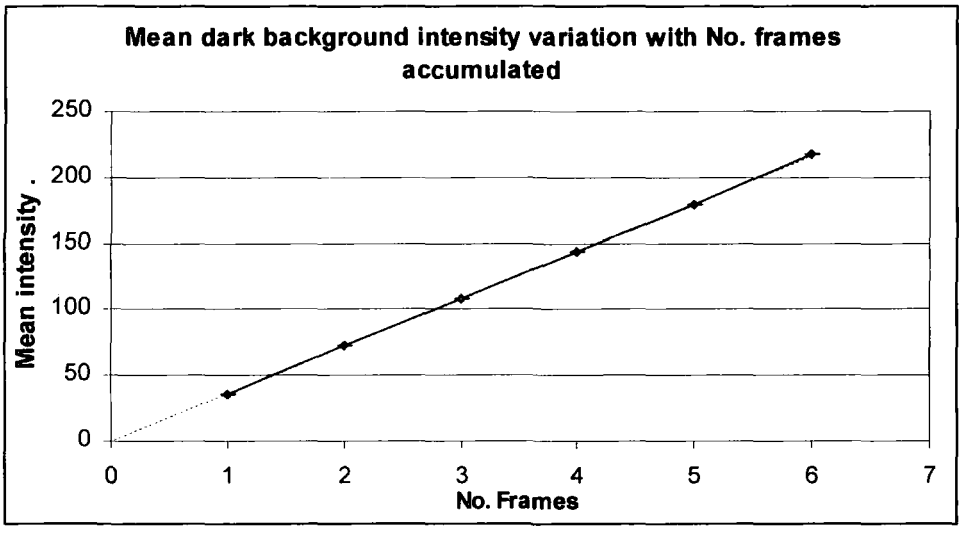

Figure 3.11: Variation of the mean dark background intensity with the number of frames accumulated

Figure 3.11 shows a linear relationship between the mean dark background intensity and the exposure time. An extrapolated line of 'best-fit' for this data intercepts with the y-axis at -0.45. An intercept so close to zero indicates that the bias is negligible for this detector.

In order to control the dark background accumulation, any images accumulated over many frames must then be averaged over that same number of frames. To check this, images were accumulated and averaged over 1 frame, 10, 50, 100, 150, 200 and 256

frames, and again the mean intensities were calculated and plotted against the number of frames. These results are shown in figure 3.12:

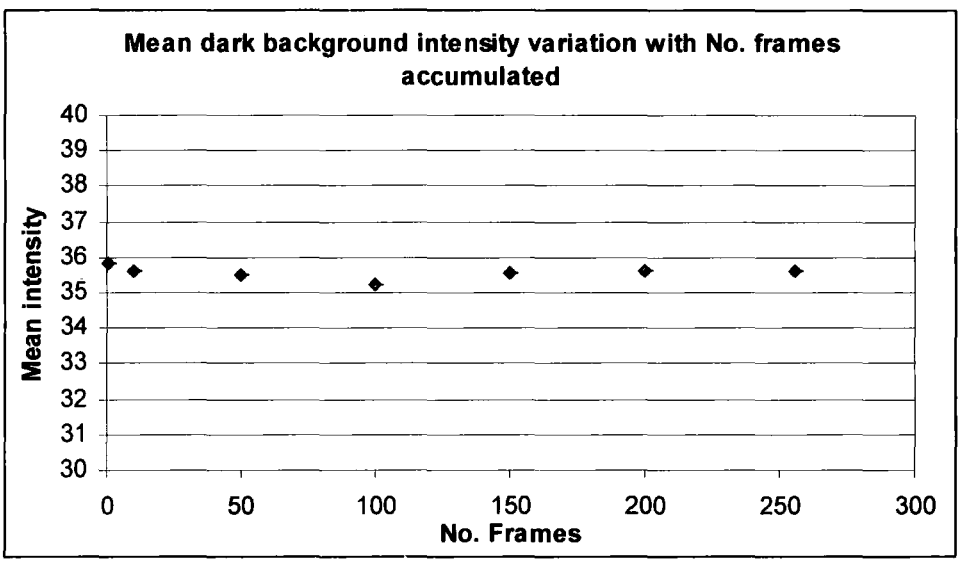

Figure 3.12: Variation of the mean dark background intensity with the number of frames averaged

Figure 3.12 illustrates that the dark background remained constant when images were accumulated and averaged over many frames. Thus the dark background could be controlled by averaging over many exposures if one frame did not provide a sufficient exposure time.

3.2.3.2 Reduction of noise contribution

The use of digital image acquisition methods introduces a certain amount of noise to the captured images. As discussed above, the dark background of the camera contributes some unwanted additional intensity to the images and this can be eliminated by subtracting a dark background from the final images. Other methods for reducing noise effects include accumulation over many images, and integrating over many line profiles.

3.2.3.2.1 Reduction of noise due to exposure time

An image resulting from the capture of a single frame can be very unreliable. Factors including vibration or a temporal dependence of the electron beam in the source can make the image in one frame slightly different to the next, an effect known as photon noise. This unreliability can be rectified by accumulating an image over a number of frames and averaging over the same number, giving a smoother image and minimizing the effects of the environmental factors. It has already been shown in figure 3.12 that when averaging over many frames the dark background can be controlled.

In order to determine by how much this noise could be reduced, accumulated images were taken of the edge of a copper sheet of 216μm thickness and were integrated over increasing numbers of frames. The numbers of frames were increased as follows: 1 frame, followed by 10, 20, 40, 80, 160 and a maximum of 256. Accumulation and averaging over 256 frames required a 40-second exposure time. For each image a horizontal line profile was used to display the intensity variation and these are shown in figure 3.13.

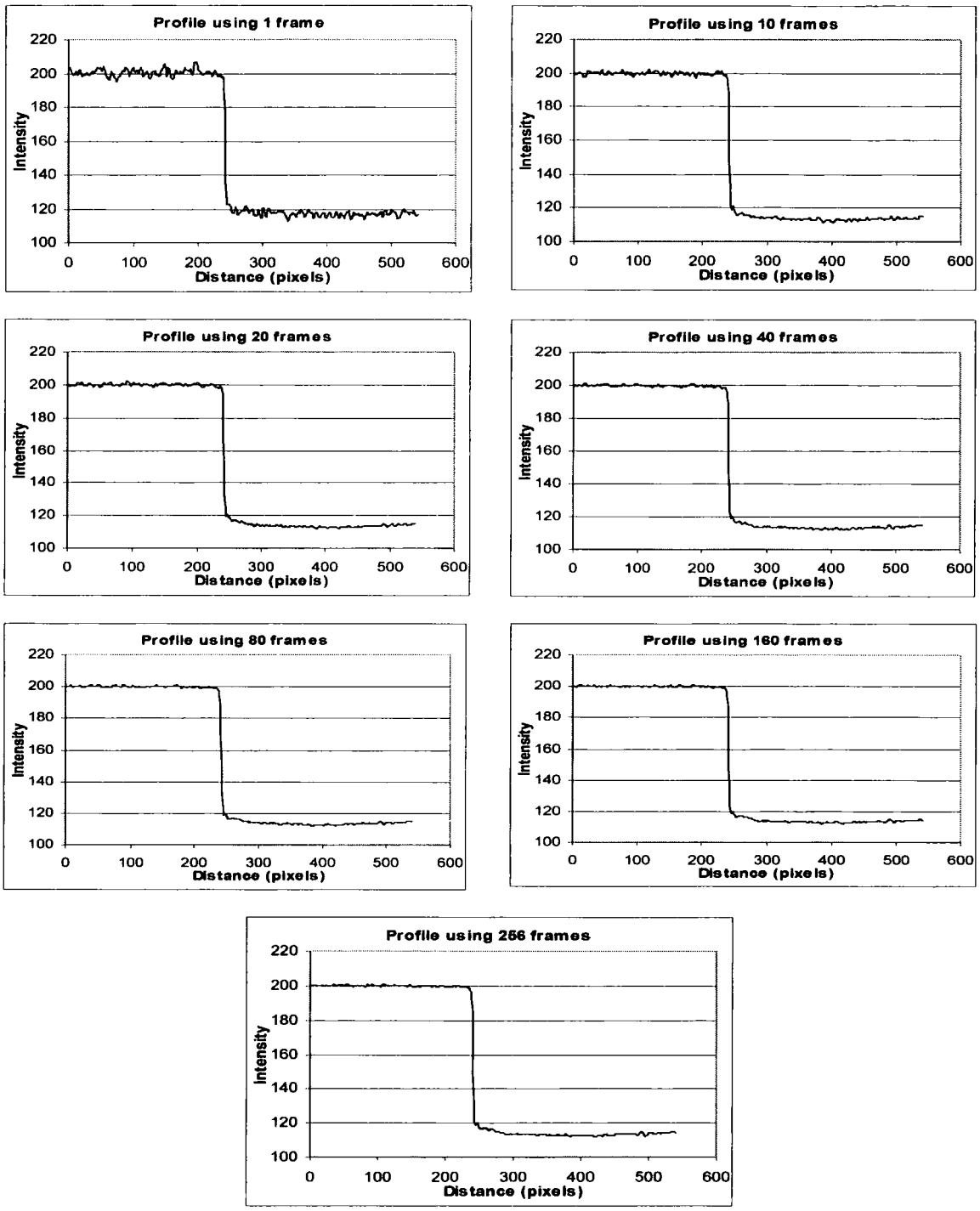

Figure 3.13: Intensity profiles of images obtained by accumulation over increasing numbers of frames

With exposure over only one frame, it is seen that the sections of the image representing constant absorption and hence constant intensity are very noisy, with an unacceptable level of deviation from the corresponding average intensity value. As the number of frames increases, this noise is seen to reduce to a more acceptable level of deviation from the average corresponding intensity. In order to quantify the noise reduction by this method, the standard deviation about the average maximum and minimum intensity was calculated for each image. This data is shown in figure 3.14.

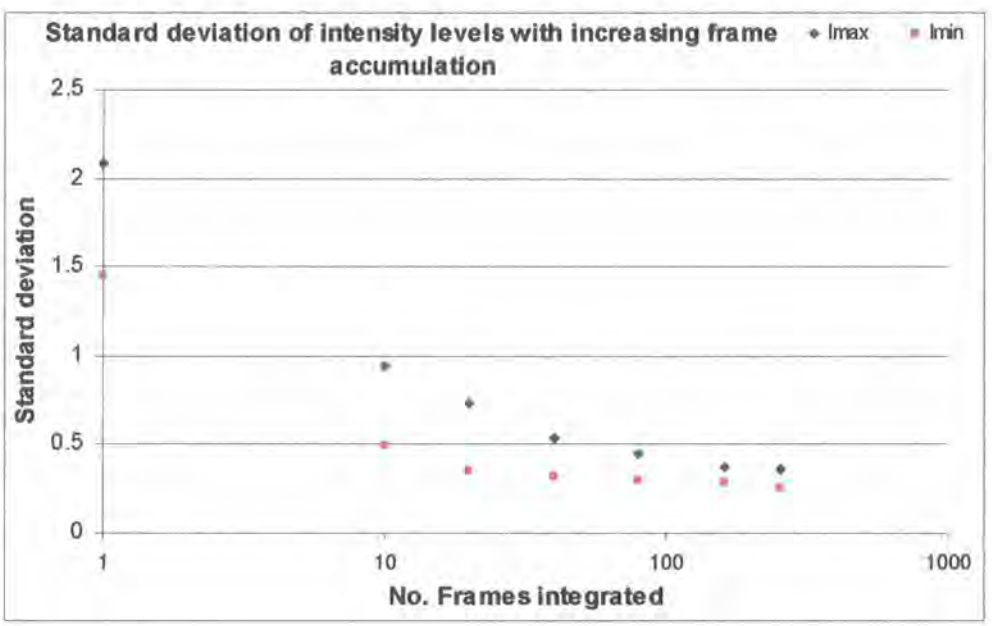

Figure 3.14: Standard deviations in maximum and minimum intensity levels as a function of the number of frames accumulated

Figure 3.14 shows the reduction in noise due to the accumulation of an image over increasing numbers of frames. The standard deviation begins to plateau for those images which were accumulated over the highest numbers of frames, and so exposure over the maximum of 256 frames clearly provides the optimal reduction of this particular contribution to the noise levels. Increasing the number of frames from 1 to 256 reduces the standard deviation for I_{max} and I_{min} by a factor of around 6.

In increasing the number of frames over which the image is recorded, it would be expected that the photon noise would be reduced (from the noise level of the single-frame image) by a factor equal to the square root of the number of frames [13]. So an increase in exposure from a single frame to 256 frames should bring with it a reduction in the photon noise of a factor of $\sqrt{256}$, or 16. This is clearly not the case for the X-ray Eye and so this may suggest the presence of some additional noise in the electronics of the receptor.

The noise in figures 4.13 and 4.14 does reach a plateau, with a coefficient of variation of just 0.2% for both I_{max} and I_{min} when exposed over 256 frames. This level of noise would only affect images significantly where there is a very low photon count.

3.2.3.2.2 Reduction of noise by intensity profile integration

Many of the results obtained during this project are based on calculations from line profiles of the images. Thus it is important to ensure that these line profiles are an accurate representation of the intensity variation. If a line of one pixel width is drawn across an image and the intensity along this line is viewed, regions of constant intensity are again seen to be very noisy with significant deviation from the applicable mean intensity. In order to reduce this noisy effect and smooth the regions of constant intensity, a 'thick' line profile can be used, which integrates over many line profiles of single-pixel width.

In order to determine by how much the noise could be reduced by this method, a 256-frame image of a standard Heaviside function sample was acquired and line profiles of increasing widths were compared for this image. The widths of the line profiles were as follows: 1 pixel, followed by 10, 20, 40, 80, 160, 320 and 500. These line profiles are shown in figure 3.15.

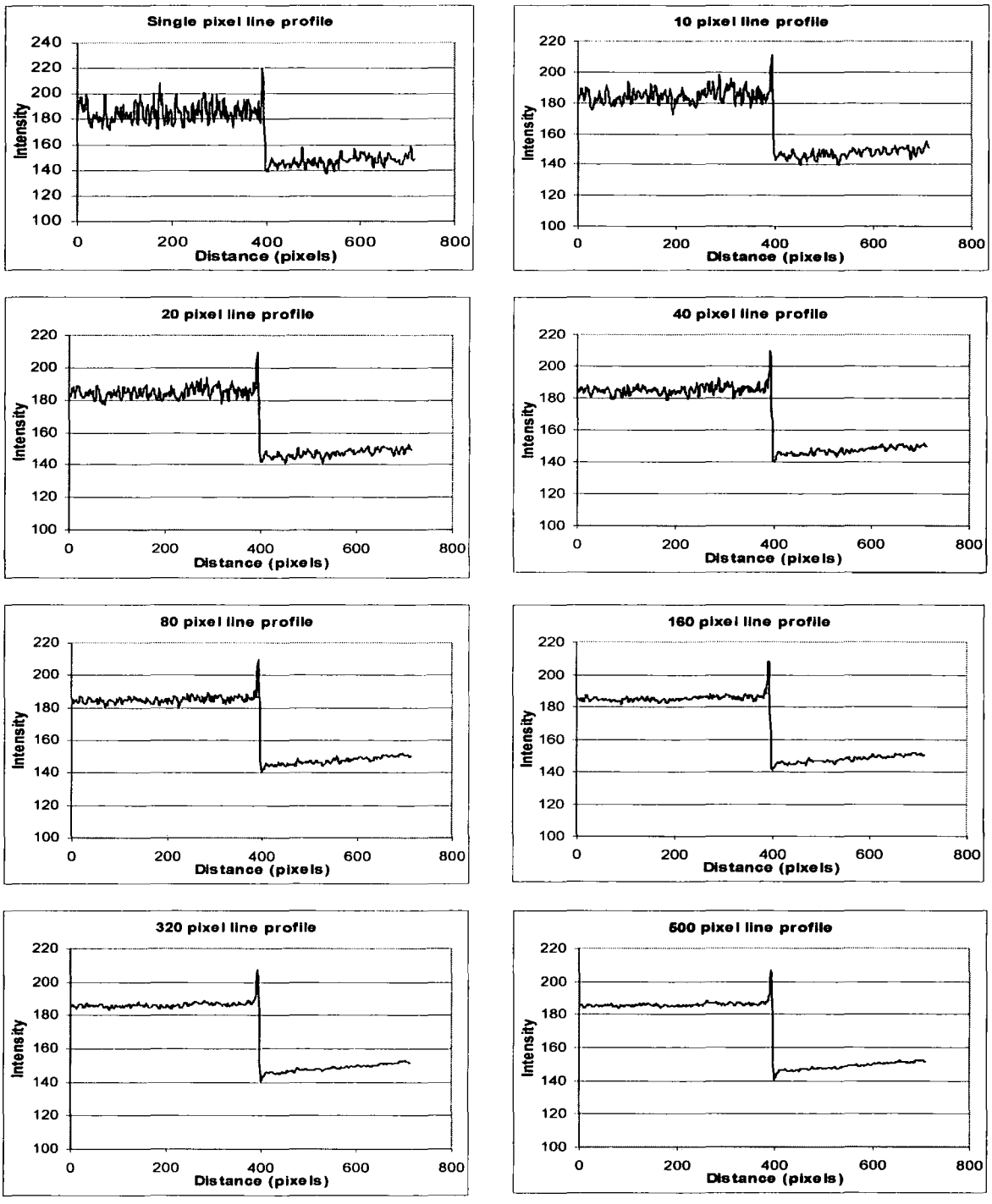

Figure 3.15: Intensity profiles of an image, integrated over increasing numbers of pixels

With a line profile of only single pixel width it is seen that the sections of the image representing constant absorption are again very noisy, with an unacceptable level of deviation from the corresponding average intensity. As the width of the line profile increases, this noise reduces to a more acceptable level. In order to quantify the noise reduction by this method, the standard deviation about the average maximum and minimum intensity was calculated for each image. These data are shown in figure 3.16.

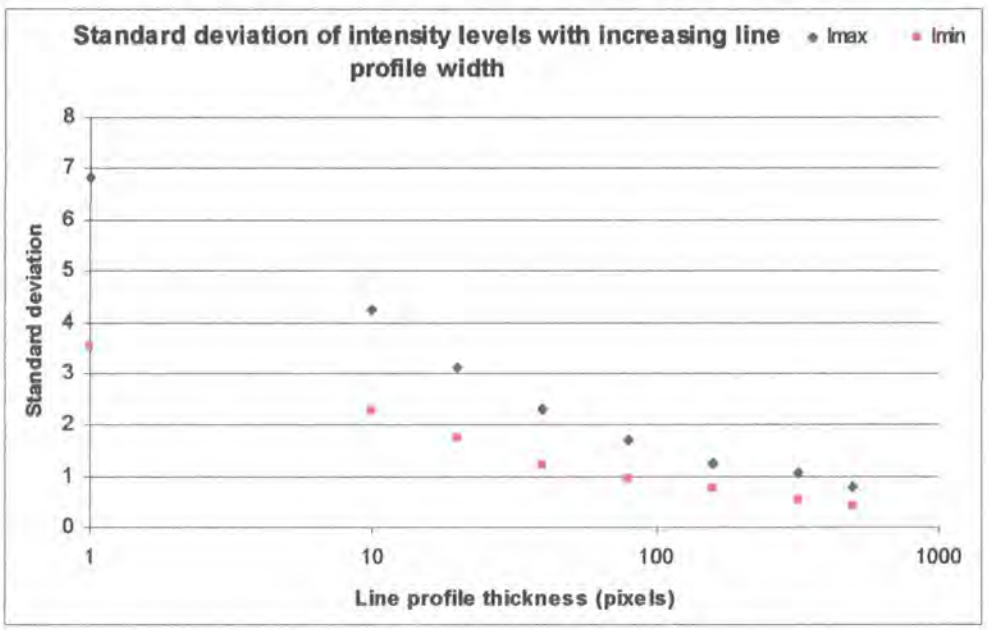

Figure 3.16: Standard deviations in maximum and minimum intensity levels as a function of the line profile width

Figure 3.16 shows the reduction in noise due to the integration of a line profile over an increasing number of pixels. From a single-pixel profile to a 500-pixel profile the coefficient of variation is seen to decrease by a factor of around 8.5 for both I_{max} and I_{min}. 320 or more pixels should be a sufficient line profile width for optimal reduction of this particular contribution to the noise levels, because the line profile should not reach the edges of the images.

3.2.3.3 Analysis of error on phase contrast calculations

It is necessary, of course, to estimate the errors in the phase contrast calculations. In order to do this, the pixels adjacent to those containing I_{max} & I_{min} (Phase) are taken into consideration. When reading off the maximum intensity, the intensities of the two adjacent pixels are checked, and that which is closer to I_{max} is recorded as the lower bound on I_{max}. In the same way, when reading off the minimum intensity, the intensities of the two adjacent pixels are checked, and that which is closer to I_{min} is recorded as the upper bound on I_{min}. This is illustrated in figure 3.17.

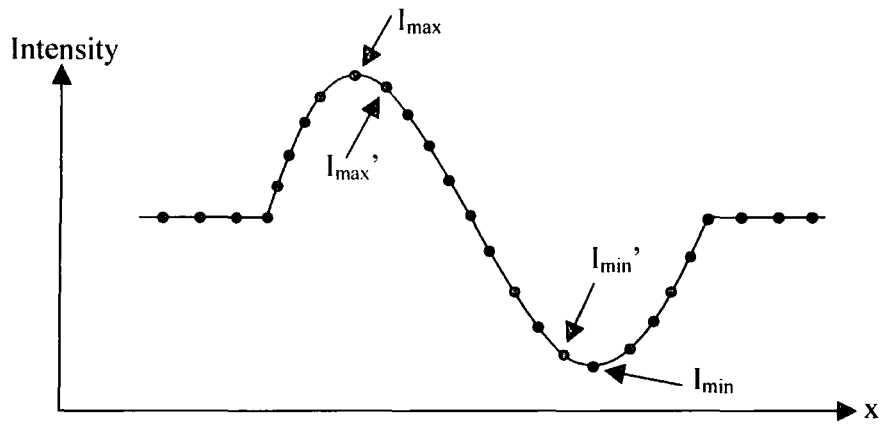

Figure 3.17: Intensity profile across phase-contrast image of sample approximating to a Heaviside function. Data points illustrate the determination of error on I_{max} & I_{min}.

The absolute errors are then given by:

$$Error(I_{Max}) = \pm\left|I_{Max} - I_{Max}'\right| \qquad (3\text{-}5)$$

$$Error(I_{Min}) = \pm\left|I_{Min}' - I_{Min}\right| \qquad (3\text{-}6)$$

So for a peak and trough which are sharp and narrow, the error is larger than for a peak and trough which are shallow and broadened out.

In addition to the error on the phase-contrast component of the image, the error on the absorption contrast must also be determined. Because the maximum and minimum

intensities in the absorption regime are determined by calculating the mean intensity value from the upper and lower flat sections of the intensity profile, a standard error is introduced. Here, the calculated mean becomes more accurate as more data points are used in the calculation, leading to the following definition of the error:

$$Error(A_{Max}) = \frac{\sigma_{(I_{Max})}}{\sqrt{N}} \qquad (3\text{-}7)$$

$$Error(A_{Min}) = \frac{\sigma_{(I_{Min})}}{\sqrt{N}} \qquad (3\text{-}8)$$

Where σ is the standard deviation from the mean for the dataset and N is the number of data points over which the mean has been calculated.

In order to calculate the error on the pure phase contrast measurement, these absolute errors are incorporated into the common error combination rules as follows:

$$Error[I_{Max} - (I_{Min} + (A_{\max} - A_{\min}))] = \sqrt{(Error(I_{Max}))^2 + (Error(I_{Min}))^2 + (Error(A_{Max}))^2 + (Error(A_{Min}))^2} \qquad (3\text{-}9)$$

$$Error[I_{Max} + (I_{Min} + (A_{\max} - A_{\min}))] = \sqrt{(Error(I_{Max}))^2 + (Error(I_{Min}))^2 + (Error(A_{Max}))^2 + (Error(A_{Min}))^2} \qquad (3\text{-}10)$$

$$Error\left(\frac{I_{Max} - (I_{Min} + (A_{\max} - A_{\min}))}{I_{Max} + I_{Min} + (A_{\max} - A_{\min})}\right) = \sqrt{\left(\frac{Error(I_{Max} - (I_{Min} + (A_{\max} - A_{\min})}{I_{Max} - I_{Min} + (A_{\max} - A_{\min})}\right)^2 + \left(\frac{Error(I_{Max} + (I_{Min} + (A_{\max} - A_{\min}))}{I_{Max} + I_{Min} + (A_{\max} - A_{\min})}\right)^2} \qquad (3\text{-}11)$$

In order to calculate the error on the absorption contrast measurement, the standard errors on A_{max} and A_{min} are incorporated into the common error combination rules in a similar fashion.

These final relative errors are converted to absolute errors by multiplying by the phase contrast or absorption contrast as appropriate, and these are illustrated in all graphs in the form of y- error bars.

3.2.3.4 Repeatability

In order to check the repeatability of the system with the source, detection, contrast quantification, noise and error considerations discussed above, a repeatability test was conducted with the rhodium and copper targets in place in turn. Ten images were taken of a fixed Heaviside Function sample, using identical source settings, one after another. Using the intensity profile of each image to quantify the phase and absorption contrast, the rhodium images are compared in figure 3.18 and the copper images compared in figure 3.19.

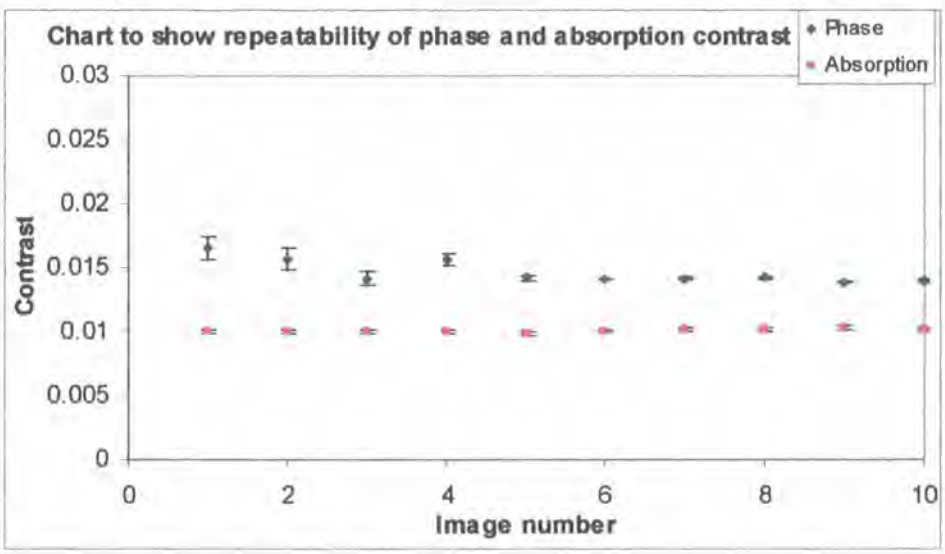

Figure 3.18: Graph of phase and absorption contrast obtained repeatedly using identical settings (Rhodium source)

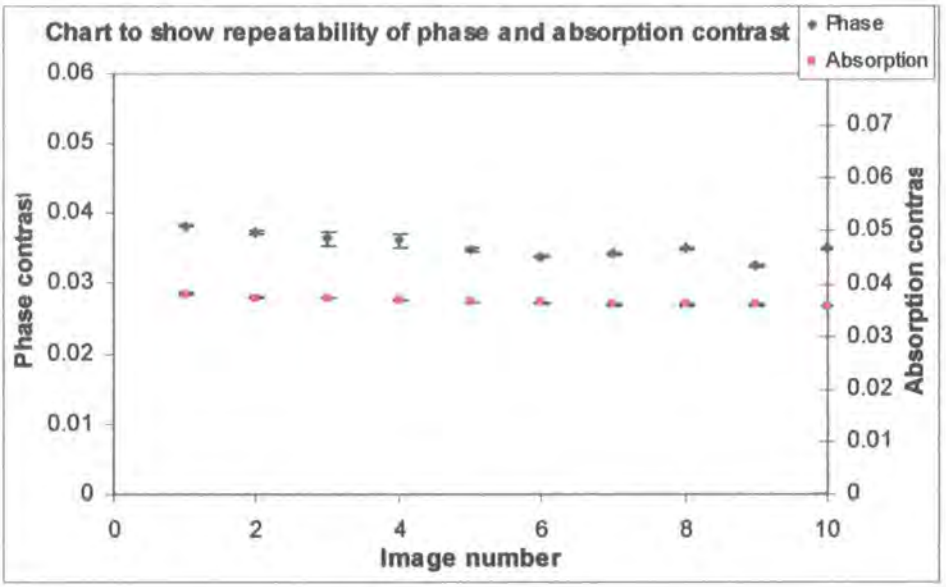

Figure 3.19: Graph of phase and absorption contrast obtained repeatedly using identical settings (Copper source)

With the rhodium target in place, the phase contrast results show a mean of 0.0146 and a standard deviation of 0.0009, which is a coefficient of variation of ±6.16%. The absorption contrast results show a mean of 0.0101 and a standard deviation of 0.0001, which is a coefficient of variation of only ±0.99%. With the copper target in place, the phase contrast results show a mean of 0.0353 and a standard deviation of 0.0016, which is a coefficient of variation of just ±4.53%. The absorption contrast results show a mean of 0.0366 and a standard deviation of 0.0007, which is a coefficient of variation of only ±1.91%. The repeatability of the system, using both targets, is satisfactory.

3.3 Sample mount

The samples take the form of planar, rectangular shapes. These are required to be fixed such that they are held vertically in the x-y plane, perpendicular to the direction of propagation of the X-rays. A mount was designed for this purpose, and a diagram of the design is shown in figure 3.20.

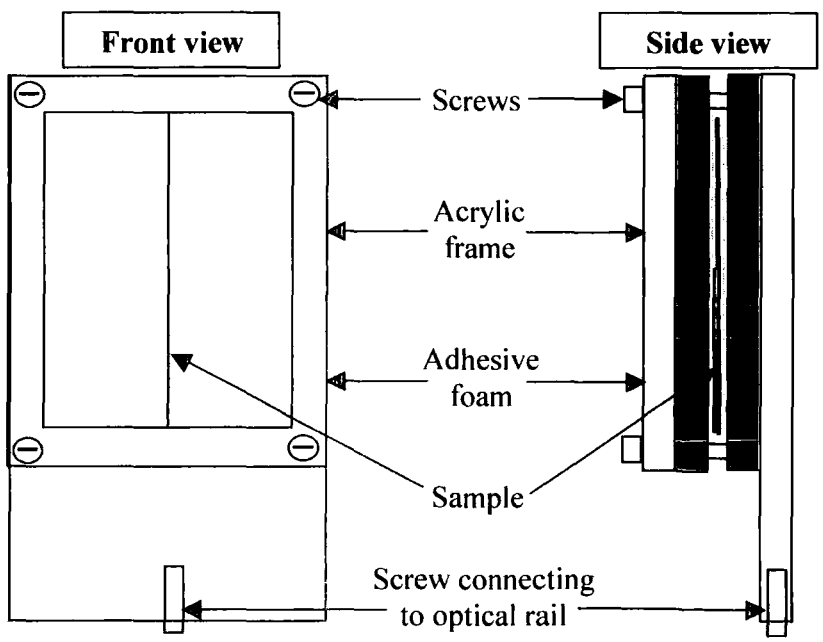

Figure 3.20: Schematic of sample mount design

The mount consists of two narrow rectangular frames made from transparent acrylic. Both frames have a hole tapped in each corner of the rectangular outline which allows them to be screwed together. An adhesive foam lines the rectangular outline on one side of each frame, and the two frames are screwed together such that the foam linings come together in the centre. This allows the mount to grip the sample securely at the edges without squashing or harming it. One frame extends below the rectangular outline and is screwed to an optical rail which runs between the source and detector, preventing the sample from moving or vibrating.

References

[1] Cloetens P. et al., *J. Phys. D.*, **32** pp.A145-A151 (1999)

[2] Kotre C. J. et al., *British Journal of Radiology*, **75** pp.170-173 (2002)

[3] Pagot E., et al, *Phys. Med. Biol.*, **50** pp.709-724 (2004)

[4] Xiao T. Q. et al, *Nucl. Instr. Meth. A.*, **548** pp.155-162 (2005)

[5] Hirano M. & Yamasaki K., *Nucl. Instr. Meth. A.*, **548** pp.187-193 (2005)

[6] David C. et al, *J. Phys. IV*, **104** pp.595-598 (2003)

[7] Becker P. et al, *Cryst. Res. Technol.*, **36** (6) pp.589-600 (2001)

[8] Arndt U. et al, *J. Appl. Cryst.* **31** (6) pp.936-944 (1998)

[9] Taylor, M. *et al*, in: *X-Ray Spectrometry, Recent Technological Advances*, eds. K Tsuji, *et al*, Wiley pp.13 (2004)

[10] Cowen A. R. *et al*, *The British Journal of Radiology*, **65** pp.528-535 (1992)

[11] Kreyszig E., *Advanced Engineering Mathematics (7th Edn)*, Wiley pp.278 (1993)

[12] Hecht, E., *Optics* (3rd Edn), Addison-Wesley pp.556 (1998)

[13] Farr R. F. et al., *Physics for Medical Imaging*, W. B. Saunders (1997)

4. Factors influencing phase contrast

This chapter discusses a number of experiments designed to investigate the influence of certain factors on the achievable phase contrast in images obtained using a laboratory-based microfocus X-ray source with the in-line method. These factors include the position of the sample, the source size, the monochromaticity of the X-ray source and the thickness of the detail within the sample.

It is an important first step to determine the optimum positioning within any imaging system. The effect of propagation distance on phase contrast features in a number of published articles. The results analyses tend to take one of two forms: either a qualitative discussion of the image detail (e.g. discussion of images of polystyrene foam taken with propagation distances of 1cm, 12cm, 22cm and 91cm [1]), or a slightly more in-depth analysis which looks at the image profiles (e.g. discussion of intensity profiles of phase contrast images of a cellulose fibre, taken with propagation distances of 25cm, 50cm, 1m and 2m [2]). The approach taken in this project is new in two respects. Firstly, the propagation distance is changed by only a few millimetres at a time, building up a more comprehensive picture of the relationship between phase contrast and propagation distance. Secondly, by quantifying the phase contrast as described in Chapter 3, this relationship will actually be plotted on a chart, so the dependence of phase contrast on propagation distance can be mapped out all the way along the optic axis. The results of this work are important because they build up a more comprehensive picture of the effect of propagation distance on phase contrast than has already been seen, and, more locally to this project, optimizing the propagation distance is obviously a vital first step to take when setting up an imaging system to record phase contrast using the propagation technique.

The theoretical effect of source size on phase contrast has been discussed in published literature, in that the transverse coherence has a dependency on source size [3], and image simulations have made use of this dependency [3]. Again, the approach taken in this project is new because the source dimensions are increased in small steps of the

order of microns, and the relationship between phase contrast and source size can be mapped out quantitatively in a graphical format. The effect of source size on phase contrast is important in any phase contrast imaging system, particularly where a balance needs to be found between the power loading per unit area on the target (which becomes greater as the source size is decreased) and the achievable phase contrast.

The claim that monochromatic X-radiation is best for phase contrast imaging has been repeated in many articles, usually followed by a discussion of a phase contrast image taken using monochromatic synchrotron radiation (examples include [2] and [4]). However Wilkins et al demonstrated that phase contrast is achievable with a polychromatic laboratory-based X-ray source [3]. It would be interesting to be able to directly compare images achieved using a polychromatic laboratory-based source, with images achieved using monochromatic X-rays from the same source. This comparison hasn't been seen, and this project attempts to make this comparison using an indicative image manipulation method and also via a filter method of partial monochromation. Since laboratory-based sources which are suitable for phase contrast imaging are so difficult to monochromate perfectly while retaining sufficient intensity levels, it is important to address this supposed need for monochromatic X-rays.

In phase contrast imaging to date, sample sizes have generally remained fairly small, varying typically from the order of 10 μm [5] to 20mm [6]. Experimental determination of the practical limits on the sample thickness for a given material has not been discussed in the published literature. This project looks at the relationship between phase contrast and the thickness of the sample boundary, and looks for a limiting thickness. It is important to know such limits on any imaging system to avoid obtaining misleading results, and knowing the relationship between sample thickness and phase contrast can lead to some form of system calibration.

All of the experiments in this chapter used the basic set-up shown in figure 4.1, with minor adjustments as described in each relevant section.

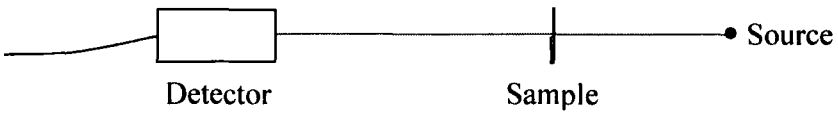

Figure 4.1: Basic experimental set-up for in-line method

The sample used in these experiments was the standard Heaviside function [7] sample as described previously in Chapters 2 and 3. The detector used to obtain the images for all of these experiments was the Photonic Science X-ray Eye i2i. Both copper and rhodium targets were used in these experiments to allow some degree of comparison between images obtained using different X-ray energies.

4.1 Sample position

4.1.1 Issues affected by sample position

The position of the sample affects a number of aspects of the imaging technique:

1. The transverse coherence length changes as the sample moves, according to the following equation [3]:

$$d = \frac{\lambda l}{\sigma} \qquad (4\text{-}1)$$

where d represents the transverse coherence length, λ the wavelength, l the source-sample distance and σ the source size. Thus the transverse coherence length increases with the source-sample distance with a coefficient of λ/σ and is dependent on the target. Consider the change in transverse coherence length for both sources as the source-sample distance increases. This is shown graphically in figure 4.2.

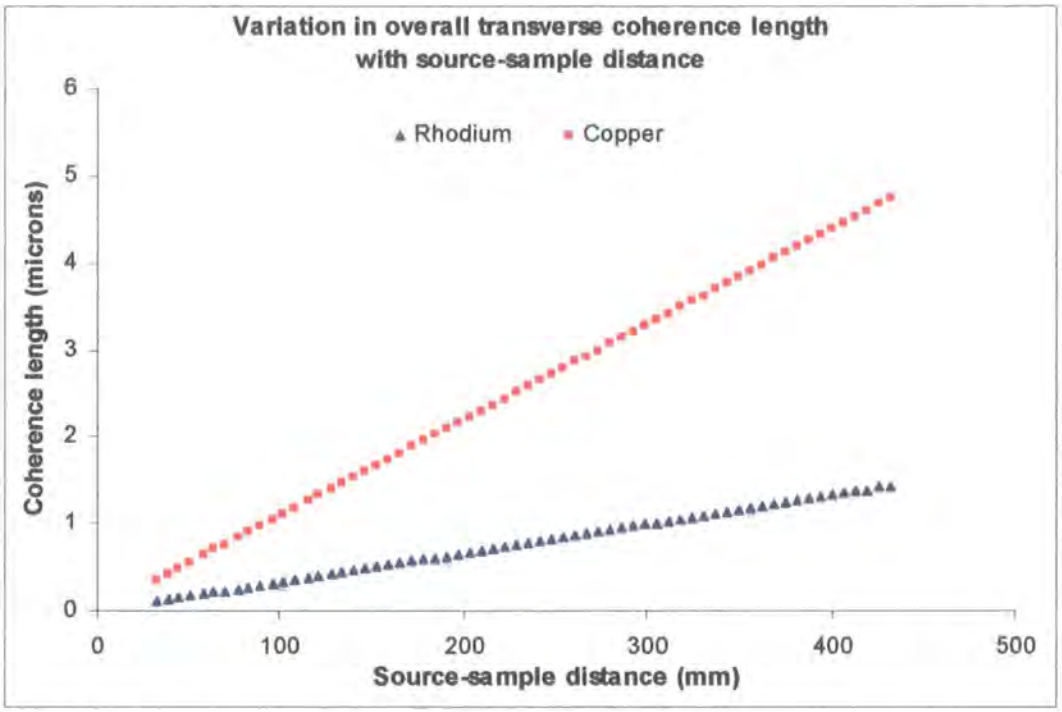

Figure 4.2: Variation in transverse coherence length with source-sample distance for copper and rhodium targets

In equation 4-1, the dimensionless coefficient of the source-sample distance is given by λ/σ, wavelength divided by source size. Using the wavelengths of the characteristic lines, for copper, this coefficient is 9.09×10^{-6}, and for rhodium it is 3.42×10^{-6}. Figure 4.2 shows that the transverse coherence length is always longer for the copper target than the rhodium target, and it increases with source-sample distance at a greater rate (a factor of approximately 2.5 greater) for the copper target than the rhodium.

2. The sample-detector distance provides the propagation distance over which the distorted wavefront is projected after transmission by the sample. By moving the sample toward the detector, this propagation distance is decreased, thus reducing the transverse propagation of the wavefront and hence the magnification of the system. This effect is illustrated in figure 4.3.

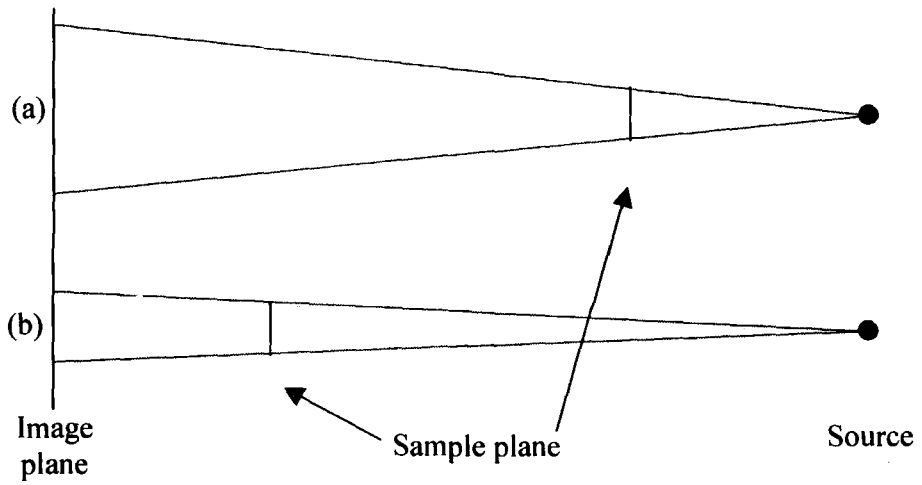

Figure 4.3: Illustration of the effect of sample position on the magnification of the system: (a) sample close to source, (b) sample close to detector.

This is a resolution issue, i.e. if two adjacent fringes representing a given boundary are not able to spread out in the plane perpendicular to the direction of propagation sufficiently to be detected by more than one pixel in the detector, this information will be lost to the image. So as the sample approaches the detector, the reduction in magnification of the system again becomes a detector resolution issue. The change in magnification with source-sample distance can be determined using similar triangles.

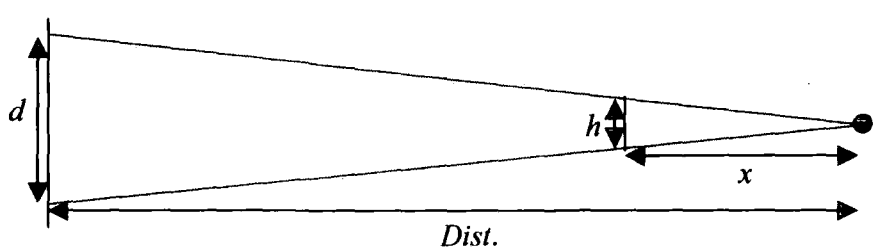

Figure 4.4: Schematic of set-up to illustrate magnification

Referring to figure 4.4, d represents the detector diameter, h the height of the sample, x the source-sample distance and $Dist$ the total distance between the source and the detector. The magnification is determined in the following way:

$$\frac{d}{Dist} = \frac{h}{x} \qquad (4\text{-}2)$$

$$Magnification = \frac{d}{h} = \frac{Dist}{x} \qquad (4\text{-}3)$$

Thus the magnification is independent of source size or X-ray energy. The magnification is calculated and is shown graphically in figure 4.5 as a function of the source-sample distance.

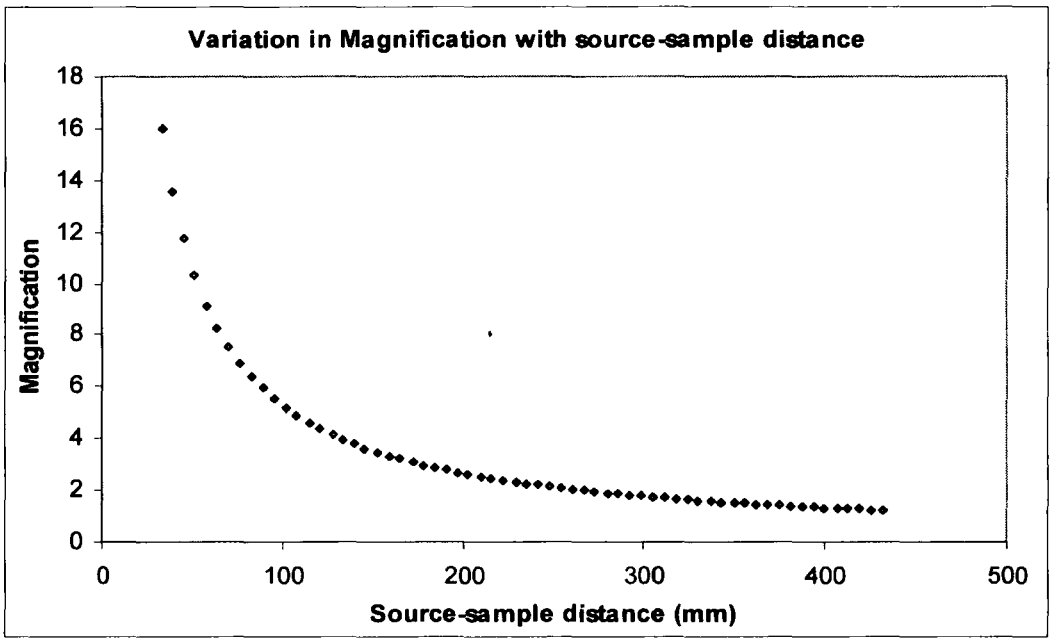

Figure 4.5: Variation in system magnification as a function of source-sample distance.

The magnification shows a non-linear relationship with the source-sample distance, and varies in the same way for both the rhodium and copper targets.

3. The effect of source blurring in the system changes with the sample position: this is reduced as the sample is moved towards the detector. This is illustrated in figure 4.6.

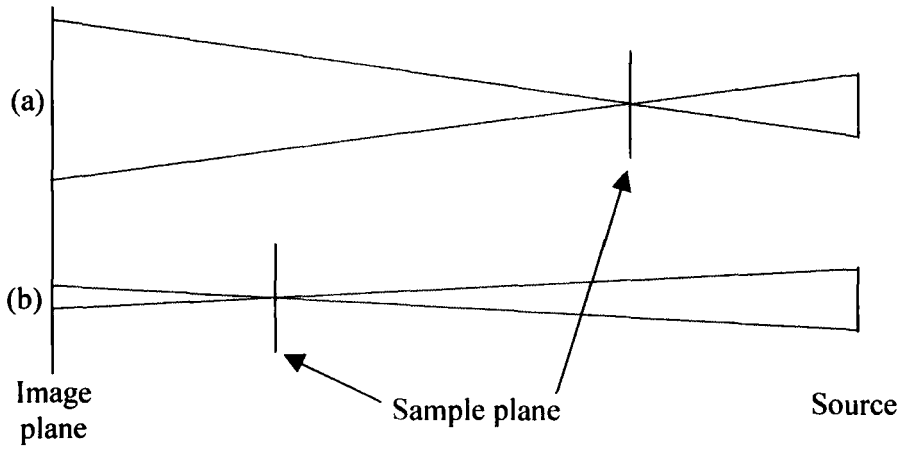

Figure 4.6: Illustration of effect of sample position on source blurring: (a) sample close to source, (b) sample close to detector.

It is seen in figure 4.6 that with a short source-sample distance and large sample-detector distance, the source blurring is much greater than that with a long source-sample distance and short sample-detector distance. As the object moves between these two extremes, the source blurring effect is continually changing.

Again, the change in source magnification with source-sample distance can be determined using similar triangles.

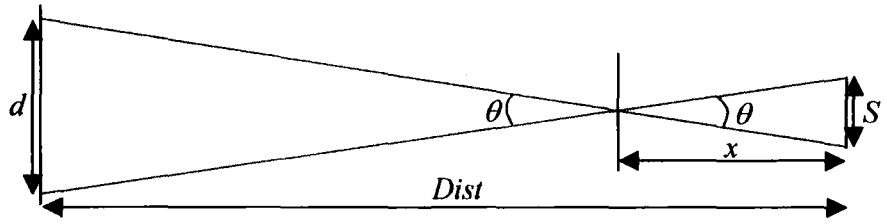

Figure 4.7: Schematic of set-up to illustrate source blurring

Referring to figure 4.7, d represents the width of the blur in the detector plane, S the diameter of the source, x the source-sample distance and *Dist* the total distance between the source and the detector. The source magnification is determined in the following way:

$$\frac{S}{x} = \frac{d}{(Dist - x)} \qquad (4\text{-}4)$$

$$Magnification = \frac{d}{S} = \frac{1}{x}(Dist - x) \qquad (4\text{-}5)$$

Thus the image blurring effect is also independent of the X-ray energy.

When plotted as a function of source-sample distance, the source blurring shows a non-linear relationship with the source-sample distance. In fact it has the same curve as the system magnification with an intercept of –1. This is shown in figure 4.8. One does not necessarily gain from using a high-magnification system due to the concomitant source-blurring effect in the system.

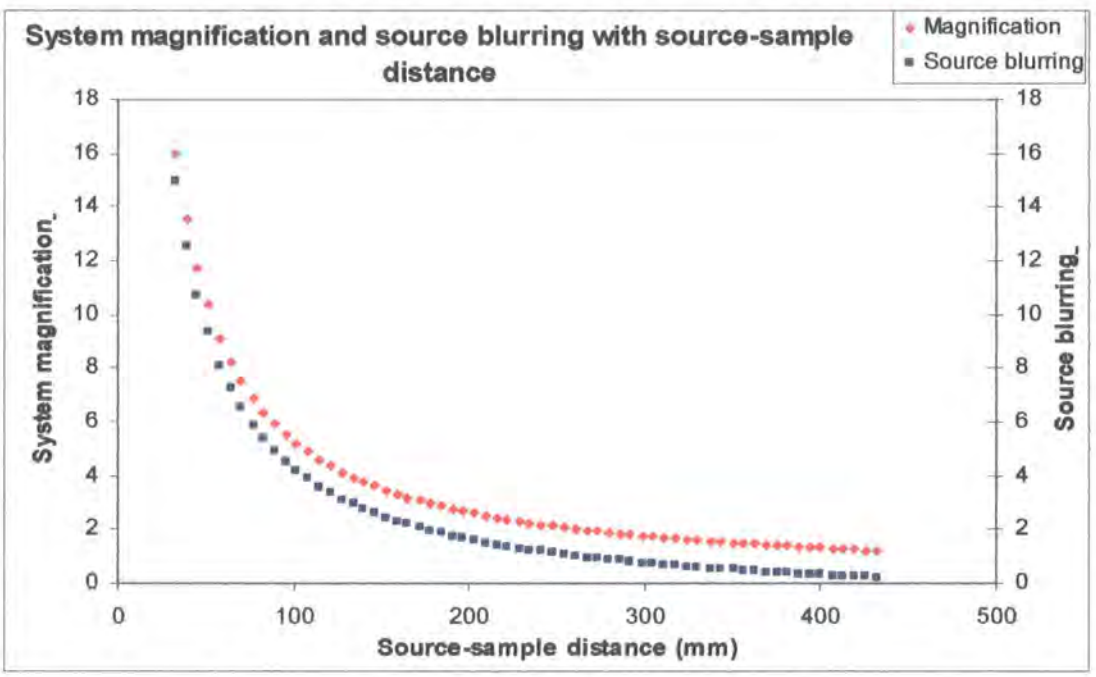

Figure 4.8: Variation in system magnification and source blurring as a function of source-sample distance

4.1.2 Experiment

The set-up for the sample position experiment is shown in figure 4.9.

Figure 4.9: Set-up of sample position experiment

The experimental set-up consisted of the source, sample and detector as shown in figure 4.9. The source and detector remained fixed at a distance of 528mm apart. The Heaviside function sample used in this experiment was made of paper, with an effective step size of 0.098mm. This was mounted on an automated moveable mount which allowed smooth movement of the sample between the source and detector while removing problems associated with the sample being vibrated or moving in the plane perpendicular to the optic axis. The phase contrast of each image was quantified as described in chapter 3, using the following formula:

$$Contrast = \frac{I_{Max} - (I_{Min} + (A_{Max} - A_{Min}))}{I_{Max} + I_{Min} + A_{Max} - A_{Min}} \qquad (4\text{-}6)$$

The experiment was conducted using rhodium and copper targets. The results obtained using each target are plotted against the propagation distance, on the same set of axis, in figure 4.10.

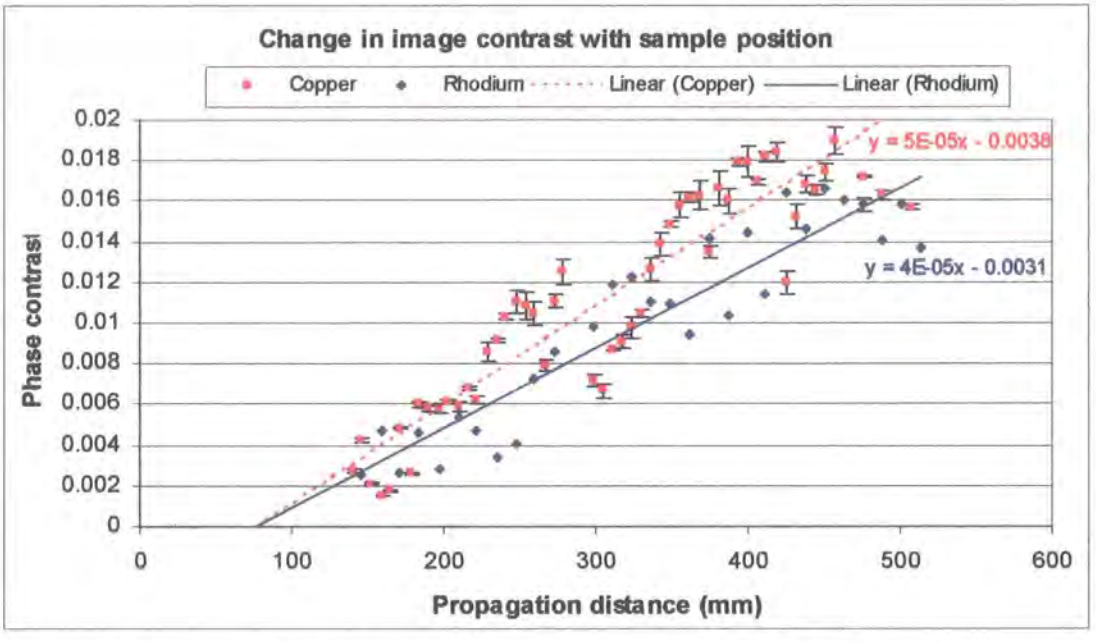

Figure 4.10: Phase contrast plotted as a function of object-image distance for rhodium and copper targets

By fitting a line of best fit to each of the plots, it is seen that the image contrast is directly proportional to the propagation distance from the sample to the detector. Thus, despite the increase in coherence length as the sample moves toward the detector, the decreasing propagation distance clearly dominates the result.

Although the copper phase contrast is seen to increase with propagation distance at a slightly faster rate than the rhodium phase contrast, the phase contrast achieved using both targets is of the same order of magnitude. This suggests that a larger difference in the δ values is required to provide a significant difference in phase contrast within the dimensions of this set-up.

The gradients of the lines of best fit are of the same order, and extrapolation of both of these shows that they should cross the x-axis at a sample-detector distance of 78±7mm. This indicates that, using this imaging system, phase contrast is not achievable with a propagation distance of 78mm or less.

4.2 Source size

4.2.1 Coherence length

Due to the high degree of spatial coherence required of the X-ray source, it is necessary to investigate the effect of source size on the phase contrast imaging technique. Again we refer back to equation 4-1 because the transverse coherence length is related to source size by the following relation [3]:

$$d = \frac{\lambda l}{\sigma} \qquad (4\text{-}1)$$

An inversely proportional relationship between transverse coherence length and source size implies that ideally a point source would give the best results. However, in reality this is not a possibility and so it is necessary to determine the tolerance of the phase contrast technique to the achievable source sizes.

From equation 4-1, it is seen that the transverse coherence length depends on wavelength and source-sample distance in addition to the source size. Thus by keeping the source, sample and detector fixed, the source-sample distance factor will not affect the results. With a polychromatic source, there is a range of wavelengths present in the X-ray beam which leads to a range of coherence lengths. By keeping the operating voltage and current settings of the microfocus X-ray source constant, these wavelengths will make a fixed contribution to the transverse coherence length throughout the experiment and thus should not affect the results.

In order to alter the source size without making a difference to the spectrum, the source is first focused down to its smallest size and is gradually defocused to spread it out while keeping the power output fixed. The focus values available on the Microsource® are unitless integers, ranging from -99 to +99.

4.2.2 Determination of Source size

In order to determine the source dimensions, a 125μm diameter crosswire was imaged using a high-resolution X-ray camera with a pixel size of 11μm. Figure 4.11 shows a schematic of a crosswire image, and two example images are shown in figure 4.12.

Figure 4.11: Schematic of typical crosswire image

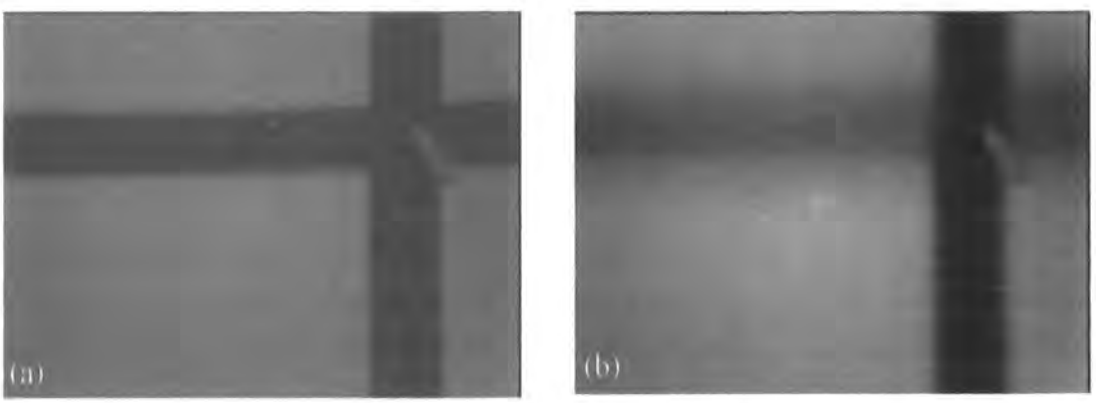

Figure 4.12: Example rhodium target crosswire images: (a) Focus = 87, with a source size of 19μm x 22μm, (b) Focus = 70, with a source size of 46μm x 122μm. The image of the horizontal wire is smeared out by the taller source size

Certain sections of the above image were used to determine the beam width and beam height, by taking thick line profiles and making use of the resulting intensity profiles. These sections are illustrated in figure 4.13.

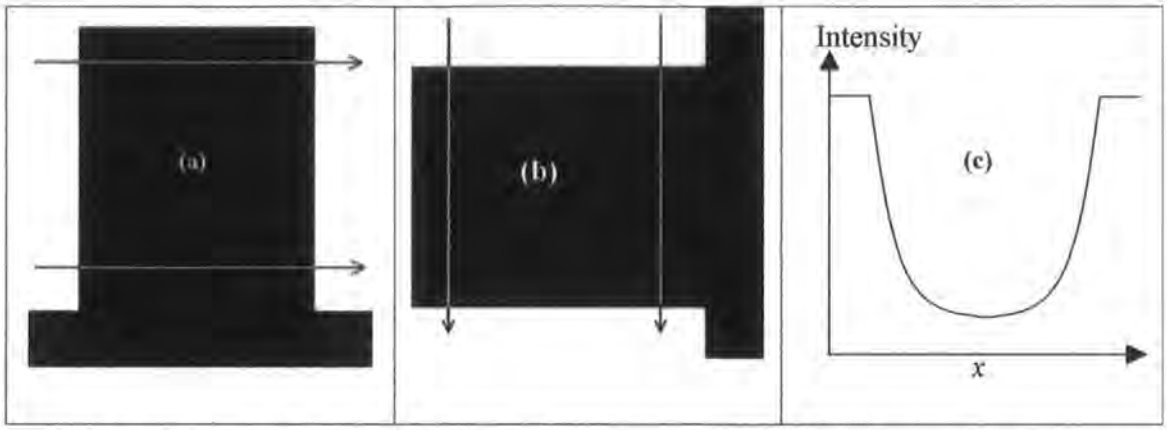

Figure 4.13: Sections of crosswire image used to determine source size: (a) thick line profile to determine source width, (b) thick line profile to determine source height, and (c) intensity profile seen in both cases

The width of the source is calculated using the part of the image showing the vertical wire (section (a) in figure 4.13) and the height of the source is calculated using the part of the image showing the horizontal wire (section (b) in figure 4.13). Details of the calculation of source size from the crosswire images are included in Appendix B.

It was determined that the source has an elliptical shape, and for the purposes of this experiment the rhodium target source size ranged from 19μm width x 18μm height to 45.5μm width x 123.5μm height. The copper target source size ranged from 12μm width x 17μm height to 62.5μm width x 125μm height.

The source-sample distance was fixed at 134mm. By including this distance in equation (4-1), along with the K_α energies and source size ranges for the copper and rhodium targets, the corresponding ranges of spatial coherence lengths can be determined. During this experiment the rhodium target's vertical coherence length ranged from 0.07μm at the largest focus to 0.47μm at the smallest focus, while its horizontal coherence length ranged from 0.17μm at the largest focus to 0.43μm at the smallest focus. The copper target's vertical coherence length ranged from 0.17μm at the largest focus to 1.22μm at the smallest focus, while its horizontal coherence length ranged from 0.33μm at the largest focus to 1.77μm at the smallest focus.

4.2.3 Effect on phase contrast

The main source size experiment was set up as shown in figure 4.14. The same paper sample was used as before.

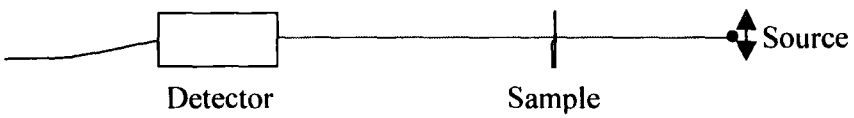

Figure 4.14: Set up of source size experiment

The source, sample and detector remained fixed in position with a source-sample distance of 134mm and a sample-detector distance of 394mm. The X-ray source operating voltage and current settings remained constant at the values stated in Chapter 3. The source size was altered by defocusing.

The first image was taken with the focus at its lower bound (for copper, imaging began with a focus value of 66, for rhodium, imaging began with a focus value of 70), and this was gradually increased by intervals of 0.5. There is some hysteresis present in the focus coils of the source, and so the focus was changed in the same direction for each set of data collected (i.e. each set of data began with the focus at its lowest value and this was increased to its highest value). The sample was imaged at each focus value with the boundary between the thin and thick layers set vertically (as demonstrated in figure 4.15(a)). Then the focus was returned to its lowest value and the sample was rotated through 90° and imaged at each focus value with the boundary between the thinner and thicker layers set horizontally (as demonstrated in figure 4.15(b)).

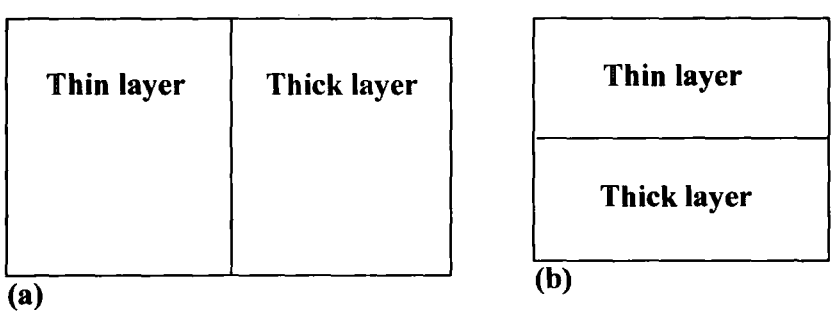

Figure 4.15: (a) Sample arranged with vertical boundary; (b) Sample arranged with horizontal boundary.

Images were taken at every integer and half-integer focus value, allowing a sample of 53 phase-contrast images for each target. The phase contrast was quantified using equation 4-6 as described in Chapter 3. In the charts showing the results of the source size experiment, the contrast with the boundary oriented vertically (as in figure 4.15(a)) is labelled "Vertical" contrast, while the contrast with the boundary oriented horizontally (as in figure 4.15(b)) is labelled "Horizontal" contrast.

4.2.3.1 Copper target

Initially, an 'effective radius' of the source was calculated by dividing the cross-sectional area of the source by π, and taking the square root, as in equation 4-9:

$$R_{eff} = \sqrt{\frac{Area}{\pi}} \qquad (4\text{-}9)$$

The phase contrast is shown as a function of the effective radius of the source in figure 4.16.

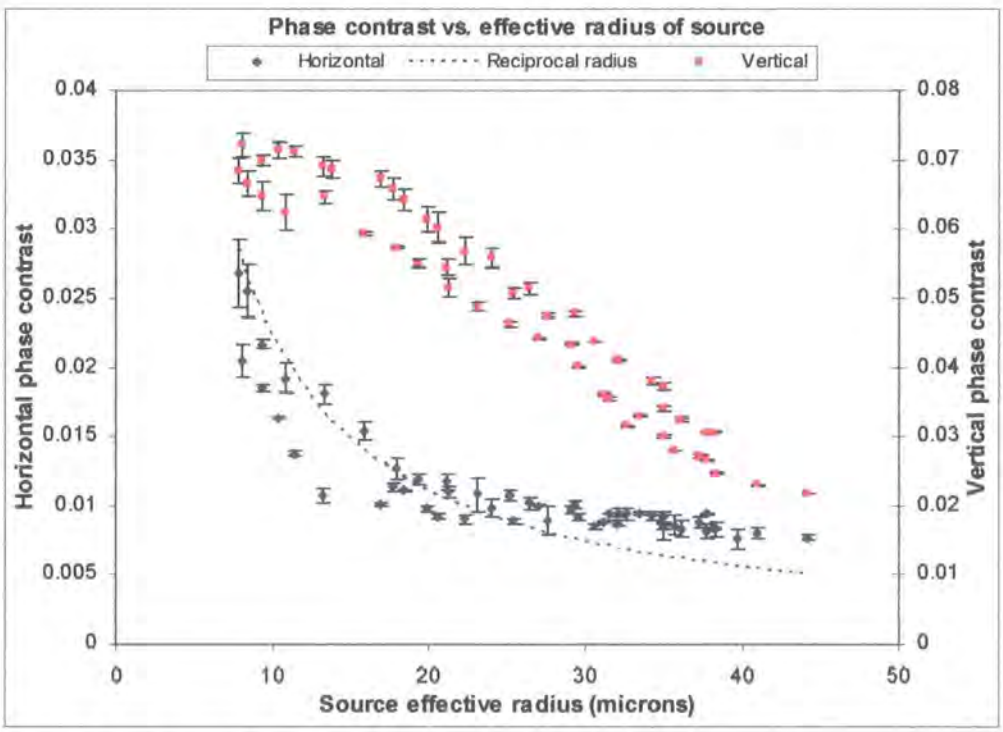

Figure 4.16: Variation in phase contrast as a function of effective radius of the copper source.

Figure 4.16 shows an overall drop in the phase contrast as the source size is increased, as expected from equation 4-1. The relationship between the phase contrast of the vertical boundary and the effective radius appears to be linear, but a plateau towards the higher effective radii suggests that a fit to a plot of reciprocal effective radius could also be appropriate. The horizontal phase contrast shows a good fit to a plot of the reciprocal of the effective radius when scaled up to a similar level. This indicates that the phase contrast of the horizontal boundary varies in proportion with the effective transverse coherence length. In order to investigate these trends in more detail, the results are plotted against the width and the height of the source separately. Figure 4.17 shows the phase contrast plotted as a function of source height and figure 4.18 shows the phase contrast plotted as a function of source width.

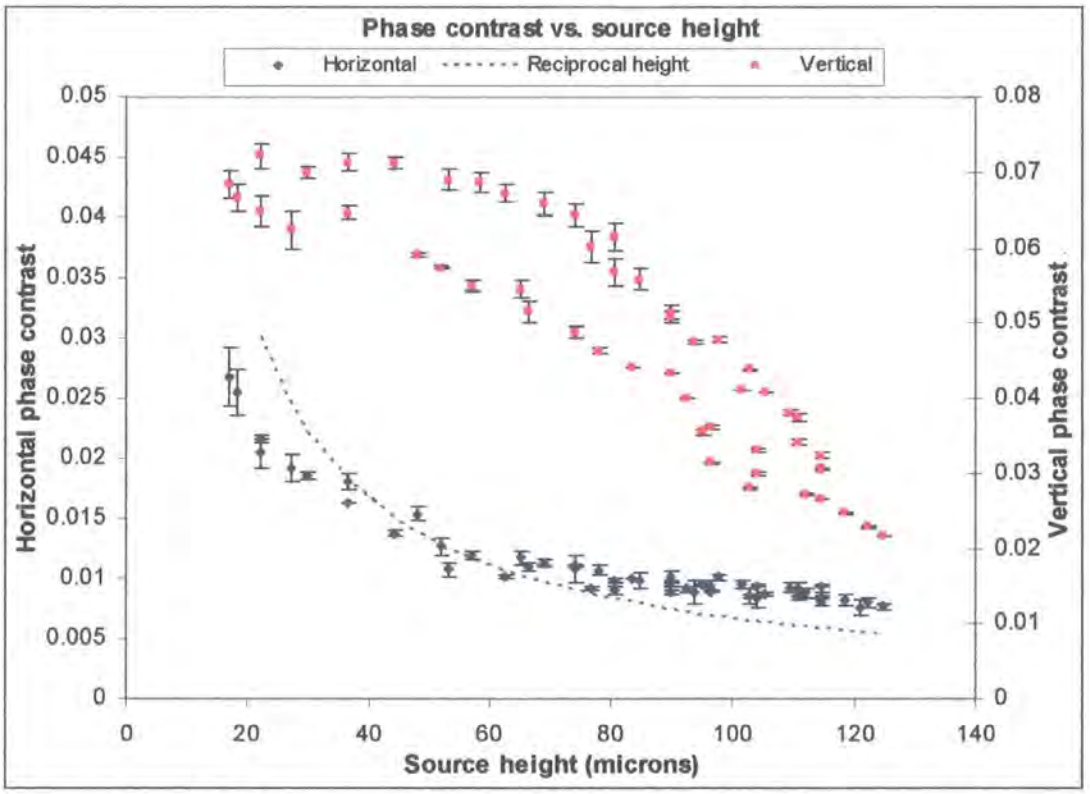

Figure 4.17: Phase contrast plotted as a function of the height of the copper source

In figure 4.17, similar trends show up again:

- The phase contrast is degraded as the source size is increased.

- The phase contrast of the horizontal boundary is quite well-fitted to a plot of reciprocal source height, demonstrating a strong proportional relationship with the transverse coherence length in the vertical direction.
- The phase contrast of the vertical boundary displays moderate correlation with the source height, and does not follow a plot of reciprocal source height.

These points indicate that while the phase contrast of the horizontal boundary is strongly affected by the transverse coherence length in the perpendicular vertical direction, the phase contrast of the vertical boundary is not affected as strongly by this.

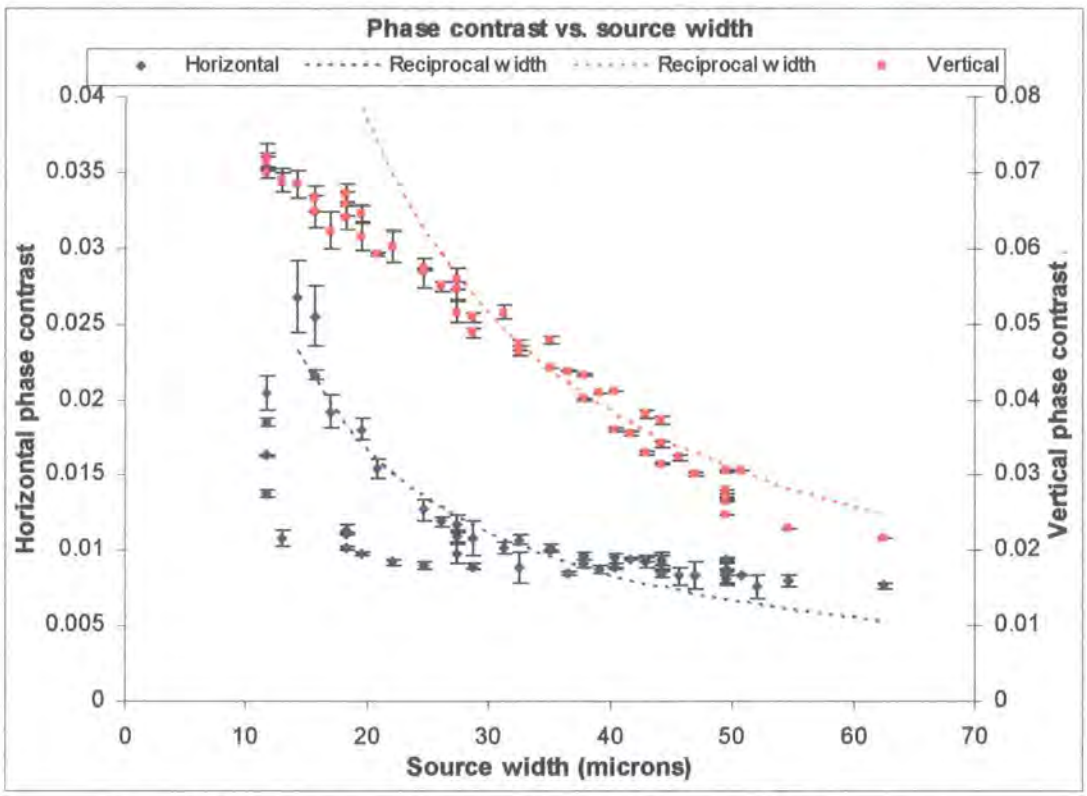

Figure 4.18: Phase contrast plotted as a function of the width of the copper source

With phase contrast plotted against the source width:

- We see degradation in the phase contrast of the horizontal and vertical boundaries.
- The phase contrast of the horizontal boundary shows weak correlation with the source width, and moderate correlation with the reciprocal of the source width. This

indicates that the phase contrast of the horizontal boundary is not affected as strongly by the width of the source as by the height, and consequently is less strongly affected by the horizontal transverse coherence length which runs in a parallel direction to it, as by the perpendicular vertical transverse coherence.

- The phase contrast of the vertical boundary shows very strong correlation with the source width. A comparison between figures 4.17 and 4.18 shows that the phase contrast of the vertical boundary is affected much more strongly by the source width than the source height.

The correlations of the phase contrast of each boundary with the effective radius, height and width of the source, and their respective reciprocals, are shown in table 4.1.

	Correlation coefficient of phase contrast with source dimensions	
	Horizontal boundary	Vertical boundary
Source effective radius	-0.804	-0.968
Reciprocal effective radius	0.940	0.829
Source height	-0.887	-0.895
Reciprocal source height	0.974	0.701
Source width	-0.692	-0.990
Reciprocal source width	0.747	0.914

Table 4.1: Correlation coefficient of phase contrast with source dimensions and their reciprocals (copper source).

For all three dimensions, the phase contrast of the horizontal boundary shows better correlation with the reciprocal of the dimension (and hence the transverse coherence), than with the dimension itself. This shows that the phase contrast of the horizontal boundary varies directly with the transverse coherence. Furthermore, the correlation with the reciprocal of the source height (and hence the transverse coherence in the vertical direction) is far stronger than that with the reciprocal of the source width. Thus

the transverse coherence in the vertical direction, i.e. perpendicular to the boundary itself, dominates the result.

The phase contrast of the vertical boundary shows strong correlation with the dimensions themselves and also with their respective reciprocals. The phase contrast shows stronger correlation with the source width than with the source height, and much stronger correlation with the reciprocal of the source width than with the reciprocal of the source height. So the horizontal direction, i.e. perpendicular to the boundary itself, dominates the result.

4.2.3.2 Rhodium target

Initially, the phase contrast achieved using the rhodium target was plotted as a function of the effective radius of the source (as per equation 4-9), to look at the general trend in the phase contrast with source size. This is shown in figure 4.19.

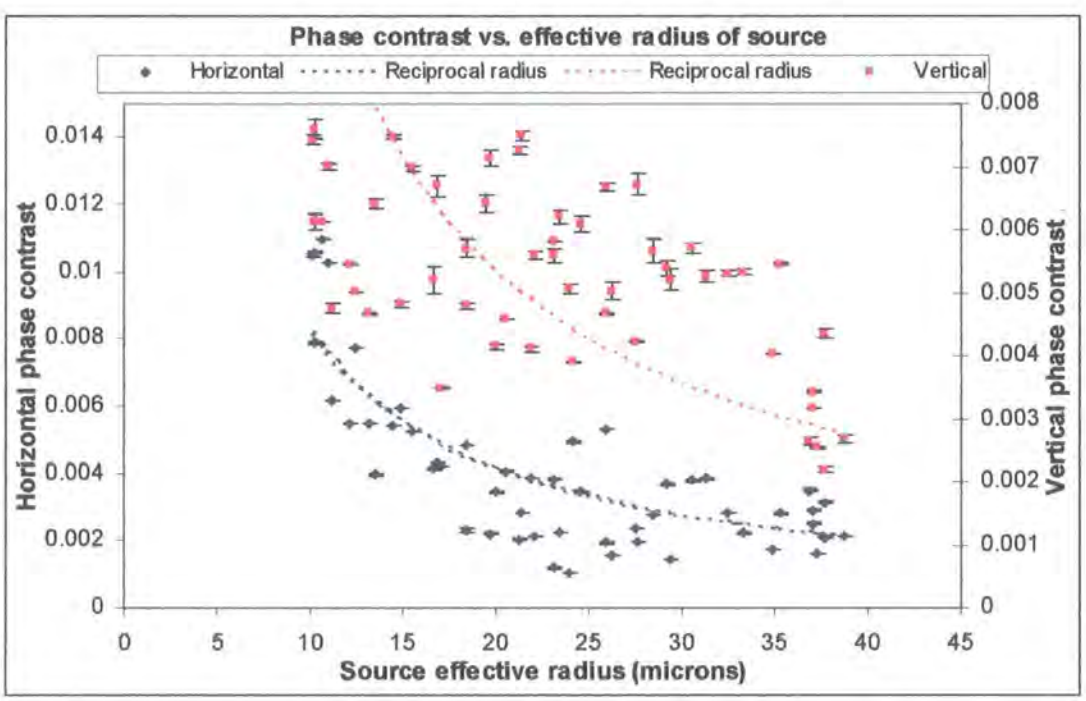

Figure 4.19: Variation in phase contrast as a function of effective radius of the rhodium source

The rhodium results are more scattered than the copper results, but the phase degradation with increasing source size is still seen. The relationship of the phase contrast of the horizontal boundary with the effective source radius again appears to be more consistent with a plot of reciprocal effective radius than a linear relationship. The phase contrast of the vertical boundary is quite scattered and could be either a linear plot or a fit to reciprocal effective radius, so the precise relationship cannot really be determined from this chart. In order to investigate these trends in more detail, the results are once again plotted against the width and the height of the source separately. Figure 4.20 shows the image contrast plotted as a function of beam height and figure 4.21 shows the image contrast plotted as a function of source width.

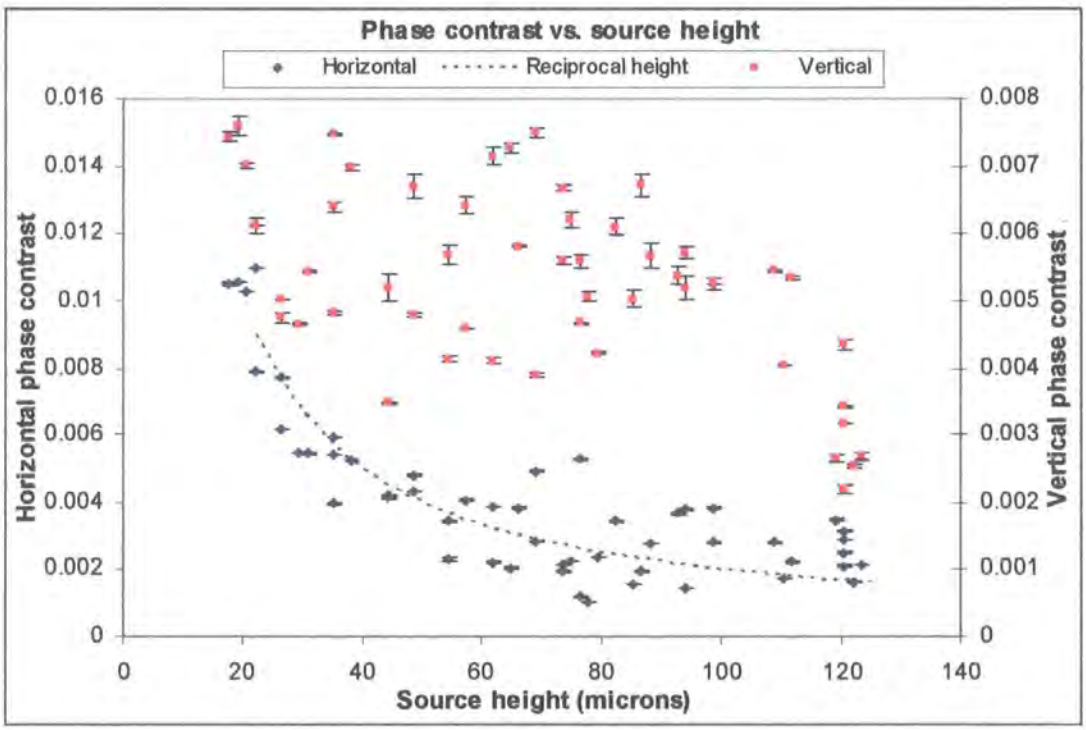

Figure 4.20: Image contrast plotted as a function of the height of the rhodium source

In figure 4.20, similar trends show up to those seen in figure 4.17:

- Phase contrast is degraded as the source size is increased.

- As before, the phase contrast of the horizontal boundary fits better to a plot of reciprocal source height than to the height itself, demonstrating a proportional relationship with the transverse coherence length in the vertical direction.
- The phase contrast of the vertical boundary displays poor correlation with the source height, and with reciprocal source height.

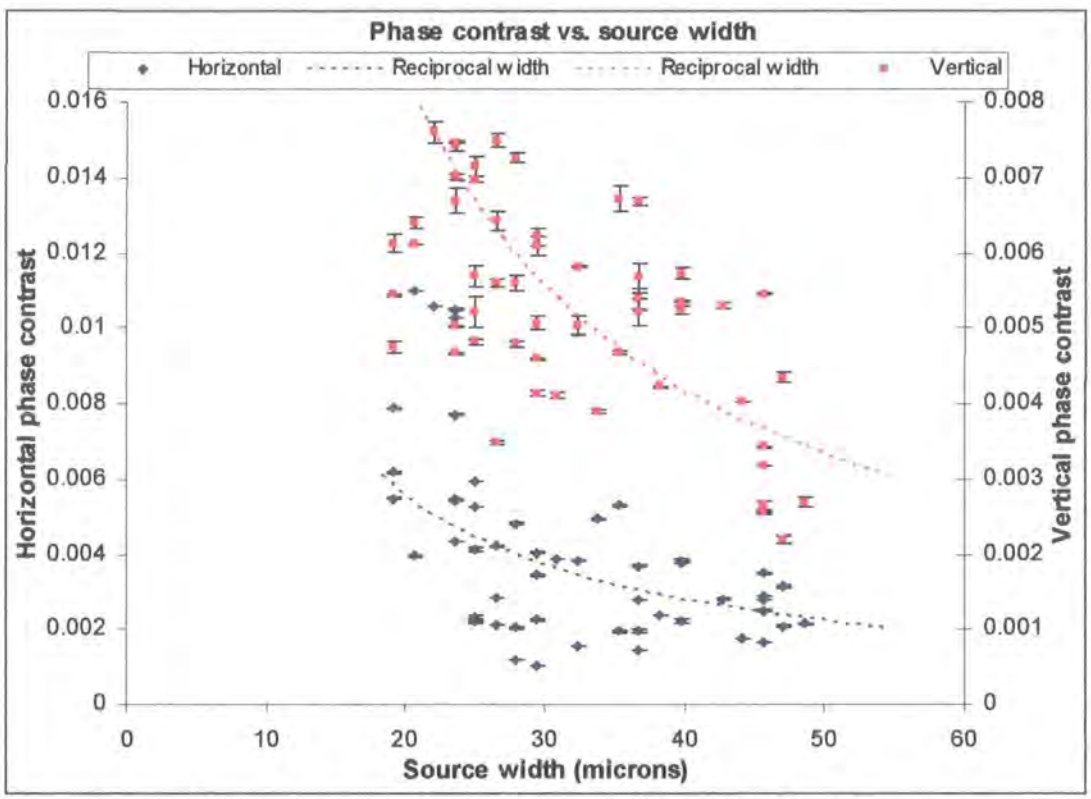

Figure 4.21: Image contrast plotted as a function of the width of the rhodium source

When plotted against the source width:

- The degradation of the phase contrast of the horizontal and vertical boundaries is evident again.
- The phase contrast of the horizontal boundary shows a weaker relationship with the reciprocal of the source width than with the reciprocal of the source height. This indicates that the phase contrast of the horizontal boundary is not affected as strongly by the width of the source as by the height, and consequently is less

strongly affected by the horizontal transverse coherence length which runs in a parallel direction to it.

- The phase contrast of the vertical boundary displays some correlation with the source width, but may follow a reciprocal width plot. It is not immediately clear whether the phase contrast of the vertical boundary is affected by the source width or the horizontal transverse coherence.

The correlations of the phase contrast of each boundary with the effective radius, height and width of the source, and their respective reciprocals, are shown in table 4.2.

	Correlation coefficient of phase contrast with source dimensions	
	Horizontal boundary	Vertical boundary
Source effective radius	-0.692	-0.691
Reciprocal effective radius	0.850	0.594
Source height	-0.734	-0.654
Reciprocal source height	0.913	0.530
Source width	-0.547	-0.731
Reciprocal source width	0.615	0.676

Table 4.2: Correlation coefficient of phase contrast with source dimensions and their reciprocals (rhodium source).

The correlation figures in Table 4.2 show weaker correlation overall than those in Table 4.1: this simply reflects the fact that the rhodium results are more scattered than the copper results. As before, for all three dimensions, the phase contrast of the horizontal boundary shows better correlation with the reciprocal of the dimension (and hence the transverse coherence), than with the dimension itself. This suggests that the phase contrast of the horizontal boundary varies directly with the transverse coherence. Furthermore, the correlation with the reciprocal of the source height (and hence the transverse coherence in the vertical direction) is very much stronger than that with the

reciprocal of the source width. Thus the transverse coherence in the vertical direction, i.e. perpendicular to the boundary itself, dominates the result.

The phase contrast of the vertical boundary actually shows slightly stronger correlation with the dimensions themselves than with their respective reciprocals. The phase contrast shows stronger correlation with the source width than with the source height, and also shows stronger correlation with the reciprocal of the source width than with the reciprocal of the source height. Thus the width of the source dominates the result.

The phase contrast in the images of the horizontal boundary has shown strong correlation with the vertical coherence length, demonstrating the importance of the perpendicular coherence length in propagation phase contrast imaging. The images of the vertical boundary have not shown the equivalent dependence on the horizontal coherence length quite as markedly, although the copper results do suggest that this dependence could be in place. The lesser effect for the vertical boundary is likely to be due to the way in which the x-ray beam is projected by the source. As the source is de-focused, the projection becomes more elliptical, spreading in the vertical direction. However, the change in the horizontal projection is minimal, particularly for the rhodium source. The increasing source width measured by the cross-wire method is likely to be an over-calculation of the actual range, due to distortion caused by the huge increase in the beam height. The apparently linear dependence of the vertical boundary phase contrast on the rhodium source width more likely represents the change over a much smaller range of widths. This range is small enough that the section of the coherence length curve is short enough to appear linear. Thus the plots of the phase contrast of the vertical boundary against the source width, more particularly for the rhodium target, perhaps tell us more about the gradient of a tangent to the curve over a narrower range of source widths around the value of the smallest width measured.

The results for both copper and rhodium targets demonstrate the importance of source size, and consequently spatial coherence, in phase contrast imaging. From this work we can conclude that with fixed wavelength range and source-sample distance, it is the

source dimension in the direction *perpendicular* to a given boundary in a sample, which dominates the image contrast at that boundary. To illustrate: with the sample oriented such that the boundary between the thin and thick sections is *horizontal* (as in figure 4.15(b)), the *vertical* dimension of the source dominates the image contrast, and vice versa.

4.3 Monochromaticity

A great deal of work on phase-contrast imaging has been performed using monochromatic synchrotron radiation. The output of a synchrotron beam comprises high intensities across a wide range of wavelengths, so phase contrast imaging with a polychromatic synchrotron beam will provide images with smeared-out phase contrast effects due to the differing behaviour of the wavelengths on transmission through a sample. Thus monochromatic synchrotron radiation is commonly used for phase-contrast imaging purposes.

Realistically, however, synchrotron radiation cannot be used for the majority of planned applications of phase-contrast imaging. For example, for possible *in-vivo* medical diagnostic applications, hospitals would need to have a synchrotron source on-site or would have to send patients away to their closest synchrotron source. Neither of these options is either practical or cost-effective, although the latter option is possible for patients living in Stanford, Hamburg or Grenoble! Further development of phase contrast imaging techniques for practical application ultimately depends on the suitability of laboratory X-ray sources. In practice, perfectly monochromatic X-ray radiation such as that obtained at synchrotron sources is not achievable for a laboratory-based microfocus X-ray source. It is therefore useful to determine whether a laboratory X-ray source can provide good phase contrast images with its natural polychromatic spectrum, and also when using methods available for partial monochromation.

All experiments in this project, other than this monochromaticity investigation, use the source's natural, polychromatic spectrum. This has produced images with sufficient

phase contrast content to measure the effects of other factors. This section concentrates on the effects of partially monochromating the X-ray beam.

4.3.1 Increasing operating voltage and image manipulation method

A simple method for viewing the phase contribution made by certain parts of the X-ray source's spectrum involves manipulation of the phase contrast images themselves. For example, spectra are collected at operating voltages of 15kV and 25kV. Subtraction of the 15kV spectrum from the 25kV spectrum produces a pseudo-spectrum with less Bremsstrahlung. Images are then taken at operating voltages of 15kV and 25kV. By subtracting the image taken at 15kV from the image taken at 25kV, one can get an idea of the image obtained by the pseudo-spectrum. This image manipulation method was used with both the copper and rhodium sources.

Using the copper target, spectra were recorded at operating voltages of 15kV, 20kV, 25kV, 30 kV, 35 kV and 40 kV. These are shown in figure 4.22.

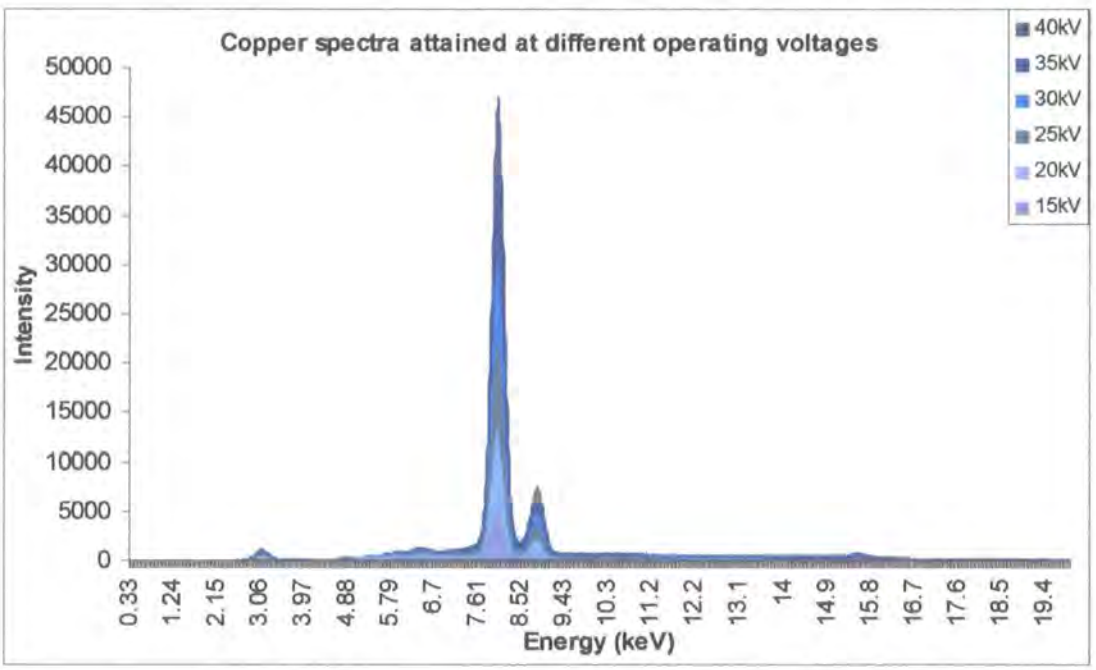

Figure 4.22: Copper spectra at different operating voltages

As the operating voltage is increased, the K_α and K_β lines increase significantly in intensity, and the Bremsstrahlung radiation at the lower end of the energy spectrum also increases. Using the spectra acquired at operating voltages of 15kV and 40kV, pseudo-spectra with less Bremsstrahlung were calculated using the following subtractions:

- (0.5 x 15kV spectrum) subtracted from 40kV spectrum
- (0.75 x 15kV spectrum) subtracted from 40kV spectrum
- (0.9 x 15kV spectrum) subtracted from 40kV spectrum

These fractions were chosen to allow subtraction of half of the 15kV spectrum intensity from the 40kV intensity, and subtraction of three quarters of the 15kV spectrum from the 40kV spectrum. Subtraction of the whole 15kV spectrum from the 40kV spectrum resulted in some negative intensity values in the Bremsstrahlung region, so a subtraction of 90% of the 15kV spectrum from the 40kV spectrum was made instead. These calculated spectra are shown in figure 4.23.

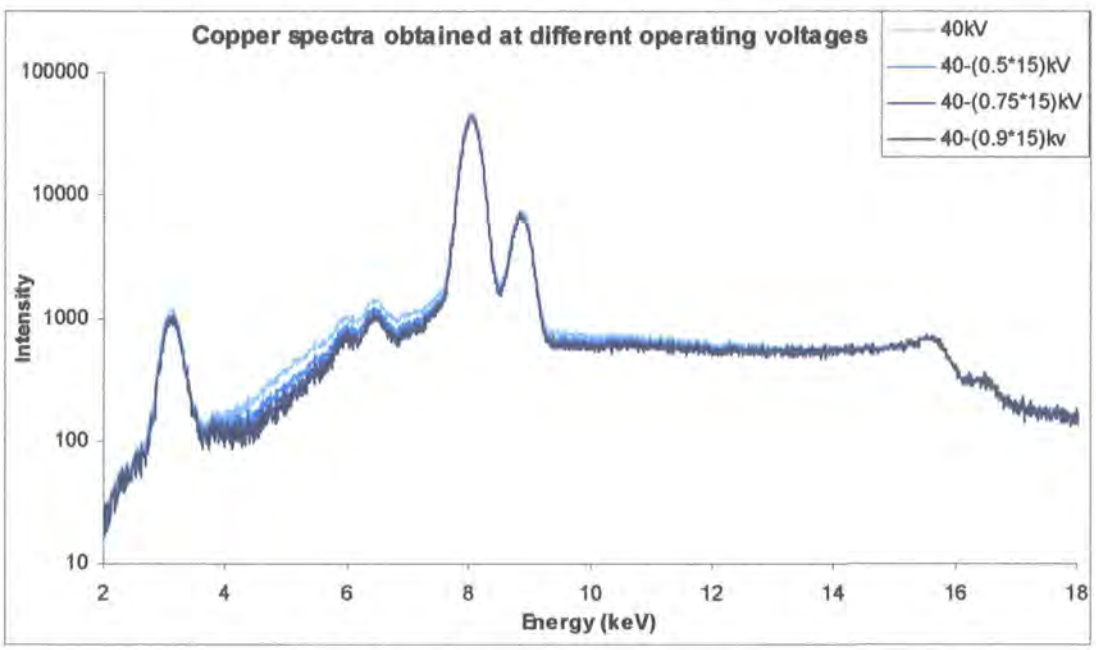

Figure 4.23: Copper spectra calculated by subtraction of 15kV spectrum from 40kV spectrum

By plotting the calculated pseudo-spectra logarithmically in figure 4.23, a difference in Bremsstrahlung intensity is seen, while the K_α and K_β peaks remain largely unaffected. This difference in Bremsstrahlung intensity is sufficient to alter the ratio of the K_α radiation to the Bremsstrahlung radiation, thus each calculated spectrum represents partial monochromation to a different extent. This K_α/Bremsstrahlung ratio is determined by summing the area under the K_α characteristic line and dividing it by the total area under the lower-energy Bremsstrahlung section, ie:

$$K_\alpha \,/\, Bremsstrahlung = \frac{Area(K_\alpha)}{Area(Bremsstrahlung)} \qquad (4\text{-}10)$$

The K_α/Bremsstrahlung ratios for all recorded and calculated copper spectra are shown in Table 4.3.

Operating voltage/calculation	K_α/Bremsstrahlung Ratio
15kV	1.011
20kV	1.107
25kV	1.250
30kV	1.343
35kV	1.420
40kV	1.603
40kV-(0.5*15kV)	1.634
40kV - (0.75 x 15kV)	1.650
40kV - (0.9 x 15kV)	1.660

Table 4.3: K_α/Bremsstrahlung Ratio for each copper spectrum

As Table 4.3 shows, the copper K_α/Bremsstrahlung Ratio of the spectra increases with the operating voltage, and by subtracting fractions of the 15kV spectrum from the 40kV spectrum, this ratio is increased further.

Using the rhodium target, spectra were recorded at operating voltages of 20kV, 25kV, 30kV, 35kV, 40kV, 45kV and 50kV. These spectra are shown in figure 4.24.

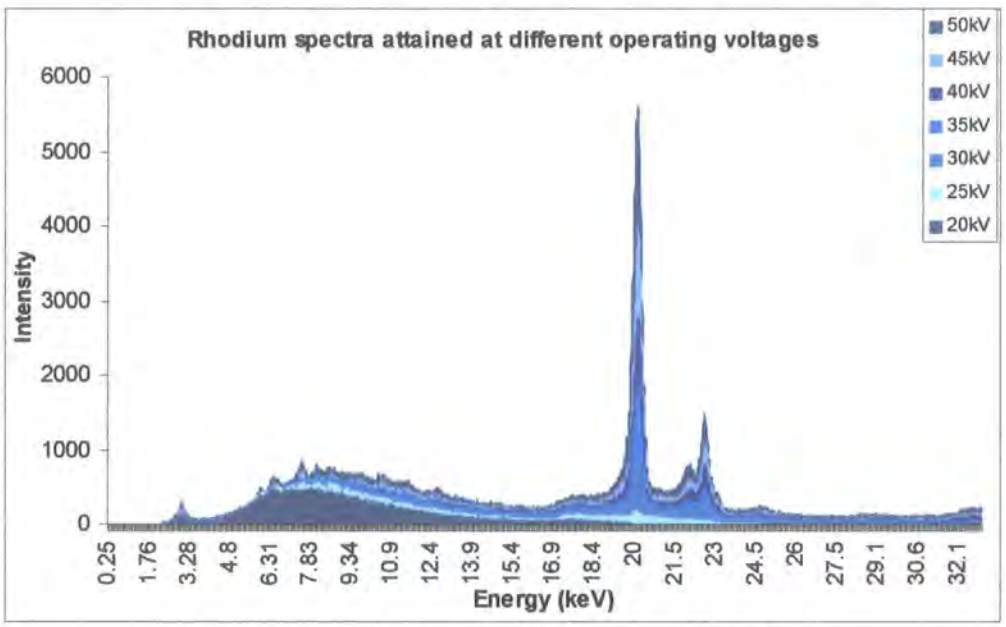

Figure 4.24: Rhodium spectra at different operating voltages

As the operating voltage is increased, it is seen again that the K_α and K_β lines increase significantly in intensity, as does the Bremsstrahlung radiation at the lower end of the energy spectrum. Using these, pseudo-spectra with lower background intensity were calculated by the following subtractions:

- (0.5 x 25kV spectrum) subtracted from 50kV spectrum
- (0.75 x 25kV spectrum) subtracted from 50kV spectrum
- (0.9 x 25kV spectrum) subtracted from 50kV spectrum

The fractions (0.5, 0.75 and 0.9) were used for consistency with the copper experiment. These calculated spectra are shown in figure 4.25.

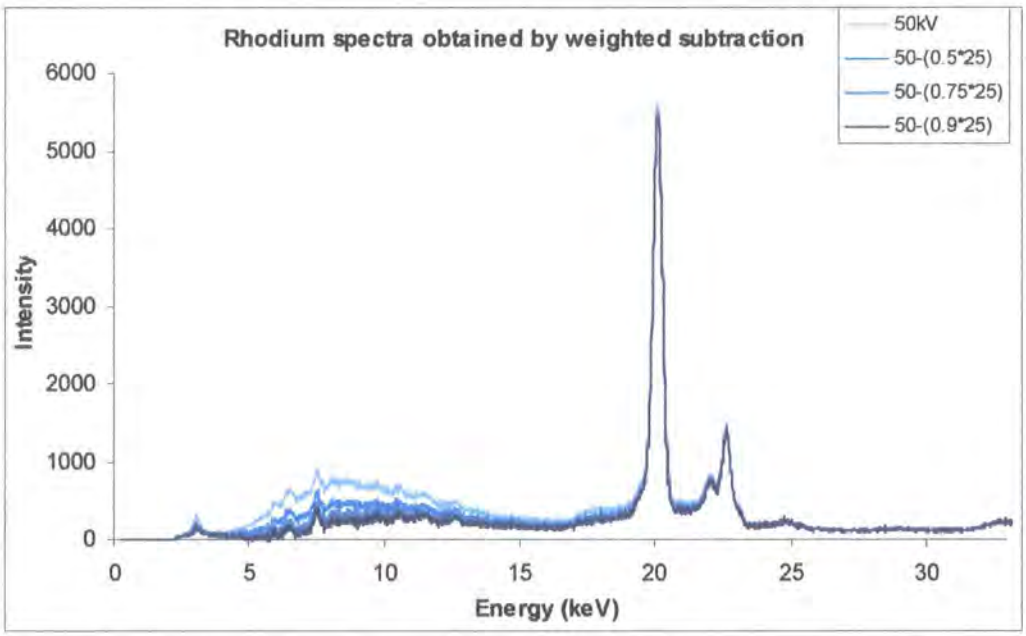

Figure 4.25: Rhodium spectra calculated by subtraction of 25kV spectrum from 50kV spectrum

A significant difference in Bremsstrahlung intensity is seen, while the K_α and K_β peaks are only slightly affected. These intensity reductions change the K_α/Bremsstrahlung Ratio of the spectra. The K_α/Bremsstrahlung ratios for all recorded and pseudo rhodium spectra, calculated using equation 4-10, are shown in Table 4.4.

Operating voltage/ calculation	K_α/Bremsstrahlung Ratio
20kV	0.002
25kV	0.032
30kV	0.087
35kV	0.141
40kV	0.187
45kV	0.211
50kV	0.249
50kV - (0.5 x 25kV)	0.308
50kV - (0.75 x 25kV)	0.352
50kV - (0.9 x 25kV)	0.385

Table 4.4: K_α/Bremsstrahlung Ratio for each rhodium spectrum

As Table 4.4 shows, the rhodium K_α/Bremsstrahlung Ratio is varied by subtracting fractions of the 25kV spectrum from the 50kV spectrum. The K_α/Bremsstrahlung Ratios are very poor for all rhodium spectra due to the unavoidably high intensity of the Bremsstrahlung at all operating voltages.

The phase contrast images of the Heaviside Function sample were subtracted in the same way as the spectra, and the phase contrast plotted as a function of the corresponding K_α/Bremsstrahlung Ratio. For example, the image taken with the rhodium source at 25kV was multiplied by 0.5 and then the resulting image was subtracted from the 50kV image. The phase contrast in the final image was determined and plotted against a K_α/Bremsstrahlung Ratio of 0.308 (value taken from Table 4.4).

4.3.2 Effect of operating voltage and image manipulation on phase contrast

The system was set up as shown in figure 4.26. At this point in the project the paper sample was replaced with a mylar sample. This consisted of a step size of 0.269mm. The main reason for the change of material was that the use of a mylar sample would allow some modelling of the system to be done because the physical properties of mylar (for example, refractive index and absorption coefficient) are well-documented, unlike those of paper. In addition, the grain size can vary slightly across a sheet of paper, while mylar sheets have a uniform thickness which is more appropriate for this work.

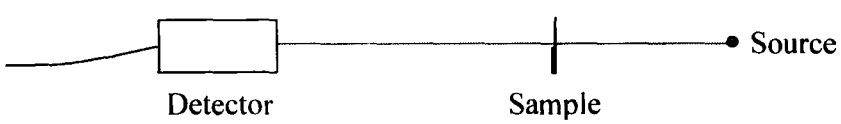

Figure 4.26: Set-up of image manipulation experiment

The source, sample and detector remained fixed in position throughout this experiment. As the operating voltage was changed, the focus was reduced in order to keep the source to its smallest possible size.

Using the copper target, images were taken of the Heaviside Function sample at operating voltages of 15kV, 20kV, 25kV, 30kV, 35kV and 40kV. The phase contrast was determined for each of these images and these results are plotted as a function of the corresponding K_α/Bremsstrahlung Ratio, shown in figure 4.27. Additional images were created by the image subtractions described in section 4.3.1. The phase contrast of these is plotted as a function of the corresponding K_α/Bremsstrahlung Ratio. The image manipulation method changes the spectra in a different way to the increasing operating voltage method, so these results are plotted separately in figure 4.28.

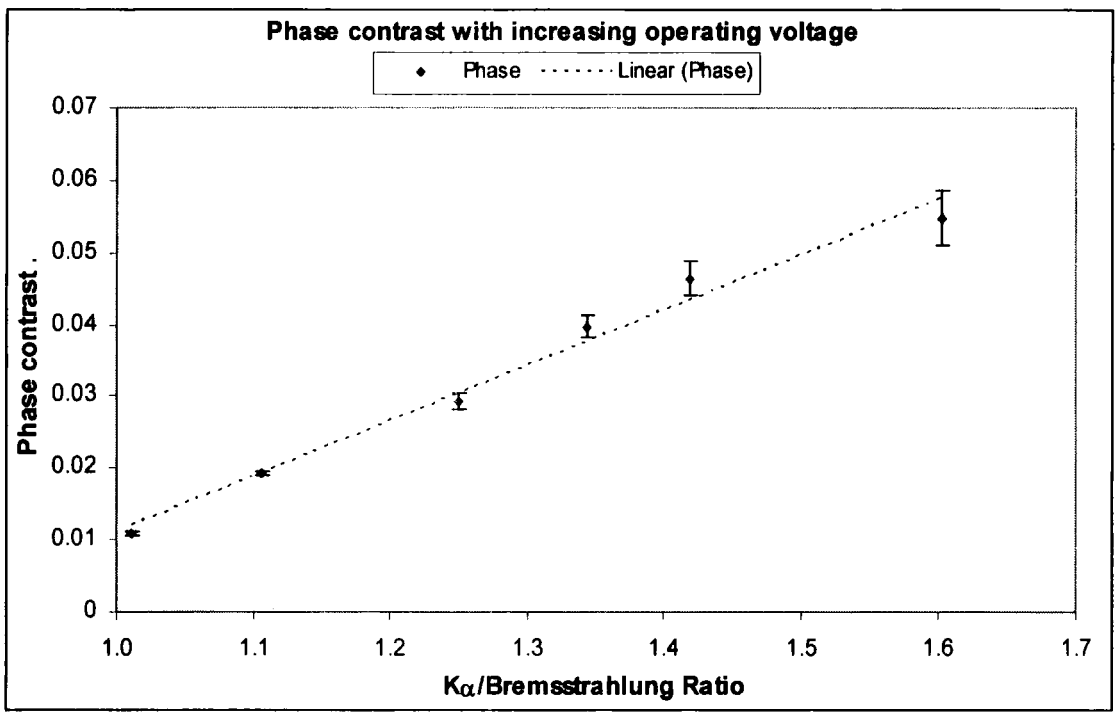

Figure 4.27: Phase contrast plotted as a function of K_α/Bremsstrahlung Ratio with increasing operating voltage for copper target

In figure 4.27 we see that the phase contrast shows a linear relationship with the K_α/Bremsstrahlung Ratio as the operating voltage is increased. Thus the phase contrast is proportional to the K_α/Bremsstrahlung Ratio. This demonstrates that phase contrast improves as the K_α line becomes more dominant, i.e. as the beam becomes more monochromatic.

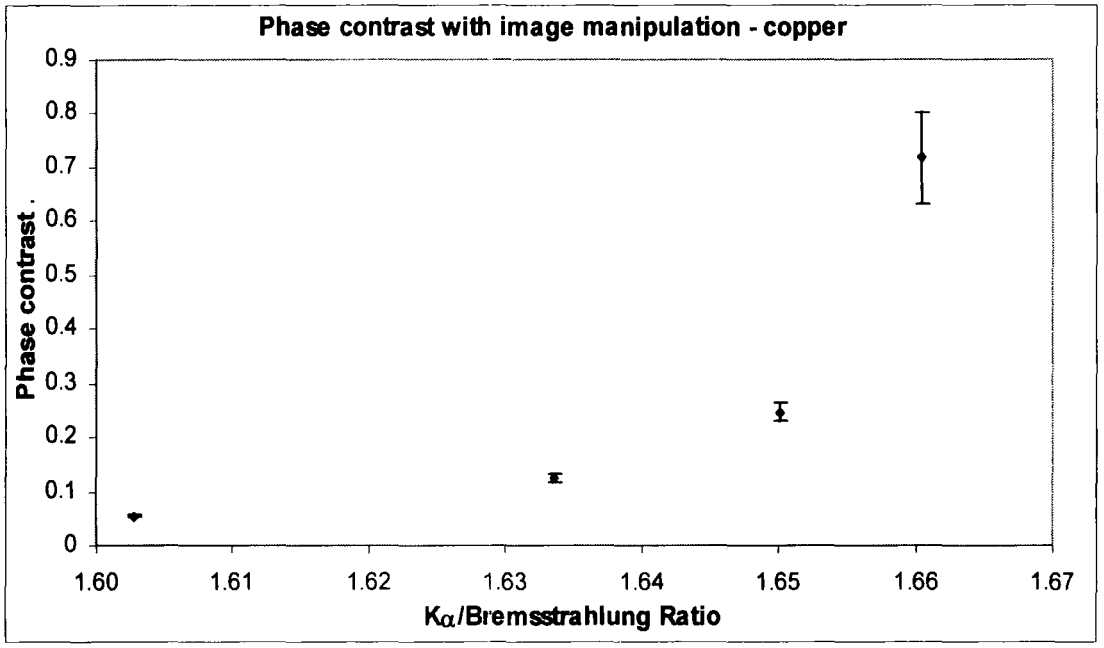

Figure 4.28: Phase contrast plotted as a function of K_α/Bremsstrahlung Ratio with image manipulation using copper target

In figure 4.28 we see that the phase contrast increases as the pseudo-K_α/Bremsstrahlung Ratio increases due to the image manipulation method. This part of the experiment is rather different to the operating voltage increase, and so the results will not necessarily paint the same picture. Because the manipulated images are the results of pseudo-spectra rather than actual spectra, no further analysis is done on the relationship between the phase contrast and the K_α/Bremsstrahlung Ratio in figure 4.28, other than to note the obvious increase in phase contrast with K_α/Bremsstrahlung Ratio. However this limited result does further demonstrate that the phase contrast is improved as the K_α line becomes more dominant and supports the previous observation that better phase contrast is achieved using a more monochromatic source.

Using the rhodium target, images were taken of the Heaviside Function sample at operating voltages of 20kV, 25kV, 30kV, 35kV, 40kV, 45kV and 50kV. The phase contrast was determined for each of these images and these results are plotted as a function of the corresponding K_α/Bremsstrahlung Ratio, in figure 4.29. Additional images were created by the image subtractions described in section 4.3.1. The phase

contrast of these is plotted as a function of the corresponding K_α/Bremsstrahlung Ratio, separately, in figure 4.30.

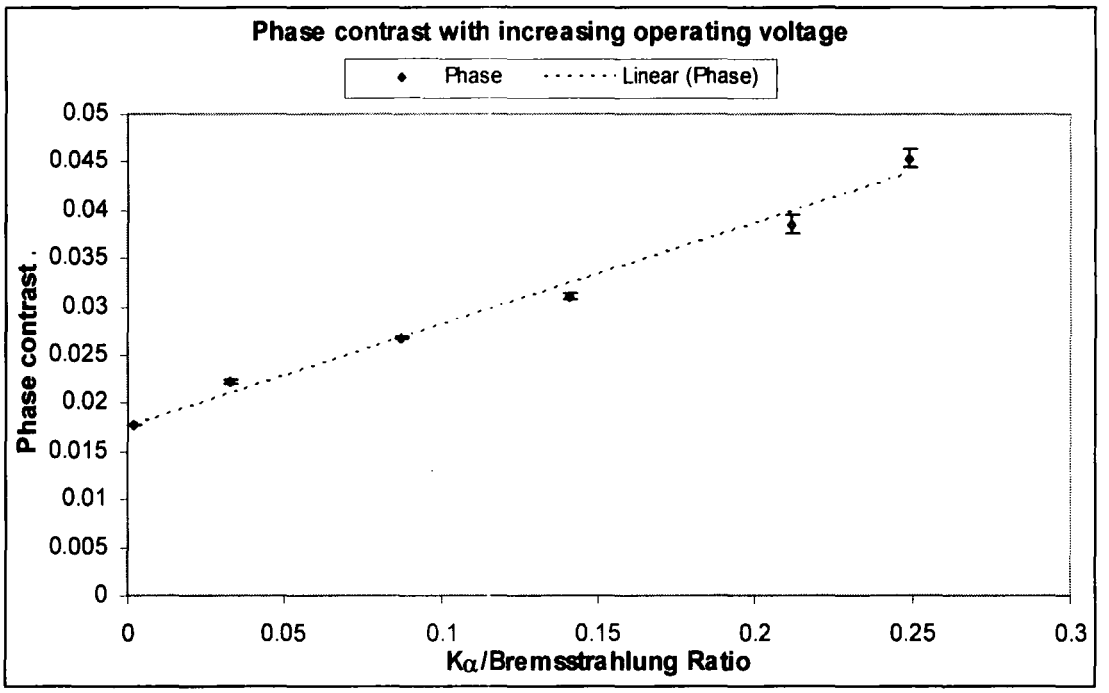

Figure 4.29: Phase contrast plotted as a function of K_α/Bremsstrahlung Ratio with increasing operating voltage for rhodium target

Again, the phase contrast shows a linear relationship with the K_α/Bremsstrahlung Ratio as the operating voltage is increased. Thus the phase contrast is proportional to the K_α/Bremsstrahlung Ratio, leading to the conclusion that better phase contrast is achieved using X-rays with a more dominant K_α line, hence a more monochromatic beam.

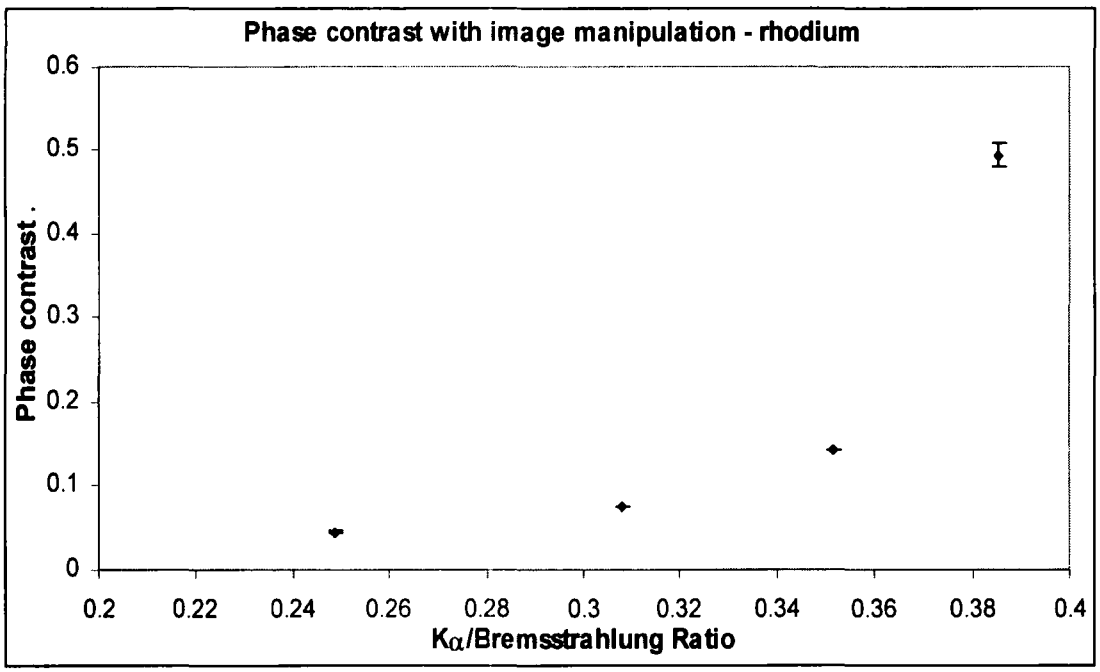

Figure 4.30: Phase contrast plotted as a function of K_α/Bremsstrahlung Ratio with image manipulation using rhodium target

In figure 4.30 we see that the phase contrast increases as the pseudo-K_α/Bremsstrahlung Ratio increases due to the image manipulation method. Again, because the manipulated images are the results of pseudo-spectra rather than actual spectra, no further analysis is done on the relationship between the phase contrast and the K_α/Bremsstrahlung Ratio in figure 4.30. However, as before, this limited result does further demonstrate that the phase contrast improves as the K_α line becomes more dominant and supports the theory that better phase contrast is achieved using a more monochromatic source.

During this experiment, as the operating voltage was increased for both targets, there was a slight increase in the dimensions of the source and the dominant (average) energy range in the spectrum increased, both factors which lead to a slight decrease in transverse coherence length. The phase contrast is seen to increase with operating voltage (and hence with K_α/Bremsstrahlung Ratio), so the decrease in transverse coherence length is not detrimental to the phase contrast in conjunction with the increasing K_α/Bremsstrahlung ratio. Thus a higher ratio of K_α intensity to

Bremsstrahlung intensity appears to provide better phase contrast images. This suggests that monochromatic radiation is more beneficial to in-line phase contrast imaging than polychromatic radiation. This is not unexpected, because as the monochromaticity of an X-ray beam increases, so too does its longitudinal coherence length. This is measured via the following [8]:

$$\Delta l_l = \frac{1}{2}\frac{\lambda^2}{\Delta\lambda}, \quad (4\text{-}11)$$

where $\Delta\lambda$ refers to the full-width half-maximum of the spectrum. In the case of monochromatic synchrotron radiation this is a simple function, but for a laboratory-based spectrum consisting of characteristic lines and Bremsstrahlung it is not straightforward.

Obviously the pseudo-spectra and the images resulting from subtraction have been calculated rather than recorded directly, and so care is taken with these results. If the pseudo-spectra were achieved in practice, the images taken using these X-rays may not necessarily be identical to those achieved by subtraction. However they may certainly be used as an indicator that monochromatic radiation is more beneficial to in-line phase contrast imaging than polychromatic radiation. Together with the results from the increase of the operating voltage using both copper and rhodium targets, this is a reasonable conclusion to draw from this work.

4.3.3 Filter method

A widely-used method for monochromating laboratory X-ray sources involves the use of filters [9, 10, 11]. K-edge filtering takes advantage of the photoelectric effect, whereby the X-ray energy incident on a material can knock an electron out of the K- or L-shell of an atom if it is greater than the binding energy of the shell. The hole created by the removal of this electron is filled by an electron falling from a higher shell, and lower energy radiation is emitted which is equal to the difference in energy between the two shells between which the electron falls. If the material is light (e.g. air), then this

radiation is absorbed immediately, resulting in emission of a lower-energy 'Auger' electron, and so all of the incident energy is effectively absorbed by the material. Photoelectric absorption contributes to the overall absorption coefficient of a material, and the probability of photoelectric absorption occurring is inversely proportional to the cube of the incident X-ray energy [12]. Overall, as incident X-ray energy increases, the absorption coefficient decreases, as shown in figure 4.31 for molybdenum. (This figure is taken from the International Tables for X-ray Crystallography Volume III [13]). At the binding energy of the material, a discontinuity is seen because below this energy, electrons are only ejected from the L-shell (i.e. absorption only occurs in the L-shell), while above this energy electrons can be ejected from the K-shell (i.e. absorption occurs in the K- and L-shells). This discontinuity in the absorption coefficient takes the form of a jump to a higher value, and then the decrease continues as the energy increases further. The discontinuity is called the K-absorption edge.

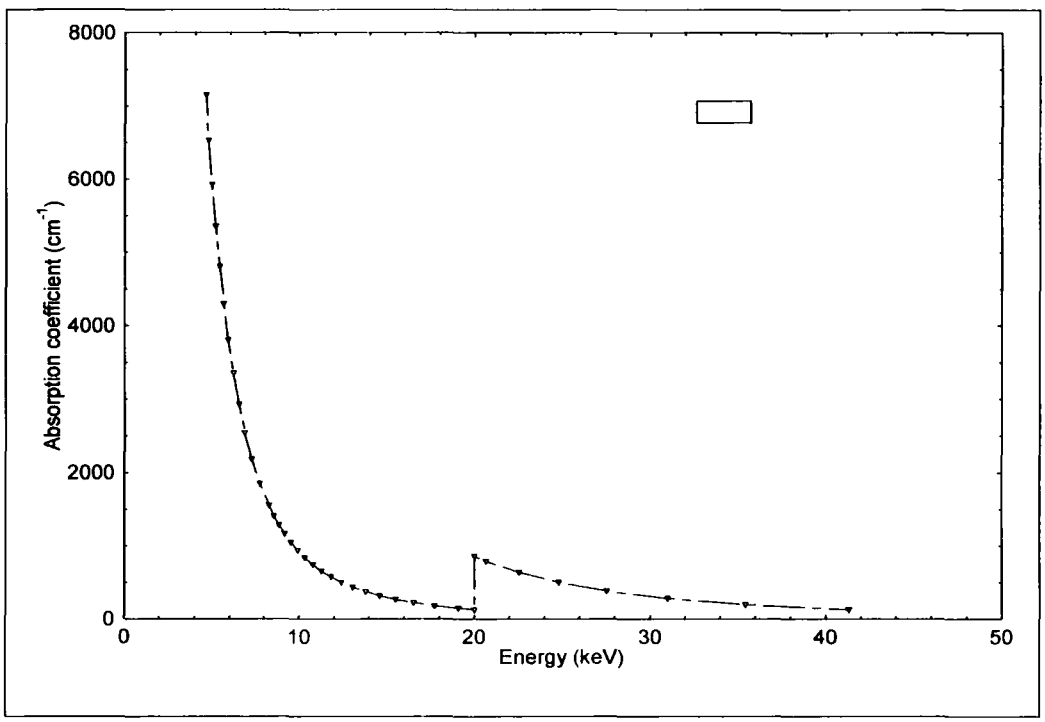

Figure 4.31: Variation of molybdenum absorption coefficient with X-ray energy [13]

It is seen in figure 4.31 that the molybdenum absorbs X-rays strongly at low energies, but absorbs very little at higher energies. Thus a molybdenum foil will absorb X-rays

strongly in the Bremsstrahlung region of the molybdenum spectrum (0keV – 17keV), but will not affect the K_α line intensity at 17.5keV to a great extent.

A suitable filter for partial monochromation of a given source is determined using the following [9]:

$$I = I_0 \exp(-\mu z) \quad (4\text{-}12)$$

where I_0 is the initial X-ray intensity, μ the absorption coefficient of a given material and z the thickness of the material. The characteristic line of the X-radiation should lie at a higher energy than the absorption edge of a filter, otherwise the filter can actually soften the beam [12] to just Bremsstrahlung. Figure 4.32 models the effect of a molybdenum foil of 10μm thickness on the spectrum of a molybdenum X-ray tube, as generated using XOP software from the ESRF, using equation (4-12).

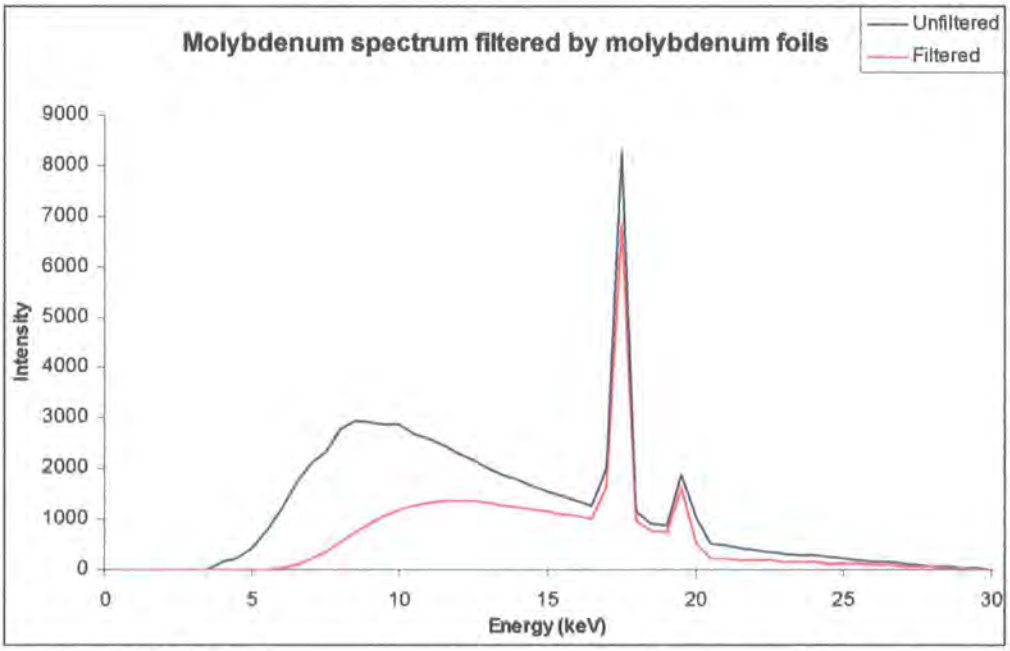

Figure 4.32: Molybdenum spectrum shown with and without 10μm molybdenum filter

The molybdenum filter is seen to reduce the Bremsstrahlung intensity significantly, while the K_α and K_β lines are not affected to such a great extent. The peak intensity within the Bremsstrahlung region is reduced to less than half its original value, while the

K_α line intensity is only reduced to ~82% of its original value. Thus the method achieves partial monochromation of the molybdenum X-ray source, and in fact molybdenum foil is often used for partial monochromation of molybdenum sources in mammography.

In order to partially monochromate the rhodium source, the effect of a number of materials on the rhodium source has been modelled, similar to the molybdenum demonstration above. The model determined that of all the materials which were readily available, chromium foil is the most effective for partial monochromation of the rhodium source. The absorption coefficient of chromium, generated by XOP software, is shown in figure 4.33.

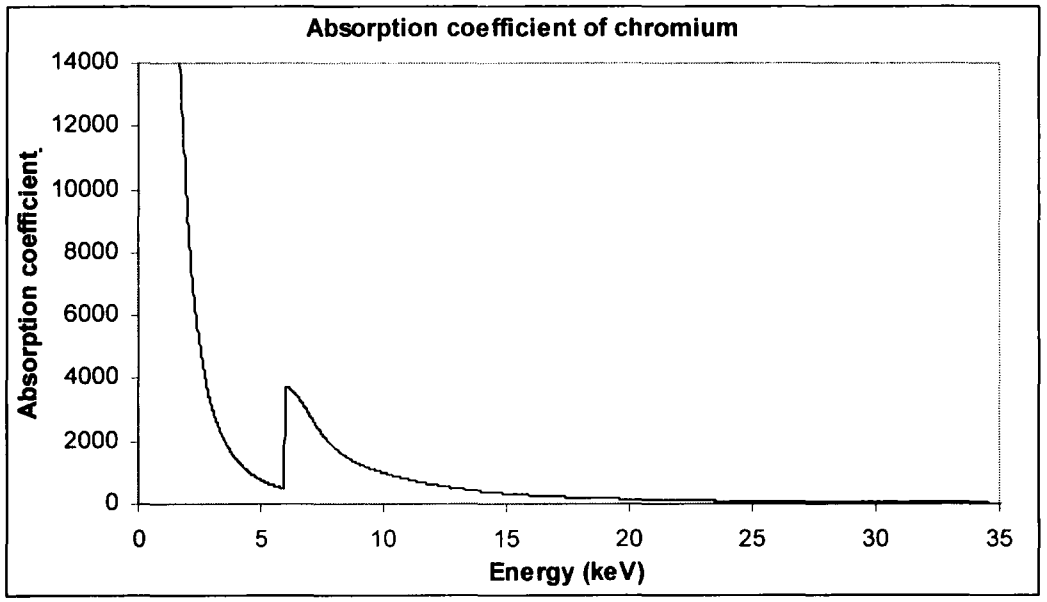

Figure 4.33: Variation of chromium absorption coefficient with X-ray energy

It is seen that chromium absorbs strongly in the Bremsstrahlung region of the rhodium spectrum (0keV – 20keV) and weakly at the K_α energy (20.2keV) and above. By substituting this absorption coefficient into equation 4-12 over the whole rhodium spectrum, the theoretical effect of filtering the spectrum by chromium was seen. The calculations were completed by applying chromium filter thicknesses of 10μm, 20μm,

30μm and 40μm to the spectrum. The absorption effect of the beryllium window was considered to be negligible and was not included in the simulation. The filtered spectra, together with the original unfiltered spectrum, are shown together for comparison in figure 4.34.

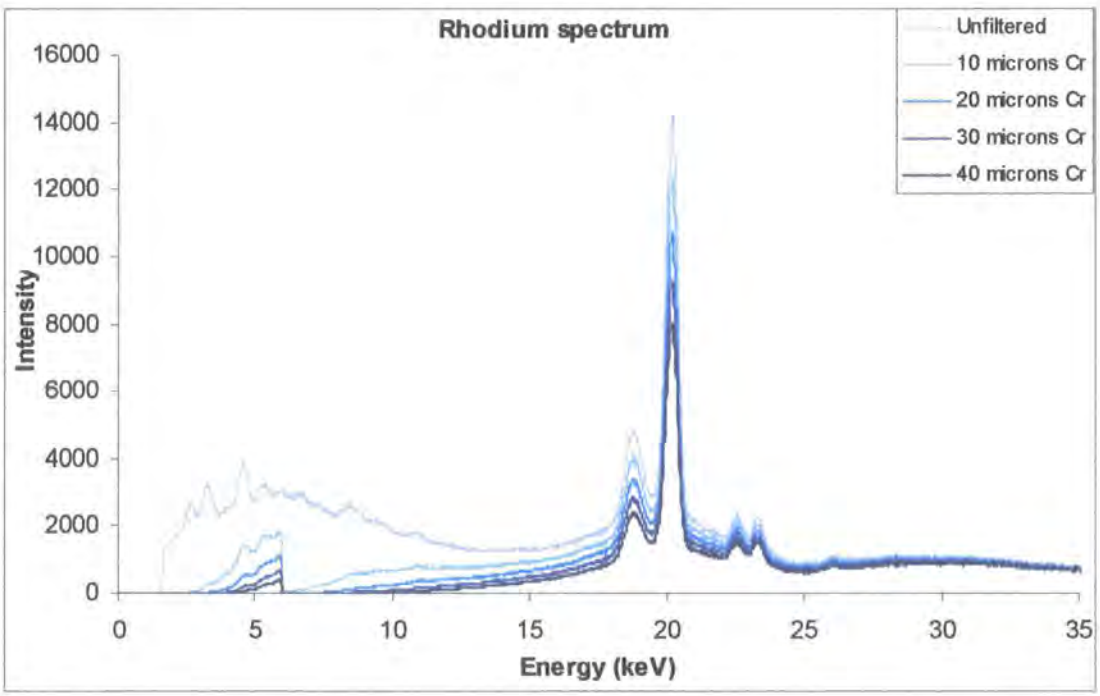

Figure 4.34: Rhodium spectrum filtered by chromium foils of increasing thickness

It is seen from figure 4.34 that the chromium filters reduce the intensity across the Bremsstrahlung energy range, as required. There is some absorption at the K_α energy, although to a lesser extent than across the Bremsstrahlung energy range. In order to quantify the partial monochromation achieved by the addition of each chromium foil, the area under each spectrum was considered as before by calculating the K_α/Bremsstrahlung ratio using equation 4-10. The K_α/Bremsstrahlung ratios for the model of the unfiltered rhodium spectrum and the subsequent filtered spectra are shown in table 4.5.

Thickness of Cr filter	K_α/Bremsstrahlung Ratio
0	0.327
10μm	0.428
20μm	0.485
30μm	0.515
40μm	0.528

Table 4.5: K_α/Bremsstrahlung Ratio for spectrum produced with each Cr filter thickness

Although the intensity of the K_α line is slightly decreased by the chromium filters, the significant absorption at the Bremsstrahlung energies causes the K_α/Bremsstrahlung Ratio to increase with the addition of each 10μm filter. Thus the filters should succeed in partially monochromating the rhodium source.

4.3.4 Effect of filter on phase contrast

The experiment is set up as shown in figure 4.35.

Figure 4.35: Set-up of filter experiment

The source, sample and detector remained fixed, and all source settings remained consistent throughout the experiment. A reference image was taken with the source's natural spectrum, and this was repeated with one 10μm chromium filter in place, then two, then three and so on. The phase and absorption contrast was calculated for each image: these are plotted in figure 4.36.

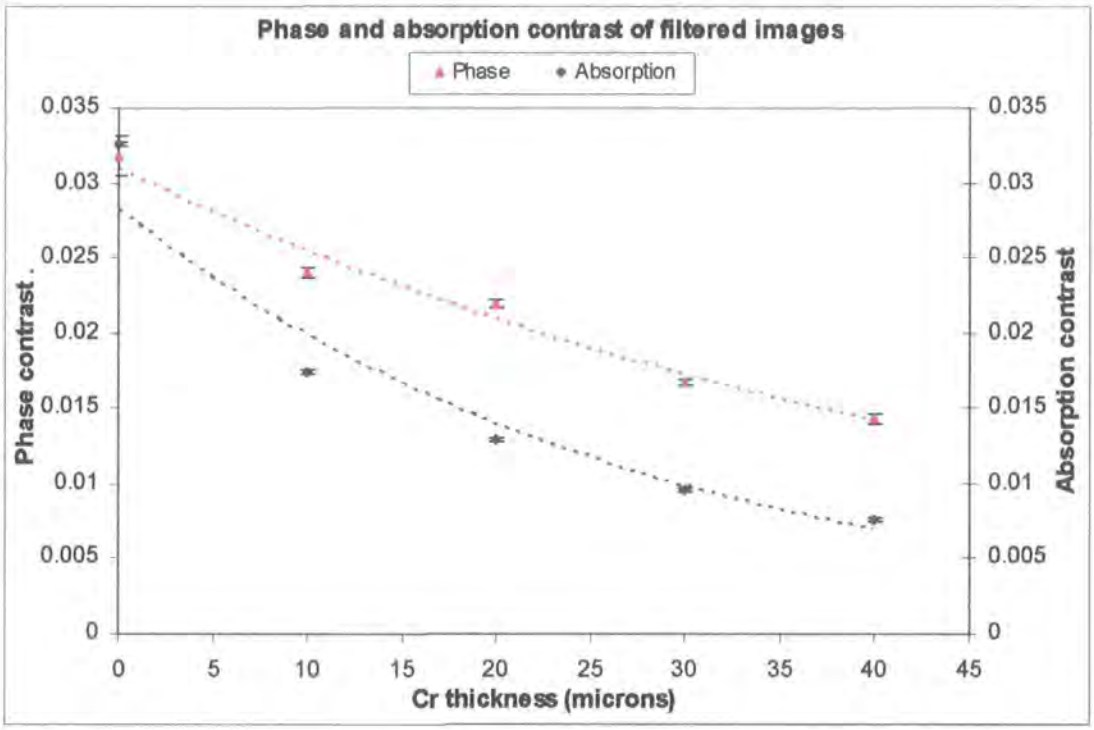

Figure 4.36: Variation in phase and absorption contrast with chromium filter thickness

Both the phase and absorption contrast are seen to decrease as the chromium filter becomes thicker. Given the increase in K_α/Bremsstrahlung Ratio with Cr filter thickness, the decrease in phase contrast implies that monochromatic X-rays do not provide better phase contrast images. However, when the previous image manipulation results are taken into consideration, together with the decrease in absorption contrast with Cr filter thickness, it emerges that another factor governs this result. Consider the absorption contrast at a single energy. This is given by substituting equation 4-12 into the absorption contrast equation from Chapter 3:

$$Contrast = \frac{A_{Max} - A_{Min}}{A_{Max} + A_{Min}} \qquad (4\text{-}13)$$

$$Contrast = \frac{I_o \exp(-\mu z_1) - I_o \exp(-\mu z_2)}{I_o \exp(-\mu z_1) + I_o \exp(-\mu z_2)} \qquad (4\text{-}14)$$

The intensity of the X-ray beam cancels both in the numerator and denominator, leaving only a dependence on the material properties, namely the absorption coefficient μ and the material thickness on either side of the boundary, z_1 and z_2. Thus a simple reduction in intensity due to the absorption by the filter is not the reason for the reduction in absorption contrast. Rather, the chromium's strong absorption of the low-energy Bremsstrahlung causes a shift in the spectrum's dominant energy range towards higher energies. This is similar to an effect called beam hardening, which is the shift in X-ray energy to higher energies due to absorption by the air within the set-up. In order to verify the presence of this effect the model spectra are used once more. Each of the filtered spectra are treated using equation 4-12, using the absorption coefficient of mylar at each energy channel along the spectrum, together with (a) the thickness of a single layer of mylar and (b) the thickness of the thicker section of mylar. A weighted average is taken of each of these as follows:

$$Average = \frac{\sum I_o \exp(-\mu t)}{\sum I_o} \qquad (4\text{-}15)$$

This calculation leads to an average absorption coefficient across each spectrum, as demonstrated in equation 4-16.

$$Avg\left(\frac{I}{I_o}\right) = \exp(-\bar{\mu} t) \qquad (4\text{-}16)$$

The exponential terms containing the average absorption coefficient with the two thicknesses are substituted into equation 4-14 as follows:

$$Contrast = \frac{\exp(-\bar{\mu} t_1) - \exp(-\bar{\mu} t_2)}{\exp(-\bar{\mu} t_1) + \exp(-\bar{\mu} t_2)} \qquad (4\text{-}17)$$

The absorption contrast calculated by this method is plotted together with that achieved during the filtering experiment (shown earlier in figure 4.36). These are shown in figure 4.37.

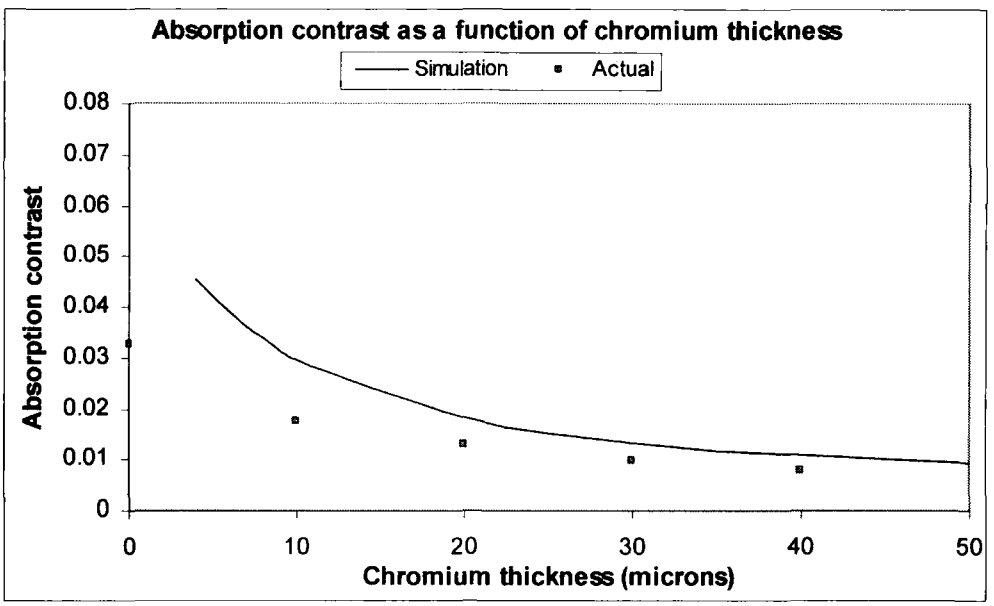

Figure 4.37: Theoretical and experimental absorption contrast as a function of chromium filter thickness

We can see in figure 4.37 that the simulation of the absorption contrast due to the 'beam hardening' effect of the chromium filters describes the actual absorption contrast quite closely. So the shift of the dominant energy to higher values accounts for the loss in absorption contrast very well. This idea is extended to the phase contrast: a shift in the dominant energy would affect the transverse coherence length, and as we have seen in section 4.2, the transverse coherence length is important in phase contrast imaging.

Each of the filtered spectra and the unfiltered spectrum are treated using the following equation:

$$\lambda = \frac{hc}{E} \qquad (4\text{-}18)$$

A weighted average is taken of each of these as follows:

$$E_{Dominant} = \frac{\sum(\lambda \times No.Photons)}{\sum No.Photons} \qquad (4\text{-}19)$$

Using this method, the unfiltered rhodium spectrum is seen to have a mean dominant wavelength of 1.16Å. This is longer than the rhodium K_α wavelength of 0.64Å due to the large contribution to the spectrum made by the low energy Bremsstrahlung radiation. As each chromium filter is placed in the path of the X-ray beam, this mean dominant wavelength is reduced to 0.71Å, 0.60Å, 0.54Å and finally 0.51Å. This reduction in the mean dominant wavelength leads to a reduction in the effective transverse coherence length of the X-rays. The effective transverse coherence length is calculated using the effective radius of the source, the source-sample distance and each mean dominant wavelength in turn. The change in the average wavelength and the effective transverse coherence with chromium filter thickness is shown in figure 4.38.

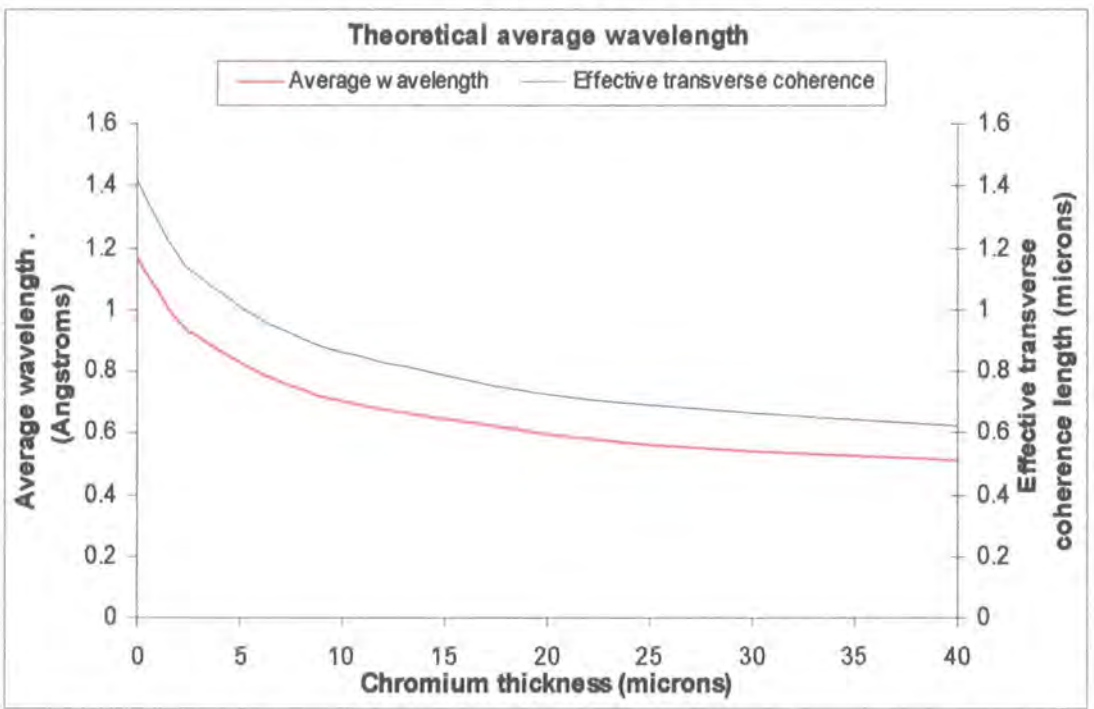

Figure 4.38: Change in average wavelength and effective transverse coherence length with increasing chromium thickness

The average wavelength and effective transverse coherence length show a similar relationship with chromium filter thickness as the phase contrast in figure 4.36. The

phase contrast of each image is plotted with the effective transverse coherence length calculated for each filter thickness: these results are shown in figure 4.39.

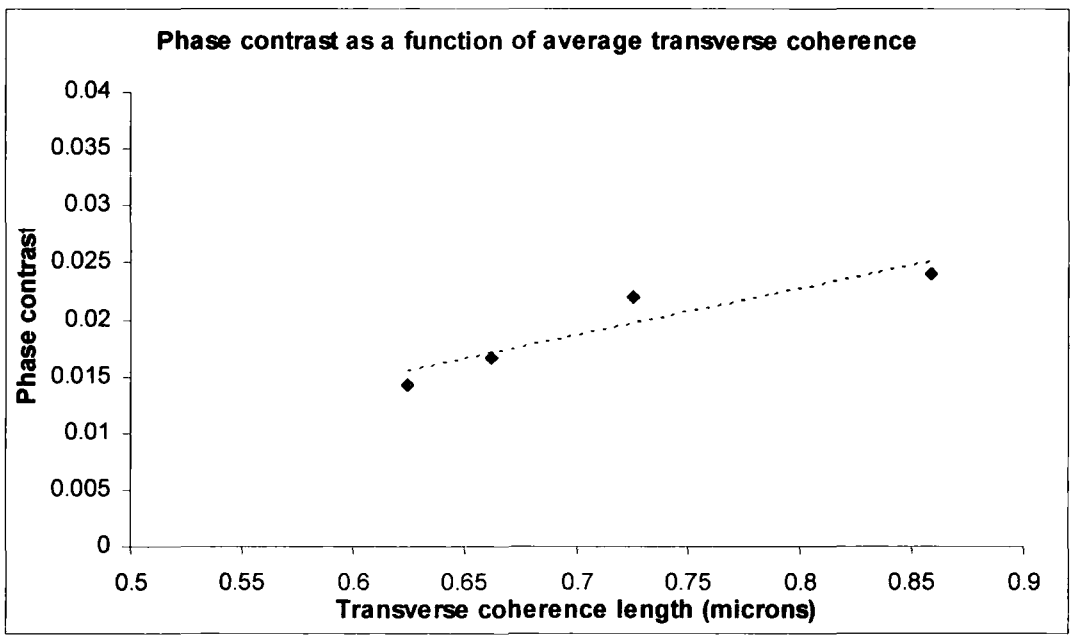

Figure 4.39: Phase contrast as a function of effective transverse coherence length

The phase contrast shows a linear, proportional relationship with the effective transverse coherence length of the source: this is confirmed by the strong, positive correlation coefficient of 0.94 between the two variables. Thus as the chromium filters shifted the dominant X-ray energy range to higher energies (and hence the dominant wavelength to lower values), the consequent reduction in the effective coherence length caused degradation of the phase contrast.

It has now been seen that the beam hardening effect brought about by the filter method of monochromation is detrimental to the phase contrast in a propagation image and also affects the absorption contrast within the image. A further point of interest is that the images achieved during this experiment showed some additional detail, caused by the chromium filters. The experiment was repeated using X-ray film in order to accumulate images over a longer exposure time; these films were viewed using a transmission

microscope and the magnified images were recorded to the computer using a visible light CCD camera. These images are shown in figure 4.40.

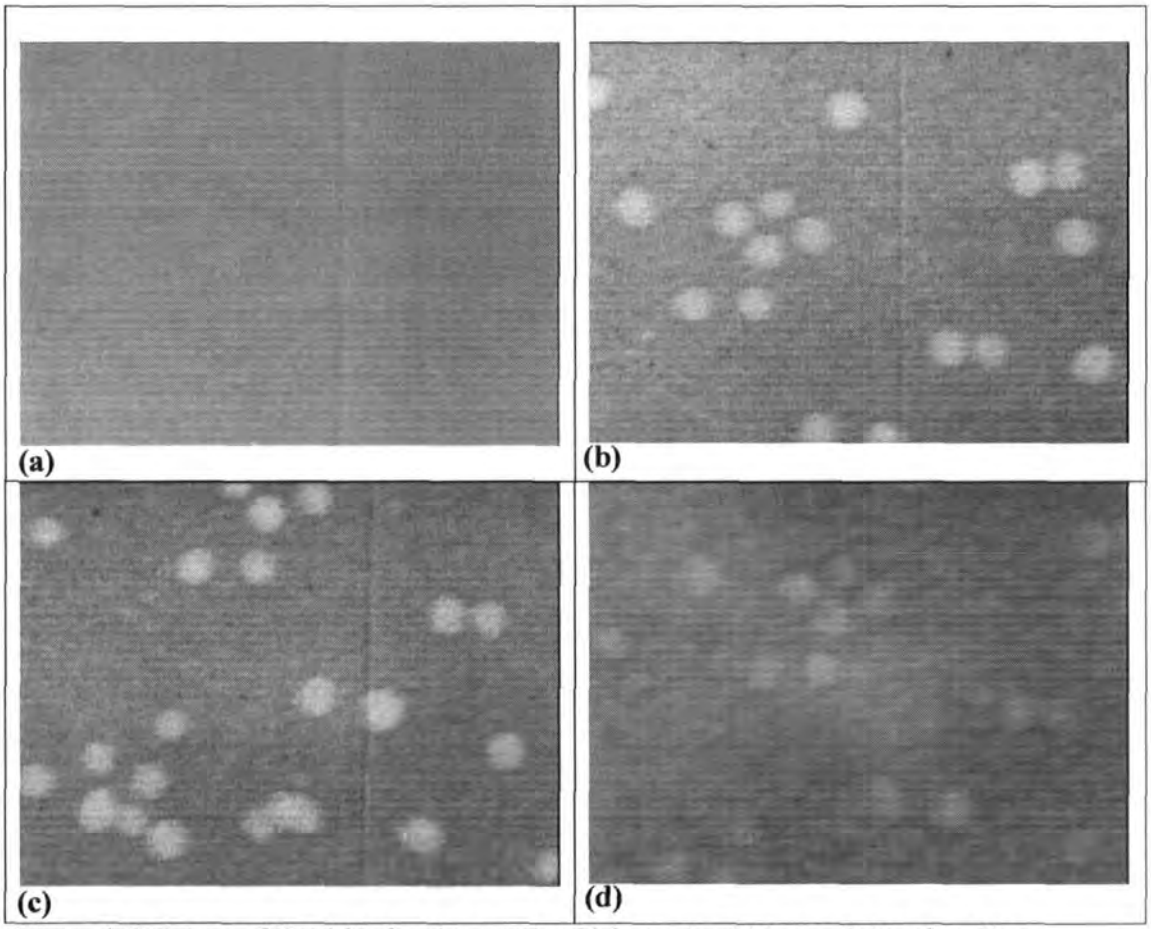

Figure 4.40: Images of Heaviside function sample with increasing thickness of chromium filter: (a) Unfiltered, (b) 10μm chromium, (c) 20μm chromium, (d) 30μm chromium

It is seen in figure 4.42 that as chromium filters are added, any minor roughness or flaws in these filters actually contribute to the final image. The wavy effect in the background of images 4.40 (b), (c) and (d) shows the roughness of the filter. The bright spots on these images show areas in the X-ray film which allowed through more of the microscope beam intensity, i.e. areas of low X-ray exposure. Therefore these bright spots indicate larger chromium particles on the filters. Although the sample boundary is visible in each image and the contrast may be determined using the intensity profile as before, any quantitative results could be misleading due to the unwanted 'spotty' effect

contributed by the filters. Evidently any filters used for phase contrast imaging would have to be polished to a particularly high standard.

The results of the monochromation experiment using filters are not encouraging, because beam hardening and filter roughness are detrimental to the phase contrast images. However, the increasing operating voltage and image manipulation results do show that a less polychromatic X-ray beam is preferable. Thus, while we have seen that monochromatic X-ray radiation is advantageous to phase contrast imaging techniques, the widely-used filter method of monochromation for laboratory-based X-ray sources is not suitable in this instance.

4.4 Sample thickness

The purpose of this experiment is to determine how the phase contrast changes as the thickness of the Heaviside sample 'step' is increased. This is useful in order to investigate the possibility of calibrating such a system to determine sample thickness. The set-up is as shown in figure 4.41 below.

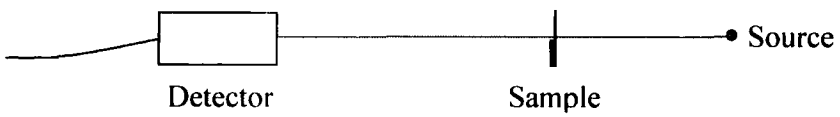

Figure 4.41: Set-up for sample thickness experiment

The source-sample and sample-detector distances were fixed as before. The samples used for this experiment all took the form of the standard Heaviside function approximation. They comprised a layer of mylar of thickness 0.051mm, with one or more smaller layers of mylar fixed over it to form a 'step' in thickness which could be imaged. Six of these samples were used, with a 'step' thickness of 1 layer, 2, 5, 7, 10 and 12 layers of mylar. The sample step sizes were as follows: 0.048mm, 0.104mm, 0.269mm, 0.428mm, 0.584m and 0.792mm. The phase and absorption contrast were determined using equations 4-6 and 4-13 respectively as described in chapter 3. These are shown for the copper results in figure 4.42.

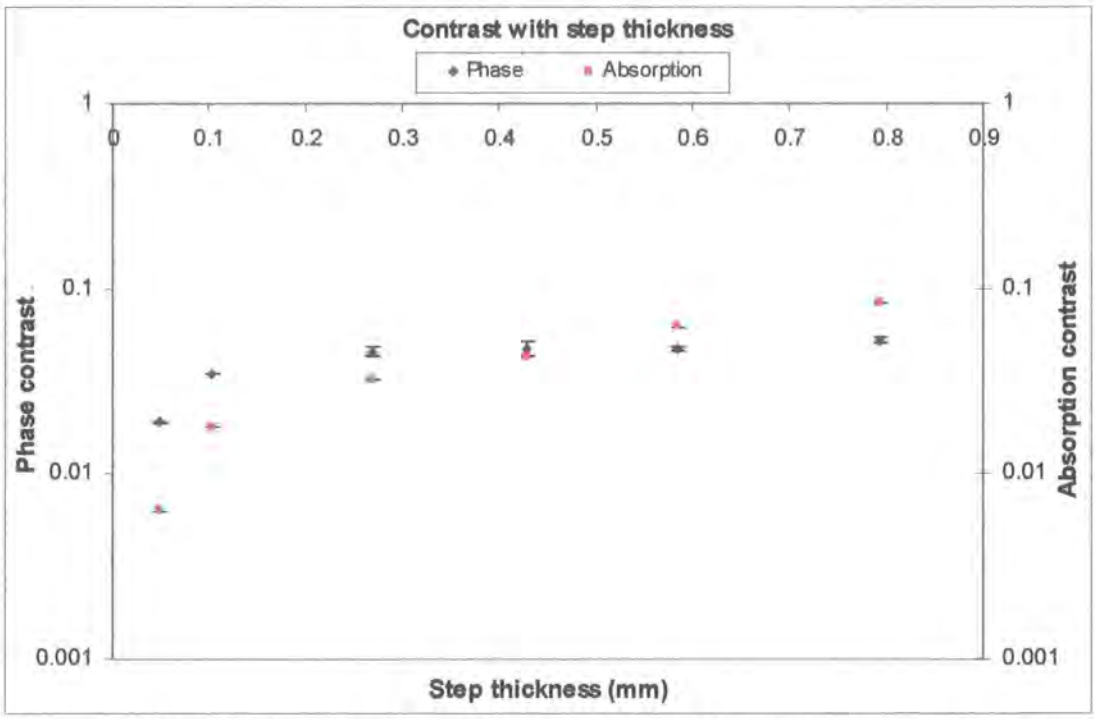

Figure 4.42: Phase & absorption contrast plotted as a function of 'step' thickness for copper source

From figure 4.42 it is seen that in consistent conditions the phase contrast content of an image shows a dependence on the thickness of the object 'step' in question. Obviously the absorption contrast increases smoothly as a function of the 'step' thickness due to the loss of X-rays through the thicker section becoming exponentially more significant as the 'step' thickness increases. The phase contrast increases initially, but this begins to plateau at a step thickness of around 0.4mm. After this, the absorption contrast provides more of the information in the image.

In order to calculate the X-ray intensity after absorption, the 'dominant', or average absorption contrast was calculated over the spectrum. For each energy channel in the spectrum, the intensity after absorption was calculated by applying equation 4-12 to each side of the sample boundary. A weighted mean intensity was taken of each side as follows:

$$Intensity_{Avg} = \frac{\sum Intensity \times No.Photons}{\sum No.Photons}, \quad (4\text{-}20)$$

The weighted mean intensity for each side of the boundary was then inserted into equation 4-13 in order to calculate an overall weighted average absorption contrast over the spectrum. The calculation was repeated for each sample thickness used in this experiment. This simulated absorption contrast is shown together with the experimental absorption contrast in figure 4.43.

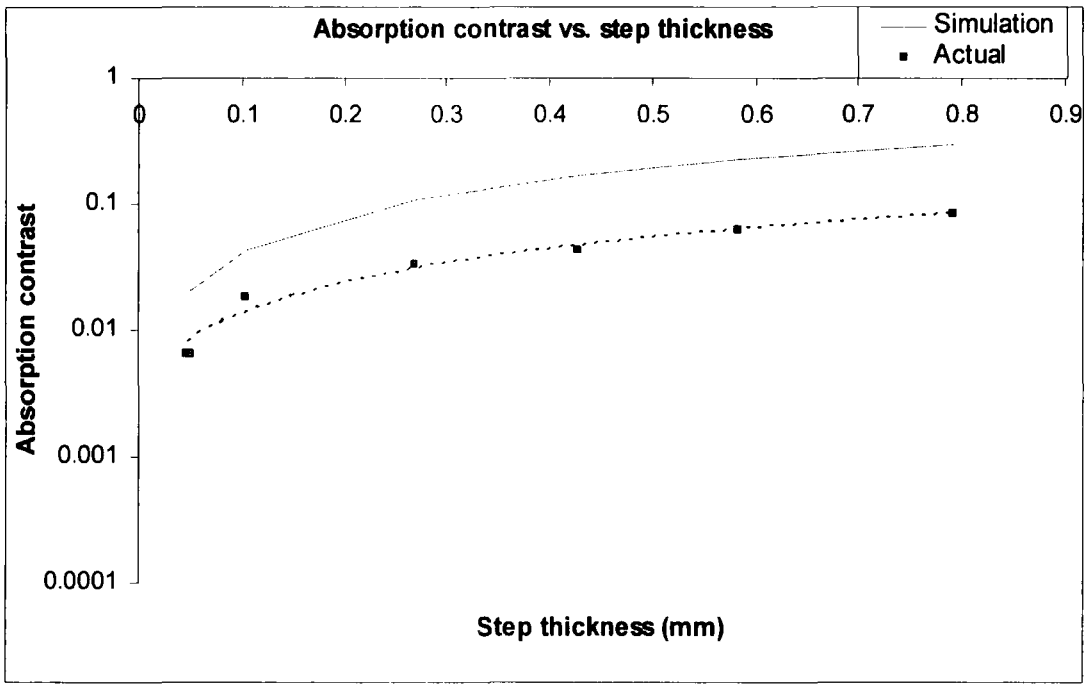

Figure 4.43: Simulated and experimental absorption contrast (copper target)

The experimental and simulated data in figure 4.43 follow close plots which show the same behaviour with sample step thickness, although they do not quite overlap.

The phase and absorption contrast achieved using the rhodium target is shown in figure 4.44.

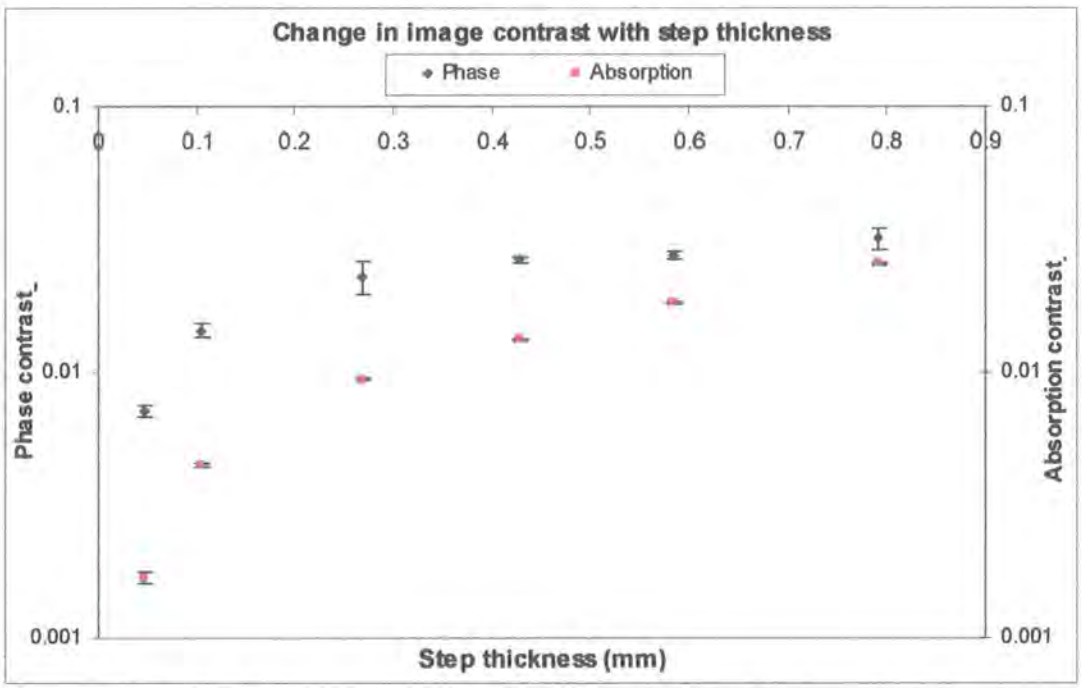

Figure 4.44: Phase & absorption contrast plotted as a function of 'step' thickness for rhodium source

In figure 4.44 the phase contrast begins to plateau again, while the absorption contrast increases smoothly. It is seen that the absorption contrast plot does not intersect the phase contrast plot within the limit of step thickness used for this experiment. This is due to the smaller absorption coefficient of mylar at higher X-ray energy.

An overall weighted mean absorption contrast was calculated over the rhodium spectrum for each sample thickness, by applying equation 4-20 to the intensities after absorption and inserting the weighted mean intensities into equation 4-13, as before. This simulated absorption contrast is shown together with the experimental absorption contrast in figure 4.45.

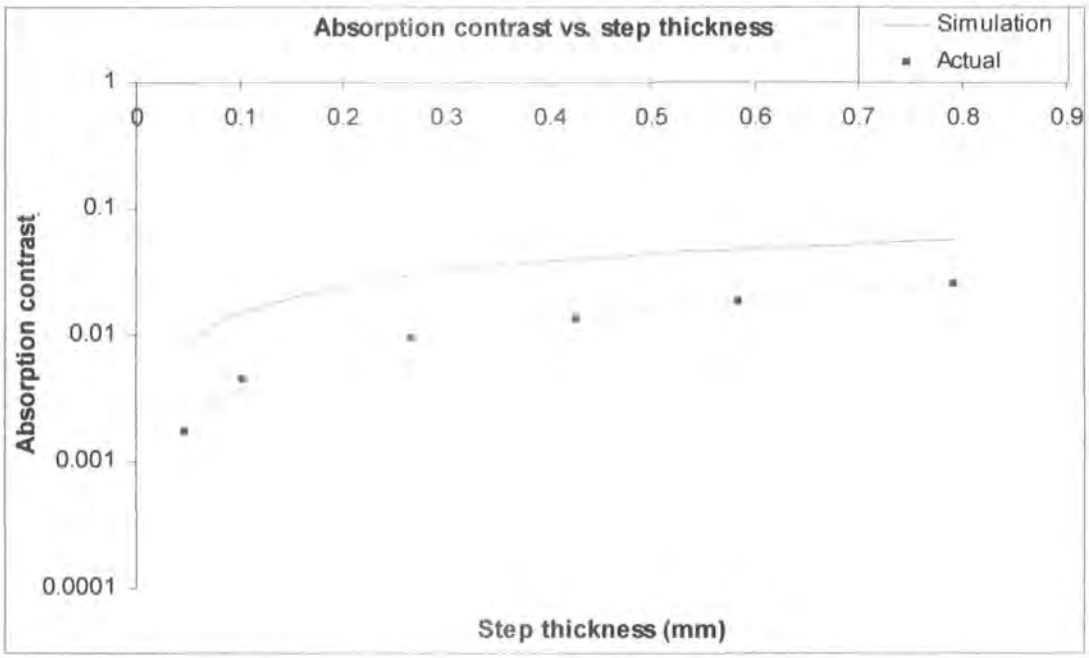

Figure 4.45: Simulated and experimental absorption contrast (rhodium target)

The experimental and simulated data in figure 4.45 also follow close plots which show the same behaviour with sample step thickness.

This experiment shows that in consistent conditions, the phase contrast content is governed by the thickness of the 'step' up to a particular step thickness. Phase only varies by a maximum of 2π: if the phase factor is outside of this range, it still represents a corresponding point within the range, which is determined by subtracting multiples of 2π until the result is within the basic range. For greater step thicknesses, the absorption property of the material begins to provide more information than the phase because the absorption factor increases exponentially without an upper limit. Thus when such an imaging system is used with objects of a given material, there will be a cut-off thickness, past which the phase contrast does not provide the bulk of the image information. It will be necessary, therefore, to calibrate such an imaging system in practice in order to set a suitable limit on sample thickness. All measurement systems have limits of operation, and for the phase-contrast imaging method to be used in medical diagnostic applications or within industry, this thickness limit will be important.

References

[1] Cloetens P. et al., *J. Phys. D.*, **32** pp.A145-A151 (1999)

[2] Snigirev A. et al., *Rev. Sci. Instr.*, **66** (12) pp.5486-5492 (1995)

[3] Wilkins S. W. et al, *Nature*, **384**, pp.335-338 (1996)

[4] Momose A. Et al., *Nature Medicine*, **2** (8) pp.552-553 (1996)

[5] Bushuev V. A. et al., *Crystallography Reports* **43** (4) pp.538-547 (1998)

[6] Gao D. et al., *Radiographics* **18** (5) pp.1257-1267 (1998)

[7] Kreyszig E., *Advanced Engineering Mathematics (7^{th} Edn)*, Wiley pp.278 (1993)

[8] Attwood D., "Soft X-rays and extreme ultraviolet radiation: principles and applications", Cambridge University Press (1999)

[9] Ross P. A., *Proc. Am. Phys. Soc.* (1926)

[10] Kirkpatrick P., *Rev. Sci. Instr.* **10** (6) pp.186-191 (1939)

[11] Soules J. A. et al, *Rev. Sci. Instr.*, **27** (1) pp.12-14 (1956)

[12] Farr R. F. et al., *Physics for Medical Imaging*, W. B. Saunders (1997)

[13] *International Tables for X-ray crystallography* Vol. III, Kynoch Press (1974)

5. Introduction of other materials

As experimental X-ray phase contrast imaging approaches applications in medical diagnostics [1,2], the influence of water on the phase contrast becomes important. All *in vivo* imaging requires the imaging system to have some degree of tolerance to water due to the inevitable high quantities of water present in most creatures' bodies. It is somewhat surprising then that despite a huge number of pathological samples (as detailed in chapter 1) and even a couple of live specimens [3,4] being used in phase contrast imaging, no work has been done to directly determine the effect of water on phase contrast. To this end, an experiment was designed to quantify the effect on X-ray phase-contrast when water is present in the sample plane. The results of this work are important because they will determine the system's tolerance to water, and hence begin to examine its ability to image pathological and living specimens.

Likewise, no work has been done to determine the effect of glass on phase contrast. But to image a glass-mounted pathological specimen, this effect needs to be investigated. So an experiment was designed to quantify the effect on X-ray phase-contrast when glass is present in the sample plane. The results of this work are important because they will demonstrate the system's tolerance to glass, allowing us to determine whether glass is a viable mount when imaging pathological specimens.

5.1 Water

5.1.1 Absorption considerations

With the introduction of water to the system, the level of absorption by the water is important. X-ray intensity after absorption by a material is given by the following expression [5]:

$$I = I_0 \exp(-\mu t) \qquad (5\text{-}1)$$

where I_0 is the initial intensity of the X-ray source, and μ and t are the absorption coefficient and thickness of the material respectively. Using XOP software created at the ESRF, the absorption coefficient for water was generated. This is shown

graphically as a function of X-ray energy in figure 5.1. Here, it is seen that the absorption coefficient is much greater at the copper K_α characteristic energy of 8.048 keV than at the rhodium K_α characteristic energy of 20.216 keV.

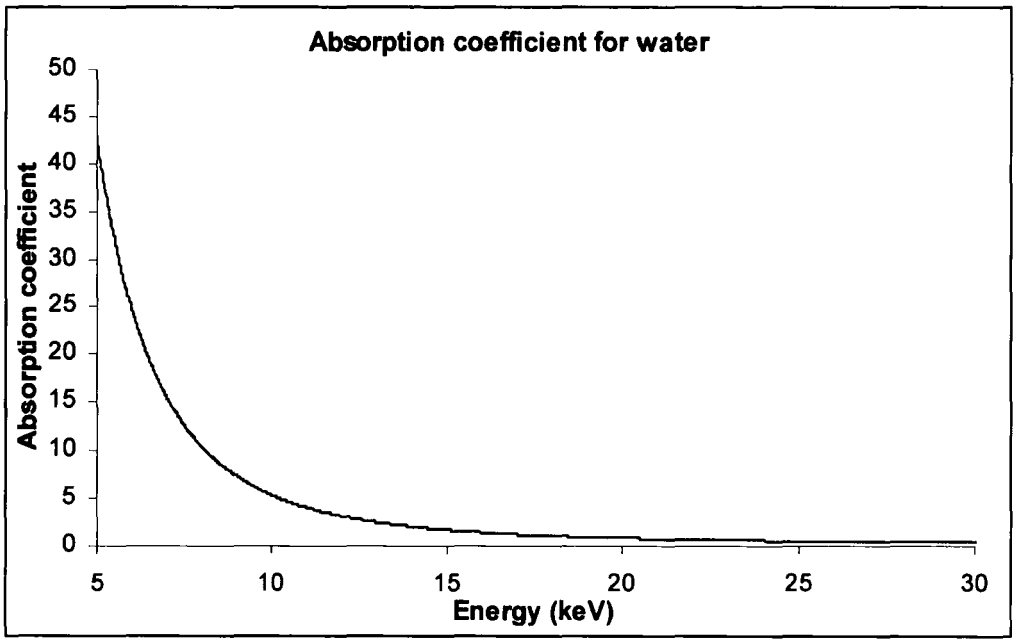

Figure 5.1: Absorption coefficient for water as a function of X-ray energy

Using expression (5-1) together with the absorption coefficient of water shown in figure 5.1, the modified copper spectrum was simulated for the introduction of different path-lengths of water to the system. The following water path-lengths are included in the model: 2.996mm, 4.992mm, 7.017mm, 10.011mm and 12.671mm. The modified copper spectra determined by this model are shown in figure 5.2.

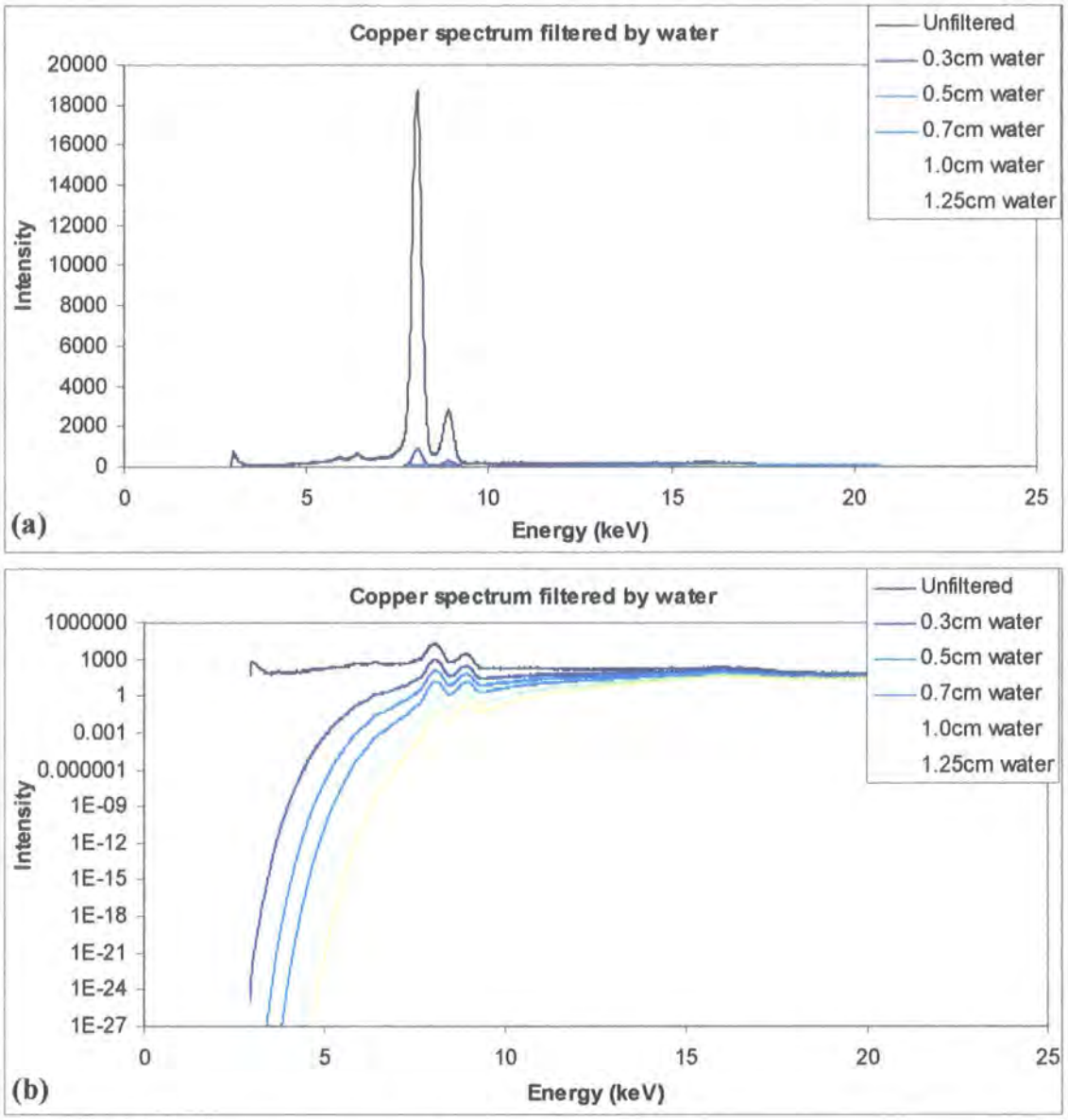

Figure 5.2: Effect of various water path-lengths on Microsource® spectrum with copper target. (a) Linear intensity scale, (b) logarithmic intensity scale to clarify lower-intensity spectra.

In figure 5.2 we see that the copper spectrum of the X-ray source is severely affected by the presence of water: the K_α characteristic line is reduced to just 4% of its full intensity with only ~3mm of water present in the system. This will reduce to a great extent the intensity of images obtained using the copper target.

Using the same technique, a model is also produced for the rhodium spectrum and is shown in figure 5.3.

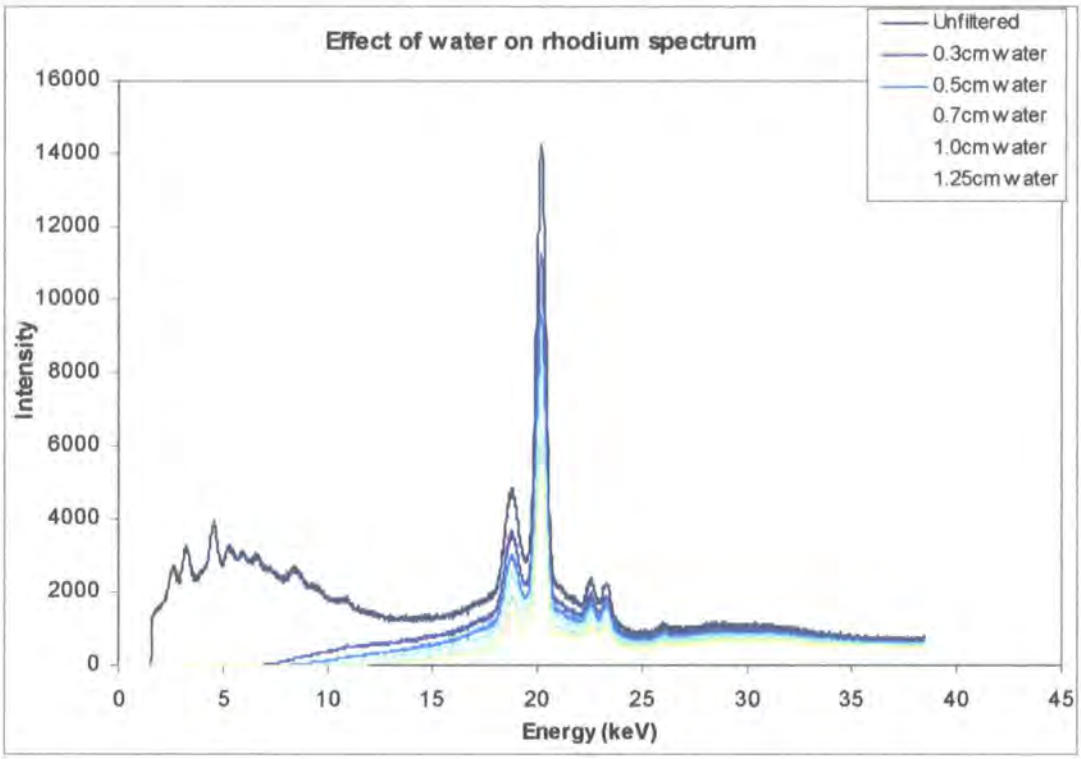

Figure 5.3: Effect of various water path-lengths on Microsource® spectrum with rhodium target.

From figure 5.3 we see that the effect of the same water path-lengths in the system is much less significant in the rhodium spectrum. For example the K_α characteristic line is reduced to 79% of its original intensity by the presence of ~3mm water in the system, which is a far less discouraging loss.

As described in Chapter 3, the absorption contrast is calculated using the following visibility equation [6]:

$$C = \frac{A_{Max} - A_{Min}}{A_{Max} + A_{Min}}, \qquad (5\text{-}2)$$

and the phase contrast is calculated as follows:

$$C = \frac{I_{Max} - (I_{Min} + (A_{Max} - A_{Min}))}{I_{Max} + I_{Min} + (A_{Max} - A_{Min})}. \qquad (5\text{-}3)$$

If an absorption image is taken of the edge of a metal sheet, A_{max} is the image intensity of the X-rays which have propagated alongside the sample, while A_{min} results from the X-rays which have propagated through the material. When considering the introduction of water to the system, both the A_{max} and A_{min} terms contain a factor representing the absorption by water. Substituting these into equation 5-2 in full, using the expression for transmitted intensity given in equation 5-1 and including possible noise effects (denoted by N), leads to the following derivation:

$$C = \frac{\left(I_o \exp(-\mu_w t_w) + N\right) - \left(I_o \exp(-\mu_w t_w - \mu_s t_s) + N\right)}{\left(I_o \exp(-\mu_w t_w) + N\right) + \left(I_o \exp(-\mu_w t_w - \mu_s t_s) + N\right)} \tag{5-4}$$

$$C = \frac{\exp(-\mu_w t_w) - \exp(-\mu_w t_w - \mu_s t_s)}{\exp(-\mu_w t_w) + \exp(-\mu_w t_w - \mu_s t_s) + 2\frac{N}{I_0}} \tag{5-5}$$

$$\therefore C = \frac{1 - \exp(-\mu_s t_s)}{1 + \exp(-\mu_s t_s) + 2\frac{N}{I_0}\exp(\mu_w t_w)} \tag{5-6}$$

As equation 5-6 shows, the presence of water should not affect the overall absorption contrast because the terms involving water cancel in the numerator and denominator. However if any significant noise results from the image acquisition, this will be magnified by the presence of water such that absorption contrast decreases as the path-length of the water increases. So it is critical that noise is kept to a minimum for this experiment, as discussed in Chapter 3.

5.1.2 Experimental issues

In order to investigate the effect of water on the X-ray phase contrast, a number of water containers were designed and made. There were two major criteria for these containers: obviously they needed to be watertight, and they were also required to have a negligible absorption coefficient at the copper and rhodium characteristic energies. A schematic of the container design is shown in figure 5.4.

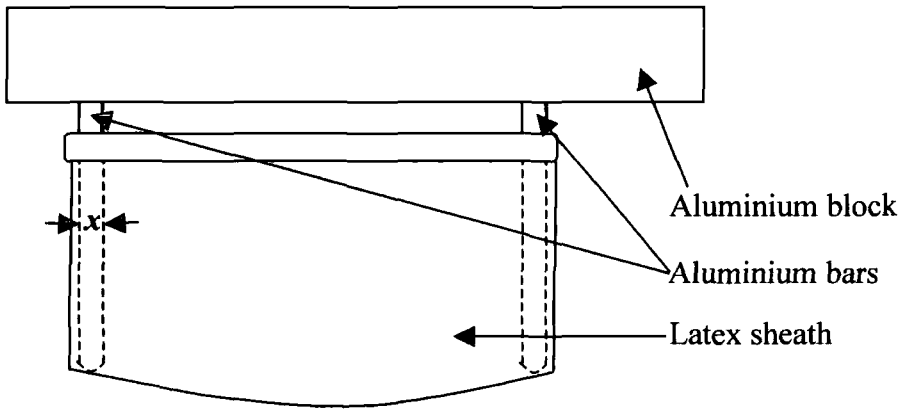

Figure 5.4: Schematic diagram of water container.

The water container comprised two identical cylindrical aluminium bars screwed into an aluminium block. A latex sheath was stretched taut over the bars such that it created a container with a width equal to the diameter of the aluminium bars (denoted x in figure 5.4). When water was added to the container, the latex walls remained in place provided they had been stretched sufficiently taut. Five of these containers were made, with widths of 2.996mm, 4.992mm, 7.017mm, 10.011mm and 12.671mm (all ±0.002mm), identical to the amounts used in the models.

It was important to determine whether the latex walls of the container were able to influence the X-rays by absorption thus affecting the image contrast. To this end, an initial check was conducted in which images were taken of the standard Heaviside function sample with each container in turn in the path of the beam. The phase contrast values were calculated according to equation 5-3 and the results are shown in figure 5.5.

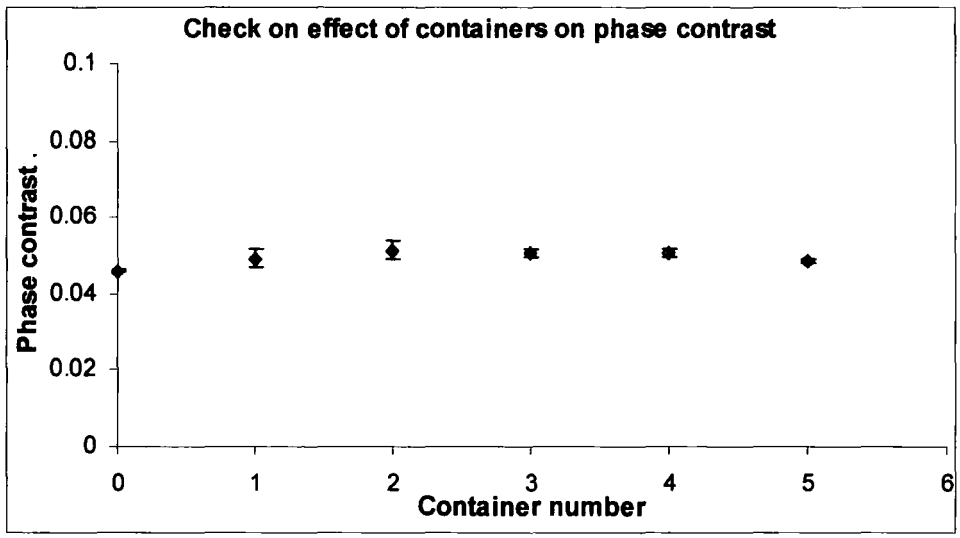

Figure 5.5: Phase contrast with each container in the path of the X-rays

It is clear from figure 5.5 that the containers did not have a detrimental effect on the phase contrast so they were suitable for use in the following experiments.

It was also important to make sure that the position of the water along the optic axis would not influence the results. To this end, images of the same Heaviside function sample were acquired as a water-filled container of width 2.996mm was positioned at various intervals along the optic axis. Again, the phase contrast values were calculated for each of these container positions. The results are shown in figure 5.6.

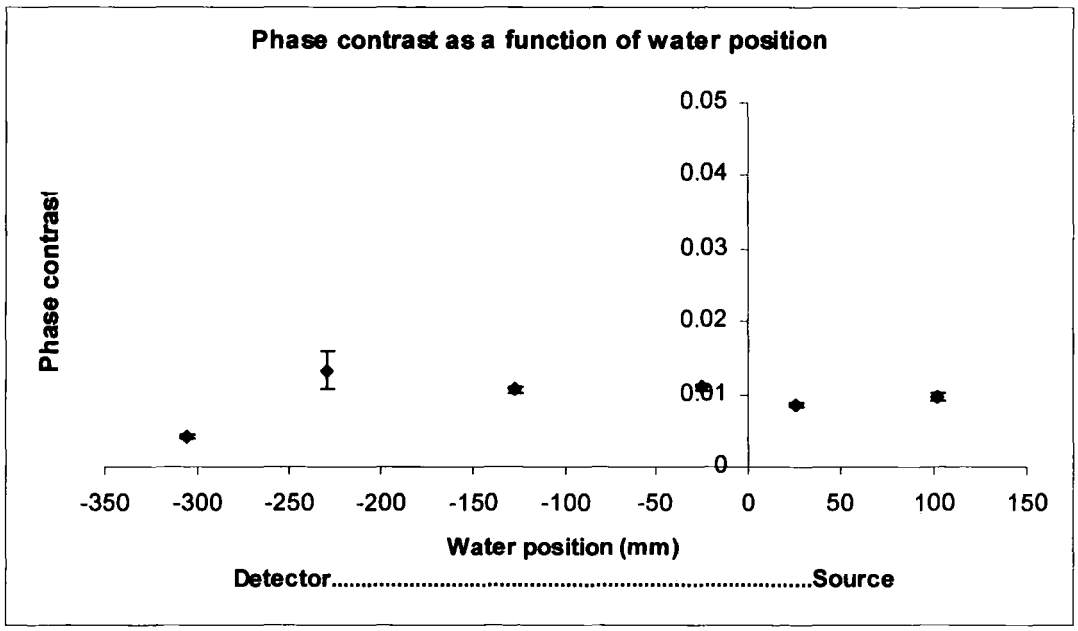

Figure 5.6: Effect of water position on phase contrast.

0mm position represents sample plane

It is seen that the position of the water does not have a significant effect on the image contrast except when it is positioned directly in front of the detector. This is not unexpected because when the water is placed directly in front of the detector, Compton scattered photons contribute to the image, distorting the phase contrast information. Provided the water is not placed directly in front of the detector, keeping in mind the requirement for an air gap [7] between the detector and all sections of the sample, its position along the optical axis is not overly important.

5.1.3 Effect on phase contrast

The water experiment was set up as follows (figure 5.7):

Figure 5.7: Set-up of water experiment

The Heaviside function sample was initially imaged without the water in place in order to provide a reference point against which subsequent images involving water may be compared. The sample was subsequently imaged with each water-filled container present in the X-ray beam, showing the effects of 2.996mm, 4.992mm, 7.017mm, 10.011mm and 12.671mm water against the benchmark provided with no water present in the system. For all normalised images, the phase contrast values were determined via equation 5-3 as discussed in Chapter 3.

The experiment was conducted using copper X-rays and rhodium X-rays. The quantified phase contrast results are shown in figure 5.8.

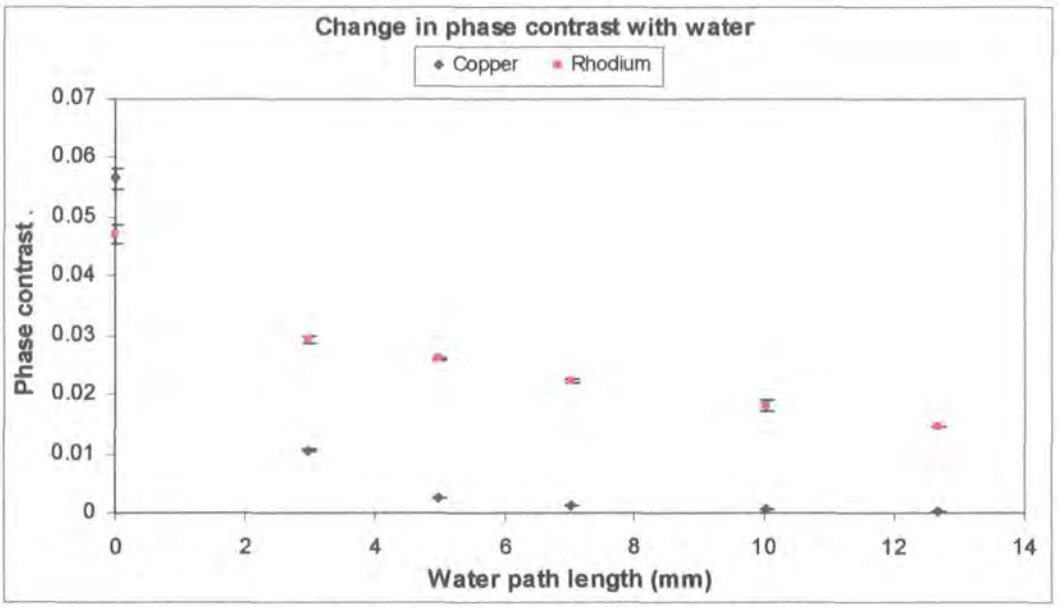

Figure 5.8: Change in phase contrast as path length of water is increased

The intensity profiles of the images achieved with the rhodium source are shown in figure 5.9(a), and those achieved with the copper source are shown in figure 5.9(b).

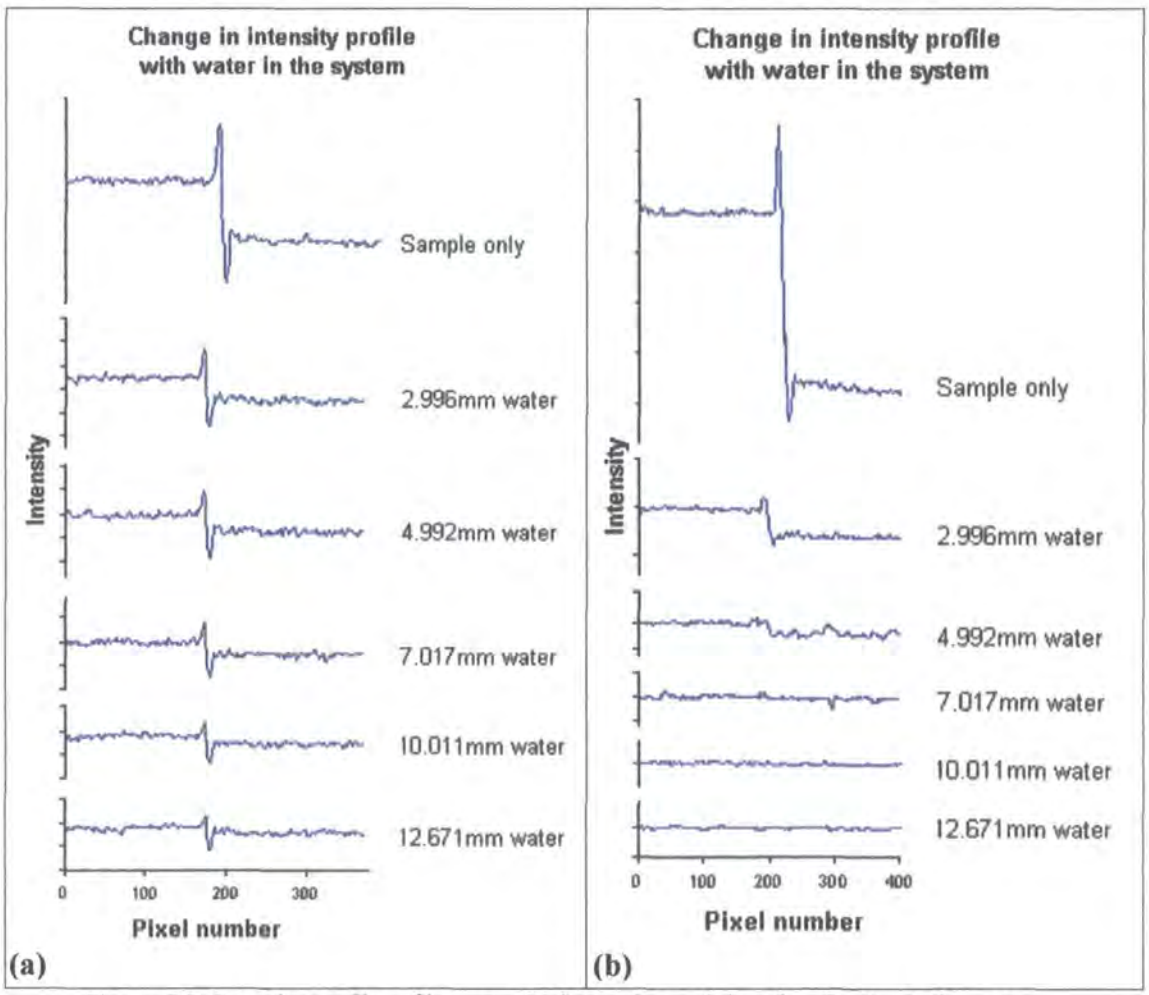

Figure 5.9: Intensity profiles of images with increasing path lengths of water in the system.
(a) Images achieved using rhodium source, (b) Images achieved using copper source

From figures 5.8 and 5.9 the image contrast is seen to be reduced considerably by the presence of water, even in a very small amount. With no water in the X-ray beam, the set-up gives good phase contrast with both targets. However, as water is added to the system this situation changes. The rhodium target continues to provide substantial phase contrast, while the phase contrast provided by the copper source is severely degraded. This suggests that the absorption property of the water has some influence over this result because the range of wavelengths provided by the copper target is absorbed more strongly than that provided by the rhodium target, as demonstrated earlier in figures 5.1, 5.2 and 5.3.

In order to investigate this further, the absorption contrast value for each image was determined as described in Chapter 3. These are plotted together with the phase contrast. The results are shown for the rhodium target in figure 5.10.

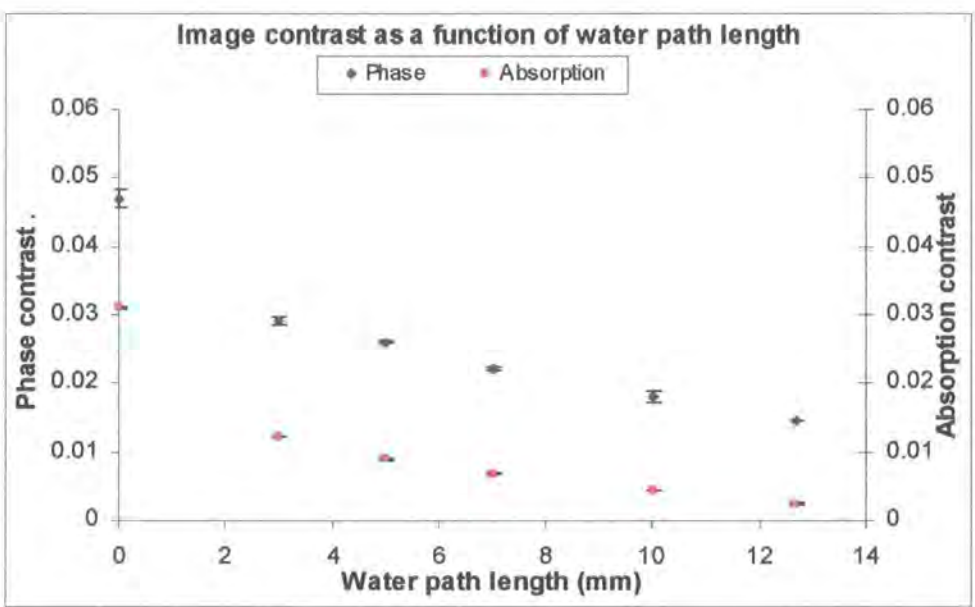

Figure 5.10: Change in phase and absorption contrast as water path length is increased (Rhodium source)

Clearly it is not only the phase contrast which is severely affected by the presence of water, but the absorption contrast also suffers a significant decrease. This is most unexpected due to the care taken to keep noise to a minimum, as described in Chapter 3. Since other experiments have been unaffected by significant noise, it is unlikely that noise is the reason for the huge drop in absorption contrast here.

However, in order to check this, equation 5-6 is modified to represent the effect of the Heaviside function sample rather than an edge. The modified version is the following.

$$C = \frac{\exp(-\mu_s t_1) - \exp(-\mu_s t_2)}{\exp(-\mu_s t_1) + \exp(-\mu_s t_2) + 2\frac{N}{I_0}\exp(\mu_w t_w)} \qquad (5\text{-}7)$$

The thicknesses on each side of the sample boundary were substituted in, where t_1 = 0.051mm and t_2 = 0.320mm, and each water path length in turn was substituted in for t_w. At the rhodium K_α energy, μ_s= 0.794503 and μ_w = 0.790434. An arbitrary figure of 1000 was assigned to I_0, and N was varied in order to find the closest fit to the absorption contrast.

The closest fit of equation 5-7 to the absorption contrast data obtained experimentally uses a value of less than 0 for N. This fit of equation 5-7 is plotted with the absorption contrast data in figure 5.11.

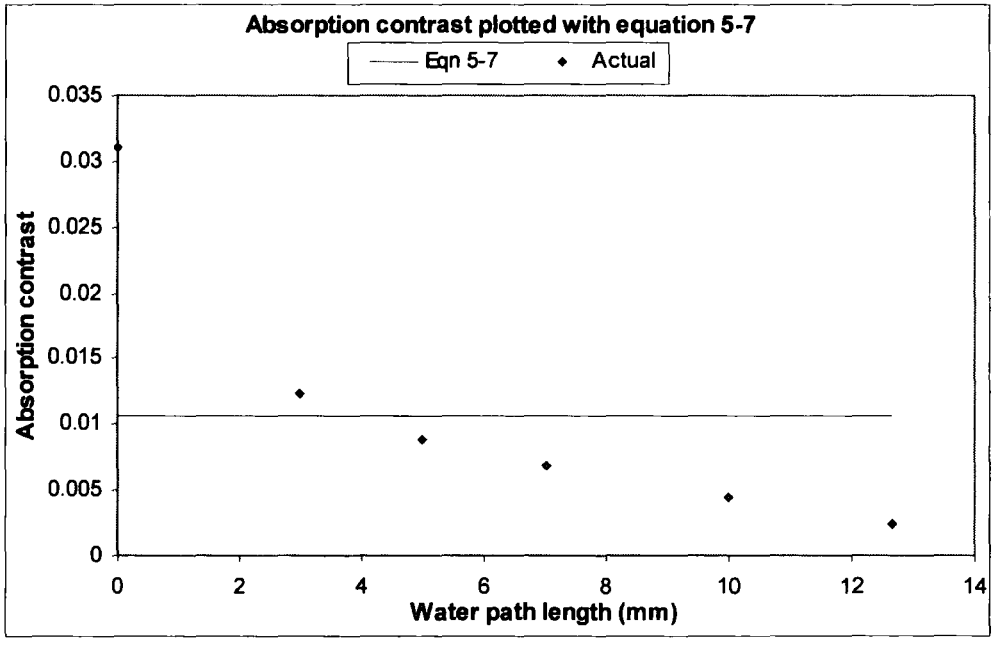

Figure 5.11: Equation 5-7 and absorption contrast plotted against water path length (rhodium source)

From figure 5.11 it is seen that not only is the noise at a negligible level when fitting equation 5-7 to the absorption contrast, but also the relationship between the

equation 5-7 fit and the water path length does not match that of the absorption contrast. So it is concluded that the presence of noise does not govern this result.

The fact that the absorption contrast is decreased on introduction of water to the system is a clue that absorption of the X-rays by water is causing the loss of phase contrast. In order to determine whether a beam hardening effect is causing the loss of phase contrast due to water, the model for this situation is applied to the rhodium spectra as before in Chapter 4. Each of the filtered spectra are treated using equation 5-1, using the absorption coefficient of mylar at each energy along the spectrum, together with (a) the thickness of a single layer of mylar (0.051mm) and (b) the thickness of the thicker section of mylar (0.320mm). A weighted average is taken of each of these as follows:

$$Average = \frac{\sum I_o \exp(-\mu t)}{\sum I_o} \qquad (5\text{-}8)$$

This calculation leads to an average absorption coefficient across each spectrum, as shown in equation 5-9.

$$Avg\left(\frac{I}{I_o}\right) = \exp(-\bar{\mu} t) \qquad (5\text{-}9)$$

The exponential terms containing the average absorption coefficient with the two thicknesses are substituted into the absorption contrast equation as follows:

$$Contrast = \frac{\exp(-\bar{\mu} t_1) - \exp(-\bar{\mu} t_2)}{\exp(-\bar{\mu} t_1) + \exp(-\bar{\mu} t_2)} \qquad (5\text{-}10)$$

The absorption contrast calculated by this method is plotted together with that achieved by the rhodium target during the water experiment (shown earlier in figure 5.10). These are shown in figure 5.12.

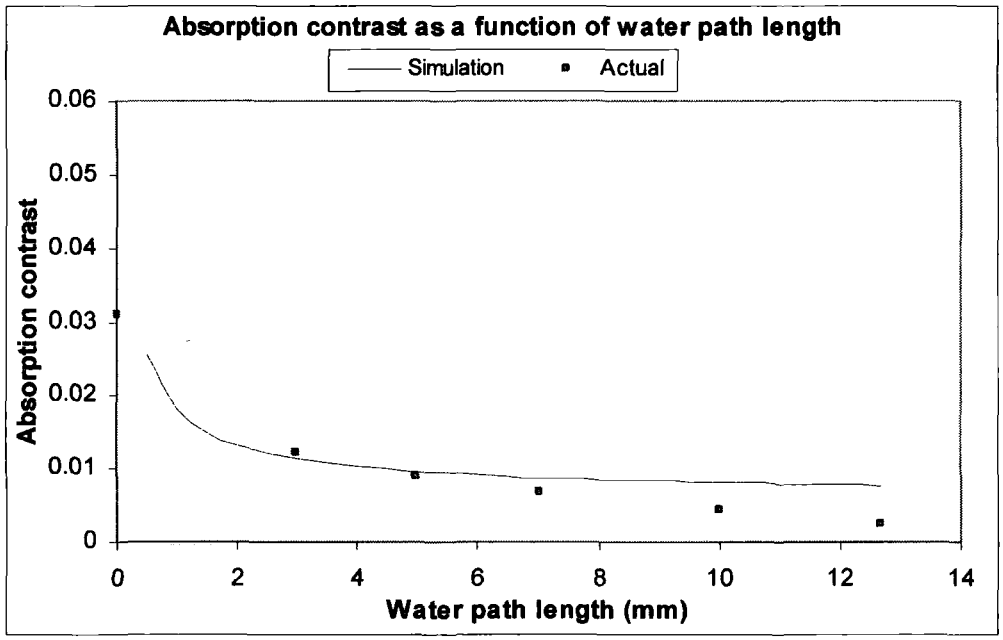

Figure 5.12: Theoretical and experimental change in absorption contrast with increasing water path length (Rhodium source)

As figure 5.12 shows, the model of the beam hardening effect for the rhodium source provides a reasonably good fit to the relationship between sample absorption contrast and water path length. The shift of the dominant energy to higher values accounts well for the loss in absorption contrast.

This idea is extended to the phase contrast: it has already been demonstrated in Chapter 4 that a shift of the dominant energy would affect the coherence length. Each of the filtered spectra are treated using the following equation:

$$\lambda = \frac{hc}{E} \qquad (5\text{-}11)$$

A weighted average is taken of each of these as follows:

$$E_{Dominant} = \frac{\sum(\lambda \times No.Photons)}{\sum No.Photons} \qquad (5\text{-}12)$$

Using this method, the unfiltered rhodium spectrum has already been seen to have a mean dominant wavelength of 1.17Å, which is longer than the rhodium K_α

wavelength of 0.64Å due to the large contribution to the spectrum made by the low energy Bremsstrahlung radiation. As the water path length in the beam is increased, this mean dominant wavelength is reduced to 0.55Å, 0.52Å, 0.51Å, 0.49Å and finally 0.47Å. This reduction in the mean dominant wavelength leads to a reduction in the effective transverse coherence length of the X-rays. The effective transverse coherence length is calculated using the effective radius of the source (6.38μm), the source-sample distance (134mm) and each mean dominant wavelength in turn. The change in the average wavelength and the effective transverse coherence with water path length is shown in figure 5.13.

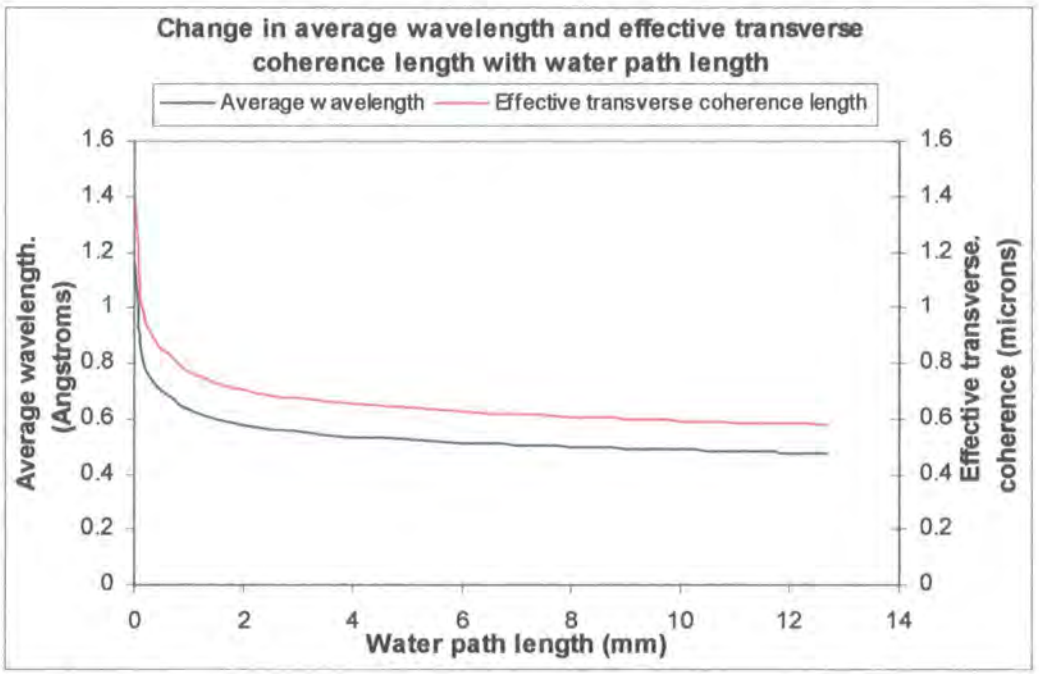

Figure 5.13: Change in average wavelength and effective transverse coherence length with increasing water path length (rhodium source)

The average wavelength and, consequently, the effective transverse coherence length, show a similar relationship with the water path length as the phase contrast in figure 5.10. The phase contrast of each image is now plotted with the effective transverse coherence length calculated for each water path length: this is shown in figure 5.14.

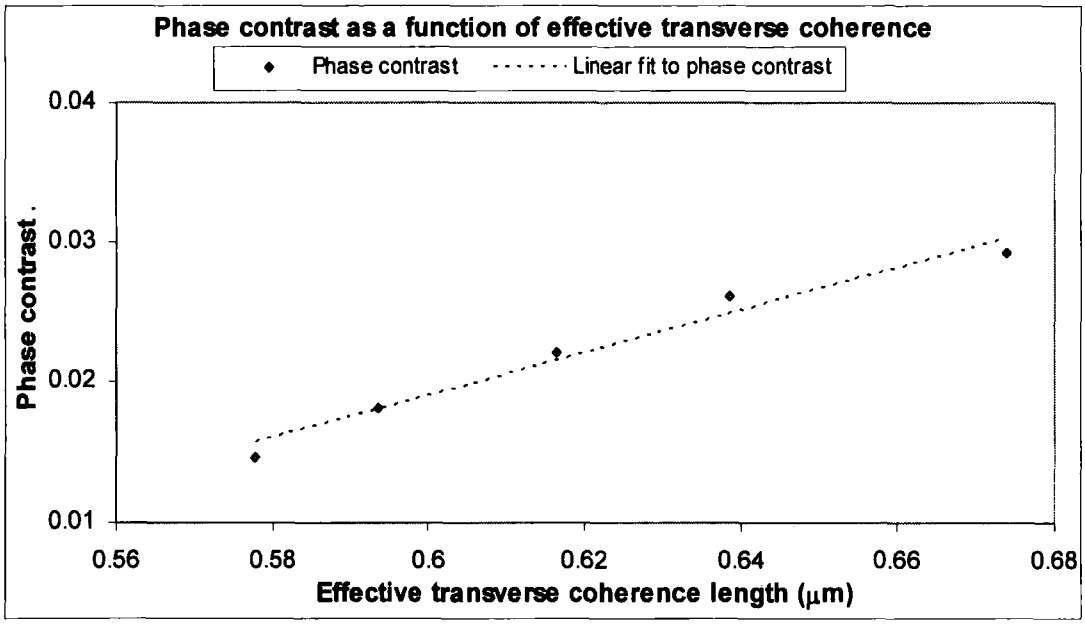

Figure 5.14: Phase contrast as a function of effective transverse coherence length for rhodium target

The phase contrast shows a linear, proportional relationship with the effective transverse coherence length of the system: this is confirmed by the strong, positive correlation coefficient of 0.99 between the two variables. Thus as the increasing water path length shifted the dominant X-ray energy range to higher energies (and hence the dominant wavelength to lower values), the consequent reduction in the effective transverse coherence length caused degradation of the phase contrast.

The copper results are also considered in the same way. The copper target phase and absorption contrast determined experimentally are shown in figure 5.15.

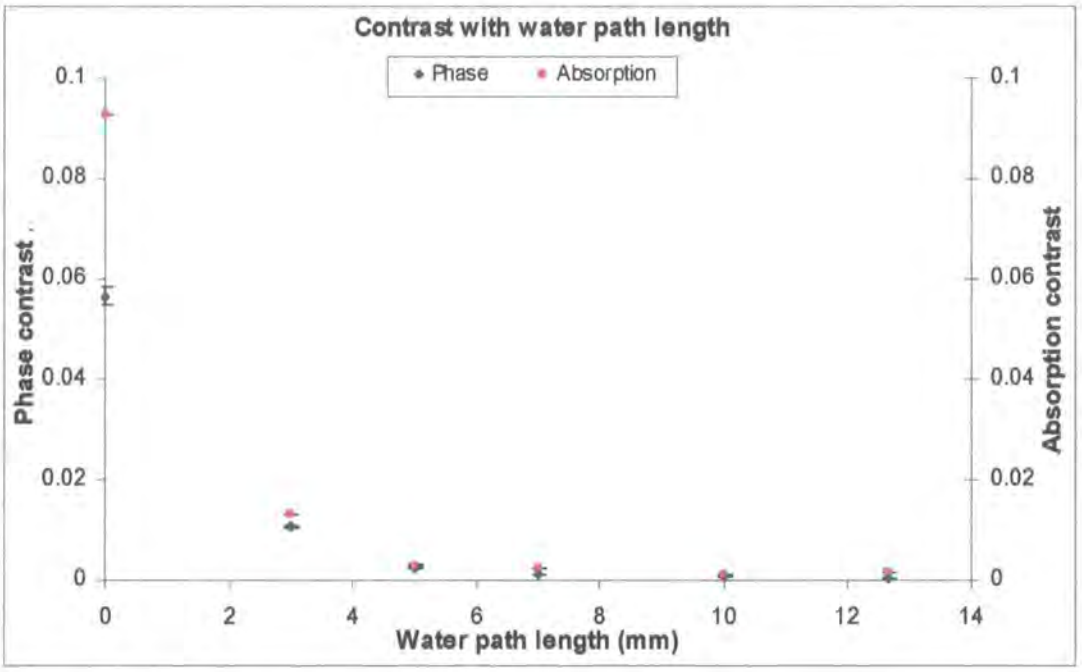

Figure 5.15: Change in phase and absorption contrast as water path length is increased (Copper source)

The copper results show the same behaviour as those obtained using the rhodium target, although the absorption contrast is higher to start with, due to the lower energy of the X-ray beam. As before, consider the filtered copper spectra. Using a similar beam hardening model, the change in absorption contrast, average wavelength and effective coherence length are calculated for the increasing water path lengths. The absorption contrast values calculated by the model are plotted together with those achieved by the copper target during the water experiment (shown earlier in figure 5.15). These are shown in figure 5.16.

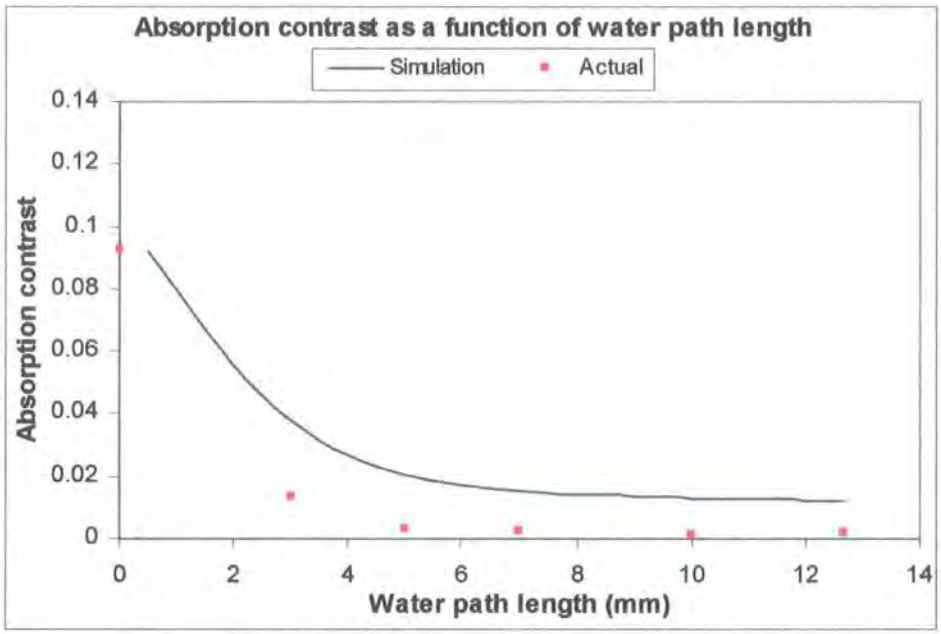

Figure 5.16: Theoretical and experimental change in absorption contrast with increasing water path length (Copper source)

As figure 5.16 shows, the model of the beam hardening effect for the copper source shows a similar relationship to that between sample absorption contrast and water path length shown by the actual results. The fit is not quite as close as for the rhodium results, but the shift of the dominant energy to higher values does account for the loss in absorption contrast reasonably well. The increasing average wavelength and the effective transverse coherence are shown in figure 5.17.

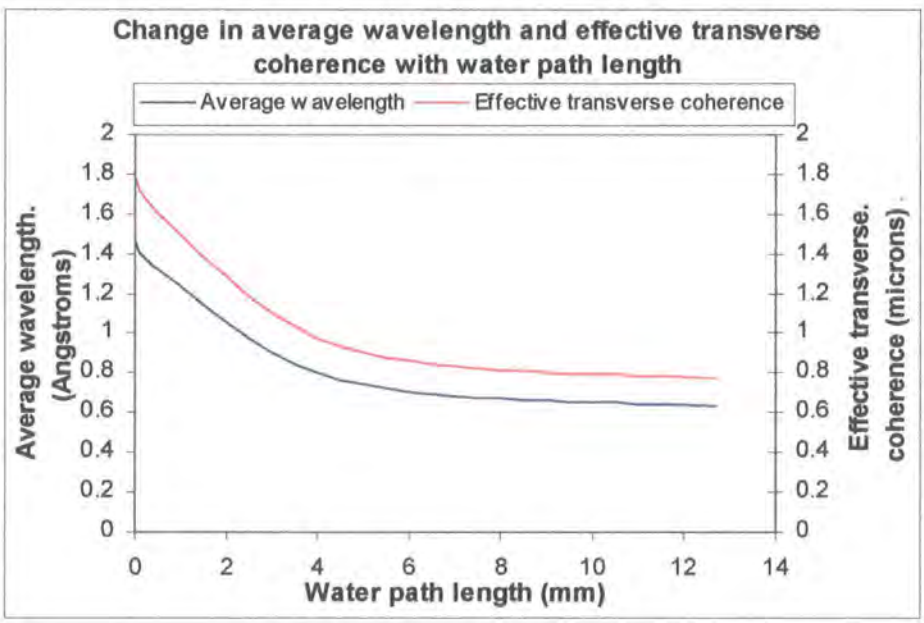

Figure 5.17: Change in average wavelength and effective transverse coherence length with increasing water path length (copper source)

The average wavelength and, consequently, the effective transverse coherence length, show a similar relationship with the water path length as the phase contrast in figure 5.15. The phase contrast of each image is now plotted with the effective transverse coherence length calculated for each water path length. This is shown in figure 5.18.

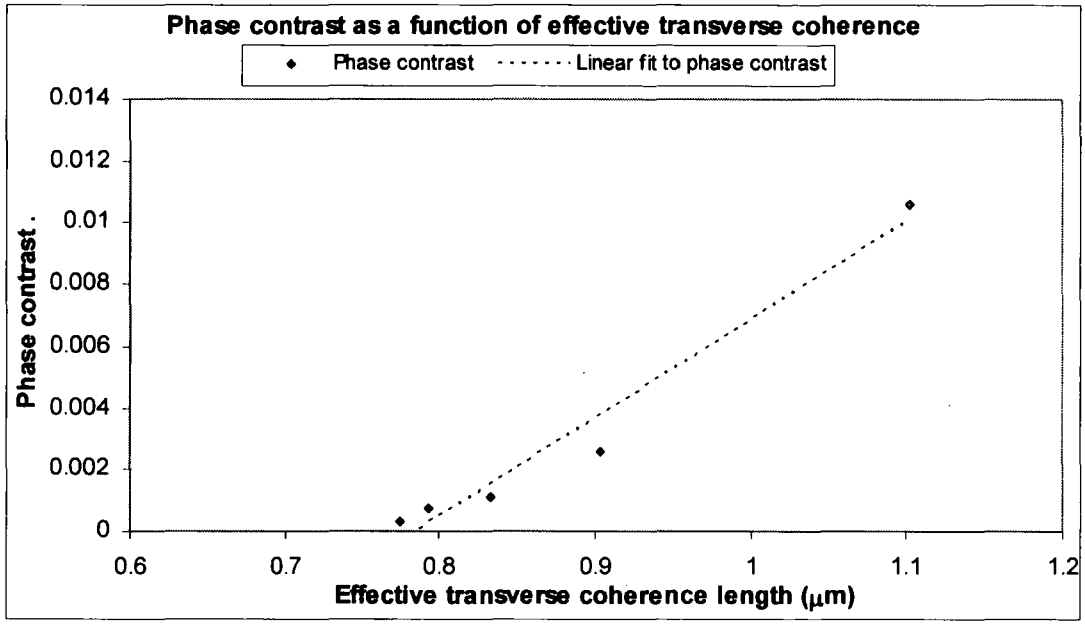

Figure 5.18: Phase contrast as a function of effective transverse coherence length for copper target

As before, the phase contrast shows a linear relationship with the effective transverse coherence length of the system, this being confirmed by the strong, positive correlation coefficient of 0.99 between the two variables. Thus as the increasing water path length shifted the dominant X-ray energy range to higher energies (and hence the dominant wavelength to lower values), the consequent reduction in the effective transverse coherence length caused degradation of the phase contrast.

The degradation of the phase and absorption contrast is explained well by a beam hardening model. This effect is a direct consequence of using a polychromatic X-ray source: a monochromatic beam would not experience beam hardening due to water absorption. The absorption over such a narrow range of wavelengths would not have any appreciable effect on the dominant X-ray energy, and so while the intensity would decrease, the actual quantifiable absorption contrast and phase contrast should not change. However, laboratory-based X-ray sources, particularly microfocus X-ray

sources, emit limited intensities and these are often insufficient for phase contrast imaging purposes after monochromation. This is a major advantage of monochromatic synchrotron X-radiation over the polychromatic laboratory-based microfocus X-ray source. This work demonstrates that copper X-rays are unsuitable for imaging biological tissue with this system, because the presence of water reduces the phase contrast significantly. However, while the phase contrast achieved using the rhodium X-rays is obviously reduced by the presence of water, it is by no means destroyed. This is a very positive result in the steps towards biological imaging and suggests that with the rhodium target in place, this system could potentially image biological specimens.

5.2 Glass

As an extension to the experiment introducing water into the system, glass is added to the sample in order to check whether it has the same effect on the phase and absorption contrast as water. It is expected that this will be the case because glass is a disordered, non-periodic material which absorbs X-rays strongly in the low-energy region.

For the purpose of this experiment, 4 simple glass microscope slides were used, each with a uniform thickness of 1.178mm. So the glass path-lengths used for this experiment were 0mm, 1.178mm, 2.356mm, 3.534mm and 4.712mm (error ±0.002mm).

5.2.1 Scattering considerations

One property of the glass which required consideration is its ability to scatter X-rays. In order to check the extent to which X-rays are Compton scattered away from the optical axis, a scattering experiment was conducted. This used a microfocus X-ray source with a copper target, together with a moveable detector which detects intensity as a function of scattering angle. The apparatus is shown in figure 5.19.

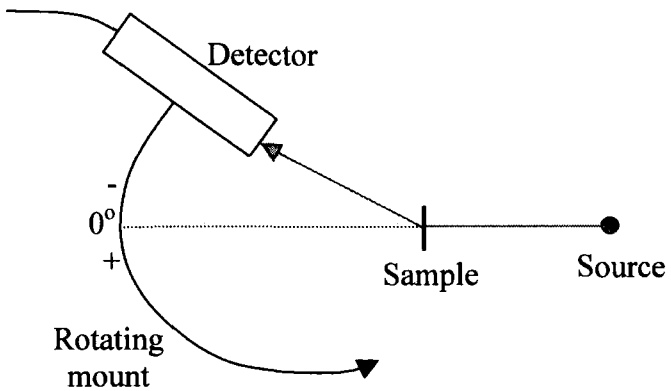

Figure 5.19: Diagram of apparatus for scattering experiment

The sheet of glass was secured perpendicular to the X-ray beam, as in the in-line imaging technique. The X-rays were propagated toward the glass sheet, and the detector recorded the intensity at angular intervals of 0.15°. The results are shown in figure 5.20.

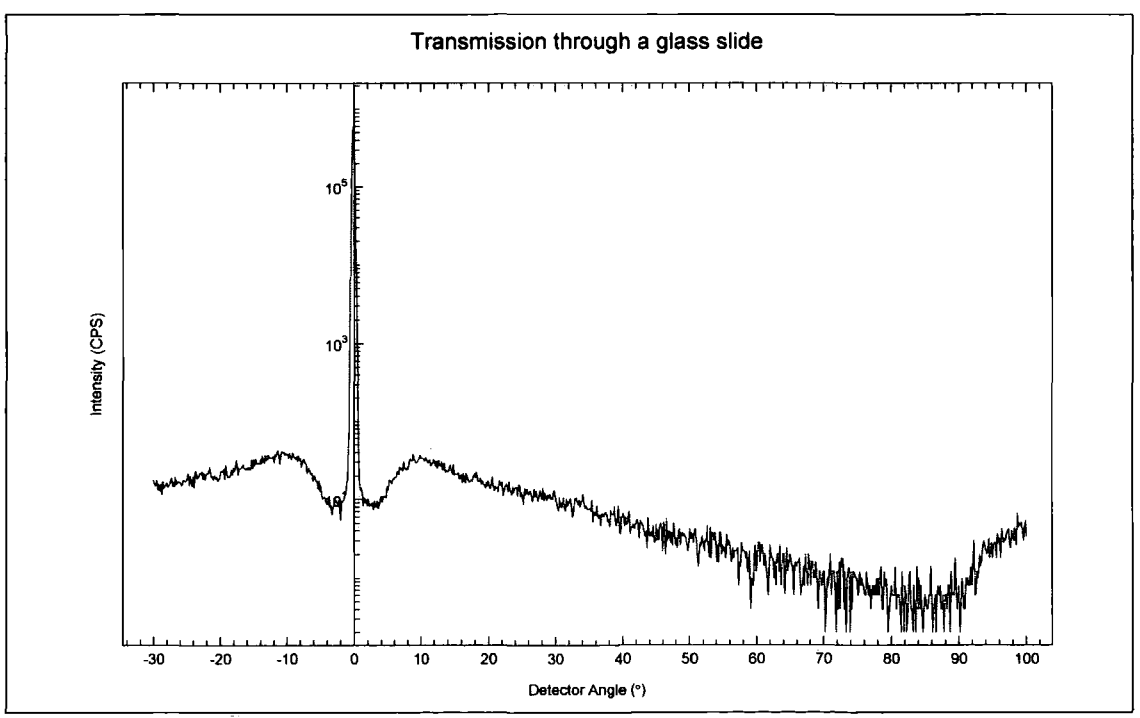

Figure 5.20: X-ray transmission and scattering through a glass slide.

The X-ray camera in the phase contrast imaging set-up detects X-rays which have deviated by up to ~0.15°. It is seen from figure 5.20 that most of the intensity of the X-ray beam passes through the glass slide normally within the solid angle required by the in-line imaging set-up. So there is no problem with X-ray transmission through the glass slide, however some Compton scattered photons have been detected so the air gap [7] will be needed between the sample/glass and the detector.

5.2.2 Absorption considerations

With the introduction of glass to the system, the level of absorption by the glass is important and so once again using the XOP software, the absorption coefficient for glass is determined. This is shown graphically as a function of X-ray energy in figure 5.21. As before, it is seen that the absorption coefficient is much greater at the copper K_α characteristic energy of 8.048 keV than at the rhodium K_α characteristic energy of 20.216 keV. In addition, it is seen that the absorption coefficient of glass is much greater across the spectrum than the absorption coefficient of water, an increase of a factor of ~6.5.

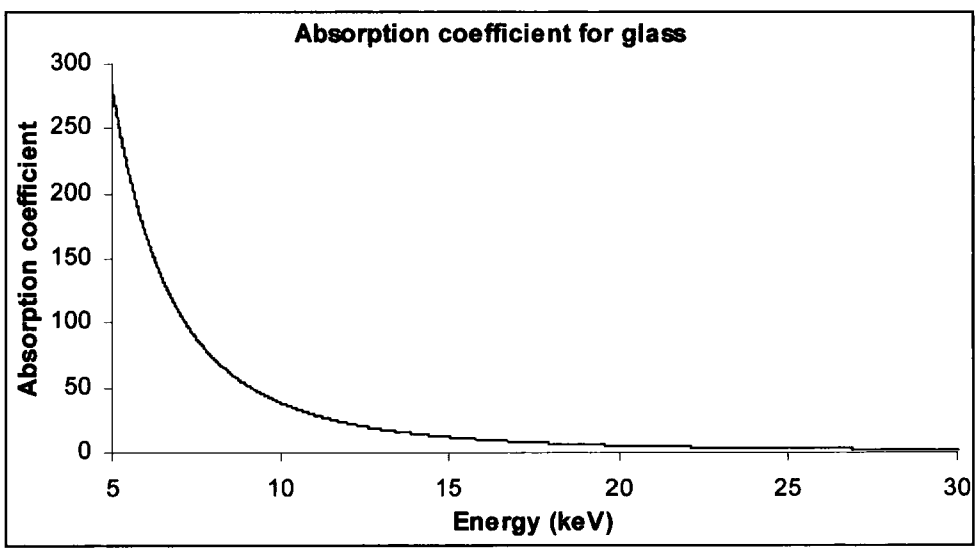

Figure 5.21: Absorption coefficient for glass as a function of X-ray energy

Using expression (5-1) together with the absorption coefficient of glass shown in figure 5.21, the modified copper spectrum was simulated for the inclusion of different thicknesses of glass in the system. The following glass thicknesses were

included in the model: 1.178mm, 2.356mm, 3.534mm and 4.712mm. The modified copper spectra determined by the model are shown in figure 5.22.

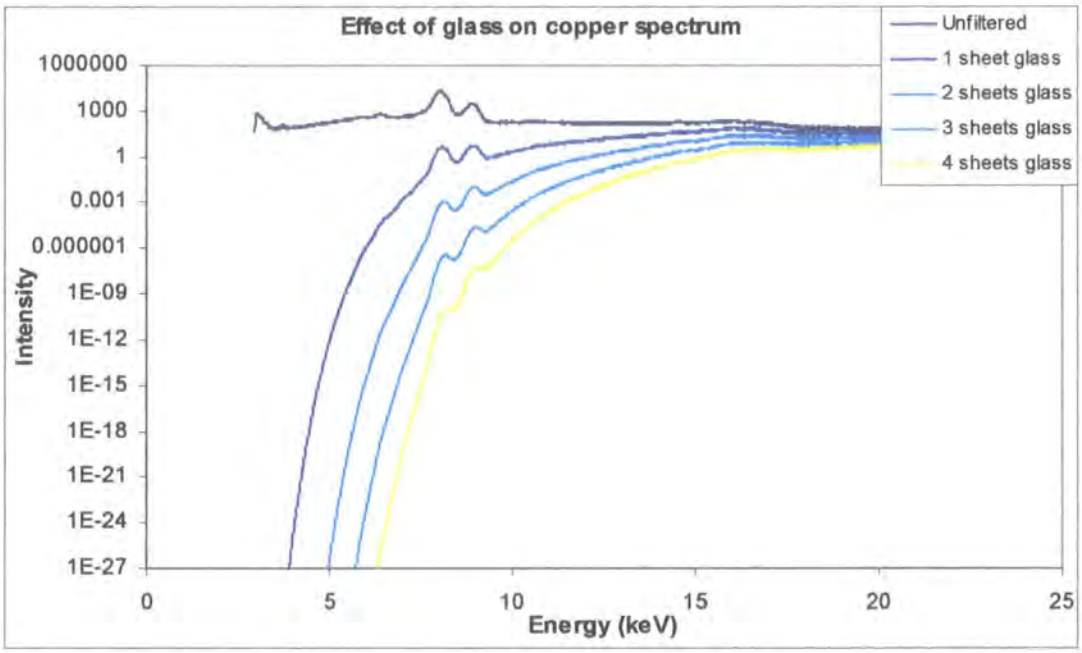

Figure 5.22: Effect of various glass thicknesses on Microsource® spectrum with copper target

It is seen from figure 5.22 that the copper X-ray spectrum is even more severely affected by the presence of glass than by water: the K_α characteristic line is reduced to just 0.02% of its full intensity with just ~1mm of glass present in the system.

Using the same technique, a model was also produced for the rhodium spectrum and is shown in figure 5.23.

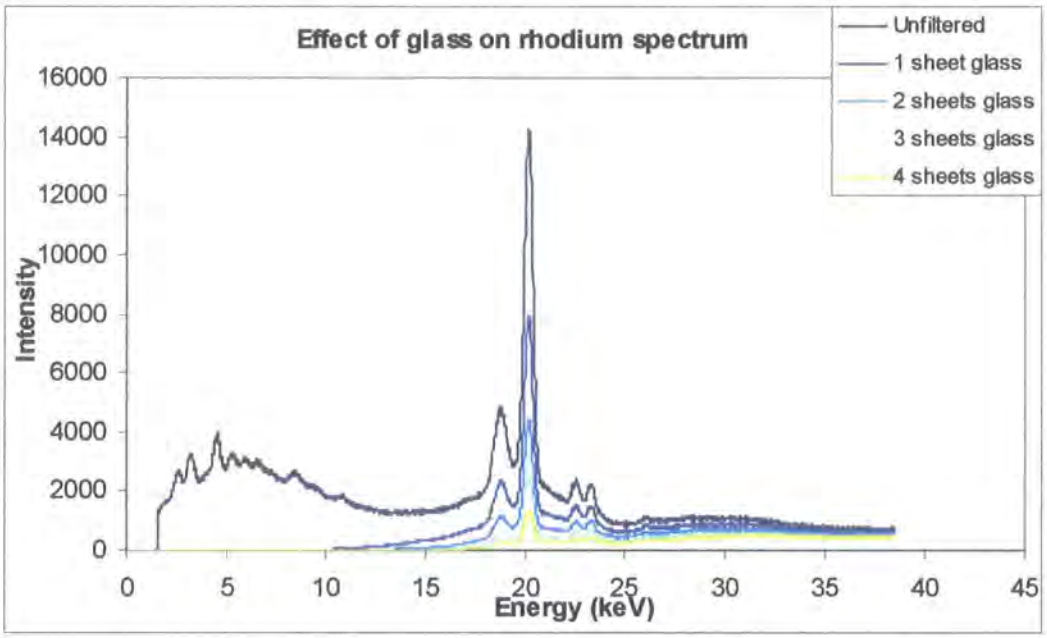

Figure 5.23: Effect of various glass thicknesses on Microsource® spectrum with rhodium target

It is seen from figure 5.23 that the effect of the same glass thicknesses in the system is much less marked in the rhodium spectrum than the copper spectrum. For example the K_α characteristic line is reduced to 55% of its original intensity by the presence of ~1mm glass in the system, which is a less discouraging loss. Again, it is a more significant loss than the attenuation of the rhodium spectrum due to water.

5.2.3 Effect on phase contrast

The main glass experiment itself was set up as follows (figure 5.24):

Figure 5.24: Set-up of glass experiment

As before, it was verified that the position of the glass along the optical axis would not influence the results. Images of the standard Heaviside function sample were acquired as a glass sheet of 1.178mm thickness was positioned at various intervals along the optical axis. Again, the phase contrast value was calculated and compared for each of these glass positions. The results are shown in figure 5.25.

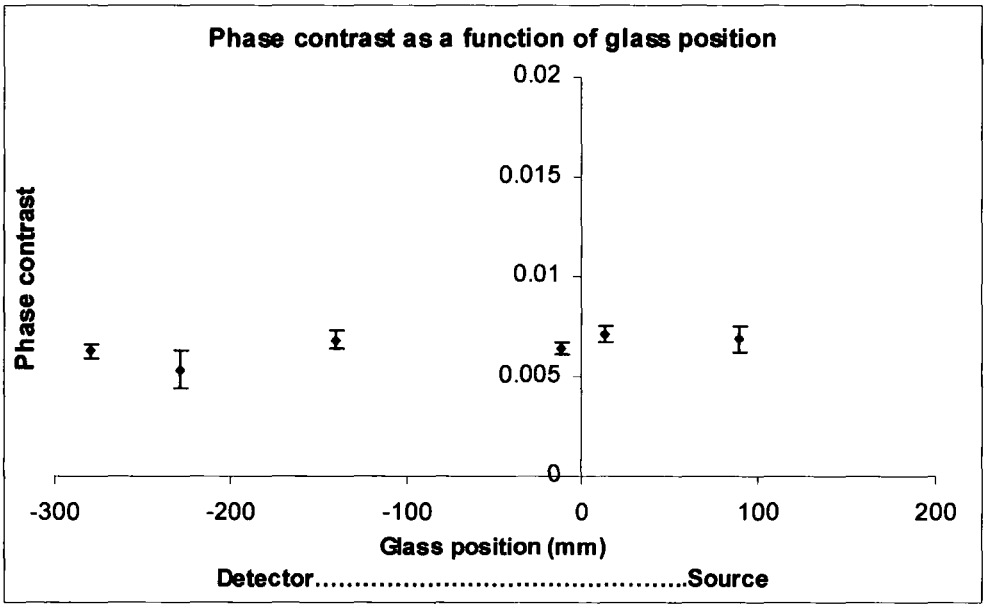

Figure 5.25: Effect of glass position on phase contrast

0mm position represents sample plane

As before with the water container, it is seen that with the glass directly in front of the detector there is a drop in the phase contrast due to some Compton scattering. Provided an air gap [7] is present between the detector and all parts of the sample and glass, the position of the glass along the optical axis is not overly important.

The sample was initially imaged without the glass in place in order to provide a reference image against which subsequent images, filtered by glass, could be compared. This was followed by inserting a 1.178mm sheet of glass into the path of the X-ray beam and recording an image. This method was repeated three times, each time with the addition of another glass slide in the X-ray beam, to compare the effects of the glass thicknesses against the benchmark provided with no glass present in the system. For all images, the phase contrast was calculated via equation 5-3 as discussed in Chapter 3.

The experiment was conducted with copper X-rays and rhodium X-rays. The quantified phase contrast results are shown in figure 5.26.

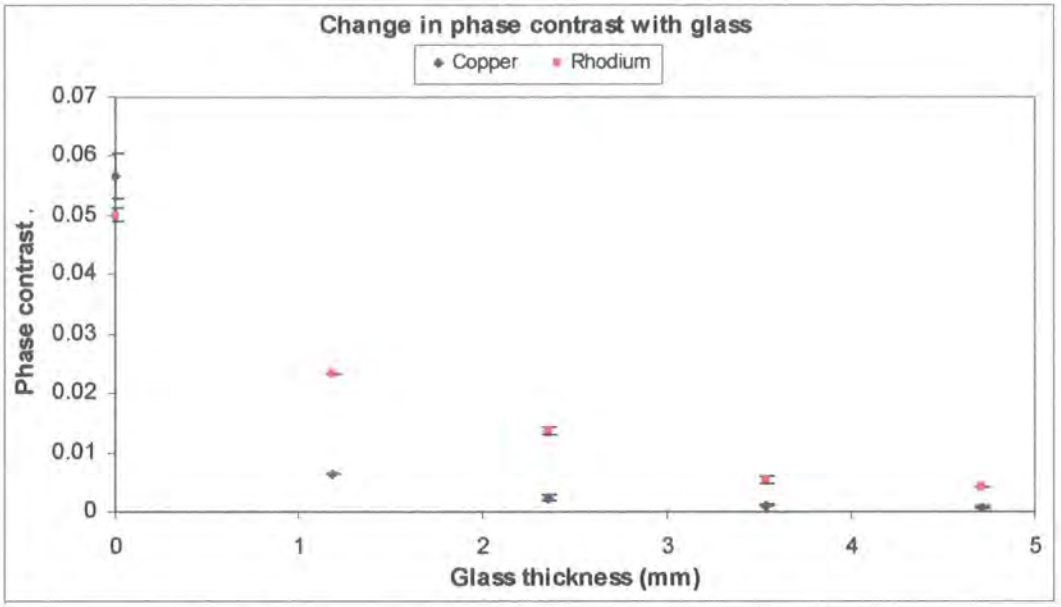

Figure 5.26: Change in phase contrast as glass thickness is increased

The intensity profiles of the images achieved with the rhodium source are shown in figure 5.27(a), those achieved with the copper source in figure 5.27(b).

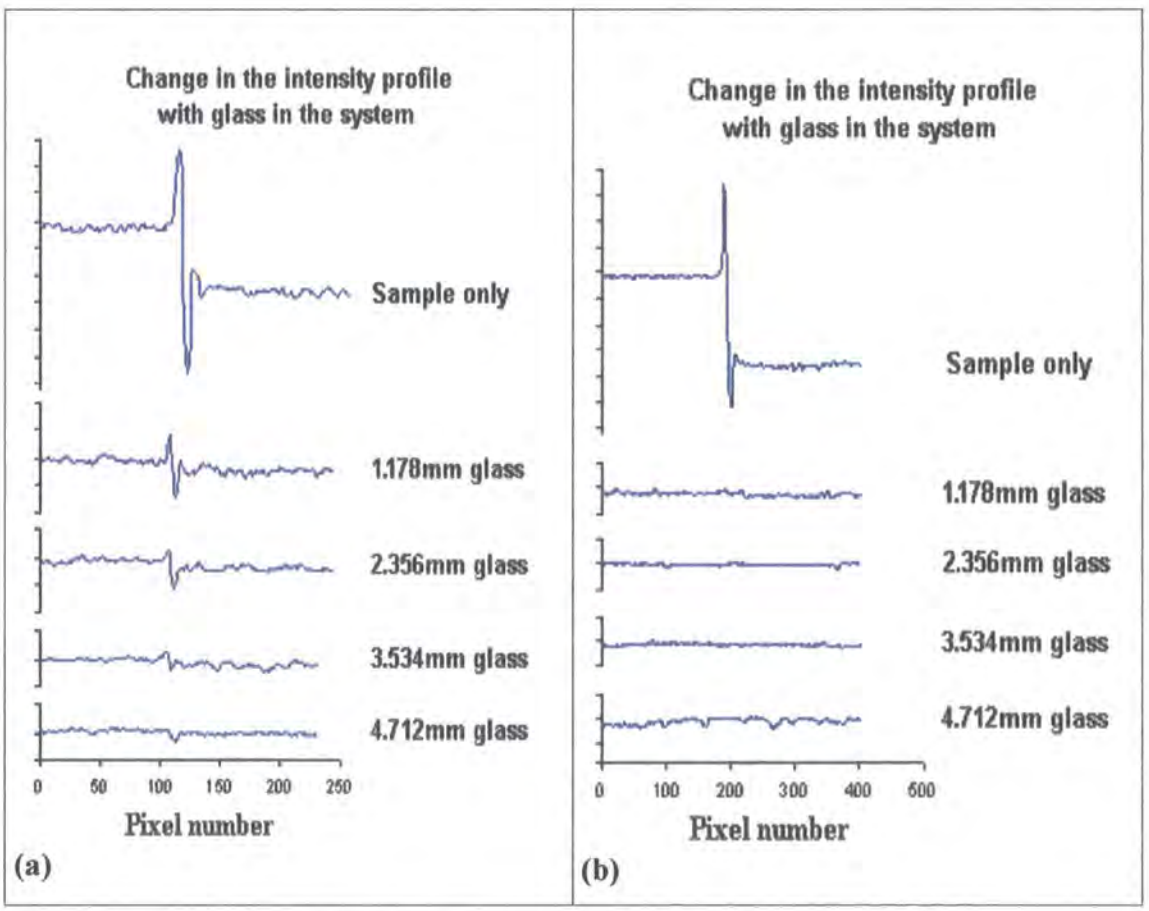

Figure 5.27: Intensity profiles of images with increasing path lengths of glass in the system.
(a) Images achieved using rhodium source, (b) Images achieved using copper source

From figures 5.26 and 5.27 it is seen that the image contrast is reduced considerably by the presence of glass, to an even greater extent than by water. With no glass in the X-ray beam, the set-up gives good image contrast with both targets, as seen before. However, as glass is added to the system the set-up with the rhodium target continues to provide some limited phase contrast while the set-up with the copper target sees the phase contrast almost completely destroyed. Once again this indicates that the absorption property of the glass has some influence over this result, for the same reason as before.

In order to investigate this further, the absorption contrast of each image is determined as described in Chapter 3. This is plotted together with the phase contrast in figure 5.28 for the rhodium images.

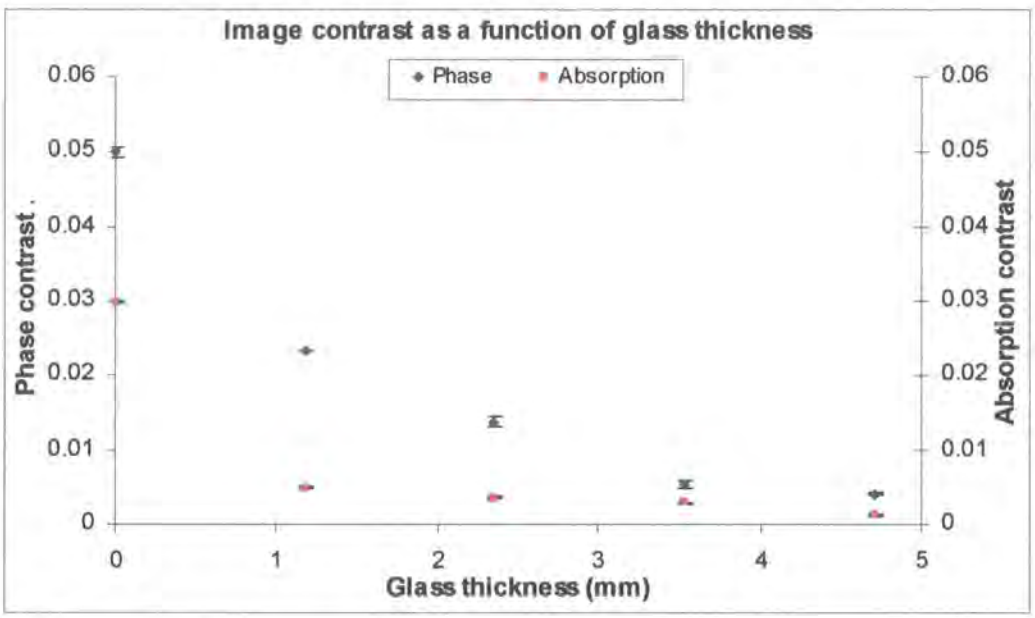

Figure 5.28: Change in phase and absorption contrast as glass thickness is increased (Rhodium source)

It is clear from figure 5.28 that, as with the previous experiment with water, it is not only the phase contrast which is severely affected by the presence of glass, but the absorption contrast also suffers a significant decrease. Once again, the decrease in absorption contrast is a clue that the loss in phase contrast is caused by X-ray absorption in glass.

As before, each of the filtered spectra are treated using equation 5-1, using the absorption coefficient of mylar at each energy along the spectrum, together with (a) the thickness of a single layer (0.051mm) and (b) the thickness of the thicker section (0.320mm). A weighted average is taken of each of these according to equation 5-8, and the resulting exponential terms containing the average absorption coefficient with the two thicknesses are substituted into equation 5-10.

The absorption contrast calculated by this method is plotted together with that achieved by the rhodium target during the glass experiment (shown earlier in figure 5.28). These are shown in figure 5.29.

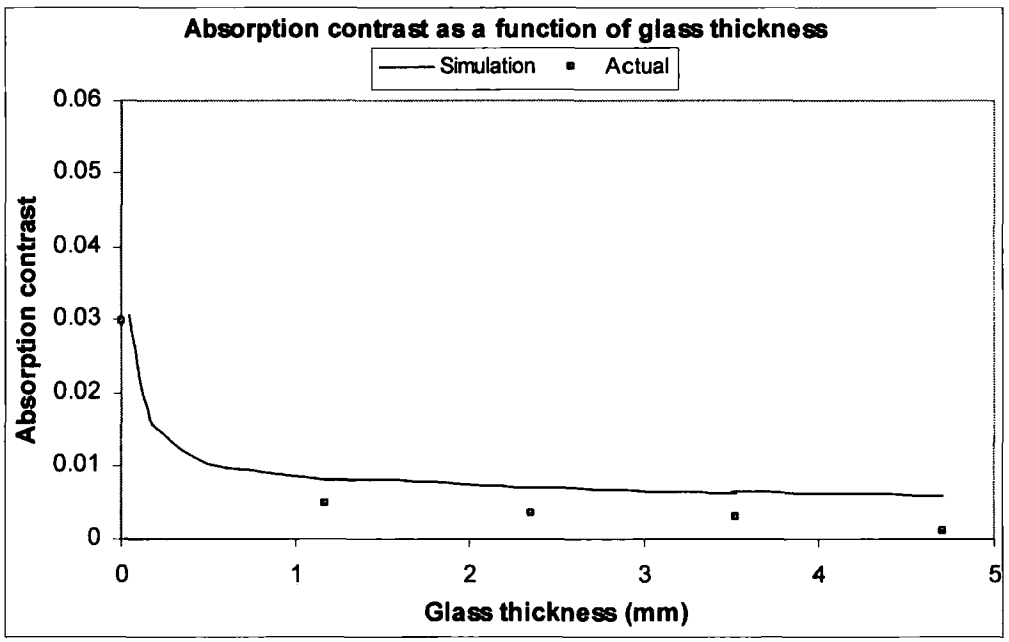

Figure 5.29: Theoretical and experimental change in absorption contrast with increasing glass thickness (Rhodium source)

As figure 5.29 shows, the model of the beam hardening effect for the rhodium source shows a good fit to the relationship between absorption contrast and water path length shown by the actual results. So, once again, the shift of the dominant energy to higher values accounts for the loss in absorption contrast quite well.

Again, this idea is extended to the phase contrast. Each of the rhodium spectra are treated using equations 5-11 and 5-12 in order to calculate an average wavelength for each spectrum. With one glass sheet in the path of the beam, this mean dominant

wavelength is reduced from 1.17Å to 0.32Å, with further decreases as more glass is added. This reduction in the mean dominant wavelength leads to a reduction in the effective transverse coherence length of the X-rays. The effective transverse coherence length is once again calculated, and the change in the average wavelength and the effective transverse coherence with water path length is shown in figure 5.30.

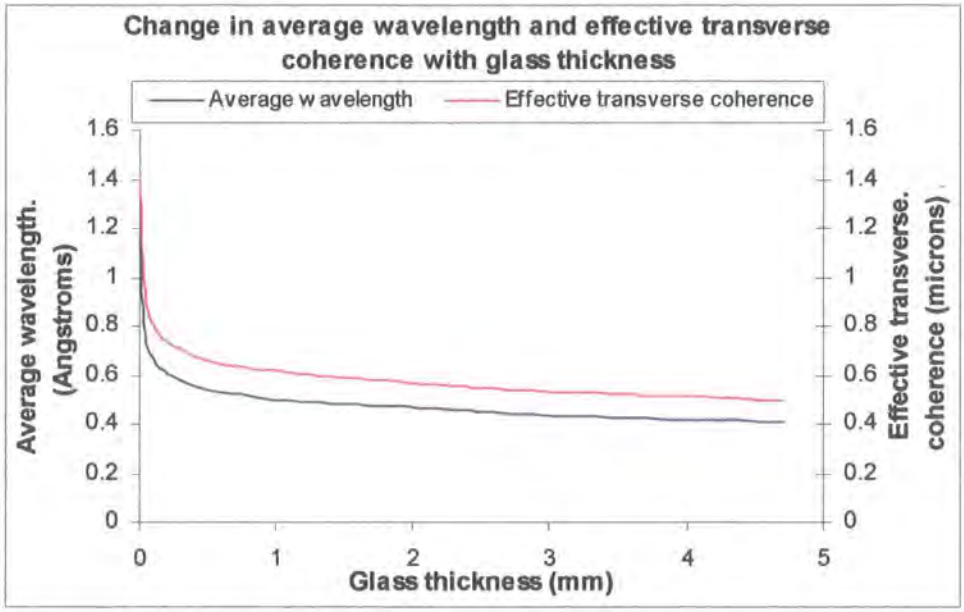

Figure 5.30: Change in average wavelength and effective transverse coherence length with increasing glass thickness (rhodium source)

The average wavelength and, consequently, the effective transverse coherence length, show a similar relationship with glass thickness as the phase contrast in figure 5.28. The phase contrast of each image is now plotted with the effective transverse coherence length calculated for each glass thickness: this is shown in figure 5.31.

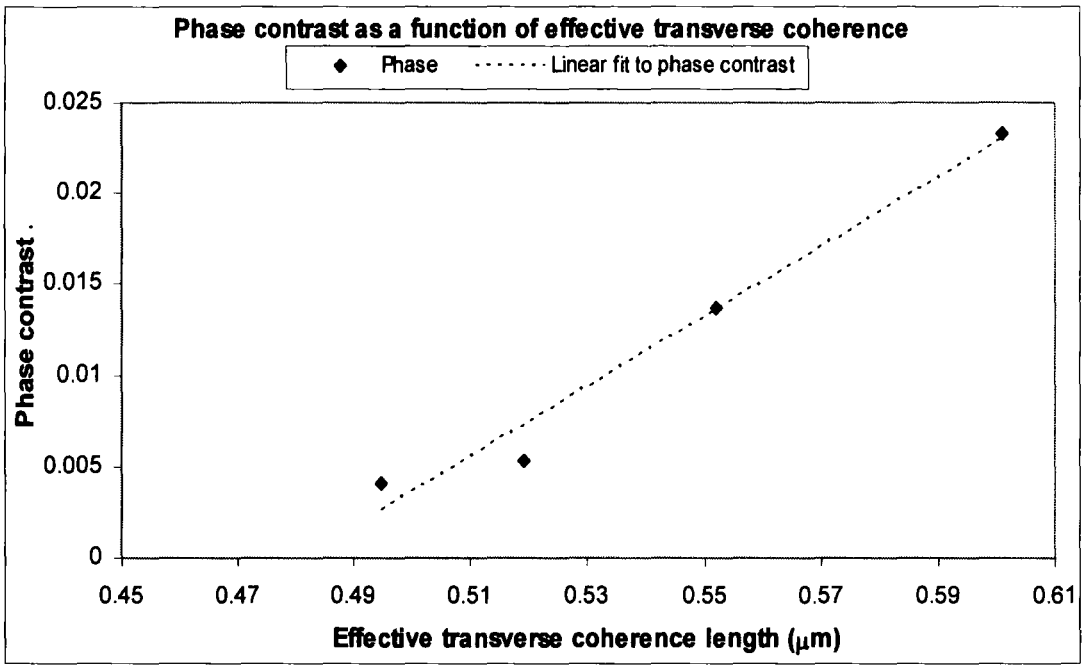

Figure 5.31: Phase contrast as a function of effective transverse coherence length for rhodium target

The phase contrast shows a linear, proportional relationship with the effective transverse coherence length of the system: this is confirmed by the strong, positive correlation coefficient of 0.96 between the two variables. Thus as the increasing glass thickness shifted the dominant X-ray energy range to higher energies (and hence the dominant wavelength to lower values), the consequent reduction in the effective transverse coherence length caused degradation of the phase contrast.

The copper results are also considered in the same way. The copper target phase and absorption contrast determined experimentally are shown in figure 5.32.

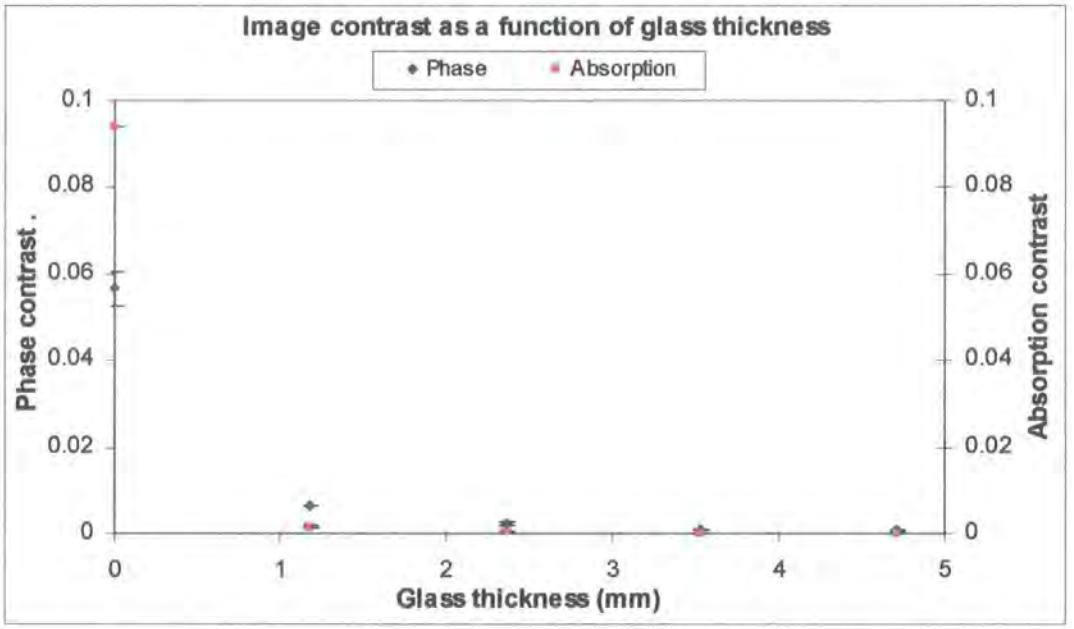

Figure 5.32: Change in phase and absorption contrast as glass thickness is increased (copper source)

The copper results show similar behaviour to the rhodium, although both the phase and absorption contrast fall off at a much faster rate. In fact, on addition of the third glass slide (an overall glass thickness of 3.534mm), the absorption contrast was so minimal that calculation of this was impossible and it was recorded as zero. Obviously this was also the case on addition of the fourth glass slide.

As before, we consider the filtered copper spectra and apply the same model as before to calculate the change in absorption contrast, the average wavelength and the effective transverse coherence length as the glass thickness is increased. The absorption contrast calculated by the model is plotted together with that achieved by the copper target during the glass experiment (shown earlier in figure 5.32). These are shown in figure 5.33.

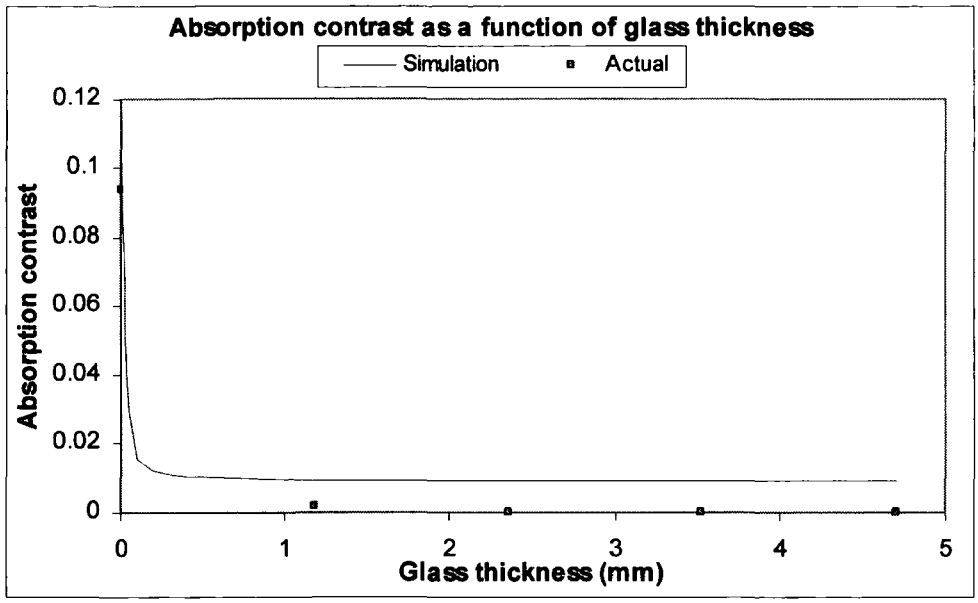

Figure 5.33: Theoretical and experimental change in absorption contrast with increasing glass thickness (copper source)

As figure 5.33 shows, the model of the beam hardening effect for the copper source shows a similar relationship to that between sample absorption contrast and glass thickness shown by the actual results. This fit is limited in that it cannot be compared to the absorption contrast with glass thicknesses of 3.354mm or 4.712mm due to the extensive loss of contrast in these images. But otherwise the shift of the dominant energy to higher values accounts for the loss in absorption contrast reasonably well.

The change in the average wavelength and effective transverse coherence with water path length is shown in figure 5.34.

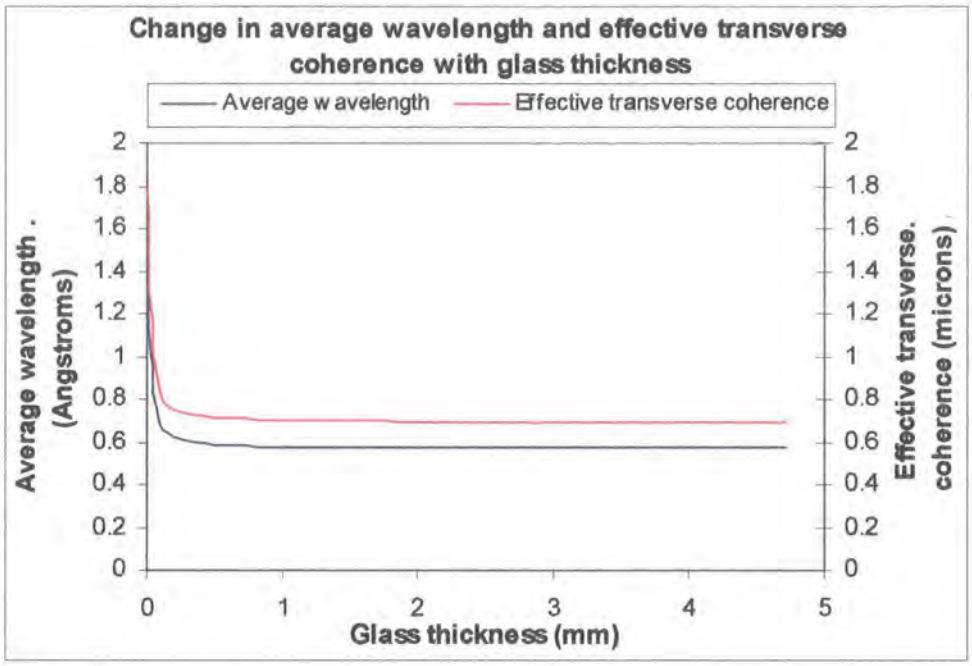

Figure 5.34: Change in average wavelength and effective transverse coherence length with increasing glass thickness (copper source)

The average wavelength and consequently the effective transverse coherence length, show a similar relationship with the glass thickness as the phase contrast in figure 5.32. The phase contrast of each image is plotted with the effective transverse coherence length in figure 5.35.

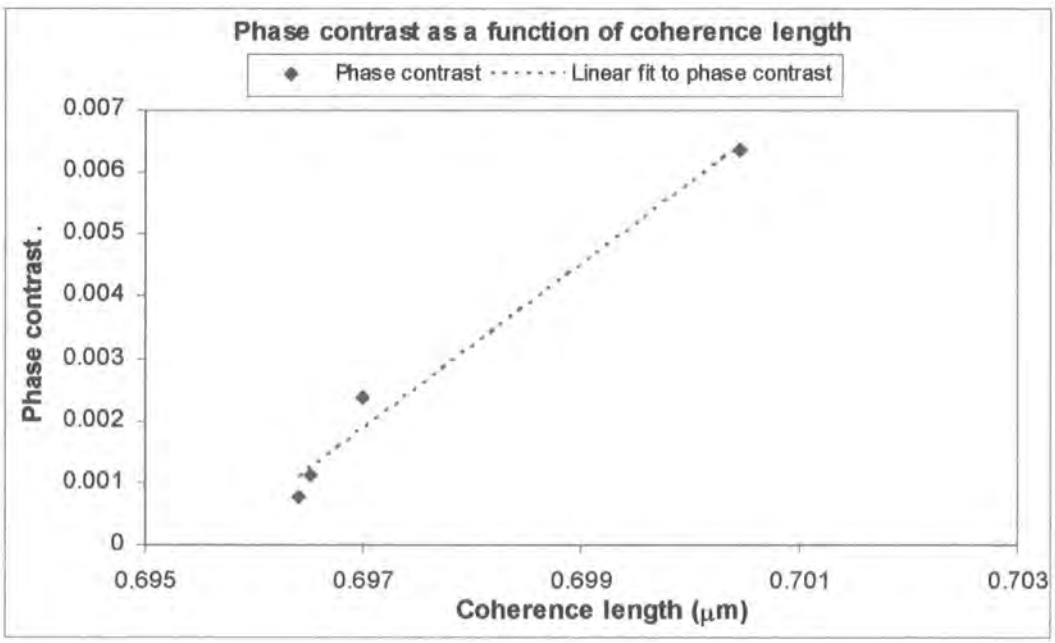

Figure 5.35: Phase contrast as a function of effective transverse coherence length for copper target

The phase contrast shows a linear relationship with the effective transverse coherence length of the system: this is confirmed by the strong, positive correlation coefficient of 0.99 between the two variables. Thus as the increasing glass thickness shifted the dominant X-ray energy range to higher energies (and hence the dominant wavelength to lower values), the consequent reduction in the effective transverse coherence length caused degradation of the phase contrast.

This work demonstrates that copper X-rays are completely unsuitable for imaging glass-mounted pathological specimens, because the presence of glass destroys the phase contrast. However the phase contrast is not destroyed for rhodium X-rays, and so glass-mounted samples could potentially be imaged by this system with the rhodium target in place, especially given the earlier results where the system achieved phase contrast with rhodium X-rays despite the presence of water.

It is unlikely that the beam hardening effect would be seen with monochromatic X-rays, and this is a major advantage of monochromatic synchrotron radiation over polychromatic laboratory-based X-ray sources. In order to combat the effects of beam hardening on phase contrast within a laboratory environment, a microfocus X-ray source capable of producing much higher intensities would be required. Monochromation of a significantly higher-intensity source would also provide a possible solution.

References

[1] Lewis R. A., *Phys. Med. Biol.* **49** pp.3573-3583 (2004)

[2] Kitchen M. J. et al, *Phys. Med. Biol.*, **49** pp.4335-4348 (2004)

[3] Han S. et al., *Rev. Sci. Instr.***75** (10) pp.3146-3151 (2004)

[4] Takeda T. et al., *Jap. J. Appl. Phys.*, **43** (9A) pp.L1144-L1146 (2004)

[5] *International Tables for X-ray crystallography Vol. III*, Kynoch Press (1974)

[6] Hecht, E., *Optics* (3rd Edn), Addison-Wesley pp.556 (1998)

[7] Webb S., *The Physics of Medical Imaging, Institute of Physics Publishing (1998)*

6. Phase contrast images of test objects

In order to determine the capability of the in-line laboratory-based set-up in a practical application of phase contrast imaging, the set-up was used to image two test objects: a Leeds Mammographic Test Object TOR[MAM] [1], and a scorpion sting.

A number of mammographic phantoms have been imaged (as discussed in Chapter 1), but the Leeds TOR[MAM] phantom has not been used in phase contrast imaging very often. Kotre et al. have imaged a Leeds TOR[MAM] phantom using an adapted mammography imaging system, with a molybdenum target in place [2,3], assigned scores to the images according to the level of detail present, and compared the scores for phase and absorption contrast images. In this project, the effects of sample position, source size, monochromaticity, sample thickness and the presence of water and glass on phase contrast have all been investigated. Having used this earlier work to gradually improve and gain a better understanding of the imaging system, phase contrast imaging of the test object is attempted in order to assess the capability of the improved system to image the phantom. Both rhodium and copper X-rays are used, and the suitability of the two X-ray energies is discussed. This work is important because it takes the initial steps towards potentially using this system for imaging of small pathological samples.

The final sample discussed in this project is the scorpion sting shown in Chapter 1. No phase contrast images of scorpion stings have been previously seen in published literature, so this is a real first for the field. An absorption image (taken at the beginning of the project) and a phase image (taken after the work discussed in Chapter 4 was completed) are compared in order to illustrate the improvements made to the system during the course of the project. This comparison visually sums up the scale of the improvement in the imaging system as a result of this work, and although this is done qualitatively, it is important to be able to see a 'before' and 'after' glimpse with a project like this.

6.1 The Leeds TOR(MAM) Phantom

The TOR[MAM] phantom has been designed at the University of Leeds to produce qualitative results via contrast details which closely approximate actual clinical mammographic features. It is thought to be the most sensitive of the mammographic test objects generally available in the UK [4].It consists of a semicircular Perspex block of 11mm thickness, within which a number of details are embedded. A detailed layout of the TOR[MAM] phantom is shown in figure 6.1.

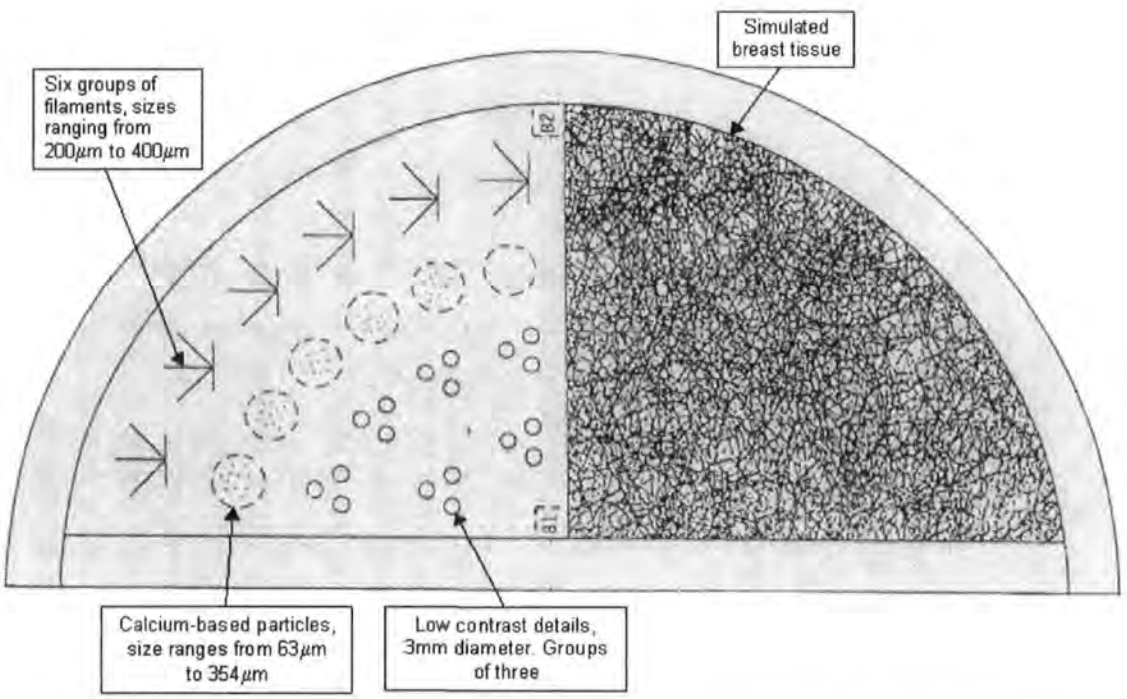

Figure 6.1: Layout of details within the Leeds TOR[MAM] Phantom (reproduced from [1])

The test details shown on the left-hand side of the diagram in figure 6.1 include three types of detail: filaments, calcium-based particles and low-contrast discs.

The filaments are arranged in six groups of four: each group has the four identical filaments arranged in four different orientations. It has already been seen that the contrast achieved for a vertical detail is not necessarily the same as that achieved for a horizontal detail, due to the variation in transverse coherence length of an elliptical beam. This arrangement allows the phase contrast imaging capability in four different

orientations to be determined. All filaments are 10mm in length, and the diameters gradually decrease from the bottom-left group (400μm) to the top-right group (200μm).

The central group of particles represent microcalcifications. These are made from a calcium-based mineral substance and all have irregular shapes. Each test group comprises a number of these particles in order to simulate a cluster of microcalcifications. The clusters each contain a range of particle sizes, starting at the bottom-left (with upper and lower limits of 354μm and 224μm respectively) and decreasing towards the top-right (with upper and lower limits of 106μm and 63μm respectively).

The bottom group of low-contrast details are 3mm diameter circular discs, made from plastic. Six thicknesses of plastic are used, providing six different contrast values in the phase contrast images. These low-contrast details approximate to mean detail sizes of 2mm to 5mm, as recommended by Kimme-Smith [5].

The detail on the right-hand side of the diagram in figure 6.1 represents breast tissue morphology. It simulates the appearance of breast tissue, although it is not claimed that the breast tissue morphology section is equivalent to breast tissue in an anatomical or radiological sense [1,6]. Rather, it determines the noise effects seen by the imaging system when imaging breast tissue, and helps to determine the overall image quality achievable by the imaging system.

The two small sections, marked B1 and B2 on the diagram in figure 6.1, are for background density measurement, to allow for comparison between films. This feature is not used in these experiments because the images are taken for a purely qualitative analysis.

The TOR[MAM] test object shown in figure 6.1 may be used in conjunction with three more D-shaped Perspex blocks, each 10mm in diameter. The total thickness of the object in this case is 41mm, and the additional sections help to simulate base attenuation

and scattering effects. Because this is a preliminary investigation into the set-up's capability of imaging the details embedded within the test object, the additional sections of the phantom were not used.

6.1.1 Evaluation of contrast detail images

Images of the detailed section of the mammographic test object were taken with the rhodium and copper targets in place in turn in order to determine the practical capability of the system with each target. Following the work with source size, discussed in chapter 4, the source dimensions were kept to a minimum (19μm width x 18μm height in the case of the rhodium target, 12μm width x 17μm height in the case of copper). We have seen that the polychromatic spectrum of both sources yields satisfactory phase contrast images and so no attempts were made to filter the X-rays. The detailed section of the test object required only a qualitative analysis, so X-ray film was used to record the images. The system was set up as shown in figure 6.2.

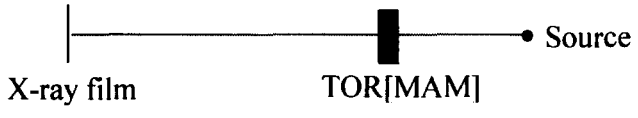

Figure 6.2: Set-up for low-contrast detail imaging

The test object was fixed 128mm from the source, and the X-ray film was fixed 684mm from the test object. We have seen that with a propagation distance greater than approximately 78mm, the system retains phase contrast in the images, and the greater the propagation distance, the better the phase contrast. A sample-detector distance of 684mm is approaching the maximum propagation distance possible within the confines of the system's enclosure, so this should give the system the best chance of retaining good phase contrast images in terms of propagation of the transmitted X-rays.

Each of the groups of filaments was imaged separately, in turn, as described above. The images on film were magnified by a microscope and acquired directly to a computer using a visible light CCD. The images obtained using the rhodium target are shown in figure 6.3, and those obtained using the copper target are shown in figure 6.4. Due to the

limited field of view of the CCD, only the junction at which each group of filaments meets is recorded in order to show the filaments in all orientations within the same image.

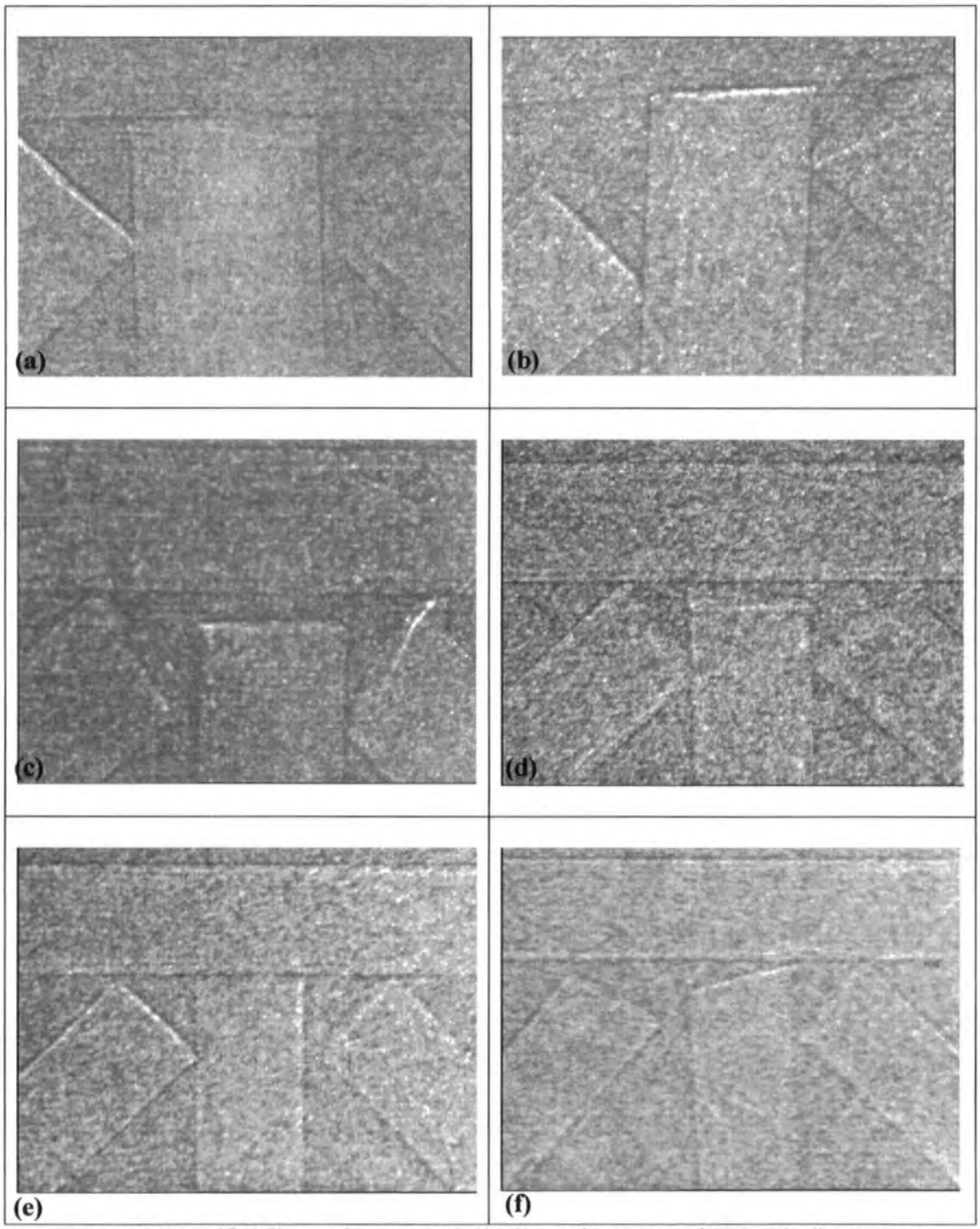

Figure 6.3: Magnified filament images acquired using a microscope and CCD (Rhodium source) Filament size: (a) 400μm, (b) 350μm, (c) 300μm, (d) 250μm (e) 225μm, (f) 200μm

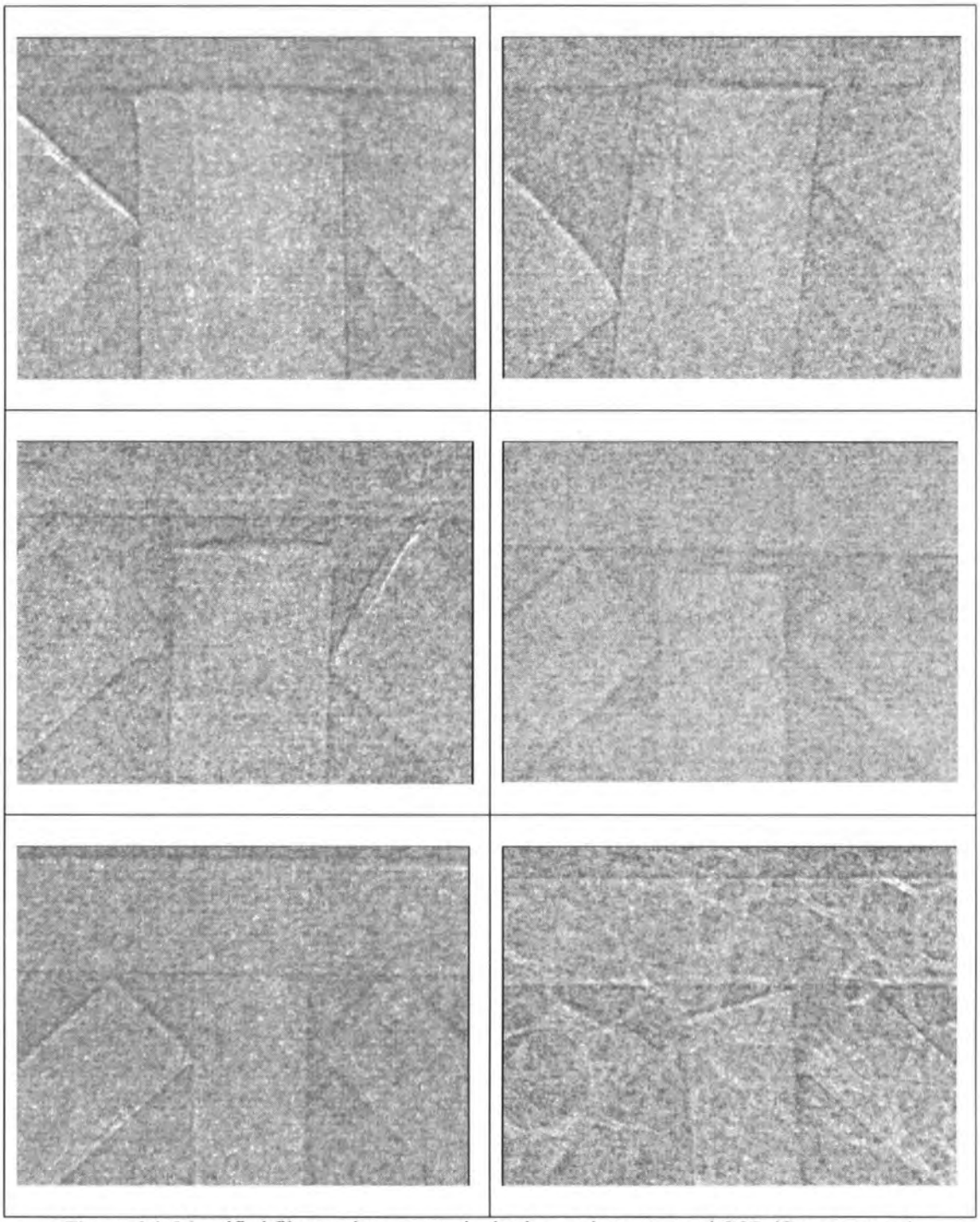

Figure 6.4: Magnified filament images acquired using a microscope and CCD (Copper source)
Filament size: (a) 400μm, (b) 350μm, (c) 300μm, (d) 250μm (e) 225μm, (f) 200μm

As figures 6.3 and 6.4 show, with both the rhodium and copper targets in place the system is capable of imaging all six groups of filaments, and so has the ability to record this type of detail at least down to 200μm in size. As expected, the strength of the phase contrast at the edges of the filaments varies within each group: it was concluded in chapter 4's discussion of the results of the source size experiment that the orientation of a sample edge is important when making use of an elliptical source. The phase contrast of an image of a given sample edge is affected more by the transverse coherence in the direction perpendicular to the orientation of the sample edge. However, the edge details in all orientations are visible here, and most show the distinctive phase contrast fringe, which is an excellent result.

An example of an intensity profile across an image of a filament is shown in figure 6.5. This is taken across the rhodium image of a filament in group D, and so it represents a filament of 250μm diameter.

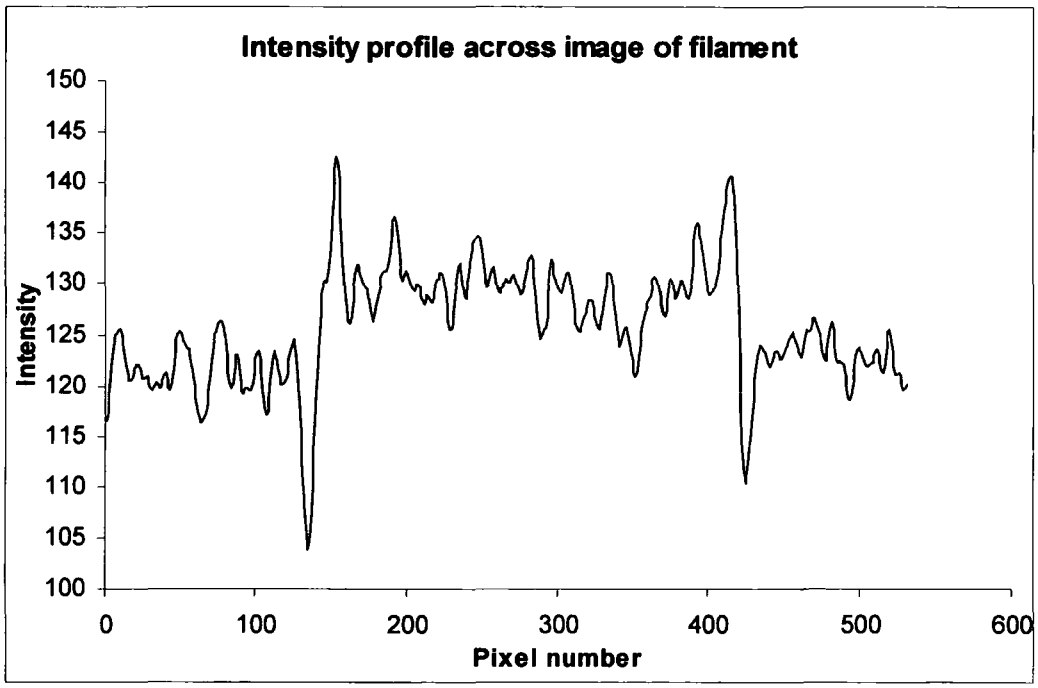

Figure 6.5: Intensity profile across rhodium image of a filament in group D

The intensity profile in figure 6.5 shows some slight absorption contrast, due to the 250μm thickness of the filament. The main points of interest are the large peak and

trough at each edge of the filament: these verify that the phase has been enhanced, as seen in all earlier experiments using the Heaviside function sample. Therefore strong phase contrast is present in the filament images.

The experiment was repeated with an identical set-up in order to obtain images of some of the pseudo-microcalcifications. Here, just one group of pseudo-microcalcifications was imaged: that containing particles ranging in size from 224μm to 354μm. Again, the images on film were magnified by a microscope and recorded by a CCD camera. Due to the limited field of view of the CCD, the group as a whole is not shown, but a number of individual particles within the group are recorded. The pseudo-microcalcification images obtained using the rhodium target are shown in figure 6.6.

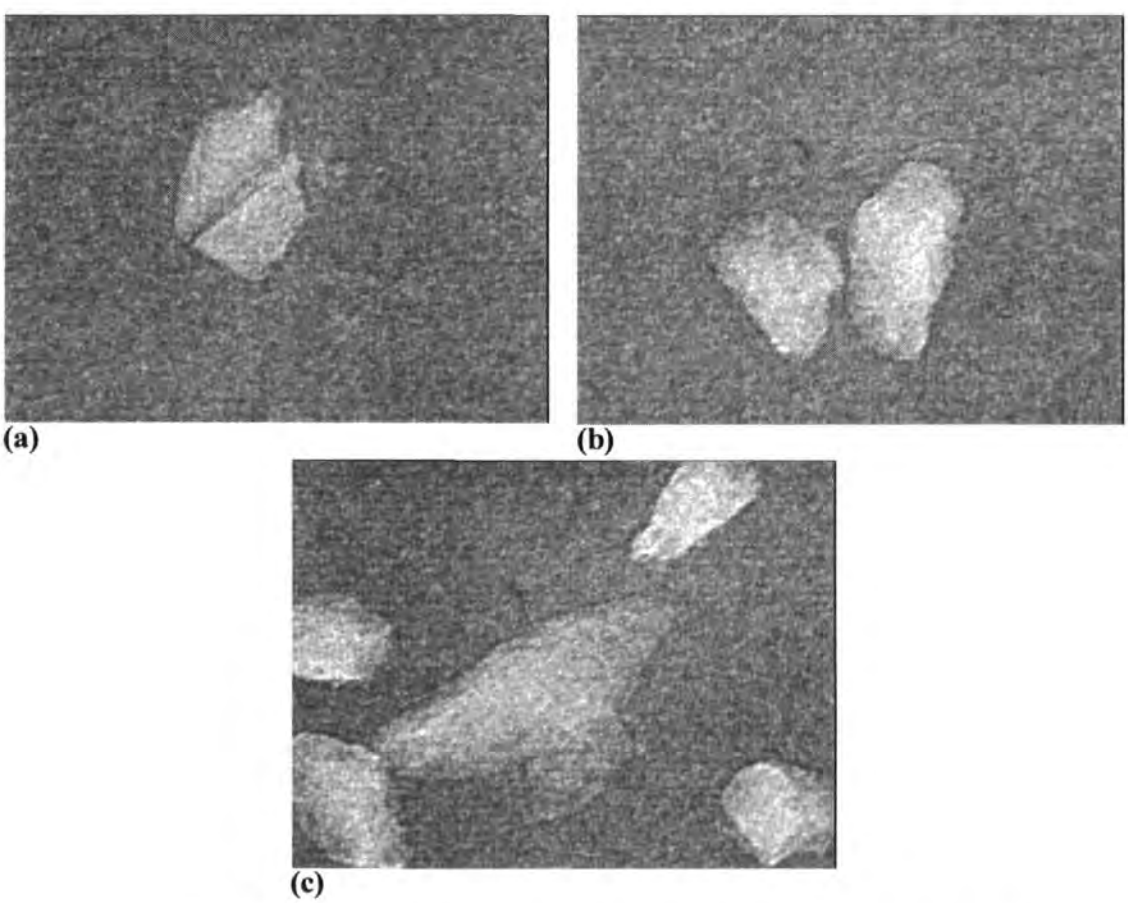

Figure 6.6: Magnified pseudo-microcalcification images acquired using a microscope and CCD (Rhodium source)

The same group of pseudo-microcalcification particles was imaged in the same way using the copper target and the images obtained are shown in figure 6.7.

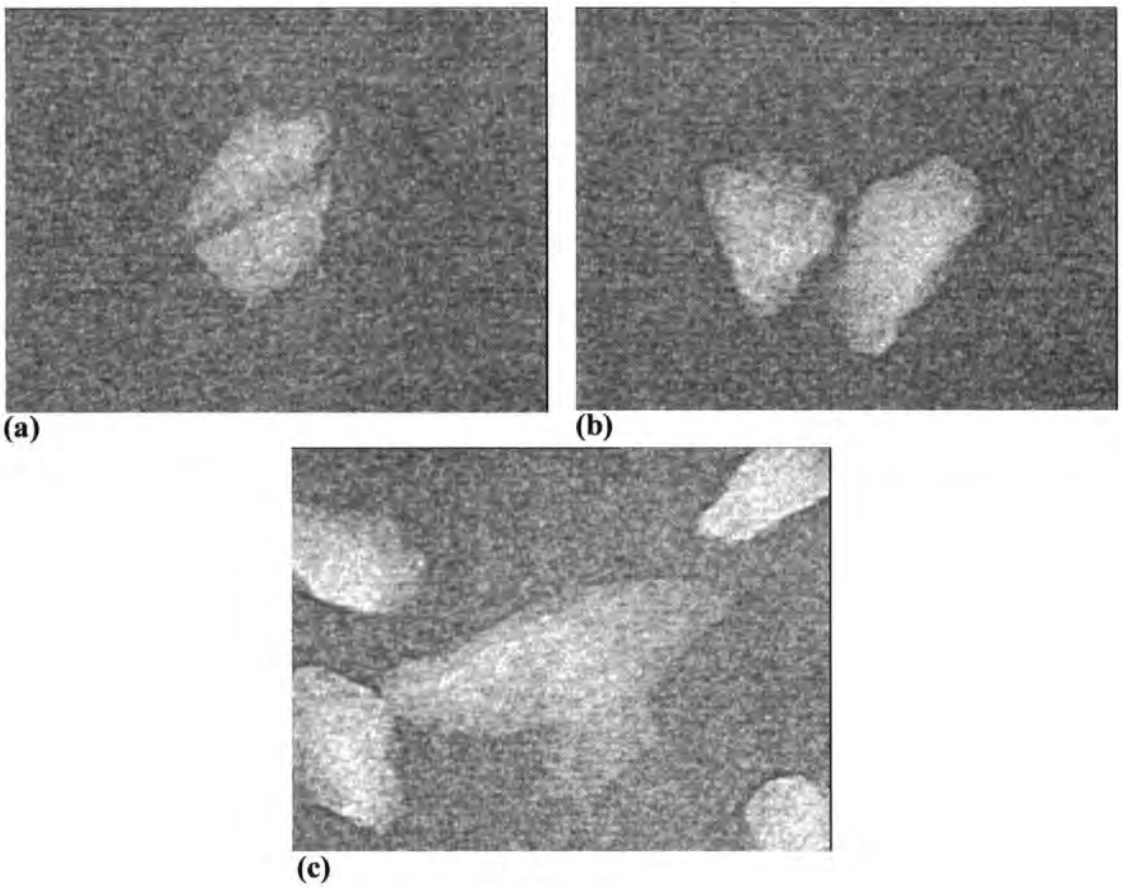

Figure 6.7: Magnified pseudo-microcalcification images acquired using a microscope and CCD (Copper source)

As figures 6.6 and 6.7 show, with both copper and rhodium targets in place the system is capable of imaging the pseudo-microcalcifications. These appear as areas of higher absorption surrounded by edge contrast, although again, the irregular shapes agree with earlier conclusions that the phase contrast varies with the orientation of the edge in question. The results obtained using both the rhodium and copper targets are very clear, however the rhodium results are seen to have slightly more well-defined edge contrast than the copper. This is illustrated by taking intensity profiles across rhodium and copper images of the same section of a given particle. The particle used here is that shown in figures 6.6 (a) and 6.7 (a). The intensity profiles are shown in figure 6.8.

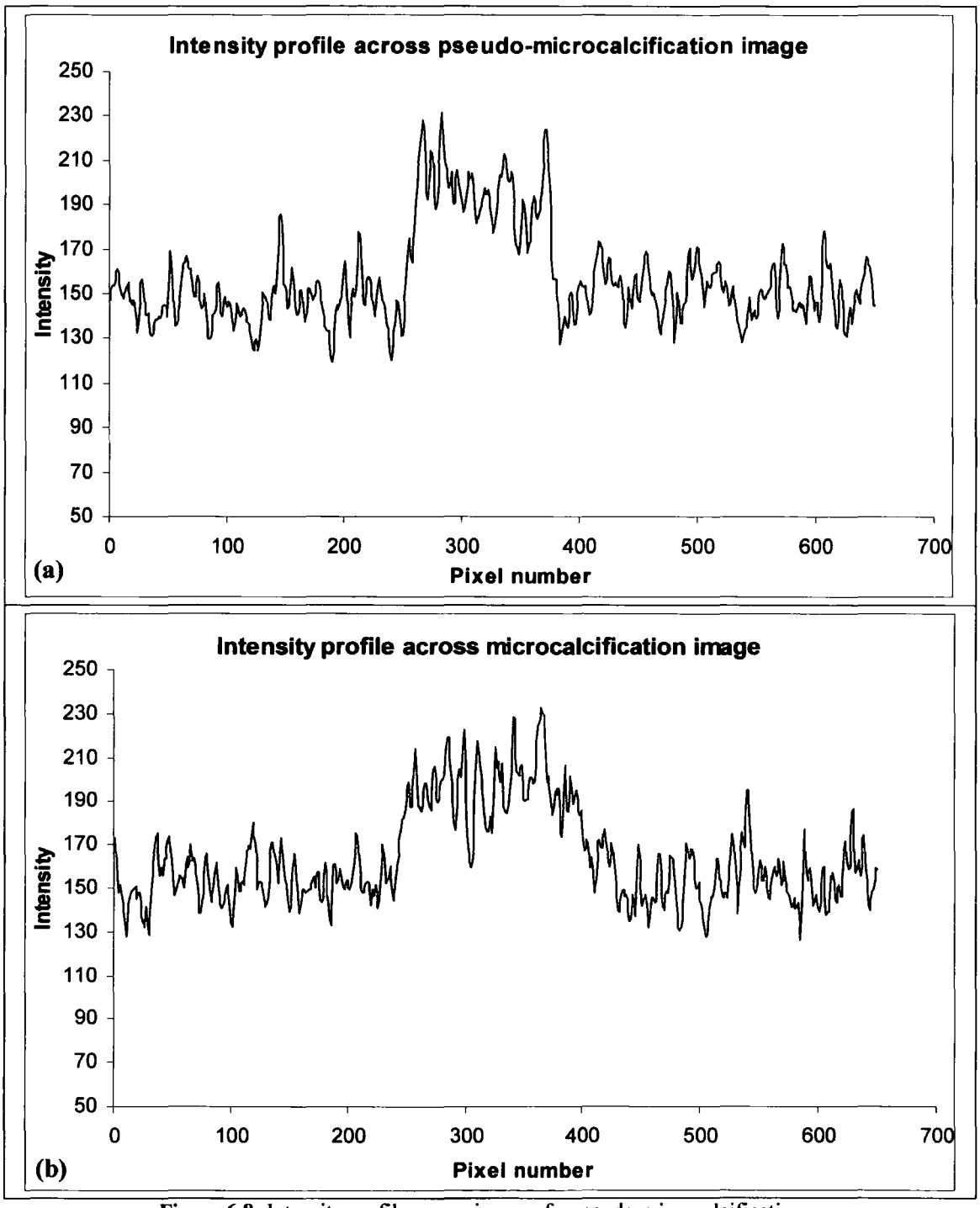

Figure 6.8: Intensity profile across image of a pseudo-microcalcification.
(a) Rhodium image, (b) Copper image

From figure 6.8 it is easily seen that the edge contrast is far more marked in the rhodium image than the copper image, because the peak and trough are very clear at the edges of

the particle. Although phase contrast is seen at the edges of the particle in the copper image, the noise within the particle area of the image is of a comparable level. Thus the images of the pseudo-microcalcifications taken with the rhodium target in place are more helpful.

The experiment was repeated again with an identical set-up in order to obtain images of some of the low-contrast discs. Again, the images on film were magnified by a microscope and recorded by a CCD. Due to the limited field of view of the CCD, only partial images of the low-contrast discs are recorded. The low-contrast disc images obtained using the rhodium target are shown in figure 6.9, and those obtained using the copper target are shown in figure 6.10. It should be noted, however, that the edges shown in figures 6.9 and 6.10 do not necessarily belong to the same discs.

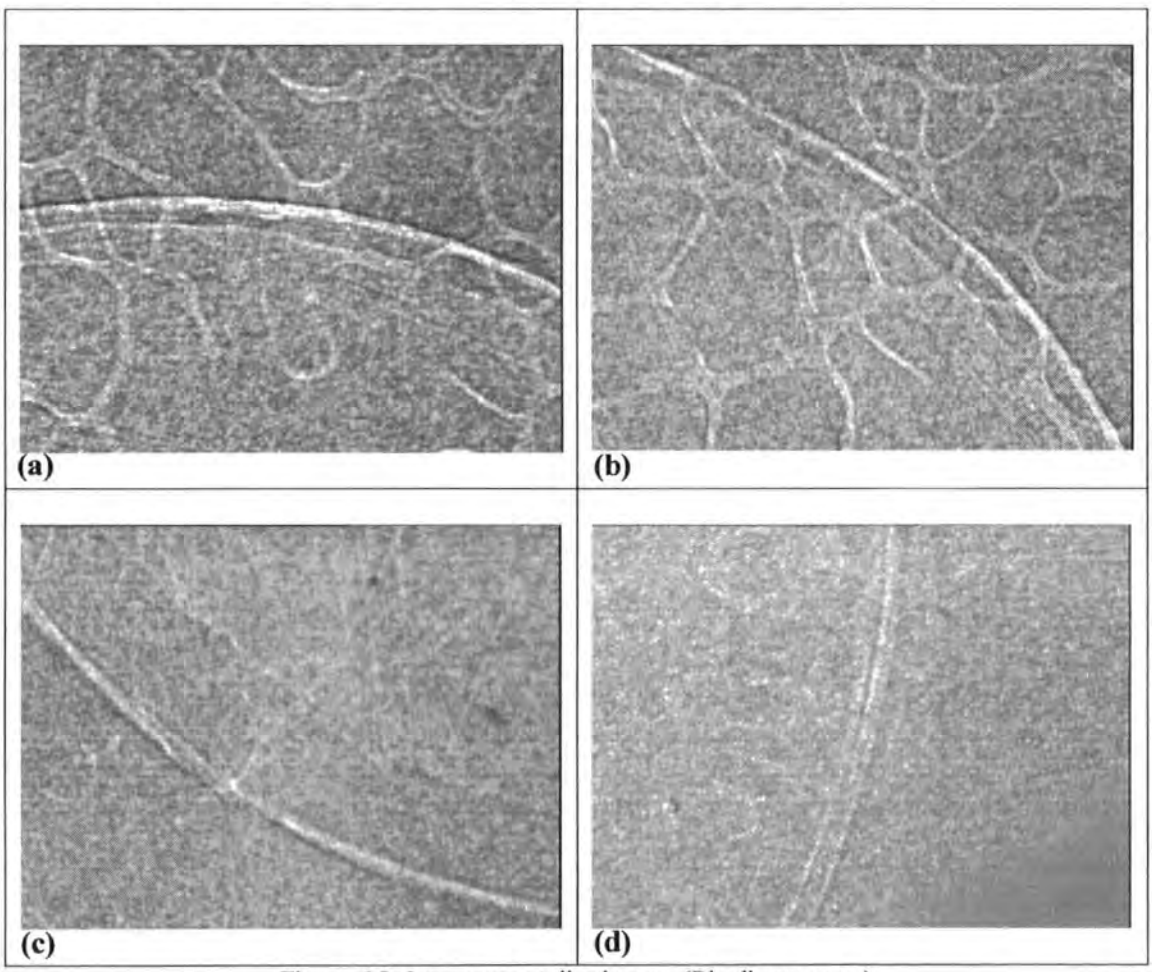

Figure 6.9: Low-contrast disc images (Rhodium source)

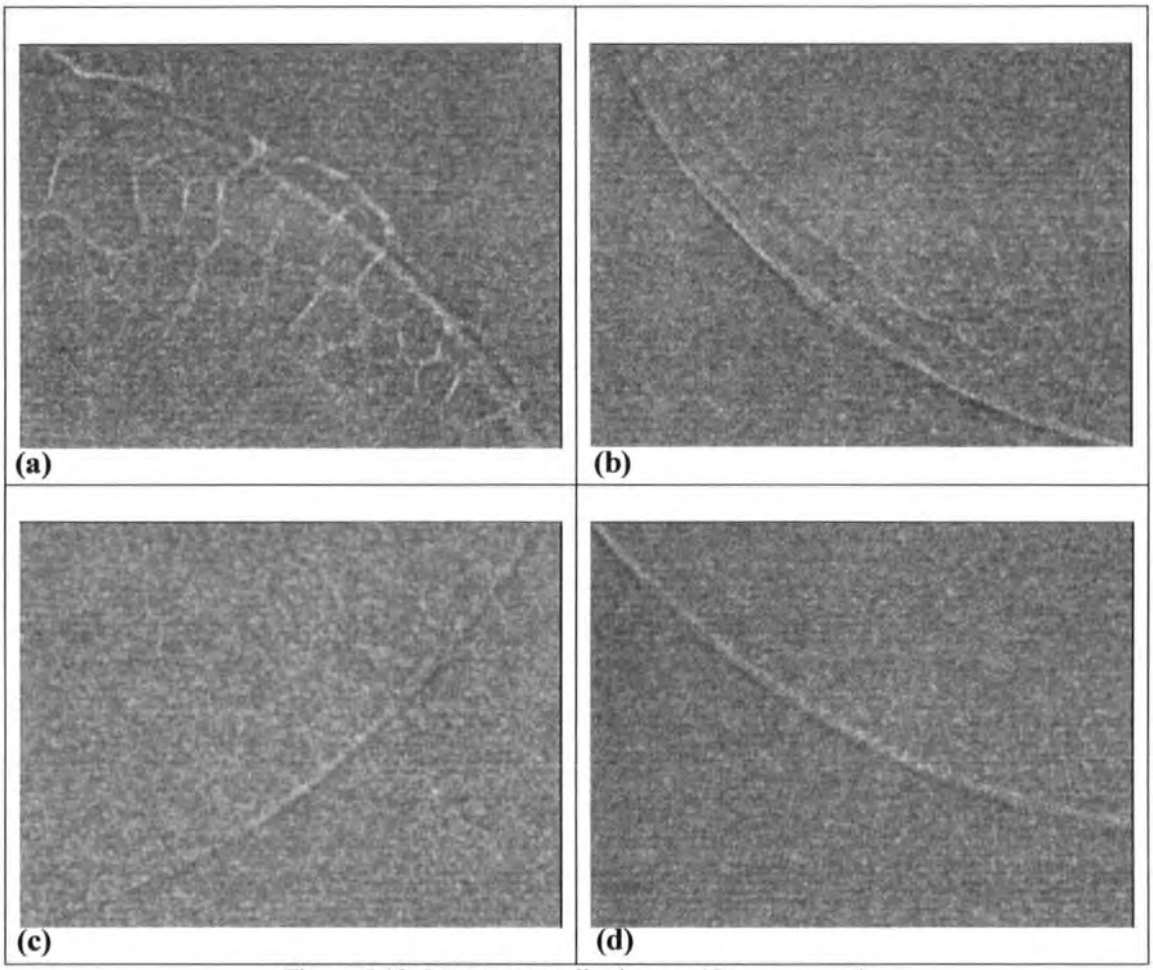

Figure 6.10: Low-contrast disc images (Copper source)

It is seen from figures 6.9 and 6.10 that with both the copper and rhodium targets in place the system is capable of imaging low-contrast circular details with various contrast values. In fact these are seen to be ideal phase objects because the edge contrast shows the dark and light lines representing the peak and trough in intensity, as seen earlier in the project, while the absorption contrast is negligible. This is shown via intensity profiles across a rhodium image and a copper image in figure 6.11.

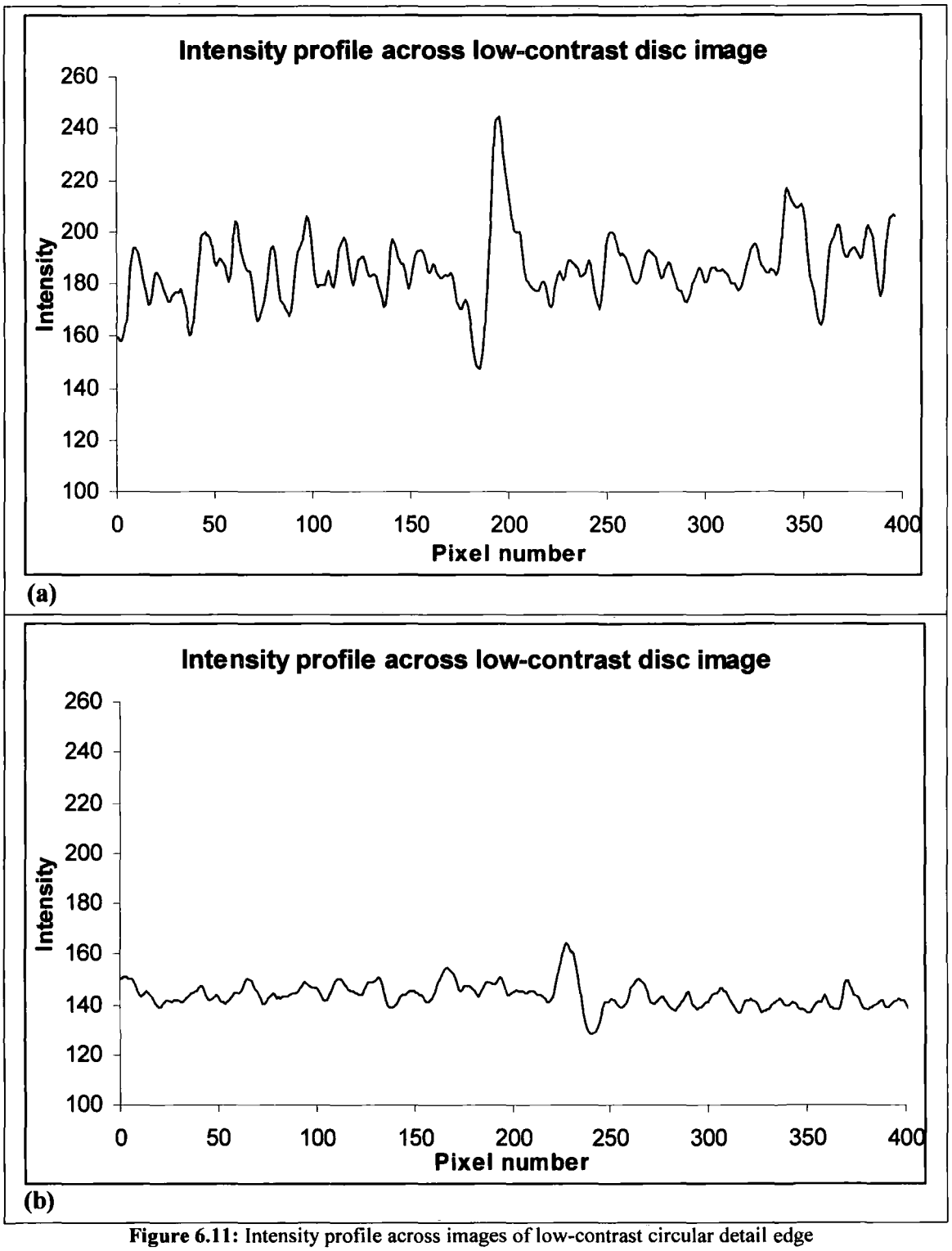

Figure 6.11: Intensity profile across images of low-contrast circular detail edge
(a) Rhodium image, (b) Copper image

The phase contrast in the images obtained using the rhodium target is very clear in all of the images, although it is seen to be reduced in image 6.9 (d), which is of one of the lowest contrast discs. The additional detail seen in images 6.9 (a) and (b) shows the adhesive holding the perspex of the test object together at the contrast detail level. The phase contrast in the images obtained using the copper target is also clear in all of the images, although it is not as highly visible as that in the majority of rhodium images. Image 6.10 (a) is also seen to show some adhesive detail.

It is possible to grade images of the test object detail section as a measure of the visibility of the image details, as described in [2]. This requires all of the test object details to be recorded in one large image. Due to the small size of the X-ray beam and the large magnification required of the system, this was impractical for this set-up. However, the in-line phase contrast imaging set-up has shown itself to be capable of qualitatively imaging practical details such as those embedded in a mammographic test object. This is a positive result towards the practical application of the system.

6.1.2 Breast tissue morphology results

The breast tissue morphology section of the test object was imaged using both the rhodium and copper targets with the source. Two experiments were done using this section: one to see the capability of the system when imaging the breast tissue morphology section, and the other to determine the attenuation effect of the breast tissue morphology section.

6.1.2.1 Images of breast tissue morphology

Images were taken of the breast tissue morphology section of the Leeds mammographic test object, using both the rhodium and copper targets with the source. The experimental set-up is shown in figure 6.12.

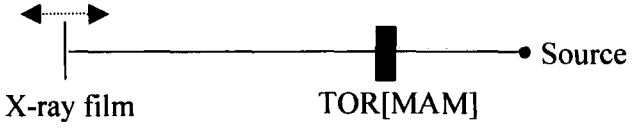

Figure 6.12: Set-up for breast tissue morphology imaging

As before, the mammographic test object was placed 128 mm from the source, with the breast tissue morphology section in the path of the X-rays. With the rhodium target in place, images were recorded on four X-ray films: with the film fixed 684mm from the test object, 382mm from the test object, 182mm from the test object and finally fixed at 0mm from the test object. Given that it has already been determined that the system cannot detect phase contrast with propagation distances of 78mm or less (as discussed in chapter 4), it would be expected that there will be no phase contrast present in the latter image. Of the remaining images, it would be expected that the 684mm image will retain the most phase contrast information and the 182mm image will retain the least phase contrast detail. This was repeated with identical source-sample and propagation distances with the copper target in place. The images recorded on X-ray film were viewed using a transmission microscope, and the magnified images were acquired directly to a computer using a visible light CCD camera. The images of the breast tissue morphology achieved using the rhodium source are shown in figure 6.13.

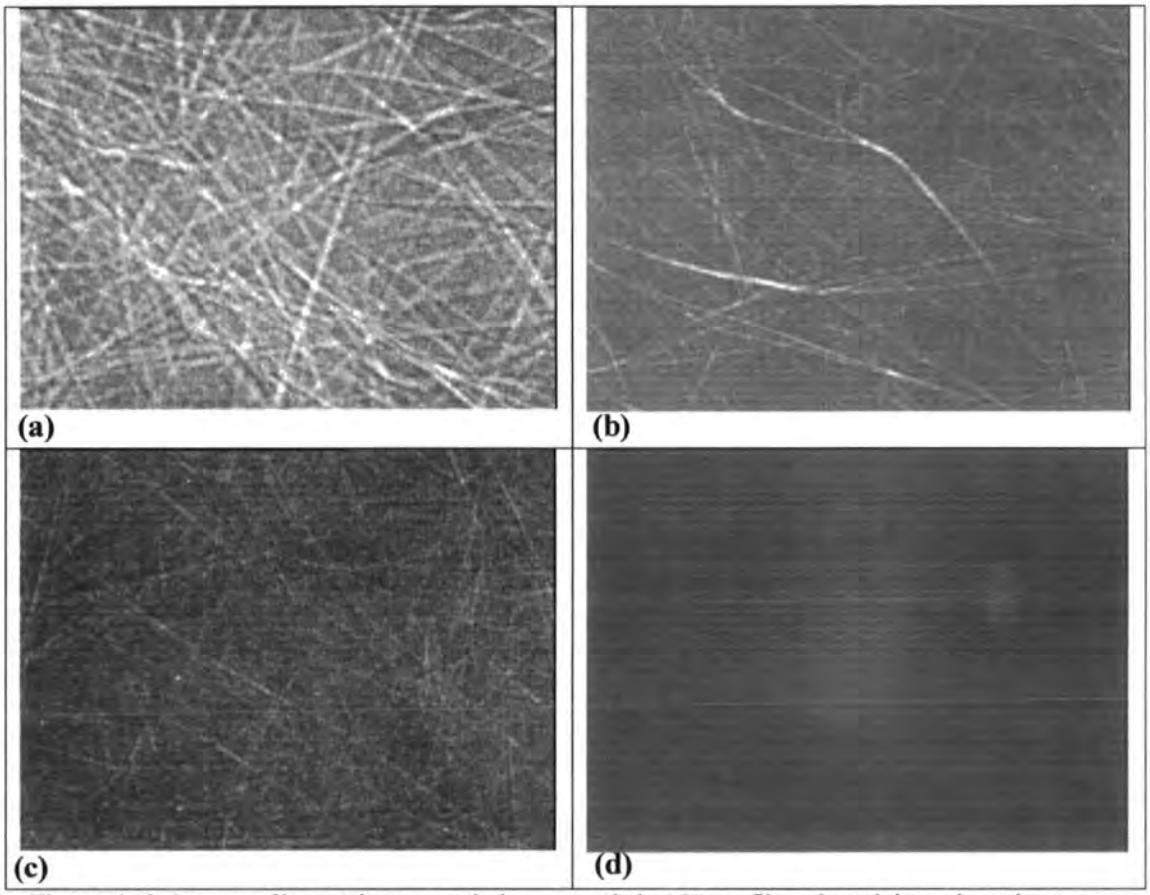

Figure 6.13: Images of breast tissue morphology recorded on X-ray film, viewed through a microscope. Film fixed at (a) 684mm, (b) 382mm, (c) 182mm and (d) 0mm from mammographic test object (Rhodium source)

The images in figure 6.13 show qualitatively how the phase contrast of the breast tissue morphology changes as the propagation distance is reduced. As expected, the breast tissue morphology detail retained in the image with the longest X-ray beam propagation distance of 684mm (figure 6.13 (a)) is excellent. The characteristic light and dark lines of phase contrast display many strands of the material. As the film is moved closer to the test object and the X-ray beam propagation distance decreases to 382mm and 182mm (figures 6.13 (b) & (c)), the phase contrast effect is less obvious and fewer strands of material show up well in the images. Finally the image taken at 0mm (figure 6.13 (d)) shows up no strands of material. In addition to relying only on the absorption property of the strands and not on the phase property, this image will have been affected by Compton scattering because of the lack of an air gap between the sample and the

film. Compton scattered photons will have been unable to propagate out of the X-ray film's field of view before reaching the image plane, leading to random photons being recorded in areas of the image which will not necessarily bear any relation to the true absorption image and distorting the image with the 'veil' effect. We have already seen a more quantitative effect of Compton scattering in Chapter 5, as a water container was placed directly in front of the detector and the phase contrast was significantly reduced as a result.

The images of the breast tissue morphology achieved using the copper source are shown in figure 6.14.

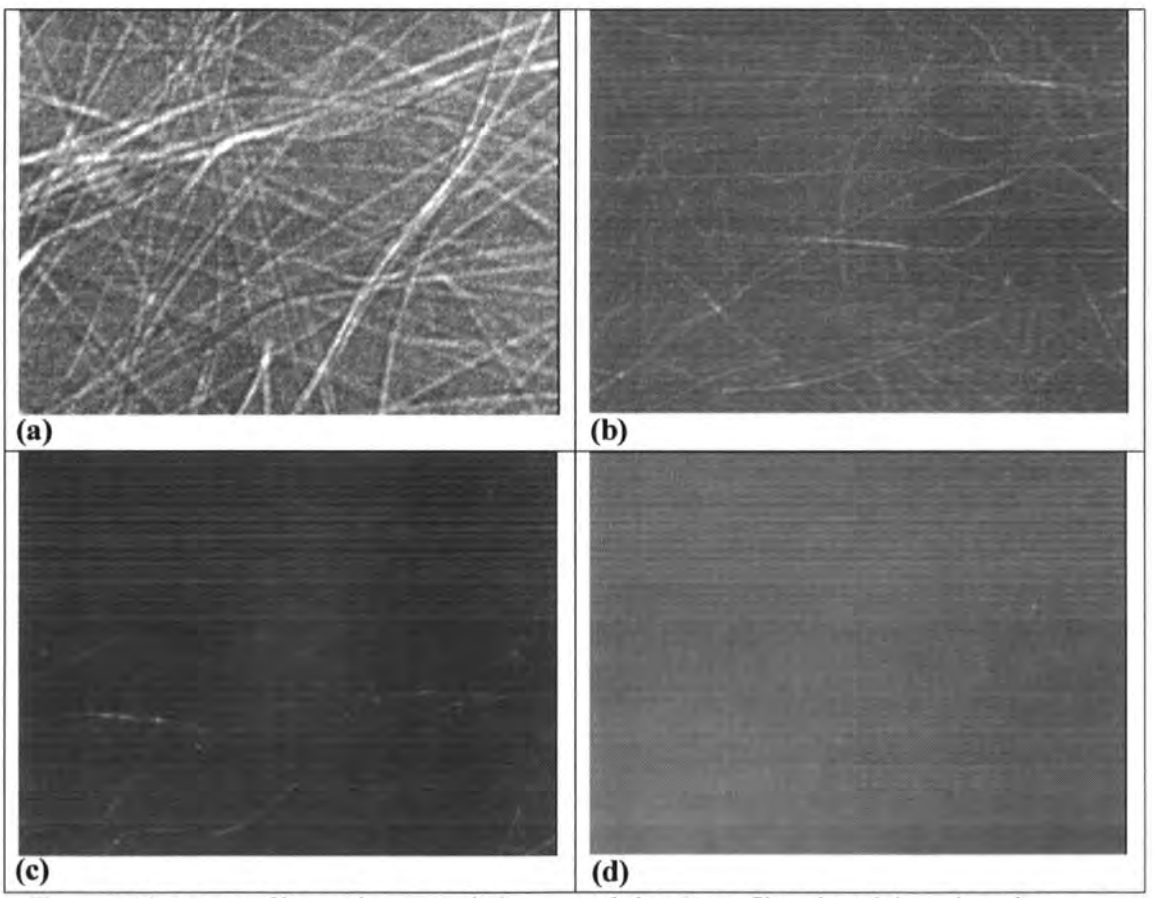

Figure 6.14: Images of breast tissue morphology recorded on X-ray film, viewed through a microscope. Film fixed at (a) 684mm, (b) 382mm, (c) 182mm and (d) 0mm from mammographic test object (Copper source)

The images in figure 6.14 show a very similar pattern to those in figure 6.13. The breast tissue morphology detail retained in the image with the longest X-ray beam propagation distance of 684mm (figure 6.14 (a)) is excellent while the phase contrast detail in the images taken at propagation distances of 382mm and 182mm (figures 6.14 (b) & (c)), becomes more difficult to see. Finally the image taken at 0mm (figure 6.14 (d)) shows up no useful detail. Again, this absorption image will have been affected by Compton scattering due to the lack of an air gap, and may not necessarily represent the true absorption image.

Comparison of figure 6.13 (a) and 6.14 (a) to figures 6.13 (c) & (d) and 6.14 (c) & (d) respectively really shows up the advantage of phase contrast imaging over absorption imaging. While the phase contrast image is rich in detail and shows some semblance of depth in the test object, the images with short or nonexistent propagation distances are not particularly helpful. The phase contrast images retain far more detail than the absorption images and are certainly the more useful of the two image types in this situation.

6.1.2.2 Attenuation effect of breast tissue morphology

The breast tissue morphology section of the Leeds mammographic test object is designed to simulate the noise contribution of breast tissue, rather than to provide an anatomically accurate representation of breast tissue. Thus it is useful to investigate the attenuation and noise effect of this breast tissue morphology on phase contrast images. In order to do this, the breast tissue morphology section of the test object was placed in the path of the X-ray beam, as shown in figure 6.15.

Figure 6.15: Set-up of attenuation experiment

The X-ray CCD camera was used to detect the images in this experiment because some quantitative analysis of the image intensity profiles was required. Images were taken of

several mylar Heaviside function samples with different 'step' thicknesses, both with and without the test object in the path of the X-rays. For each object the intensity profile of the attenuated image was compared to that of the corresponding non-attenuated image for each sample.

The sample 'step' thicknesses used with the rhodium source were the following: 929μm, 792μm, 584μm and 269μm. The phase contrast of the attenuated and non-attenuated images was calculated as described in chapter 3, and these results are plotted in figure 6.16.

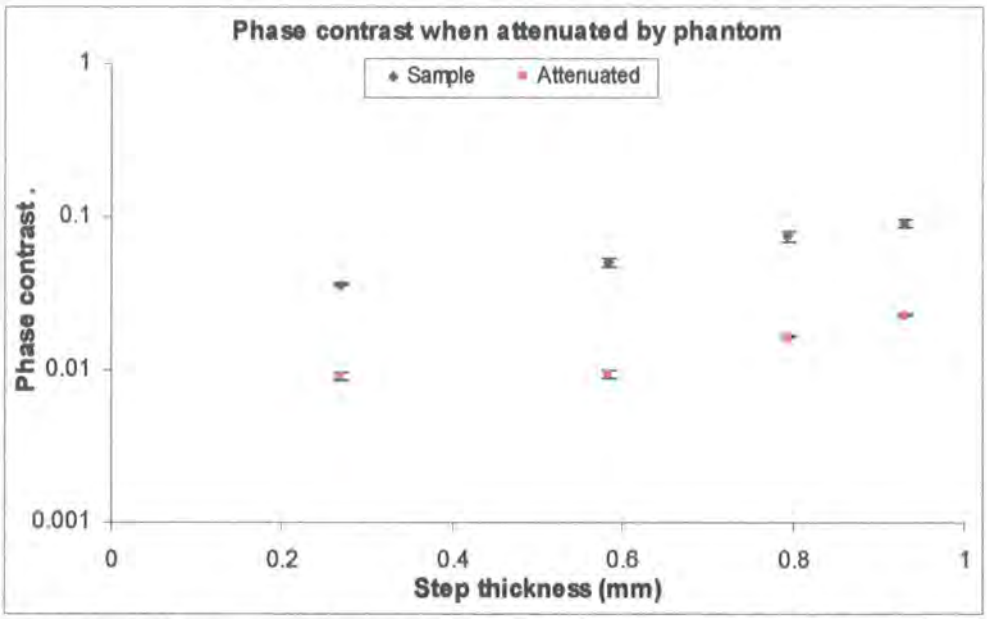

Figure 6.16: Phase contrast of attenuated and non-attenuated images plotted as a function of 'step' thickness (Rhodium target)

From figure 6.16 it is seen that the phase contrast increases with 'step' thickness as seen in chapter 4, whether attenuated by the phantom or not. However, when each sample is attenuated by the phantom, the phase contrast is seen to fall by a fairly constant factor of approximately 4 - 5, which is a significant loss of information.

The intensity profile comparisons for the resulting images are also compared visually. These are shown in figure 6.17.

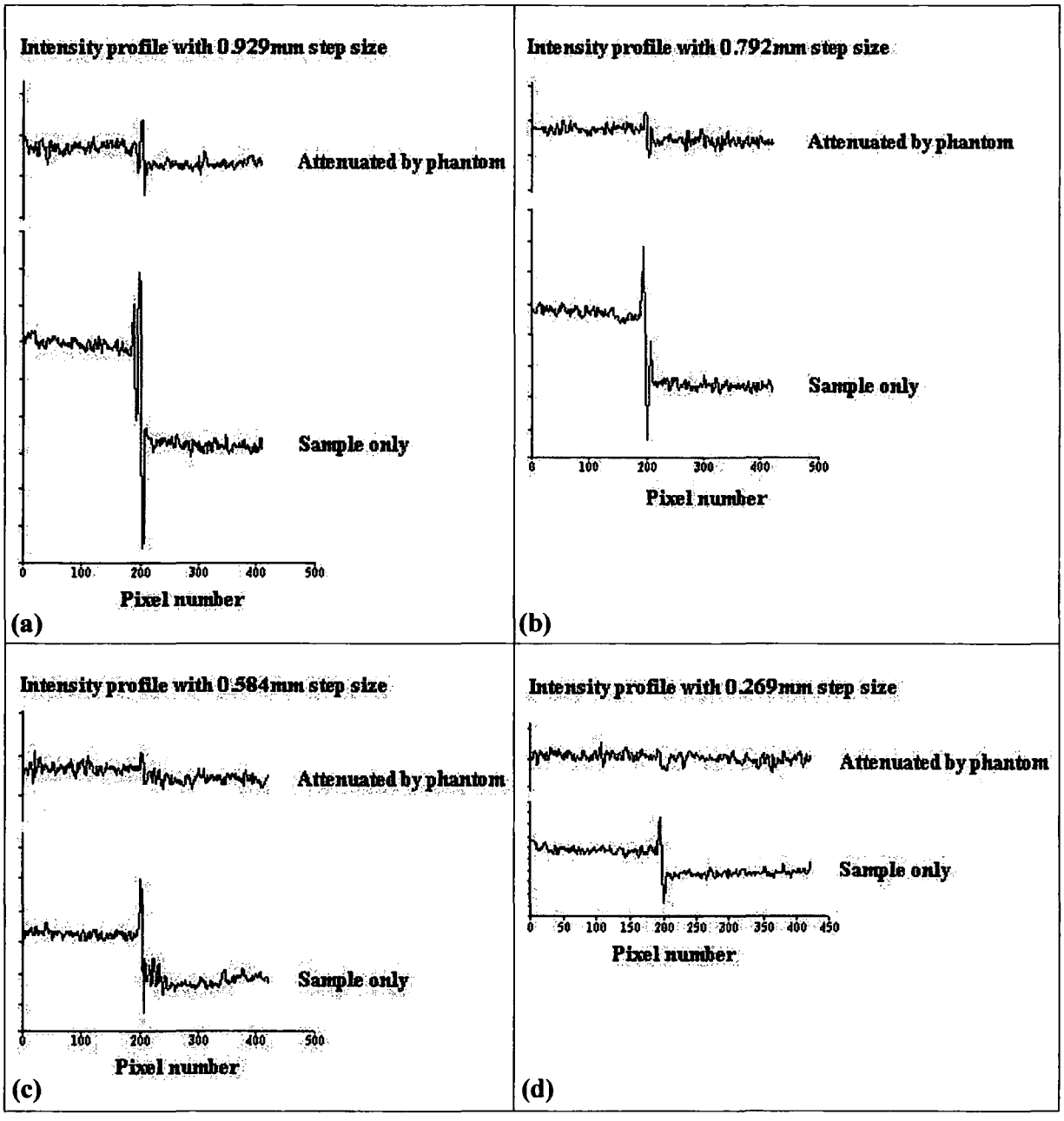

Figure 6.17: Comparison of intensity profiles with and without test object in X-ray path for 'step' thicknesses: (a) 929μm, (b) 792μm, (c) 584μm and (d) 269μm. (Rhodium target)

It is seen in figure 6.17 that the presence of the simulated breast tissue has a significant, detrimental effect on the phase contrast achieved by the imaging set-up. Good phase contrast is clearly visible for all non-attenuated Heaviside samples, as expected. The attenuated samples with 'step' thicknesses of 929μm and 792μm are clearly visible,

although with the phase and absorption contrast very much reduced. The attenuated sample with 584μm 'step' also shows some visible phase contrast over the appropriate pixel range, although the absorption contrast is difficult to discern. This is the same effect as that seen in Chapter 5 when the introduction of other materials (specifically water and glass) caused the X-ray beam to harden. The breast tissue morphology also causes the X-ray beam to shift to higher energies, reducing both the phase and absorption contrast. The attenuated images also show more significant image noise, which is caused by the breast tissue morphology and which is detrimental to the quantifiable phase contrast. The phase contrast of the attenuated sample with 269μm 'step' is comparable to the image noise, despite the use of a thick line profile to minimise this effect. Thus with the rhodium target in place, a practical limit on anomaly size detectable by the system is set at around 500μm.

The experiment was repeated with the copper source using the same 929μm, 792μm, 584μm samples, and a 428μm sample. The phase contrast of the attenuated and non-attenuated images was calculated as described in Chapter 3, and these results are plotted in figure 6.18.

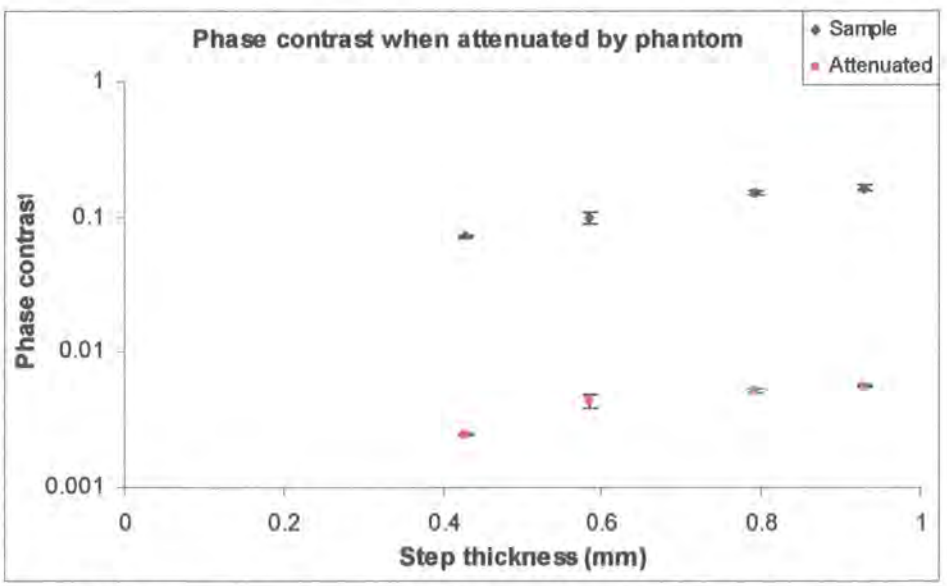

Figure 6.18: Phase contrast of attenuated and non-attenuated images plotted as a function of 'step' thickness (Copper target)

From figure 6.18 it is seen again that the phase contrast increases with 'step' thickness as seen in Chapter 4, whether attenuated by the phantom or not. However the phase contrast is seen to fall by a fairly constant factor of approximately 30 for every sample, which is an extremely significant loss of information.

The intensity profile comparisons for the resulting images are also compared visually. These are shown in figure 6.19.

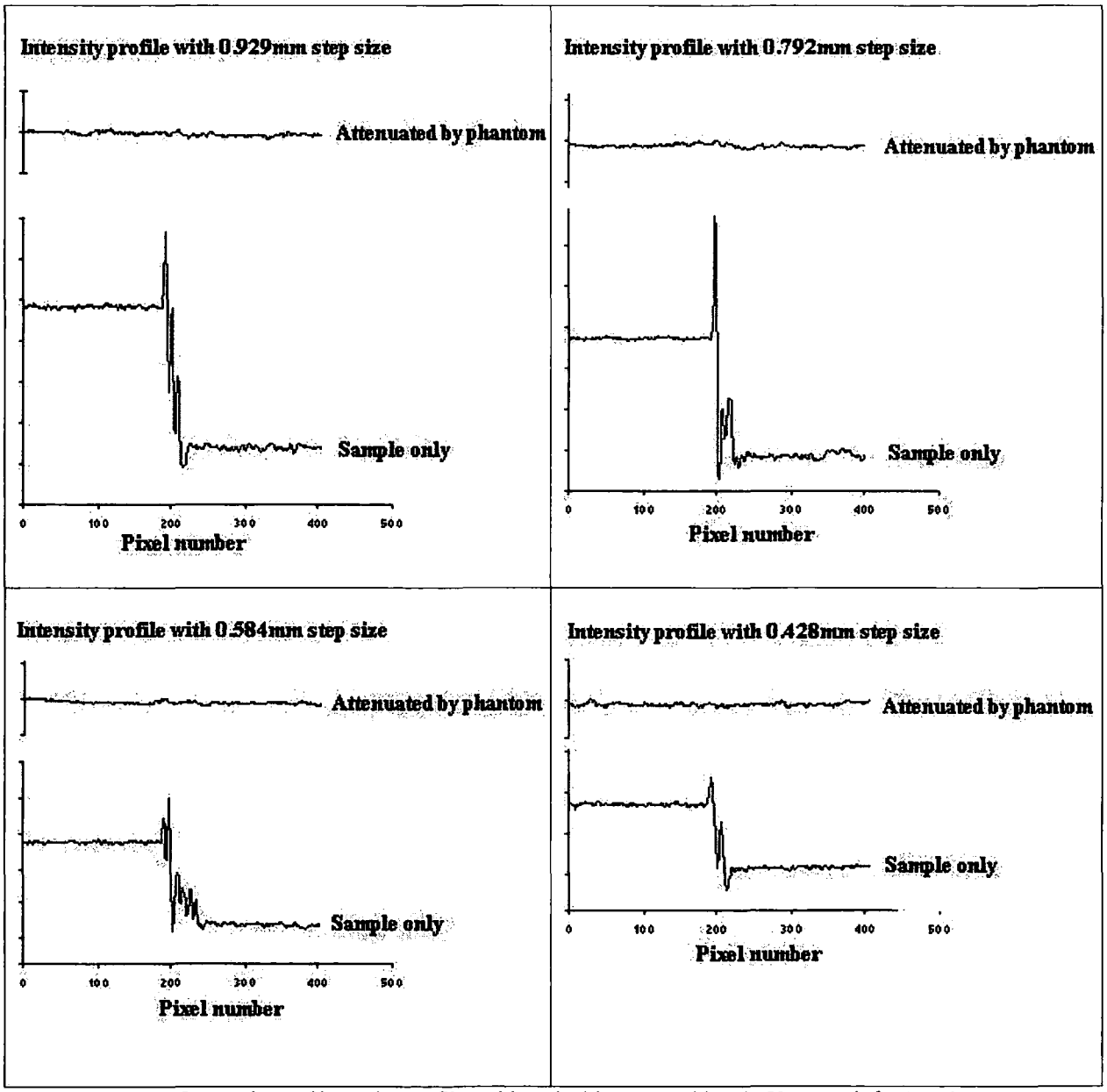

Figure 6.19: Comparison of intensity profiles with and without test object in X-ray path for 'step' thicknesses: (a) 929μm, (b) 792μm, (c) 584μm and (d) 428μm. (Copper target)

It is seen in figure 6.19 that the presence of the simulated breast tissue has a severely detrimental effect on the phase contrast achieved by the imaging set-up. Good phase contrast is clearly visible for all non-attenuated Heaviside samples. However the phase contrast of all of the attenuated samples is lost amid the image noise, despite the use of a thick line profile. The absorption contrast is barely discernible in the attenuated images. The absorption contrast values of the images of both the non-attenuated and attenuated sample are plotted as a function of sample 'step' size in figure 6.20.

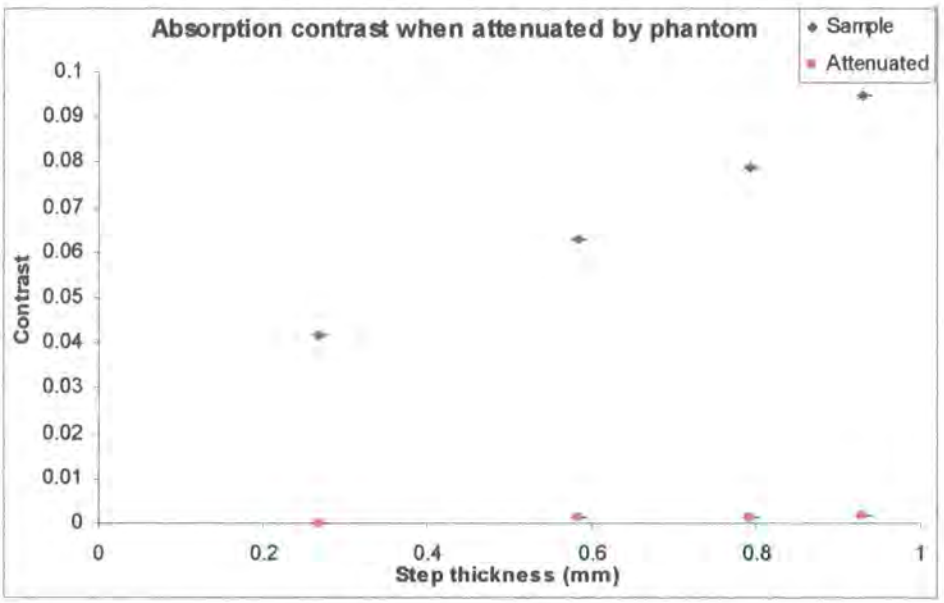

Figure 6.20: Absorption contrast of attenuated and non-attenuated images plotted as a function of 'step' thickness (Copper target)

It is clear from figures 6.19 and 6.20 that the absorption contrast achieved using the copper source is very severely affected by the presence of the mammographic test object. The lower-energy X-rays emitted by the copper source are unable to penetrate the phantom sufficiently to retain the information required for a phase contrast image. This is the same as the problem seen when glass was placed in the path of the beam, as discussed in Chapter 5: the low-energy absorption by the breast tissue morphology section of the phantom causes the beam to harden toward higher energies at which the beam intensity is too low to provide a useful image.

These attenuated phase and absorption contrast results make it clear that X-rays provided by a copper target are unsuitable for imaging a mammographic test object, and consequently mammographic samples, due to the noise and X-ray attenuation caused by the breast tissue. However, the images achieved using X-rays provided by the rhodium source are very promising.

A good direction to take this work would be to gradually scale down the operating settings of the microfocus X-ray source, with the rhodium target in place, to match those of a mammographic specimen radiography system (a low energy unit with a very small focal spot for high magnification imaging of biopsy tissue [7]). While the rhodium images of the phantom show good potential, the voltage is currently set too high to be used on tissue samples.

6.2 A scorpion sting: absorption and phase imaging

The final step in this project is to demonstrate the system's phase contrast imaging capability on an actual pathological sample. A number of pathological samples have been imaged in the past using phase contrast methods according to published literature, as discussed in some detail in Chapter 1. However, most of these have been imaged using synchrotron radiation: comparatively few have used laboratory-based in-line techniques. Some examples of pathological samples imaged using in-line techniques in the laboratory include the following: a goldfish [8], a section of liver [9], a small bone [10], a fly [11], and a shrimp [12]. A number of dead scorpions became available to this project at an early stage, and because at present none of the published literature includes phase contrast images of scorpions, this is a new possibility in the field.

During the early stages of the project, before any of the work discussed in Chapters 4 and 5 had been completed, the system was used to image a scorpion sting with a maximum cross-sectional diameter of 4mm. The system was set up as shown in figure 6.21. The set-up included a propagation distance of 55mm, and source dimensions of 26μm width by 44μm height. This image was taken with the rhodium target in place.

Figure 6. 21: Set-up for scorpion sting image

At a later stage in the project, the scorpion sting was imaged again in order to see whether the system had been improved significantly by the work on propagation distance and source size. Again the set-up was as shown in figure 6.21, using the rhodium target, but this time with propagation distance increased to the maximum available to the set-up, at 684mm: we have already seen in Chapter 4 that a propagation distance of less than 78mm is not sufficient for phase contrast imaging with this system. The source dimensions were reduced to their minimum of 19μm width by 18μm height. No attempt was made to partially monochromate the beam because good phase contrast images of the heaviside function sample have already been achieved using the source's natural spectrum.

The initial and final images of the sting are shown in figure 6.22: the initial (absorption) image in 6.22 (a) and the final (phase) image in 6.22 (b).

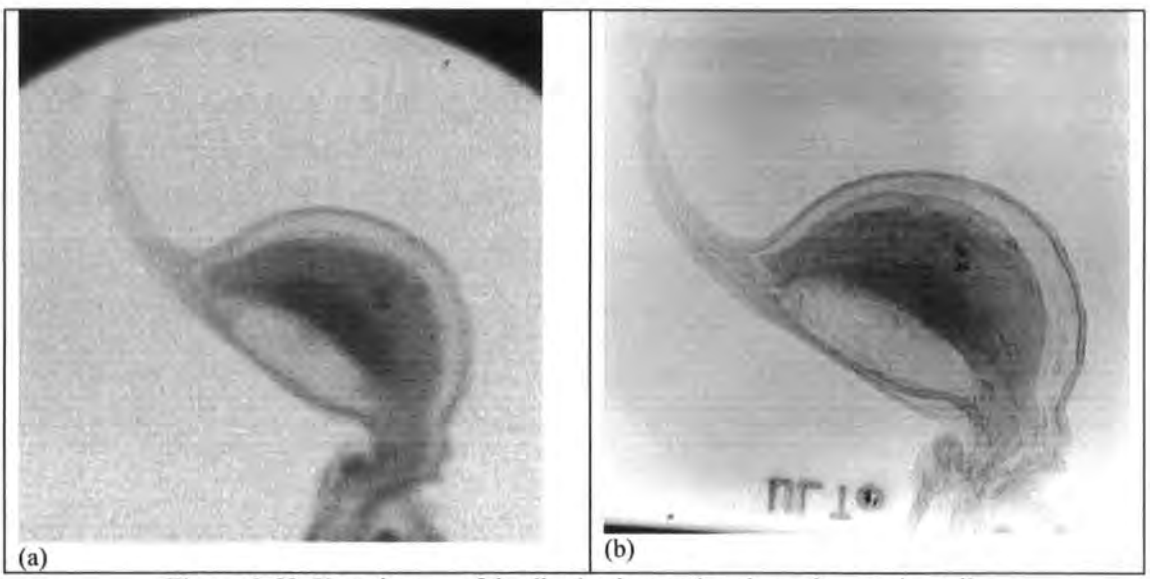

Figure 6. 22: X-ray images of the distal, telsen and aculeus of a scorpion tail:
(a) Absorption contrast, (b) Phase contrast.

The images in Figure 6.22 both show a section of a scorpion tail comprising an aculeus (sting), telsen (vesicle containing venom gland and muscles) and distal (segment connecting the telsen to the tail).

The absorption image (Figure 6.22 (a)) does include some useful details. The hinge-like connection between the telsen and the distal can be seen at the bottom of the image. The venom gland and muscular area show up within the telsen, although they are indistinguishable from one another and simply appear as one strongly-absorbing section. The general shape of the aculeus can be determined from the absorption contrast image. However no additional detail within the aculeus is seen.

The phase contrast image (Figure 6.22 (a)) shows up more useful detail. Again, the connection between the telsen and the distal is seen, but the tissue within this area is resolved and the absorption property does not dominate the section. The telson itself shows a crisp outline, and within this outline the venom gland and its muscles all show enhanced detail. The absorption contrast here is unavoidable due to the stronger absorption of this section. However it is not detrimental to the enhanced edge details. The weakly-absorbing areas within the telson also display plenty of detail which the absorption image could not record. The aculeus in the phase contrast image really demonstrates the improvement facilitated by the phase contrast method: in addition to displaying a good outline of the shape, the shaft through which the poison travels into the scorpion's prey is well-resolved from the telson to the tip.

In addition to breaking some new ground in the field of phase contrast imaging, the scorpion sting images provide a 'before' and 'after' type glimpse of this project. The phase image is an unquestionable improvement on the absorption image, not only demonstrating the advantage of phase contrast over absorption contrast when imaging weakly-absorbing samples, but also highlighting the improvement to the imaging system during the course of this project.

References

[1] Cowen A. R. et al, *British Journal of Radiology,* **65** pp.528-535 (1992)

[2] Kotre C. J. & Birch I. P., *Phys. Med. Biol.* **44** pp. 2853-2866 (1999)

[3] Kotre C. J. et al., *British Journal of Radiology,* **75** pp.170-173 (2002)

[4] Underwood A. C. et al, *British Journal of Radiology*, **70** pp.186-187 (1997)

[5] Kimme-Smith C., Medical Physics, **16** (5) pp.758-765 (1989)

[6] Kotre C. J. et al., *British Journal of Radiology*, **67** pp.856-859 (1994)

[7] Birch I. P. Et al., *British Journal of Radiology,* **79** pp.239-243 (2006)

[8] Wilkins S. W., et al, *Nature* **384**, pp.335-338 (1996)

[9] Pogany A. et al., *Rev. Sci. Instr.* **68** (7) pp.2774-2782 (1997)

[10] Gureyev T. E. et al., *J. Digital Imaging,* **13** (2) Suppl 1 pp.121-126 (2000)

[11] Mayo S. C. et al., *Opt. Express* **11** (19) pp.2289-2302 (2003)

[12] Han S. et al., *Rev. Sci. Instr.***75** (10) pp.3146-3151 (2004)

7. Conclusions, further work and future developments

7.1 Summary of conclusions

During the course of this project it has been demonstrated that good phase contrast images are achievable using a laboratory-based microfocus X-ray source in an in-line set-up. The differences between absorption and phase contrast images have been demonstrated theoretically via a program in Matlab, which simulates the interference effects caused by a simple phase object in an in-line set-up.

Using a phase object comprising an abrupt boundary between two sections of mylar of slightly differing thicknesses, quantifiable phase contrast images have been acquired.

With the in-line system set up on a laboratory scale, it has been determined that the limiting factor in system positioning is the propagation distance between the sample and the detector. This must be sufficient for the transmitted X-rays to interfere in order to provide the phase detail. With the source and detector positions fixed, the phase contrast has been seen to vary in direct proportion to the propagation distance. The results using both copper and rhodium targets have suggested that phase contrast is not achievable by this system with a propagation distance of 78mm or less.

It has been demonstrated that in the absence of other variations in conditions, optimum phase contrast images are achieved with a small source size, and hence a longer transverse coherence length. It has been further determined that the source dimension in the direction perpendicular to a given boundary in the sample dominates the phase contrast of that boundary within the image.

By manipulating images taken at different operating voltages, via weighted subtractions, it has been determined that more monochromatic X-rays provide images with higher phase contrast values. However, it has been demonstrated that the widely-used filter method for partial X-ray monochromation is unsuitable for phase contrast imaging due to the 'beam-hardening' effect caused by the filter's absorption of X-rays at low

energies, and the filter self-image which is superimposed with the phase contrast image of the sample.

By imaging a number of mylar samples of different thicknesses, it has been determined that the phase contrast increases initially with sample thickness, but reaches a plateau at a certain sample thickness. For samples thicker than this, the absorption contrast provides most of the information in the image. This phase contrast plateau is different for rhodium and copper X-rays. This means that in practice, a phase contrast imaging system is limited in terms of sample thickness, and for a given material this limiting thickness is dependent on the energy of the incident X-rays.

Introduction of disordered materials, represented here by water and glass, to the system, have been seen to be detrimental to both the phase and absorption contrast. This is due to the 'beam hardening' effect caused by the strong absorption of low-energy X-rays by water and glass. It causes a reduction in the effective transverse coherence length and the average absorption coefficient of the sample material, thereby affecting both the phase and absorption contrast imaging capabilities of the system. This effect is a direct consequence of the use of polychromatic X-rays and can be eliminated only by the use of monochromatic X-rays.

With the copper target in place, the system was found to be unsuitable for imaging pathological samples because water significantly reduced the phase contrast and glass destroyed it, due to the low energy of the copper spectrum. However, although the phase contrast achieved with the rhodium target in place was reduced by the introduction of water and glass, it was not destroyed. So the system does show some potential for phase contrast imaging of pathological samples.

Using a Leeds mammographic test object, TOR[MAM], the system was tested to determine its capability in the field of mammography. Using both the rhodium and copper targets, good phase contrast images were recorded of all the contrast details embedded in one side of the test object, and also of the breast tissue morphology detail

embedded in the other side. An investigation using the breast tissue morphology section and a mylar Heaviside sample, with the rhodium target in place in the source, determined that with the noise and attenuation caused by breast tissue, the system is capable of detecting an anomaly of ≥584μm thickness. However, with the copper target in place the system was unable to detect any anomalies up to and including the thickest sample, 929μm in thickness.

The system was used to image a scorpion sting at the beginning of this project and again towards the end. These images provide a practical demonstration of the following:

- The application of the system to a pathological test object;
- The differences between absorption contrast images and phase contrast images;
- The significant improvement in the system as a result of this project.

This project has demonstrated that monochromatic X-rays are better for phase contrast imaging because they do not suffer beam hardening effects as samples absorb low energy X-rays. However, for weakly absorbing materials, polychromatic X-rays have provided good phase contrast images, with both rhodium and copper targets in place. For a pure phase object, X-rays produced with copper and rhodium targets have been seen to provide similar levels of phase contrast. However, for more strongly-absorbing materials, the higher-energy X-rays produced with the rhodium target have been seen to provide better phase contrast because the beam-hardening and intensity loss effects of low-energy absorption are less significant than for copper X-rays. In practice it is unlikely that this system would be applied only to pure phase objects, so high-energy X-rays are likely to be the more suitable choice for most applications, with their ability to penetrate samples further.

7.2 Suggestions for further work

Further work which could be completed in relation to this project could include the following.

1. It has been seen that for a given material, the phase contrast imaging system has an operational limit in terms of sample thickness, past which the absorption contrast provides more information (as discussed in Chapter 4). By repeating the thickness experiment with Heaviside function samples of different materials and thicknesses, using copper, rhodium and other targets, a map of these operational limits could be built up for a number of sample materials and X-ray energies.

2. Using the same Heaviside function sample, the experiments involving path lengths of water and glass in the X-ray beam (as described in Chapter 5) could be repeated using synchrotron radiation via a suitable beamline, for example ID19 or BM05 at the European Synchrotron Radiation Facility (ESRF). Ideally, this would use monochromatic 8keV and 20keV X-ray beams for consistency with the copper and rhodium targets used during this project. Because the X-rays would be monochromatic and of high intensity, it is expected that the phase and absorption contrast would not be degraded as water or glass is introduced to the system.

3. While the in-line system demonstrated that it is capable of detecting details in a mammographic test object, it was not possible to quantify the results via image grading because this requires the whole test object to appear within the same image. The size constraints of the shielded enclosure did not allow for sufficient magnification to achieve such an image. If a larger shielded area were available to this project, gradable images could be acquired and a robust numerical comparison could be drawn between the rhodium and copper results.

4. A natural progression for this project would be to try imaging small biological tissue samples, subject to health and safety regulations for the location of the system. The operational settings of the X-ray source, as used for this project, are outside of the

range allowed for *in-vivo* imaging, but by using pathological samples for guidance these settings could be gradually brought down to the correct levels.

7.3 Future developments

In the future, other laboratory-based X-ray sources could provide a more suitable X-ray beam for phase contrast imaging. It has already been seen that a microfocus X-ray source, providing a high-brightness X-ray beam, is suitable for phase contrast imaging. Such sources are improving and higher-brightness sources can be expected in the future. Another possible source is the X-ray laser [1]: a tuned, monochromatic X-ray laser with an expanded beam would provide the high intensity required. However, these lasers are pulsed, which would be unsuitable for this application, and are currently highly experimental.

A realistic possibility is the laboratory-based synchrotron source. Several such sources, developed by Photon Production Laboratory, have been developed, and it is claimed that they provide results almost as good as a mainstream synchrotron source. The largest, MIRRORCLE 20 [2], accelerates electrons up to 20MeV with an orbit radius of 0.15m, using a magnet of 1.2m in diameter. This produces X-rays ranging from 1keV up to 5keV. However its cost (U.S.$3 million) and dimensions (3m x 7m x 2m) make it far less practical and cost-effective than the microfocus X-ray source. A further development is the tabletop synchrotron source MIRRORCLE 6X by Hasegawa *et al* [3]. This accelerates electrons up to 6MeV with an orbit radius of 0.15m using a magnet of 0.6m in diameter, and takes up an area of just 2 square metres. This provides a continuous spectrum ranging from 1keV to 6 MeV, with an expected brilliance of $\sim 10^{11}$ photons/s/mrad^2/mm^2/0.1%λ. Another, similar source offers a dedicated X-ray range of 10keV to 30keV. Again, the cost of both is prohibitively high. When the scaled-down synchrotron source is available at a realistic price, laboratory-based phase contrast imaging should improve vastly.

References

[1] Li Y. L., *J. Opt. Soc. Am. B*, **17** (6) pp.1098-1101 (2000)

[2] Yamada H., *Nucl. Instr. Meth. B* **199** pp.509-516 (2003)

[3] Hasegawa D. *The 14th Symposium on accelerator science and technology* (2003)

Appendices

Appendix A:

Matlab programs modelling phase changes through system

A1. Object approximating to a Heaviside function:

```
% program to simulate the phase effects of an
% object approximating to a Heaviside function

x=42;
y=42;

Wavefront=zeros(x,y);
Step=zeros(x,y);
Propagate=zeros(x,y);
Image=zeros(x,y);
Dist=0.3;
DeltaMylar=4.74517e-6;
MuMylar=8.96278;
DeltaAir=3.87519e-9;
MuAir=0.0111423;
PropagateSum=0;


% Create a flat wavefront:

for tmpy = -y/2:1:y/2-1
   for tmpx = -x/2:1:x/2-1
      Wavefront((tmpy+y/2+1),(tmpx+x/2+1)) = 1000*exp(0);
   end
end

% Map the wavefront amplitude:
mesh(abs(Wavefront))

% Map the wavefront phase:
mesh(angle(Wavefront))


% Propagate wavefront through 'step' function:

for tmpy = -y/2:1:y/2-1
   for tmpx = -x/2:1:x/2-1
      % One half of sample has thickness = 100 microns
      if tmpx <= 0
         Step((tmpy+y/2+1),(tmpx+x/2+1)) =
         Wavefront((tmpy+y/2+1),(tmpx+x/2+1))*exp(-MuMylar*0.01)*exp(-
         2*i*pi*DeltaMylar*100e-6/1.545e-10);
```

```
        %Square for intensity:
        Intensity((tmpy+y/2+1),(tmpx+x/2+1)) = Step((tmpy+y/2+1),(tmpx+x/2+1))^2;
      end
      % Other half of sample has thickness = 200 microns
      if tmpx > 0
        Step((tmpy+y/2+1),(tmpx+x/2+1)) =
        Wavefront((tmpy+y/2+1),(tmpx+x/2+1))*exp(-MuMylar*0.02)*exp(-
        2*i*pi*DeltaMylar*200e-6/1.545e-10);
         %Square for intensity:
        Intensity((tmpy+y/2+1),(tmpx+x/2+1)) = Step((tmpy+y/2+1),(tmpx+x/2+1))^2;
      end
    end
end

% Map the transmitted wavefront amplitude:
mesh(abs(Step))

% Map the transmitted wavefront phase:
mesh(angle(Step))

% Transmitted absorption image:
mesh(abs(Intensity))


% Propagate transmitted wavefront to detector:

% Horizontal deflection on image:
for t = -x/2:1:x/2-1
  % Vertical deflection on image:
  for s = -y/2:1:y/2-1
    % Vertical deflection on object:
    for tmpy = -y/2:1:y/2-1
      % Horizontal deflection on object:
      for tmpx = -x/2:1:x/2-1

        % Vertical position on image:
        Yimage = (s*10e-3)/y;
        % Horizontal position on image:
        Ximage = (t*10e-3)/x;
        % Vertical position on object:
        Yobject = (tmpy*2e-3)/y;
        % Horizontal position on object:
        Xobject = (tmpx*2e-3)/x;

        % Angle theta, subtended by object at image in vertical direction:
```

```
            theta = atan((abs(Yimage-Yobject))/Dist);

            % Angle phi, subtended by object at image in horizontal direction:
            phi = atan((abs(Ximage-Xobject))/Dist);

            %Propagation of wavefront section to point in image:
            Propagate((tmpy+y/2+1),(tmpx+x/2+1)) =
             Step((tmpy+y/2+1),(tmpx+x/2+1))*exp(-
             MuAir*Dist*100/(cos(phi)*cos(theta)))*exp(-
             2*i*pi*Dist/(cos(phi)*cos(theta)*1.545e-10));

            %Sum contributions from all parts of wavefront to point on image:
            PropagateSum = PropagateSum +
             (Propagate((tmpy+y/2+1),(tmpx+x/2+1))^2);
          end
        end

        % Record final sum of contributions to image co-ordinate:
        Image((s+y/2+1),(t+x/2+1)) = PropagateSum;
      end
    end

    % Intensity map of final image:
    surf(abs(Image))
```

A2. Object approximating to a graded function:

```
% program to simulate the propagation image of an
% object approximating to a graded function.

x=42;
y=42;

Wavefront=zeros(x,y);
Graded=zeros(x,y);
DeltaMylar=4.74517e-6;
MuMylar=8.96278;
Thickness=0


% Create a flat wavefront:
for tmpy = -y/2:1:y/2-1
   for tmpx = -x/2:1:x/2-1
      Wavefront((tmpy+y/2+1),(tmpx+x/2+1)) = 1000*exp(0);
   end
end

% Map the wavefront amplitude:
mesh(abs(Wavefront))

% Map the wavefront phase:
mesh(angle(Wavefront))


% Propagate wavefront through graded function:

for tmpy = -y/2:1:y/2-1
   for tmpx = -x/2:1:x/2-1
      % Section of sample with thickness = 100 microns:
      if tmpx <= -10
         Thickness=100e-6;
      end
      % Section of sample with graded thickness:
      if ((tmpx > -10) & (tmpx < 10))
         Thickness = 100e-6+((tmpx+11)*100e-6/20);
      end
      % Section of sample with thickness = 200 microns:
      if tmpx > 10
         Thickness = 200e-6;
      end

      % Absorption and phase effects of mylar object:
```

```
      Graded((tmpy+y/2+1),(tmpx+x/2+1)) =
       Wavefront((tmpy+y/2+1),(tmpx+x/2+1))*exp(-MuMylar*Thickness*100)*exp(-
       2*i*pi*DeltaMylar*Thickness/1.545e-10);

      %Square for intensity:
      Intensity((tmpy+y/2+1),(tmpx+x/2+1)) = Graded ((tmpy+y/2+1),(tmpx+x/2+1))^2;
   end
end

% Map the transmitted wavefront amplitude:
mesh(abs(Graded))

% Map the transmitted wavefront phase:
mesh(angle(Graded))

% Transmitted absorption image:
mesh(abs(Intensity))


% Propagate transmitted wavefront to detector:

% Horizontal deflection on image:
for t = -x/2:1:x/2-1
   % Vertical deflection on image:
   for s = -y/2:1:y/2-1
      % Vertical deflection on object:
      for tmpy = -y/2:1:y/2-1
         % Horizontal deflection on object:
         for tmpx = -x/2:1:x/2-1

            % Vertical position on image:
            Yimage = (s*10e-3)/y;
            % Horizontal position on image:
            Ximage = (t*10e-3)/x;
            % Vertical position on object:
            Yobject = (tmpy*2e-3)/y;
            % Horizontal position on object:
            Xobject = (tmpx*2e-3)/x;

            % Angle theta, subtended by object at image in vertical direction:
            theta = atan((abs(Yimage-Yobject))/Dist);

            % Angle phi, subtended by object at image in horizontal direction:
            phi = atan((abs(Ximage-Xobject))/Dist);

            %Propagation of wavefront section to point in image:
```

```
            Propagate((tmpy+y/2+1),(tmpx+x/2+1)) = Graded
            ((tmpy+y/2+1),(tmpx+x/2+1))*exp(-
            MuAir*Dist*100/(cos(phi)*cos(theta)))*exp(-
            2*i*pi*Dist/(cos(phi)*cos(theta)*1.545e-10));

            %Sum contributions from all parts of wavefront to point on image:
            PropagateSum = PropagateSum +
            (Propagate((tmpy+y/2+1),(tmpx+x/2+1))^2);
        end
    end

    % Record final sum of contributions to image co-ordinate:
    Image((s+y/2+1),(t+x/2+1)) = PropagateSum;
  end
end

% Intensity map of final image:
surf(abs(Image))
```

Appendix B:

Calculation of source size

Here, the method for measuring the source size is explained in detail.

B.1 Derivation of source size calculation

The method uses the image of a wire shadow, taken as shown in figure B.1:

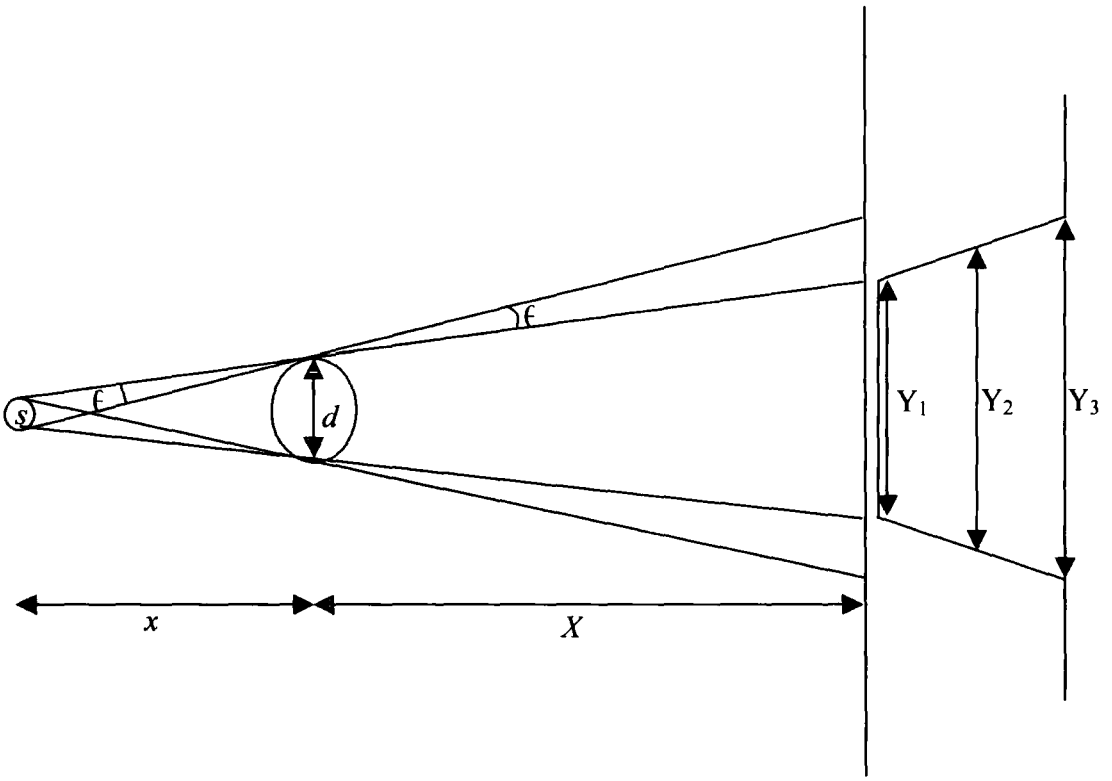

Figure B.1: Schematic diagram of imaging system with a wire in the path of the beam

Using figure B.1 together with some trigonometry, the source size can be determined via the following set of equations:

$$\theta = \frac{Y_3 - Y_1}{2}\frac{\text{Re}\,solution}{X} \qquad \text{(B-1)}$$

$$\theta \approx \frac{s}{x} \qquad \text{(B-2)}$$

$$\therefore s = \frac{Y_3 - Y_1}{2} \frac{x}{X} \text{Re}\, solution \qquad \text{(B-3)}$$

$\frac{x}{X}$ is equal to the ratio $\frac{d}{Y_2}$, and these give the reciprocal of the magnification, M. Thus the source size is calculated via the following:

$$s = \frac{Y_3 - Y_1}{2} \frac{\text{Re}\, solution}{M} \qquad \text{(B-4)}$$

B.2 Equivalent Gaussian FWHM dimension

In reality, the boundaries are not well-defined in the images obtained by the detector, unlike the image suggested in figure B.1. The image will take the form of a broadened intensity distribution. An accurate method is required to determine the correct points at which to measure Y_3-Y_1. The FWHM of a beam is often used in cases where edges are broadened out, so it makes sense to use this approach. By plotting a Gaussian distribution together with its cumulative curve, such that they cover the same range along the x-axis but use different y-axes, the percentiles coinciding with the Gaussian FWHM can be determined. This is illustrated in figure B.2.

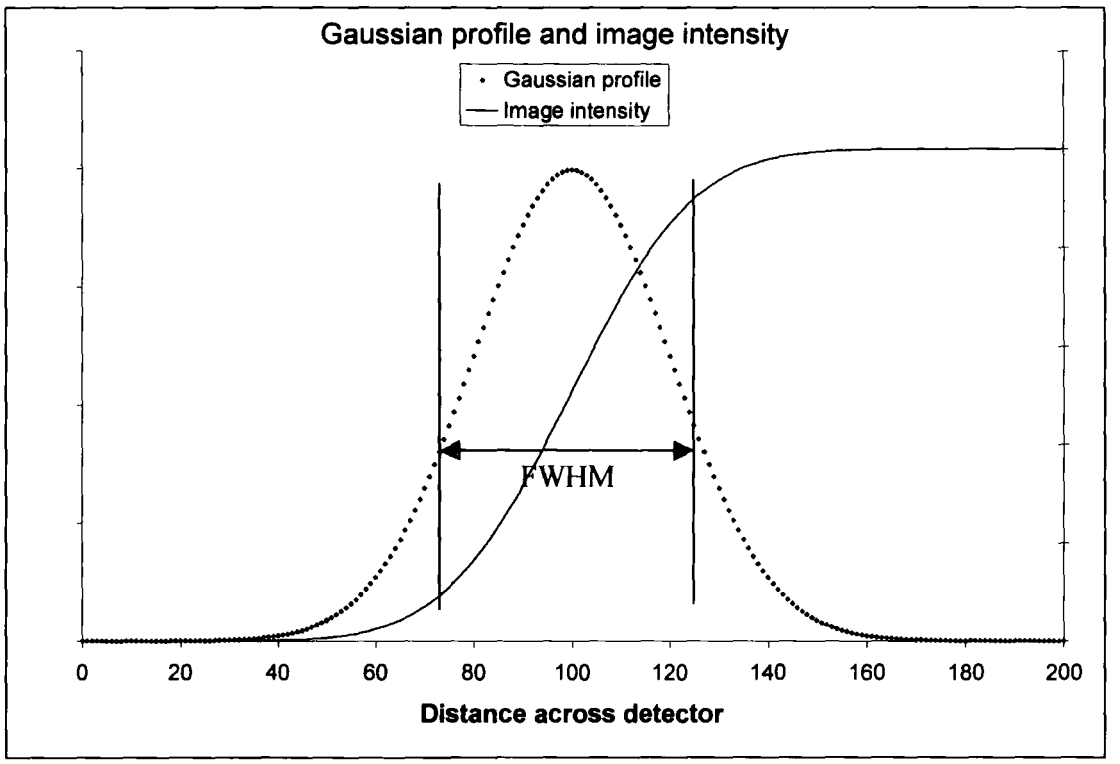

Figure B.2: Gaussian distribution and image intensity profile plotted together

The FWHM of the Gaussian distribution is seen to coincide with the image intensity profile contained within the 12% and 88% intensity range. Thus an accurate estimate of Y_1 and Y_3 may be taken at 12% and 88% of the intensity range respectively, and 76% of the beam energy is used in the measurement.

B.3 Deconvolution

An additional consideration is that the wire is not opaque to the X-rays and the absorption effect must be accounted for in the image calculations. This is done by considering the absorption image of the wire if no source magnification occurs. In constructing a theoretical ideal image, we must calculate the propagation distance across the wire at each point along the wire's diameter. This simply uses Pythagoras' Theorem, based on figure B.3.

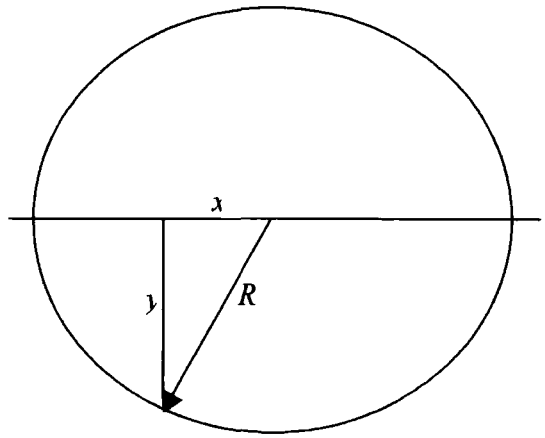

Figure B.3: Cross section of cylindrical wire

In figure B.3, R is the radius of the cross-section, x the distance from the centre of the cross-section to the point of entry of the photon, and y the propagation distance from the centre of the cross-section to the edge of the wire. The distance y is calculated as follows:

$$x^2 + y^2 = R^2 \qquad \text{(B-5)}$$

$$y = \sqrt{R^2 - x^2} \qquad \text{(B-6)}$$

The photon propagation distance is double the distance y shown in figure B2, and so is given by:

$$propagation = 2\sqrt{R^2 - x^2} \qquad \text{(B-7)}$$

A typical profile of propagation distance across a 125μm cylindrical wire cross-section would look like the profile shown in figure B.4.

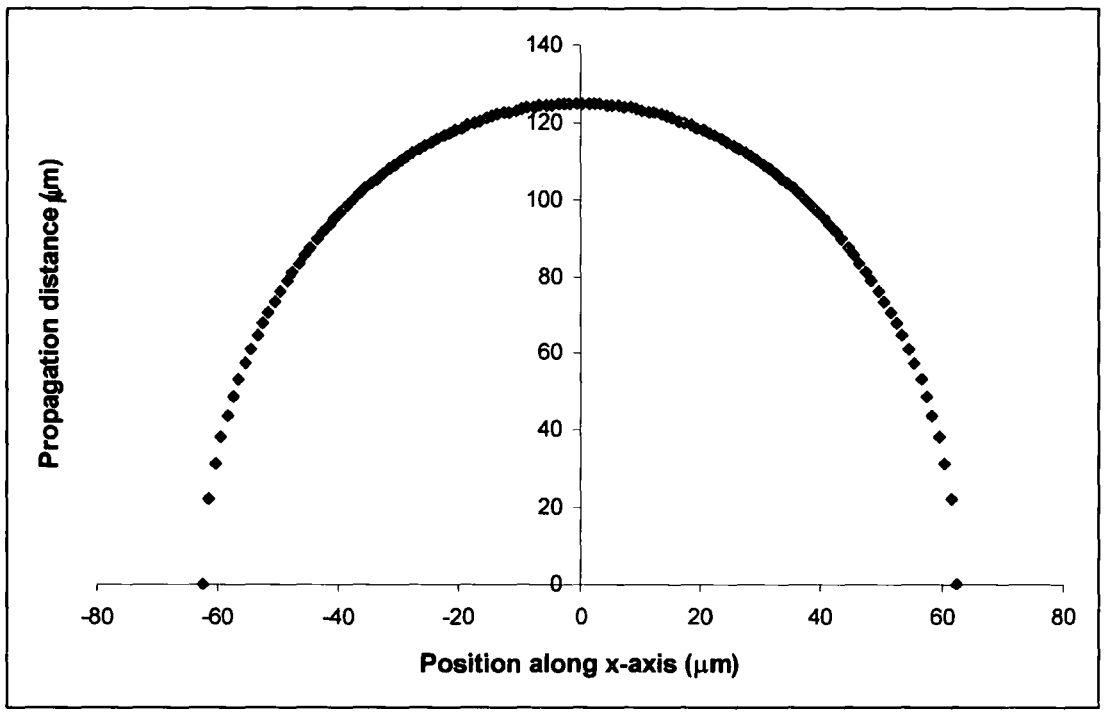

Figure B.4: Typical profile of propagation distance across a 125μm cylindrical wire

The propagation distance is then included in the standard absorption formula,

$$I = I_0 \exp(-\mu t) \qquad \text{(B-8)}$$

where I and I_0 are the transmitted and incident intensities respectively, μ the absorption coefficient and t the wire thickness, or propagation distance. Using equations B-7 and B-8, together with the absorption coefficient of mylar at the copper K_α energy and an arbitrary incident intensity, we can construct an ideal image of a 125μm mylar wire by way of example. This is shown in figure B.5.

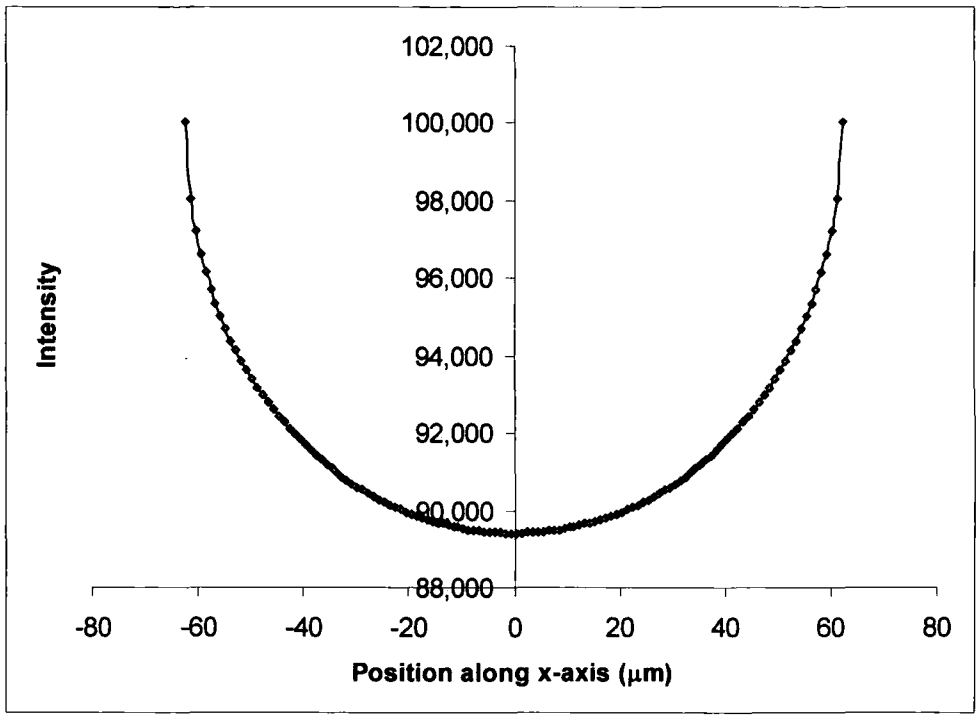

Figure B.5: Ideal image of a 125μm mylar wire with no source magnification present

With source magnification present, we would expect the final image obtained to be a convolution of figure B.5 with the source distribution [1], leading to a broadened intensity distribution curve as shown in figure B.6.

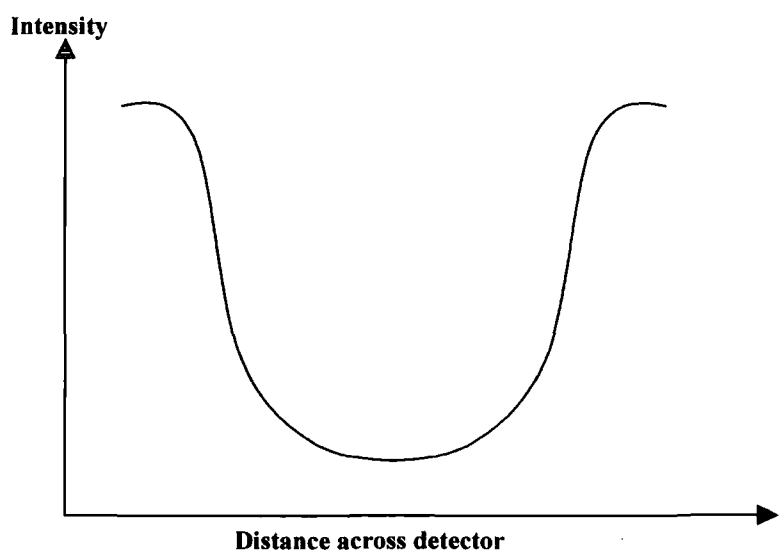

Figure B. 6: Realistic intensity profile across wire shadow image

In order to correctly calculate the source size, the ideal image intensity profile must be deconvolved from the intensity profile of the image obtained by the detector. This provides an intensity profile representing the source magnification effect. Equation B-4 can then applied to the intensity profile obtained by deconvolution.

In preparing for this deconvolution work, the ideal image profiles must be constructed for the tungsten wire, at both copper and rhodium K_α energies. To do this we apply the following variables to equations B-7 and B-8:

- Radius, $R = 125\mu m$;
- Arbitrary incident intensity, $I_0 = 100{,}000$;
- Absorption coefficient of tungsten at rhodium K_α energy, $\mu = 1{,}195$;
- Absorption coefficient of tungsten at copper K_α energy, $\mu = 3{,}137$.

The ideal images for rhodium and copper are shown in figures B.7 and B.8 respectively.

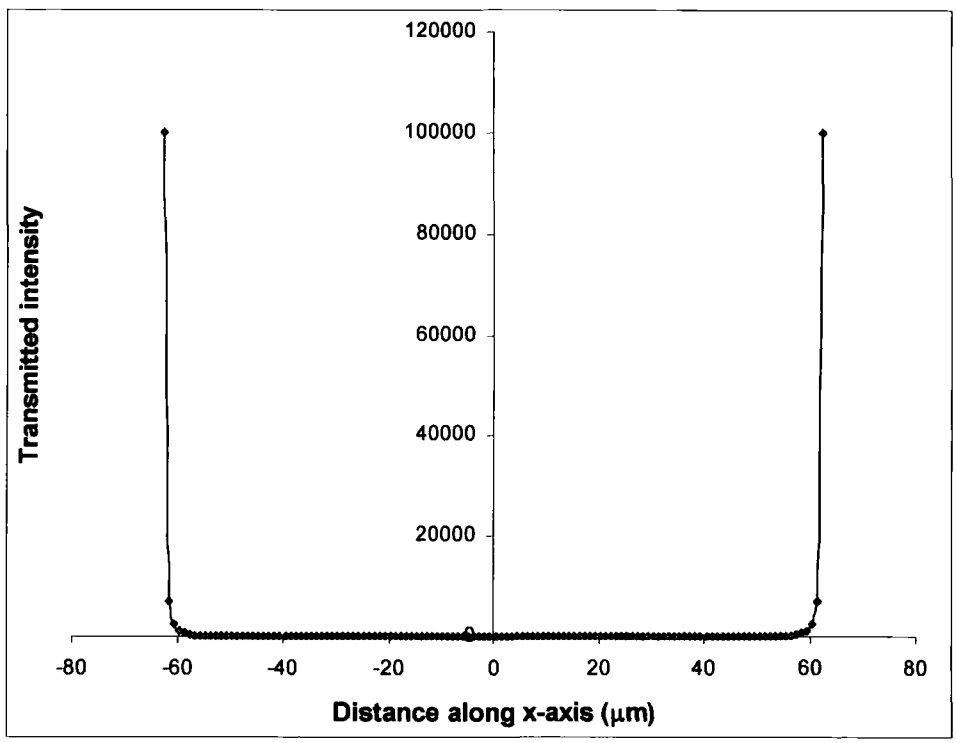

Figure B.7: Ideal image profile of tungsten wire with no source magnification (rhodium source)

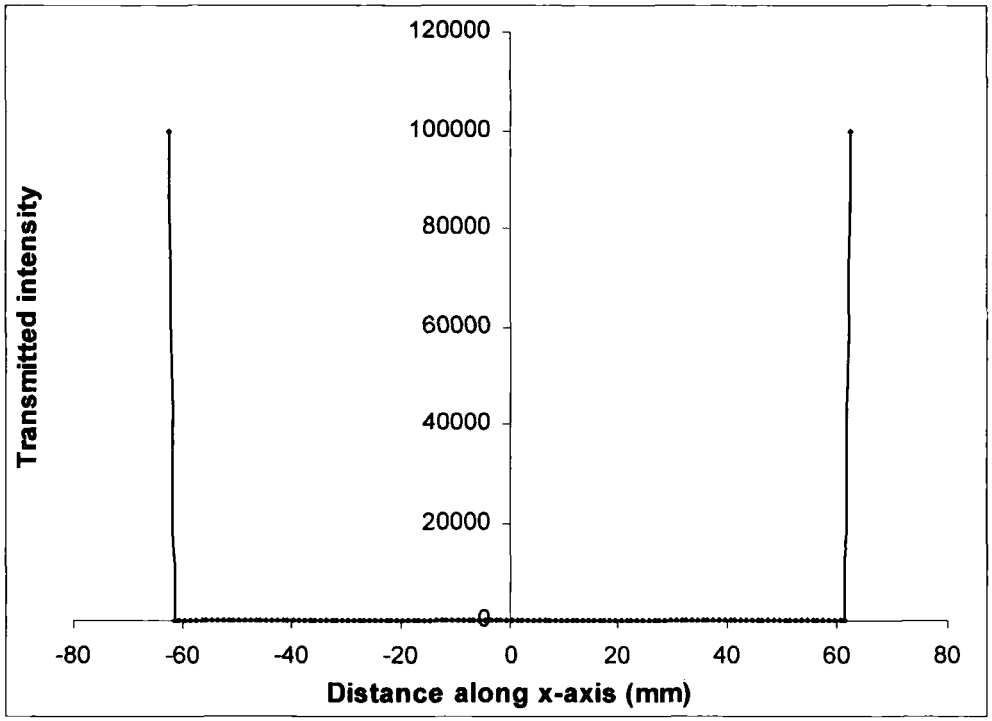

Figure B.8: Ideal image profile of tungsten wire with no source magnification (copper source)

From figures B.7 and B.8 we see that, due to the high absorption property of the tungsten, the ideal image profiles approximate to a perfect pulse at both rhodium and copper energies. In this situation, deconvolution of the ideal image from the image obtained by the detector will have little effect because with such high levels of absorption at these energies the tungsten wire effectively behaves as if it is opaque to the X-rays. Thus, equation B-4 can be applied directly to the profiles of the images obtained by the detector.

References

[1] Mayo S. C. et al., *Proc. 8th Int. Conf. X-ray Microscopy,* pp.343-345 (2005)

Bibliography

Optical phase contrast:

[1] Zernike F, "How I discovered phase contrast", *Science*, **121**, pp.345-349 (1955)

Balanced filters:

[1] Ross P A, "Polarization of X-rays", *Phys. Rev.* **28** pp.425A (1926)

[2] Kirkpatrick P, "On the theory and use of Ross filters", *Rev. Sci. Instr.* **10** pp.186-191 (1939)

[3] Soules J A, Gordon W L, Shaw C H, "Design of X-ray filters for low-intensity scattering experiments", *Rev. Sci. Instr.*, **27**, (1), pp.12-14 (1956)

X-ray phase contrast:

[1] Snigirev A, Snigireva I, Kohn V, Kuznetsov S, Schelokov I, "On the possibilities of X–ray phase contrast microimaging by coherent high-energy synchrotron radiation", *Rev. Sci. Instr.*, **66** (12) pp.5486-5492 (1995)

[2] Raven C, Snigirev A, Snigireva I, Spanne P, Suvorov A, "Phase-contrast computed microtomography with 50keV synchrotron X-rays", *Rev. Sci. Instr.*, **67** (9), 3359-3363 (1996)

[3] Raven C, Snigirev I, Snigireva P, Spanne A, Souvorov A, Kohn V, "Phase contrast microtomography with coherent high-energy synchrotron X-rays", *Appl. Phys. Lett.*, **69** (13), pp.1826-1828 (1996)

[4] Momose A, Takeda T, "Seeing how we hear", *Nature Medicine* **2** (8) pp.852-853 (1996)

[5] Wilkins S W, Gureyev T E, Gao D, Pogany A, Stevenson A W, "Phase-contrast imaging using polychromatic hard X-rays", *Nature* **384**, pp.335-338 (1996)

[6] Snigirev A, Snigireva I, Bösecke P, Lequien S, Schelokov I, "High energy X-ray phase contrast microscopy using a circular Bragg-Fresnel lens", *Opt. Comms.* **135**, pp.378-384 (1997)

[7] Pogany A, Gao D, Wilkins S W, "Contrast and resolution in imaging with a microfocus X-ray source", *Rev. Sci. Instr.* **68** (7) pp.2774-2782 (1997)

[8] Lagomarsino S, Cedola A, Cloetens P, Di Fonzo S, Jark W, Soullié G, Riekel C, "Phase contrast hard X-ray microscopy with submicron resolution", *Appl. Phys. Lett.* **71** (18) pp.2557-2559 (1997)

[9] Bushuev V A, Ingal V N, Beliaevskaya E A, "Wave theory of X-ray phase-contrast radiography", *Crystallography Reports* **43** (4) pp.538-547 (1998)

[10] Gureyev T E, Wilkins S W, "On X-ray phase retrieval from polychromatic images", *Opt. Comms* **147** pp.229-232 (1998)

[11] Gureyev T E, Wilkins S W, "On X-ray phase imaging with a point source", *J. Opt. Soc. Am. A* **15** (3) pp.579-585 (1998)

[12] Yun W, Pratt S T, Miller R M, Cai Z, Hunter D B, Jarstfer A G, Kemner K M, Lai B, Lee H-R, Legnini D G, Rodrigues W, Smith C I, "X-ray imaging and microspectroscopy of plants and fungi", *J. Synchrotron Rad.* **5** pp.1390-1395 (1998)

[13] Gao D, Pogany A, Stevenson A W, Wilkins S W, "Phase-contrast radiography", *Radiographics* **18** (5) pp.1257-1267 (1998)

[14] Arfelli F, Assante M, Bonvicini V, Bravin A, Cantore G, Castelli E, Dalla Palma L, Di Michiel M, Longo R, Olivo A, Pani S, Pontoni D, Poropat P, Prest M, Rashensky A, Trombat G, Bacchi A, Vallazza E, Zanconati F, "Low-dose phase contrast X-ray medical imaging", *Phys. Med. Biol* **43** pp.2845-2852 (1998)

[15] Kotre C J, Birch I P, "Phase contrast enhancement of X-ray mammography a design study", *Phys. Med. Biol.* **44** pp. 2853-2866 (1999)

[16] Jark W, Di Fonzo S, Soullié G, Cedola A, Lagomarsino S, "Thin film waveguides: 'Condenser systems' for experiments with X-ray beams of 0.1□m dimension", *Journal of Alloys and Compounds,* **286** pp.9-13 (1999)

[17] Beckmann F, Heise K, Kölsch B, Bonse U, Rajewsky M F, Bartscher M, Biermann T, "Three-dimensional imaging of nerve tissue by X-ray phase-contrast microtomography", *Biophysical Journal*, **76** pp. 98-102 (1999)

[18] Cloetens P, Ludwig W, Baruchel J, Guigay J-P, Pernot-Rejmánková P, Salomé-Pateyron M, Schlenker M, Buffiére J-Y, Maire E, Peix G, "Hard X-ray phase imaging using simple propagation of a coherent synchrotron radiation beam", *J. Phys. D.* **32** pp.A145-A151 (1999)

[19] Kowalski G, Moore M, Nailer S, "Application of X-ray phase-contrast imaging to polycrystalline CVD diamond", *J. Phys. D.* **32** pp.A166-A171 (1999)

[20] Gureyev T E, Raven C, Snigirev A, Snigireva I, Wilkins S W, "Hard X-ray quantitative non-interferometric phase-contrast microscopy", *J. Phys. D.* **32** pp.563-567 (1999)

[21] Mori K, Hyodo K, Shikano N, Ando M, "First observation of small fractures on a human dried proximal phalanx by synchrotron X-ray interference radiography", *Jpn. J. Appl. Phys.* **38** pp.L1339-L1341 (1999)

[22] Moran C J, Pierret A, Stevenson A W, "X-ray absorption and phase contrast imaging to study the interplay between roots and soil structure", *Plant and Soil,* **223** pp99-115 (2000)

[23] Gureyev T E, Stevenson A W, Paganin D, Mayo S C, Pogany A, Gao D, Wilkins S W, "Quantitative methods in phase-contrast X-ray imaging" *J. Digital Imaging,* **13** (2) Suppl 1 pp.121-126 (2000)

[24] Fitzgerald R, "Phase-sensitive X-ray imaging", *Physics Today*, **53** (7) pp.23-26 (2000)

[25] Pogany A, Stevenson A W, Gureyev T, Wilkins S W, "Hard X-ray phase-contrast imaging", *Acta Physica Sinica* **49** (12) pp.2357-2368 (2000)

[26] Arfelli F, Bonvicini V, Bravin A, Cantatore G, Castelli E, Palma L D, Di Michiel M, Fabrizioli M, Longo R, Menk R H, Olivo A, Pani S, Pontoni D, Poropat P, Prest M, Rashevsky A, Ratti M, Rigon L, Tromba G, Vacchi A, Vallazza E, Zanconati F, "Mammography with synchrotron radiation: phase-detection techniques", *Radiology* **215** pp.286-293 (2000)

[27] Gureyev T E, Evans R, Stevenson A W, Gao D, Wilkins S W, "X-ray phase-contrast microscopy of paper", *Tappi Journal* Feb 2001, p.52 (2001)

[28] Xu J, Stevenson A W, Gao D, Tykocinski M, Lawrence D, Wilkins S W, Clark G M, Saunders E, Cowan R, "The role of radiographic phase-contrast imaging in the development of intracochlear electrode arrays", *Otology & Neurotology"* **22** pp.862-868 (2001)

[29] Gureyev T E, Mayo S, Wilkins S W, Paganin D, Stevenson A W, "Quantitative in-line phase-contrast imaging with multienergy X-rays", *Phys. Rev. Lett.* **86** (25) pp.5827-5830 (2001)

[30] Kagoshima Y, Ibuki T, Yokoyama Y, Tsusaka Y, Matsui J, Takai K, Aino M, "10keV X-ray phase-contrast microscopy for observing transparent specimens", *Jpn. J. Appl. Phys.* **40** pp.L1190-L1192 (2001)

[31] Kotre C J, Birch I P, Robson K J, "Anomalous image quality phantom scores in magnification mammography: evidence of phase contrast enhancement", *British Journal of Radiology,* **75** pp.170-173 (2002)

[32] Donnelly E F, Price R R, "Quantification of the effect of kVp on edge-enhancement index in phase-contrast radiography", *Med. Phys.* **29** (6) pp.999-1002 (2002)

[33] Gureyev T E, Stevenson A W, Paganin D M, Weitkamp T, Snigirev A, Snigireva I, Wilkins S W, "Quantitative analysis of two-component samples using in-line hard X-ray images", *J. Synchrotron Rad.* **9** pp.148-153 (2002)

[34] Suzuki Y, Yagi N, Uesugi K, "X-ray refraction-enhanced imaging and a method for phase-retrieval for a simple object", *J, Synchrotron Rad.* **9** pp.160-165 (2002)

[35] Bushuev V A, Ingal V N, Beliaevskaya E A, Sergeev A A, "X-ray phase-contrast tomography" *Metallofiz. Noveish. Tekhnol.* **24** (4) pp.559-569 (2002)

[36] Barbosa L B, Reyes Ardila D, Cusatis C, Andreeta JP, "Growth and characterization of crack-free scheelite calcium molybdate single crystal fiber" *J. Crystal Grow.* **235** pp.327-332 (2002)

[37] Paganin D, Mayo S C, Gureyev T E, Miller P R, Wilkins S W, "Simultaneous phase and amplitude extraction from a single defocused image of a homogeneous object", *J. Microscopy* **206** (1) pp.33-40 (2002)

[38] Mayo S C, Miller P R, Wilkins S W, David T J, Gao D, Gureyev T E, Paganin D, Parry D J, Pogany A, Stevenson A W, "Quantitative X-ray projection microscopy: phase-contrast and multi-spectral imaging", *J. Microscopy* **207** (2) pp.79-96 (2002)

[39] Ohara H, Honda C, Ishisaka A, Shimada F, "Image quality in digital phase contrast imaging using a tungsten anode X-ray tube with a small focal spot size",

Medical imaging 2002: Physics of medical imaging, Proceedings of SPIE Vol 4682 pp.713-723 (2002)

[40] Stevenson A W, Gureyev T E, Paganin D, Wilkins S W, Weitkamp T, Snigirev A, Rau C, Snigireva I, Youn H S, Dolbnya I P, Yun W, Lai B, Garrett R F, Cookson D J, Hyodo K, Ando M, "Phase-contrast X-ray imaging with synchrotron radiation for materials science applications", *Nucl. Instr. Meth. Phys. B* **199** pp427-435 (2003)

[41] Kagoshima Y, Yokoyama Y, Niimi T, Koyama T, Tsusaka Y, Matsui J, Yakai K, "Hard X-ray phase-contrast microscope for observing transparent specimens", *J. Phys IV France* **104** pp.49-52 (2003)

[42] Homstad R, Antoine C, Nygård P, Helle T, "Quantification of the three-dimensional paper structure: Methods and potential", *Pulp & Paper Canada* **104** (7) pp.T186-T189 (2003)

[43] Donnelly E F, Price R R, Pickens D R, "Dual focal-spot imaging for phase extraction in phase-contrast radiography", *Med. Phys.* **30** (9) pp.2292-2296 (2003)

[44] Stock S R, Ignatiev K, Dahl T, Barss J, Fezzaa K, Veis A, Lee W K, De Carlo F, "Multiple microscopy modalities applied to a sea urchin tooth fragment", *J. Synchrotron Rad.* **10** pp.393-397 (2003)

[45] Hong Y U, Pin-Pin Z H U, Shen-Sheng H A N, Zhen-Lin L U O, Chen G A O, "in-line phase-contrast imaging using partially coherent hard X-ray", *Chin. Phys. Lett.* **20** (2) pp220-222 (2003)

[46] Wu X, Liu H, "A general theoretical formalism for X-ray phase contrast imaging, *J. X-ray Sci. Tech.* **11** pp.33-42 (2003)

[47] Wu X, Liu H, "Clinical implementation of X-ray phase-contrast imaging: theoretical foundations and design considerations", *Med. Phys.* **30** (8) pp.2169-2179 (2003)

[48] Mayo S C, Davis T J, Gureyev T E, Miller, P R, Paganin D, Pogany A, Stevenson A W, Wilkins S W, "X-ray phase-contrast microscopy and microtomography", *Opt. Express* **11** (19) pp.2289-2302 (2003)

[49] Salvo L, Cloetens P, Maire E, Zabler S, Blandin J J, Buffière J Y, Ludqig W, Boller E, Bellet D, Josserond C, "X-ray microtomography an attractive characterisation technique in materials science", *Nucl. Instr. Meth. Phys. B* **200** pp. 273-286 (2003)

[50] Freedman M T, Lo S-C B, Honda C, Makariou E, Sisney G, Pien E, Ohara H, Ishisaka A, Shimada F, "Phase contrast digital mammography using molybdenum X-ray: Clinical implications in detectability improvement", Medical Imaging 2003: Physics of medical Imaging, Proceedings of SPIE Vol.5030 pp.533-540 (2003)

[51] Gureyev T E, Pogany A, Paganin D M, Wilkins S W, "Linear algorithms for phase retrieval in the Fresnel region", *Opt. Comms.* **231** pp.53-70 (2004)

[52] Rao D V, Takeda T, Kawakami T, Uesugi K, Tsuchiya Y, Wu J, Lwin T T, Itai Y, Zeniya T, Yuasa T, Akatsuka T, "Microtomographic images of rat's lumbar vertebra microstructure using 30keV synchrotron X-rays: an analysis in terms of 3D visualisation", *Nucl. Instr. Meth. A* **523** pp.206-216 (2004)

[53] Gureyev T E, Davis T J, Pogany A, Mayo S C, Wilkins S W, " Optical phase retrieval by use of first Born-and Rytov-type approximations ", *Appl. Opt.* **43** (12) pp.2418-2430 (2004)

[54] Van der Veen F, Pfeiffer F, "Coherent X-ray Scattering", *J. Phys.: Condens. Matter* **16** pp.5003-5030 (2004)

[55] Lewis R A, "Medical phase contrast x-ray imaging: current status and future prospects", *Phys. Med. Biol.* **49** pp.3573-3583 (2004)

[56] Faulkner H M L, Rodenburg J M, "Moveable aperture lensless transmission: A novel phase retrieval algorithm", *Phys. Rev. Lett.* **93** (2) pp.023903-1-023903-4 (2004)

[57] Wu X, Liu H, "An experimental method of determining relative phase-contrast factor for X-ray imaging systems", *Med. Phys.* **31** (5) pp.997-1002 (2004)

[58] Giersch J, Niederlöhner D, Anton G, "The influence of energy weighting on X-ray imaging quality", *Nucl. Instr. Meth. A* **531** pp.68-74 (2004)

[59] Yokosuka H, Watanabe N, Ohigashi T, Aoki S, Ando M, "Phase-contrast hard X-ray microscope with a zone plate at the photon factory", *J. Phys. IV* **104** pp.591-594 (2004)

[60] Neuhäusler U, Schneider G, Ludwig W, Hambach D, "Phase contrast X-ray microscopy at 4keV photon energy with 60nm resolution", *J. Phys. IV* **104** pp.567-570 (2004)

[61] Mayo S C, Miller P R, Wilkins S W, Davis T J, Gao D, Gureyev T E, Paganin D, Parry D J, Pogany A, Stevenson A W, "Applications of phase-contrast X-ray microscopy in an SEM", *J. Phys. IV* **104** pp.543-546 (2004)

[62] Falcone P M, Baiano A, Zanini F, Mancini L, Tromba G, Montanari F, Del Nobile M A, "A novel approach to the study of bread porous structure: phase-contrast X-ray microtomography", *J. Food Science* **69** (1) pp.38-43 (2004)

[63] Hu Z W, Chu Y S, Lai B, Thomas B R, Chernov A A, "Diffraction and imaging study of imperfections of crystallized lysome with coherent X-rays", *Acta Crystallographica D* **60** pp.621-629 (2004)

[64] Paganin D, Gureyev T E, Mayo S C, Stevenson A W, Nesterets Y I, Wilkins S W, "X-ray omni microscopy", *J. Microscopy* **214** (3) pp.315-327 (2004)

[65] Gureyev T E, Stevenson A W, Nesterets Y I, Wilkins S W, "Image deblurring by means of defocus", *Opt. Comm.*, **240** pp.81-88 (2004)

[66] Kocsis M, Snigirev A, "Imaging using synchrotron radiation", *Nucl. Instr. Meth. A*, **525** pp.79-84 (2004)

[67] Pagot E, Fiedler S, Cloetens P, Bravin A, Coan P, Fezzaa K, Baruchel J, Härtwig J, "Quantitative comparison between two phase contrast techniques: diffraction enhanced imaging and phase propagation imaging", *Phys. Med. Biol.*, **50** pp.709-724 (2004)

[68] Gureyev T E, Paganin D M, Stevenson A W, Mayo S C, Wilkins S W, "Generalized eikonal of partially coherent beams and its use in quantitative imaging", *Phys. Rev. Lett.*, **93** (6) pp.068103/1-068103/4 (2004)

[69] Pavlov K M, Gureyev T E, Paganin D Nesterets Y I, Morgan M J, Lewis R A, "Linear systems with slowly varying transfer functions and their application to X-ray phase-contrast imaging", *J. Phys. D: Appl. Phys.* **37** pp.2746-2750 (2004)

[70] Han S, Yu H, Cheng J, "Contrast and resolution in direct Fresnel diffraction phase-contrast imaging with partially coherent X-ray source", *Rev. Sci. Instr.***75** (10) pp.3146-3151 (2004)

[71] Peele A G, Nugent K A, "Phase measurement using X-rays", *Rev. Sci. Instr.*, **75** (10) pp.3382-3386 (2004)

[72] Montgomery D S, Nobile A, Walsh P J, "Charaterization of National Ignition Facility cryogenic beryllium capsules using X-ray phase contrast imaging", *Rev. Sci. Instr.*, **75** (10) pp.3986-3988 (2004)

[73] Bailat C J, Hamilton T J, Rose-Petruck C, Diebold G J, "Acoustic radiation pressure: a 'phase contrast' agent for X-ray phase contrast imaging", *Appl. Phys. Lett.*, **85** (19) pp.4517-4519 (2004)

[74] Kitchen M J, Paganin D, Lewis R A, Yagi N, Uesugi K, Mudie S T, "On the origin of speckle in X-ray phase contrast images of lung tissue", *Phys. Med. Biol.*, **49** pp.4335-4348 (2004)

[75] Hamilton T J, Bailay C J, Rose-Petruck C, Diebold G J, "Acoustically modulated phase contrast imaging", *Phys. Med. Biol.*, **49** pp.4985-4996 (2004)

[76] Monin P, Bulling S, Hoszowska J, Valley J-F, Meuli R, Verdun F R, "Quantitative characterization of edge enhancement in phase contrast X-ray imaging", *Med. Phys.*, **31** (6) pp.1372-1383 (2004)

[77] Wu, X, Liu H, Yan A, "Optimization of X-ray phase-contrast imaging based on in-line holography", *Nucl. Instr. Meth. B.*, **234** pp.563-572 (2004)

[78] Krimmel S, Stephan J, Baumann J, "3D computed tomography using a microfocus X-ray source: Analysis of artifact formation in the reconstructed images using simulated as well as experimental projection data", *Nucl. Instr. Meth. A.*, **542** pp.399-407 (2005)

[79] Coan P, Pagot E, Fiedler S, Cloetens P, Baruchel J, Bravin A, "Phase-contrast X-ray imaging combining free space propagation and Bragg diffraction", *J. Synchrotron Rad.*, **12** pp.241-245 (2005)

[80] Lewis R A, "Medical applications of synchrotron radiation in Australia", *Nucl. Instr. Meth. A.*, **548** pp.23-29 (2005)

[81] Antunes A, Hönnicke M G, Cusatis C, Morelhão S L, "High contrast radiography of normal and cataractous canine lenses", *J. Phys. D.*, **38** pp.A85-A88 (2005)

[82] Agliozzo S, Brunello E, Klein H, Mancini L, Härtwig J, Baruchel J, Gastaldi J, "Extended investigation of porosity in quasicrystals by synchrotron X-ray phase contrast radiography – I: In icosahedral AlPgMn grains", *J. Cryst. Growth,* **281** pp.623-638 (2005)

[83] Brunello E, Agliozzo S, Klein H, Mancini L, Härtwig J, Baruchel J, Gastaldi J, "Extended investigation of porosity in quasicrystals by synchrotron X-ray phase contrast radiography – Part II: In grains of other alloys and structures than AlPgMn", *J. Cryst. Growth,* **282** pp.228-235 (2005)

[84] Xiao T Q, Bergamaschi A, Dreossi D, Longo R, Olivo A, Pani S, Rigon L, Rokvic T, Venanzi C, Castelli E, "Effect of spatial coherence on application of in-line phase contrast imaging to synchrotron radiation mammography", *Nucl. Instr. Meth. A.*, **548** pp.155-162 (2005)

[85] Hirano M, Yamasaki K, "Estimation of contrast of refraction contrast imaging compared with absorption imaging-basic approach", *Nucl. Instr. Meth. A.*, **548** pp.187-193 (2005)

[86] Olivo A, "Towards the exploitation of phase effects in clinical synchrotron radiation radiology", *Nucl. Meth. Phys. A.,* **548** pp.194-199 (2005)

[87] Abrami A, Arfelli F, Barroso R C, Bergamaschi A, Bille F, Bregant P, Brizzi F, Casarin K, Castelli E, Chenda V, Dalla Palma L, Dreossi D, Fava C, Longo R, Mancini L, Menk R-H, Montanari F, Olivo A, Pani S, Pillon A, Quai E, Ren Kaiser S, Venanzi C, Zanconati F, Zanetti A, Zanini F, "Medical applications of synchrotron radiation at the SYRMEP beamline of ELETTRA", *Nucl. Instr. Meth. A.,* **548** pp.221-227 (2005)

[88] Kitchen M J, Paganin D, Lewis R A, Yagi N, Uesugi K, "Analysis of speckle patterns in phase-contrast images of lung tissue", *Nucl. Instr. Meth. A.*, **548** pp.240-246 (2005)

[89] Peele A G, De Carlo F, McMahon P J, Dhal B B, Nugent K A, "X-ray phase contrast tomography with a bending magnet source", *Rev. Sci. Instr.* **76** (8) pp.083707

[90] Yu B, Peng X, Tian J D, Niu H B, Diao L H, Li H, "Simulation study of phase retrieval for hard X-ray in-line phase contrast imaging", *Science in China Series G,* **48** (4) pp.450-458 (2005)

[91] Momose A, "Recent advances in X-ray imaging", *Jap. J. Phys.*, **44** (9A) pp.6355-6367 (2005)

[92] Nesterets Y I, Wilkins S W, Gureyev T E, Pogany A, Stevenson A W, "On the optimization of experimental parameters for x-ray in-line phase-contrast imaging", *Rev. Sci. Instr.*, **76** (9) pp.093706 (2005)

[93] Wei X, Xiao T Q, Liu L X, Du G H, Chen M, Luo Y Y, Xu H J, "Application of x-ray phase contrast imaging to microscopic identification of Chinese medicines", *Phys. Med. Biol.*, **50** (18) pp.4277-4286 (2005)

[94] Wei X, Xiao T Q, Liu L X, Du G H, Chen M, Luo Y Y, Xu H J, "Typical microstructures of Chinese medicines with x-ray microscopy in phase contrast", *Chinese Phys. Lett.*, **22** (9) pp.2255-2258 (2005)

[95] Otten A, Koster S, Struth B, Snigirev A, Pfohl T, "Microfluidics of soft matter investigated by small-angle X-ray scattering", *J. Synchrotron Rad.*, **12** pp.745-750 (2005)

[96] Kitchen M J, Lewis R A Yagi N, Uesugi K, Paganin D, Hooper S B, Adams G, Jureczek S, Singh J, Christensen C R, Hufton A P, Hall C J, Cheung K C, Pavlov K M, "Phase contrast X-ray imaging of mice and rabbit lungs: a comparative study", *Brit. J. Radiol.*, **78** (935) pp.1018-1027 (2005)

[97] Lewis R A, Yagi N, Kitchen M J, Morgan M J, Paganin D, Siu K K W, Pavlov K, Williams I, Uesugi K, Wallace M J, Hall C J, Whitley J, Hooper S B, "Dynamic imaging of lungs using x-ray phase contrast", *Phys. Med. Biol.*, **50** (21) pp.5031-5040 (2005)

[98] Peterzol A, Olivo A, Rigon L, Pani S, Dreossi D, "The effects of the imaging system on the validity of the limits of the ray-optical approach to phase contrast imaging", *Med. Phys. Biol.*, **32** (12) pp.3617-3627 (2005)

[99] Snigireva I, Snigirev A, "X-ray microanalytical techniques based on synchrotron radiation", *J. Environmental Monitoring*, **8** (1) pp.33-42 (2006)

[100] Gureyev T E, Nesterets Y I, Paganin D M, Wilkins S W, "Effects of incident illumination on in-line phase-contrast imaging", *J. Opt. Soc. Am. A.*, **23** (1) pp.34-42 (2006)

[101] Nesterets Y I, Gureyev T E, Pavlov K M, Paganin D M, Wilkins S W, "Combined analyser-based and propagation-based phase contrast imaging of weak objects", *opt. Comm.*, **259** (1) pp.19-31 (2006)

[102] Yu Y Q, Xiong Z, Lv Y Z, Jiang S P, Tian Y L, "In vivo evaluation of early disease progression by X-ray phase contrast imaging in the adjuvant-induced arthritic rat", *Skeletal radiology*, **35** (3) pp.156-164 (2006)

[103] Gureyev T E, Nesterets Y L, Paganin D M, Poganu A, Wilkins S W, "Linear algorithms for phase retrieval in the Fresnel region. 2. Partially coherent radiation", *Opt. Comm.*, **259** (2) pp.569-580 (2006)

[104] Petukhov A V, Thijssen J H J, Hart D C't, Imhof A, van Blaaderen A, Dolbnya I P, Snigirev A, Moussaid A, Snigireva I, "Microradian X-ray diffraction in colloidal photonic crystals", *J. Appl. Cryst,*, **39** pp.137-144 (2006)

[105] Mayo S. C., Miller . R., Sheffield-Parker, J., Gureyev T., Wilkins S. W., "Attainment of <60nm Resolution in Phase-Contrast X-ray Microscopy using an add-on to an SEM", *Proc. 8th Int. Conf. X-ray Microscopy,* pp.343-345 (2005)

Diffraction enhanced imaging

[1] Davis T J, Gao D, Gureyev T E, Stevenson A W, Wilkins S W, "Phase-contrast imaging of weakly absorbing materials using hard X-rays", *Nature* **373** pp.595-598 (1995)

[2] Gao D, Davis T J, Wilkins S W, "X-ray phase-contrast imaging study of voids and fibres in a polymer matrix", *Aust. J. Phys.* **48** pp.103-111 (1995)

[3] Davis T J, Gureyev T E, Gao D, Stevenson A W, Wilkins S W, "X-ray image contrast from a simple phase object" *Phys. Rev. Lett.* **74** (16) pp.3173-3177 (1995)

[4] Davis T J, Stevenson A W, "Direct measure of the phase shift of an X-ray beam", *J. Opt. Soc. Am. A* **13** (6) pp.1193-1198 (1996)

[5] Ingal, V N, Beliaevskaya E A, "Phase dispersion radiography of biological objects", *Phys. Med.* **12** (2) pp.75-81 (1996)

[6] Ingal V N, Beliaevskaya E A, "Phase dispersion introscopy technique", *Zh. Tekh. Fiz.* **67** (1) pp.68-77 (1997)

[7] Ingal, V N, Belyaevskaya E A, "Method of phase dispersion introscopy", *Tech. Phys.* **42** (1) (1997)

[8] Bushuev V A, Beliaevska E A, Ingal V N, "Wave-optical description of X-ray phase contrast images of weakly absorbing non-crystalline objects", *Il Nuovo Cimento* **19D** (2-4) pp.513-520 (1997)

[9] Gureyev T E, Wilkins S W, "Regimes of X-ray phase-contrast imaging with perfect crystals", *Il Nuovo Cimento* **19D** (2-4) pp.545-552 (1997)

[10] Chapman D, Thomlinson W, Johnston R E, Washburn D, Pisano E, Gmur N, Zhong Z, Menk R, Arfelli F, Sayers D, "Diffraction enhanced X–ray imaging", *Phys. Med. Biol.* **42** pp.2015-2025 (1997)

[11] Ingal V N, Beliaevskaya E A, Brianskaya A P, Merkurieva R D, "Phase mammography – a new technique for breast investigation", *Phys. Med. Biol.* **43** pp.2555-2567 (1998)

[12] Bushuev V A, Sergeev A A, "Inverse problem in the X-ray phase contrast method", *Tech. Phys. Lett.* **25** (2) pp.83-85 (1999)

[13] Menk R H, "Interference imaging and its application to material and medical imaging", *Nucl. Phys. B (Proc. Suppl.)* **78** pp.604-609 (1999)

[14] Dilmanian F A, Zhong Z, Ren B, Wu X Y, Chapman L D, Orion I, Thomlinson W C, "Computed tomography of X-ray index of refraction using the diffraction enhanced imaging method", *Phys. Med. Biol.* **45** pp.933-946 (2000)

[15] Zhong Z, Thomlinson W, Chapman D, Sayers D, "Implementation of diffraction-enhanced imaging experiments: at the NSLS and APS", *Nucl. Instr. Meth. A* **450** pp.556-567 (2000)

[16] Pisano E D, Johnston R E, Chapman D, Geradts J, Iacocca M V, Livasy C A, Washburn D B, Sayers D E, Zhong Z, Kiss M Z, Thomlinson W C, "Human breast cancer specimens: diffraction-enhanced imaging with histologic correlation – improved conspicuity of lesion detail compared with digital radiography", *Radiology* **214** pp.895-901 (2000)

[17] Kobayashi K, Izumi K, Kimura H, Kimura S, Ibuki T, Yokoyama Y, Tsusaka Y, Kagoshima Y, Matsui J, "X-ray phase-contrast imaging with submicron resolution by using extremely asymmetric Bragg diffractions", *Appl. Phys. Lett.* **78** (1) pp.132-134 (2001)

[18] Bushuev V A, Petrakov A P, "X-ray phase contrast of laser-heated air space", *Cryst. Rep.* **46** (2) pp.171-175 (2001)

[19] Zhong Z, Chapman D, Hasnah M, Johnston E, Kiss M Z, Oltulu O, Rigon L, Zhong N, Pisano E, Sayers D, Thomlinson W, "X-ray diffraction order selection with a prism in DEI (abstract)", *Rev. Sci. Instr.* **73** (3) pp.1614 (2002)

[20] Hasnah M, Oltulu O, Zhong Z, Chapman D, "Application of absorption and refraction matching techniques for diffraction enhanced imaging", *Rev. Sci. Instr.* **73** (3) pp.1657-1659 (2002)

[21] Zhong Z, Chapman D, Connor D, Dilmanian A, Gmür N, Hasnah M, Johnston R E, Kiss M Z, Li J, Muehleman C, Oltulu O, Parham C, Pisano E, Rigon L, Sayers D, Thomlinson W, Yaffe M, Zhong H, "Diffraction enhanced imaging of soft tissues", *Synchrotron Radiation News* **15** (6) pp.27-34 (2002)

[22] Mollenhauer J, Aurich M E, Zhong Z, Muehleman C, Cole A A, Hasnah M, Oltulu O, Kuettner K E, Margulis A, Chapman L D, "Diffraction-enhanced X-ray imaging of articular cartilage", *Osteoarthritis and Cartilage* **10** pp.163-171 (2002)

[23] Keyriläinen J, Fernández M, Suortti P, "Refraction contrast in X-ray imaging", *Nucl. Instr. Meth. A* **488** pp.419-427 (2002)

[24] Kagoshima Y, Yokoyama Y, Ibuki T, Niimi T, Tsusaka Y, Takai K, Matsui J, "High-resolution hard X-ray phase-contrast microscopy with a large-diameter and high-numerical-aperture zone plate", *J. Synchrotron Rad.* **9** pp.132-135 (2002)

[25] Kiss M Z, Sayers D E, Zhong Z, "Comparison of X-ray detectors for a diffraction enhanced imaging system" *Nucl. Instr. Meth. A* **491** pp.280-290 (2002)

[26] Hasnah M O, Zhong Z, Oltulu O, Pisano E, Johnston R E, Sayers D, Thomlinson W, Chapman D, "Diffraction enhanced imaging contrast mechanisms in breast cancer specimens", *Med. Phys.* **29** (10) pp.2216-2221 (2002)

[27] Hasnah M, Oltulu O, Zhong Z, Chapman D, "Single-exposure simultaneous diffraction-enhanced imaging", *Nucl. Instr. Meth A* **492** pp.236-240 (2002)

[28] Lewis R A, Rogers K D, Hall C J, Hufton A P, Evans S, Menk R H, Tromba G, Arfelli F, Rigon L, Olivo A, Evans A, Pinder S E, Jacobs E, Ellis I O, Dance D R, "Diffraction enhanced imaging: improved contrast, lower dose X-ray imaging", Medical Imaging 2002: Physics of medical imaging, Proceedings of SPIE Vol 4682 pp.286-297(2002)

[29] Petrakov A P, "X-ray phase-contrast method and its application to the study of blood vessels with a model object", *Tech. Phys.* **48** (5) pp.607-611 (2003)

[30] Cheung K-C, Fayz K, Laundy D, Lewis R, Dobson B, Hall C, "First test pictures from X-ray diffraction enhanced imaging camera for high contrast medical imaging at SRS", *Nucl. Instr. Meth. A* **513** pp.32-35 (2003)

[31] Bravin A, "Exploiting the X-ray refraction contrast with an analyzer: the state of the art", *J. Phys. D* **36** pp.A24-A29 (2003)

[32] Hirano K, "Angle-resolved X-ray imaging using a resolution-tunable double-crystal analyzer", *J. Phys. D* **36** pp.1469-1472 (2003)

[33] Pagot E, Cloetens P, Fiedler S, Bravin A, Coan P, Baruchel J, Härtwig J, Thomlinson W, "A method to extract quantitative information in analyzer-based X-ray phase contrast imaging", *Appl. Phys. Lett.* **82** (20) pp.3421-3423 (2003)

[34] Kiss M Z, Sayers D E, Zhong Z, "Measurement of image contrast using diffraction enhanced imaging", *Phys. Med. Biol.* **48** pp.325-340 (2003)

[35] Oltulu O, Zhong Z, Hasnah M, Wernick, M N, Chapman D, "Extraction of extinction, refraction and absorption properties in diffraction enhanced imaging", *J. Phys. D* **36** pp.2152-2156 (2003)

[36] Muehleman C, Chapman L D, Kuettner K E, Rieff J, Mollenhauer J A, Massuda K, Zhong Z, "Radiography of rabbit articular cartilage with diffraction-enhanced imaging", *The Anatomical Record A* **272** (A) pp.392-397 (2003)

[37] Li J, Zhong Z, Lidtke R, Kuettner K E, Peterfy C, Aliteva E, Muehleman C, "Radiography of soft tissue of the foot and ankle with diffraction enhanced imaging", *J. Anat.* **202** pp.463-470 (2003)

[38] Giles C, Hönnicke M G, Lopes R T, Rocha H S, Gonçalves O D, Mazzaro I, Cusatis C, "First experiments on diffraction-enhanced imaging at LNLS", *J. Synchrotron Rad.* **10** pp.421-423 (2003)

[39] Rigon L, Besch H-J, Arfelli F, Menk R-F, Heitner G, Plothow-Besch H, "A new DEI algorithm capable of investigating sub-pixel structures", *J. Phys. D* **36** pp.A107-A112 (2003)

[40] Lewis R A, Hall C J, Hufton A P, Evans S, Menk R H, Arfelli F, Rigon L, Tromba G, Dance D R, Ellis I O, Evans A, Jacobs E, Pinder S E, Rogers K D, "X-ray refraction effects: application to the imaging of biological tissues", *British Journal of Radiology* **76** pp.301-308 (2003)

[41] Dendy P, Harrison R, "Diffraction enhanced imaging", *British Journal of Radiology* **76** pp.289 (2003)

[42] Bravin A, Fiedler S, Coan O, Labiche J-C, Ponchut C, Peterzol A, Thomlinson W, "Comparison between a position sensitive germanium detector and a taper optics CCD "FRELON" camera for diffraction enhanced imaging", *Nucl. Instr. Meth A* **510** pp.35-40 (2003)

[43] Muehleman C, Majumdar A, Issever A S, Arfelli F, Menk R-F, Rigon L, Heitner G, Reime B, Metge J, Wagner A, Kuettner K E, Mollenhauer J, "X-ray detection of structural orientation in human articular cartilage", *Osteoarthritis and Cartilage* **12** pp.97-105 (2004)

[44] Nesterets Y I, Gureyev T E, Paganin D, Pavlov K M, Wilkins S W, "Quantitative diffraction-enhanced X-ray imaging of weak objects", *J. Phys. D.* **37** pp.1262-1272 (2004)

[45] Fiedler S, Bravin A, Keyriläinen J, Fernández M, Suortti P, Thomlinson W, Tenhunen M, Virkkunen P, Karjalainen-Lindsburg M-L, "Imaging lobular breast carcinoma: comparison of synchrotron radiation DEI-CT technique with clinical CT, mammography and histology", *Phys. Med. Biol.* **49** pp.175-188 (2004)

[46] De Almeida Silva R, de Camargo A S S , Cusatis C, Nunes L A O, Andreeta J P, "Growth and characterization of columbite $CaNb_2O_6$ quality single crystal fiber", *J. Cryst. Growth* **262** pp.246-250 (2004)

[47] Levine L E, Long G G, "X-ray scattering with ultra-small-angle X-ray scattering as a contrast mechanism", *J. Appl. Crystallography* **37** pp.757-765 (2004)

[48] Petrakov A P, Kryazhev A A, "X-ray phase-contrast study of dissolution of NaCl Crystals", *Tech. Phys.*, **49** (10) pp.1381-1383 (2004)

[49] Li G, Wang N, Wu Z, "Hard X-ray diffraction enhanced imaging only using two crystals", *Chinese Science Bulletin* **49** (20) pp.2120-2125 (2004)

[50] Jiang X M, Li G, Chen Z H, Tang J T, "Refractive contrast in X-ray diffraction enhanced imaging", *High Energy Physics and Nuclear Physics*, **28** (12) pp.1282-1290 (2004)

[51] Li J, Williams J M, Zhong Z, Kuettner K E, Aurich M, Mollenhauer J, Muehleman C, "Reliability of diffraction enhanced imaging for assessment of cartilage lesions, *ex vivo*", *Osteoarthritis and Cartilage* **13** pp.187-197 (2005)

[52] Yeo A, Yang P, Fane A G, White T, Moser H O, "Non-invasive observation of external and internal deposition during membrane filtration by X-ray microimaging", *J. Membrane Sci.*, **250** pp.189-193 (2005)

[53] Zhu P-P, Wang J-Y, Yuan Q-X, Tian Y-L, Huang W-X, Li G, Hu T-D, Jiang X-M, Wu Z-Y, "Study on the methods for diffraction-enhanced imaging with two crystals", *Acta Physica Sinica*, **54** (1) pp.58-63 (2005)

[54] Huang W-X, Yuan Q-X, Tian Y-L, Zhu P-P, Jiang X-M, Wang J-Y, "Diffraction-enhanced imaging experiments in BSRF", *Acta Physica Sinica*, **54** (2) pp.677-681 (2005)

[55] Hasnah M O, Parham C, Pisano E D, Zhong Z, Oltulu O, Chapman D, "Mass density images from the diffraction enhanced imaging technique", *Med. Phys.*, **32** (2) pp.549-552 (2005)

[56] Keyriläinen J, Fernández M, Fiedler S, Bravin A, Karjalainen-Lindsberg M-L, Virkkunen P, Elo E-M, Tenhunen M, Suortti P, Thomlinson W, "Visulaisation of calcifications and thin collagen strands in human breast tumour specimens by the diffraction-enhanced imaging technique: a comparison with conventional mammography and histology", *European J. Radiology* **53** pp.226-237 (2005)

[57] Liu C, Zhang Y, Zhang X, Yang W, Peng W, Shi D, Zhu P, Tian Y, Huang Z, "X-ray diffraction-enhanced imaging of uterine leiomyomas", *Med. Sci. Monit.*, **11** (5) pp.MT33-MT38 (2005)

[58] Wagner A, Aurich M, Sieber N, Stoessel M, Wetzel W-D, Schmuck K, Lohmann M, Reime B, Metge J, Coan P, Bravin A, Arfelli F, Rigon L, Menk R-H, Heitner G, Irving T, Zhong Z, Muehleman C, Mollenhauer J A, "Options and limitations of joint cartilage imaging: DEI in comparison to MRI and sonography", *Nucl. Instr. Meth. A.*, **548** pp.47-53 (2005)

[59] Mannan K A, Schültke E, Menk R A, Siu K, Pavlov K, Kelly M, McLoughlin G, Beveridge T, Tromba G, Juurlink B H, Chapman D, Rigon L, Griebel R W,

"Synchrotron supported DEI/KES of a brain tumor in an animal model: The search for a microimaging modality", *Nucl. Instr. Meth. A.*, **548** pp.106-110 (2005)

[60] Pavlov K M, Gureyev T E, Paganin D, Nesterets Y I, Kitchen M J, Siu K K W, Gillam J E, Uesugi K, Yagi N, Morgan N J, Lewis R A, "Unification of analyser-based and propagation-based X-ray phase-contrast imaging", *Nucl. Instr. Meth. A.*, **548** pp.163-168 (2005)

[61] Siu K K W, Kitchen M J, Pavlov K M, Gillam J E, Lewis R A, Uesugi K, Yagi N, "An improvement to the diffraction-enhanced imaging method that permits imaging of dynamic systems", *Nucl. Instr. Meth. A.*, **548** pp.169-174 (2005)

[62] Rocha H S, Lopes R T, Valiante P M, Tirao G, Mazzaro I, Hönnicke M G, Cusatis C, Giles C, "Diagnosis of thyroid multinodular goiter using diffraction-enhanced imaging", *Nucl. Instr. Meth. A.*, **548** pp.175-180 (2005)

[63] Ibison M, Cheung K C, Siu K, Hall C J, Lewis R A, Hufton A, Wilkinson S J, Rogers K D, Round A, "Diffraction-enhanced imaging at the UK synchrotron radiation source", *Nucl. Instr. Meth. A.*, **548** pp.181-186 (2005)

[64] Gang L, Zhihua C, Ziya W, Ando M, Lin P, Wang J Y, Jiamg X M, "Image quality dependence on thickness of sliced rat kidney taken by a simplest DEI construction", *Nucl. Instr. Meth. A.*, **548** pp.200-206 (2005)

[65] Hönnicke M G, Foerster L A, Navarro-Silva M S, Menk R-H, Rigon L, Cusatis C, "Preliminary studies of enhanced contrast radiography in anatomy and embryology of insects with Elettra synchrotron light", *Nucl. Instr. Meth. A.*, **548** pp.207-212 (2005)

[66] Menk R-H, Rigon L, Arfelli F, "Diffraction-enhanced X-ray medical imaging at the ELETTRA synchrotron light source", *Nucl. Instr. Meth. A.*, **548** pp.213-220 (2005)

[67] Rocha HS, Lopes R T, Pessôa L M, Hönnicke M G, Tirao G, Cusatis C, Mazzaro I, Giles C, "Diffraction-enhanced imaging for studying pattern recognition in cranial ontogeny of bats and marsupials", *Nucl. Instr. Meth. A.*, **548** pp.228-233 2005)

[68] Connor D M, Sayers D, Sumner D R, Zhong Z, "Identification of fatigue damage in cortical bone by diffraction enhanced imaging", *Nucl. Instr. Meth. A.*, **548** pp.234-239 (2005)

[69] Antunes A, Hönnicke M G, Safatle A M V, Cusatis C, Moraes Barros P S, Morelhão S L, "Diffraction enhanced X-ray imaging of mammals crystalline lens", *Nucl. Instr. Meth. B.*, **238** pp.28-31 (2005)

[70] Briedis D, Siu K K W, Paganin D M, Pavlov K M, Lewis R A, "Analyser-based mammography using single-image reconstruction", *Phys. Med. Biol.*, **50** (15) pp.3599-3611 (2005)

[71] Hönnicke M G, Kellerman G, Rocha H S, Gile C, Tirao C, Mazzaro I, Lopes P R T, Cusatis C, "Enhanced contrast radiography with channel-cut crystals at the LNLS", *Rev. Sci. Instr.*, **76** (9) pp.093703 (2005)

[72] Hönnicke M G, M G, Rigon L, Menk R H, Cusatis C, "Quantitative and qualitative studies on high-contrast X-ray radiography with an asymmetrical crystal set-up at Elettra", *J. Synchrotron. Rad.*, **12** pp.701-706 (2005)

[73] Tseng P K, Pong W F, Chang C L, Hsu C P, Lin F Y, Hwang C S, Sheu H S, "Initial results on the feasibility of hybrid X-ray microscopy", *Chinese J. Phys.*, **43** (5) pp.979-985 (2005)

[74] Ignatiev K I, Lee W K, Fezzaa K, Stock S R, "Phase contrast stereometry: fatigue crack mapping in three dimensions", *Philosophical Magazine*, **85** (28) pp.3273-3300 (2005)

[75] Koyama I, Momose A, Wu J, Lwin T-T, Takeda T, "Biological imaging by X-ray phase tomography using diffraction-enhanced imaging", *Jap. J. Appl. Phys*, **44** (11) pp.8219-8221 (2005)

[76] Huang Z F, Li Z, Kang K J, Zhu P P, Yuan Q X, Huang W X, Wang J Y, Li G, Zhang D, Yu A M, "Study on extraction method of phase information in X-ray diffraction enhanced imaging", *High Energy Physics and Nuclear Physics*, **29** pp.133-136 (2005)

[77] Liu C L, Zhang Y, Zhang X Y, Peng W J, Shi D R, Zhu P P, Huang W X, Yuan Q X, "Diffraction enhanced imaging of breast tissue", *High Energy Physics and Nuclear Physics*, **29** pp.130-132 (2005)

[78] Nesterets Y I, Gureyev T E, Wilkins S W, "Polychromaticity in the combined propagation-based/analyser-based phase-contrast imaging", *J. Phys. D.*, **38** (24) pp.4259-4271 (2005)

[79] Zhu P P, Yuan Q, X, Huang W X, Wang J Y, Shu H, Wu Z Y, Xian D C, "Principles of X-ray diffraction enhanced imaging", *Acta Physica Sinica.*, **55** (3) pp.1089-1098 (2006)

Interferometry

[1] Bonse U, Hart M, "An X-ray interferometer", *Appl. Phys. Lett.* **6** (8) pp.155-156 (1965)

[2] Momose A, "Demonstration of phase-contrast X-ray computed tomography using an X-ray interferometer", *Nucl. Instr. Meth A* **352** pp.622-628 (1995)

[3] Momose A, Takeda T, Itai Y, "Phase-contrast X-ray computed tomography for observing biological specimens and organic materials", *Rev. Sci. Instr.* **66** (2) pp.1434-1436 (1995)

[4] Takeda T, Momose A, Itai Y, Wu J, Hirano K, "Phase-contrast imaging with synchrotron X-rays for detecting cancer lesions", *Acad. Radiol.* **2** pp.799-803 (1995)

[5] Momose A, Takeda T, Itai Y, "Contrast effect of blood on phase-contrast X-ray imaging" *Acad. Radiol.* **2** pp.883-887 (1995)

[6] Momose A, Takeda T, Itai Y, Hirano K, "Phase-contrast X-ray computed tomography for observing biological soft tissues", *Nature Medicine* **2** (4) pp.473-475 (1996)

[7] Momose A, Takeda T, Itai Y, Hirano K, "Erratum: Phase-contrast X-ray computed tomography for observing biological soft tissues", *Nature Medicine* **2** (5) pp.596 (1996)

[8] Hirano K, Momose A, "Investigation of the phase shift in X-ray forward diffraction using an X-ray interferometer", *Phys. Rev. Lett.* **76** (20) pp.3735-3737 (1996)

[9] Beckmann F, Bonse U, Busch F, Günnewig O, "X-ray microtomography(□CT) using phase contrast for the investigation of organic matter", *J. Computer Assisted Tomography* **21** (4) pp.539-553 (1997)

[10] Momose A, Yoneyama A, Hirano K, "Operation of a two-crystal X-ray interferometer at the photon factory", *J. Synchrotron Rad.* **4** pp.311-312 (1997)

[11] Momose A, Takeda T, Itai Y, Yoneyama A, Hirano K, "Phase-contrast tomographic imaging using an X-ray interferometer", *J. Synchrotron Rad.* **5** pp.309-314 (1998)

[12] Yoneyama A, Momose A, Seya E, Hirano K, Takeda T, Itai Y, "Operation of a separated-type X-ray interferometer for phase-contrast X-ray imaging", *Rev. Sci. Instr.* **70** (12) pp.4582-4586 (1999)

[13] Hirano K, Momose A, "Development of an X-ray interferometer for high-resolution phase-contrast X-ray imaging", *Jpn. J. Appl. Phys* **38** pp.L1556-L1558 (1999)

[14] Takeda T, Momose A, Hirano K, Haraoka S, Watanabe T, Itai Y, "Human carcinoma: early experience with phase-contrast X-ray CT with synchrotron radiation – comparative specimen study with optical microscopy", *Radiology* **214** pp.298-301 (2000)

[15] Takeda T, Momose A, Yu Q, Yuasa T, Dilmanian F A, Akatsuka T, Itai Y, "New types of X-ray computed tomography (CT) with synchrotron radiation: fluorescent X-ray CT and phase-contrast X-ray CT using interferometer", *Cellular and Molecular Biology* **46** (6) pp.1077-1088 (2000)

[16] Takeda T, Momose A, Yu Q, Wu J, Hirano K, Itai Y, "Phase-contrast X-ray imaging with a large monolithic X-ray interferometer", *J. Synchrotron. Rad.* **7** pp.280-282 (2000)

[17] Bergamin A, Cavagnero G, Mana G, Massa E, Zost G, "Measuring small lattice distortions in Si-crystals by phase-contrast X-ray topography", *J. Phys. D* **33** pp.2678-2682 (2000)

[18] Momose A, Takeda T, Itai Y, "Blood vessels: depiction at phase-contrast X-ray imaging without contrast agents in the mouse and rat – feasibility study", *Radiology* **217** pp.593-596 (2000)

[19] Momose A, Takeda T, Yoneyama A, Koyama I, Itai Y, "Wide-area phase-contrast X-ray imaging using large X-ray interferometers", *Nucl. Instr. Meth. A* **467-468** pp.917-920 (2001)

[20] Takeda T, Momose A, Wu J, Zeniya T, Yu Q, Lwin T-T, Itai Y, "Phase-contrast X-ray computed tomography of non-formalin fixed biological objects", *Nucl. Instr. Meth A* **467-468** pp.1322-1325 (2001)

[21] Momose A, Takeda T, Yoneyama A, Koyama I, Itai Y, "Phase-contrast X-ray imaging using an X-ray interferometer for biological imaging", *Analytical Sciences* **17** pp.i527 (2001)

[22] Yoneyama A, Momose A, Koyama I, "Feasibility test of a nonplanar three-beam case X-ray interferometer for high-resolution phase-contrast X-ray imaging", *Jpn. J. Appl. Phys.* **41** pp.L161-L163 (2002)

[23] Momose A, "Phase-contrast X-ray imaging based on interferometry", *J. Synchrotron Rad.* **9** pp.136-142 (2002)

[24] Yoneyama A, Momose A, Koyama I, Seya E, Takeda T, Itai Y, Hirano K, Hyodo K, "Large-area phase-contrast X-ray imaging using a two-crystal X-ray interferometer", *J. Synchrotron Rad.* **9** pp.277-281 (2002)

[25] Takeda T, Momose A, Wu J, Yu Q, Zeniya T, Lwin T-T, Yoneyama A, Itai Y, "vessel imaging by interferometric phase-contrast X-ray technique", *Circulation* **105** pp.1708-1712 (2002)

[26] David C, Nöhammer B, Solak H H, Ziegler E, "Differential X-ray phase contrast imaging using a shearing interferometer", *Appl. Phys. Lett.* **81** (17) pp.3287-3289 (2002)

[27] Koyama I, Momose A, "Simulation study of spatial resolution in phase-contrast X-ray imaging with Takagi-Taupin equation", *Nucl. Instr. Meth. B* **199** pp.446-450 (2003)

[28] Koyama I, Yoshikawa H, Momose A, "Phase-contrast X-ray imaging with a triple-Bragg-case interferometer", *Jpn. J. Appl. Phys.* **42** pp.L80-L82 (2003)

[29] Kohmura Y, Ishikawa T, Takano H, Suzuki Y, "Shearing X-ray interferometer with an X-ray prism", *J. Appl. Phys.* **93** (4) pp.2283-2285 (2003)

[30] Momose A, Kawamoto S, Koyama I, Hamaishi Y, Takai K, Suzuki Y, "Demonstration of X-ray Talbot interferometry", *Jpn. J. Appl. Phys.* **42** pp.L866-L868 (2003)

[31] Momose A, "Phase-sensitive imaging and phase tomography using X-ray interferometers", *Optics Express* **11** (9) pp.2303-2314 (2003)

[32] Kohmura Y, Takano H, Suzuki Y, Ishikawa T, "Shearing X-ray interferometer with an X-ray prism and its improvement", *J. Phys. IV* **104** pp.571-574 (2003)

[33] David C, Nöhammer B, Solak H H, Ziegler E, "Hard X-ray shearing interferometry", *J. Phys. IV* **104** pp.595-598 (2003)

[34] Momose A, Koyama I, Hamaishi Y, Yoshikawa H, Takeda T, Wu J, Itai Y, Takai K, Uesugi K, Suzuki Y, "Phase-contrast microtomography using an X-ray interferometer having a 40-μm analyzer", *J. Phys. IV* **104** pp.599-602 (2003)

[35] Yoneyama A, Takeda T, Tsuchiya Y, Wu J, Lwin T-T, Koizumi A, Hyodo K, Itai Y, "A phase-contrast X-ray imaging system – with a 60 x 30mm field of view – based

on a skew-symmetric two-crystal X-ray interferometer", *Nucl. Instr. Meth. A* **523** pp.217-222 (2004)

[36] Kohmura Y, Sakurai T, Ishikawa T, Suzuki Y, "Phase retrieval with two-beam off-axis X-ray holography", *J. Appl. Phys.* **96** (4) pp.1781-1784 (2004)

[37] Takeda T, Yoshinori T, Yoneyama A, Lwin T T, Aiyoshi Y, Zeniya T, Hyodo K, Ueno E, "Interferometric X-ray imaging of breast cancer specimens at 51keV X-ray energy", *Jap. J. Appl. Phys.*, **43** (8A) pp.5652-5656 (2004)

[38] Takeda T, Yoneyama A, Wu J, Lwin T T, Tsuchiya Y, Hyodo K, "In-vivo imaging of cancer implanted in nude mice by two-crystal interferometer-based phase-contrast X-ray computed tomography", *Jap. J. Appl. Phys.*, **43** (9A) pp.L1144-L1146 (2004)

[39] Yabashi M, Tamasaku K, Goto S, Ishikawa T, "Degradation of transverse coherence with a phase object in synchrotron radiation", *J. Phys. D: Appl. Phys.*, **38** pp.A11-A16 (2005)

[40] Yoneyama A, Takeda T, Tsuchiya Y, Wu J, Lwin T T, Hyodo K, Hirai Y, "High-energy phase-contrast X-ray imaging using a two-crystal X-ray interferometer", *J. Synchrotron Rad.*, **12** pp.534-536 (2005)

[41] Chang S-L, Stetsko Y P, Tank M-T, Lee Y-R, Sun W-H, Yabashi M, Ishikawa T, "X-ray resonance in crystal cavities: realization of Fabry-Perot resonator for hard X-rays", *Phys. Rev. Lett.*, **94** pp.174801/1-174801/4 (2005)

[42] Takeda T, "Phase-contrast and fluorescent X-ray imaging for biomedical researches", *Nucl. Instr. Meth. A.*, **548** pp.38-46 (2005)

[43] Yoneyama A, Takeda T, Tsuchiya Y, Wu J, Lwin T-T, Hyodo K, "Coherence-contrast x-ray imaging based on x-ray interferometry", *Appl. Opt.*, **44** (16) pp.3258-3261 (2005)

[44] Vogt U, Lindblom M, Jansson P A C, Tuohimaa T T, Holmberg A, Hertz H M, Wieland M, Wilhein T, "Single-optical-element soft x-ray interferometry with a laser-plasma x-ray source", *Opt. Lett.*, **30** (16) pp.2167-2169 (2005)

[45] Momose A, Fujii A, Kadowaki H, Jinnai H, "Three-dimensional observation of polymer blend by X-ray phase tomography", *Macromolecules*, **38** (16) pp.7179-7200 (2005)

[46] Momose A, Kawamoto S, "X-ray Talbot interferometry with capillary plates", *Jap. J. Appl. Phys.*, **45** (1A) pp.314-316 (2006)

Miscellaneous

[1] Rontgen W, "Ube rein neue art von strahlen (About a new type of rays)", Nature **52** pp.274

[2] Hart M, "Bragg reflection X-ray optics", *Rep. Prog. Phys.* **34** pp.435-490 (1971)

[3] Sasaki I, Payne D N, Mansfield R J, "Endface index profiling of optical fiber performs", *Applied Optics* **21** (23) pp.4246-4252 (1982)

[4] Bonse U, Hartmann-Lotsche I, Lotsch H, "The X-ray interferometer for high-resolution measurement of anomalous dispersion at Hasylab", *Nucl. Instr. Meth.* **208** pp.603-604 (1983)

[5] Wilkins S W, "Statistical Geometry. III. Accelerated convergence using contrast amplification", *Acta Cryst. A* **39** pp.896-898 (1983)

[6] Wilkins S W, "Statistical Geometry. IV. Maximum-entropy-based extension of multiple isomorphously phased X-ray data to a 4Å resolution for α-Lactalbumin", *Acta Cryst. A* **42** pp.197-202 (1986)

[7] Wilkins S W, Stevenson A W, Nugent K A, Chapman H, Steenstrup S, "On the concentration, focusing and collimation of X-rays and neutrons using microchannel plates and configurations of holes", *Rev. Sci. Instr.* **60** (6) pp.1026-1036 (1989)

[8] Chapman H N, Nugent K A, Wilkins S W, "X-ray focusing using cylindrical-channel capillary arrays. 1. Theory", *Applied Optics* **32** (31) pp.6316-6332 (1993)

[9] Chantler C T, Deslattrs R D, Henins A, Hudson L Y, "Flat and curved crystal spectrography for mammographic X-ray sources", *The British Journal of Radiology* **69** pp.636-649 (1996)

[10] Hudson L T, Deslattes R D, Henins A, Chantler C T, Kessler E G, Schweppe J E, "A curved crystal spectrometer for energy calibration and spectral characterization of mammographic X-ray sources", *Med. Phys.* **23** (10) pp.1659-1670 (1996)

[11] Snigirev A, Kohn V, Snigireva I, Lengeler B, "A compound refractive lens for focusing high-energy X-rays", *Nature* **384** pp.49-51 (1996)

[12] Lentle B, Aldrich J, "Radiological sciences, past and present", *Lancet* **350** pp.280-285 (1997)

[13] Hillman B J, "Medical imaging in the 21st century", *Lancet* **350** pp.731-733 (1997)

[14] Kotre C J, "the effect of background structure on the detection of low contrast objects in mammography", *The British Journal of Radiology* **71** pp.1162-1167 (1998)

[15] Dudchik Y I, Kolchevsky N N, "A microcapillary lens for X-rays", *Nucl. Instr. Meth. A* **421** pp.361-364 (1999)

[16] Kohmura Y, Awaji M, Suzuki Y, Dudchik T I, Kolchevsky N N, Komarov F F, "X-ray focusing test and X-ray imaging test by a microcapillary X-ray lens at an undulator beamline", *Rev. Sci. Instr.* **70** (11) pp.4161-4167 (1999)

[17] Dudchik Y I, Kolchevsky N N, Komarov F F, Kohmura Y, Awaji M, Ishikava T, "Glass capillary X-ray lens: fabrication technique and ray tracing calculations", *Nucl. Instr. Meth A* **454** pp.512-519 (2000)

[18] Wilkins S, "Background highlights in X-ray imaging", *Physics Today* **53** (11) pp.81 (2000)

[19] Dabin Y, Draperi A, Elleaume H, Charvet A-M, Brochard T, Perez M, Nemoz C, Blattman G, Renier M, Fournier F, Dupuy J-L, Lemoine B, Bouhaniche P, Thomlinson W, Suortti P, "A patient positioning system for the ESRF medical imaging facility", *Nucl. Instr. Meth A* **467** pp.1342-1345 (2001)

[20] Becker P, Bonse U, Dettmer A, Dubus F, Zawisky M, "Neutron Interferometer with very thin lamellae", *Cryst. Res. Technol.* **36** pp.589-600 (2001)

[21] Miao J, Ishikawa T, Johnson B, Anderson E H, Lai B, Hodgson K O, "High resolution 3D X-ray diffraction microscopy", *Phys. Rev. Lett.* **89** (8) pp.088303.1-088303.4 (2002)

[22] Faigel G, Tegze M, Belakhovsky M, Marchesini S, Bortel G, "X-ray holography", *Nucl. Instr. Meth. B* **199** pp.464-468 (2003)

[23] Moser H O, Chew E P, Kempson V C, Kong J R, Li Z W, Nyunt T, Qian H J, Rossmanith R, Tor P H, Wilhelmi O, Yang P, Zheng H W, Underhay I J, "Singapore synchrotron light source – status, first results, program", *Nucl. Instr. Meth B* **199** pp.536-540 (2003)

[24] Takahashi Y, Hayashi K, Matsubara E, "Complex X-ray holography", *Phys. Rev. B* **68** pp.052103.1-052103.4 (2003)

[25] McMahon P J, Allman B E, Jacobson D L, Arif M, Werner S A, Nugent K A, "Quantitative phase radiography with polychromatic neutrons", *Phys. Rev. Lett.* **91** (14) pp.145502.1-145502.4 (2003)

[26] Wernick M N, Wirjadi O, Chapman D, Zhong Z, Galtsanos N P, Yank Y, Brankov J G, Oltulu O, Anastacio MA, Muehleman C, "Multiple-image radiography", *Phys. Med. Biol.* **48** pp.3875-3895 (2003)

[27] Kardjilov N, Lehmann E, Steichele E, Vontobel P, "Phase-contrast radiography with a polychromatic neutron beam", *Nucl. Instr. Meth A* **527** pp.519-530 (2004)

[28] Jacobson D L, Allman B E, McMahon P J, Nugent K A, Paganin D, Arif M, Werner S A, "Thermal and cold neutron phase-contrast radiography", Applied Radiation and Isotopes **61** pp.547-550 (2004)

[29] Yuelin L, Dunn J, Nilsen J, Barbee T W Jr., Osterheld A L, Shlyaptsev V N, "Saturated tabletop X-ray laser system at 19nm", *J. Opt. Soc. Am. B*, **17** (6) pp.1098-1101 (2000)

[30] Yamada H, Kitazawa Y, Kanai Y, Tohyama I, Ozaki T, Sakai Y, Sak K, Kleev A I, Bogomolov G D, "Development of the hard X-ray source based on a tabletop electron storage ring", *Nucl. Instr. Meth A*, **467-468** pp.122-125 (2001)

[31] Yamada H, "Novel X-ray source based on a tabletop synchrotron and its unique features", *Nucl. Instr. Meth. B* **199** pp.509-516 (2003)

[32] Hasegawa D, Yamada H, Kleev A I, Toyosugi N, Hayashi T, Yamada T, Tohyama I, Ro Y D, "The tabletop synchrotron MIRRORCLE-6X", The 14th Symposium on Accelerator Science and technology", (2003)

[33] Arndt U W, Long J V P, Duncumb P, "A microfocus X-ray tube used with focusing collimators", *J. Appl. Cryst.*, **31** pp.936-944 (1998)

[34] "World's first phase-contrast-based digital X-ray mammography system, Konica Minolta", M*edical News Today*, Feb (2005)

[35] Kotre C J, Robson K J, Faulkner K, "Measurements of the frequency distribution of optical density in screening mammography", *The British Journal of Radiology*, **67** pp.856-859 (1994)

[36] Zawisky M, Bonse U, Dubus F, Hradil Z, Rehacek J, "Neutron phase contrast tomography on isotope mixtures", *Europhysics Letters* **68** (3) pp.337-343 (2004)

[37] Dubus F, Bonse U, Zawisky M, Baron M, Loidl R, "First phase-contrast tomography with thermal neutrons", *IEEE Transactions on Nuclear Science*, **52** (1) pp.364-370 (2005)

[38] Chen J W, Gao H Y, Zhu H F, Xie H L, Li R X, Xu Z Z, "Neutron phase contrast tomographic imaging method", *Acta Physica Sinica*, **54** (3) pp.1132-1135 (2005)

[39] Kühne G, Frei G, Lehmann E, Vontobel P, "CNR – the new beamline for cold neutron imaging at the Swiss spallation neutron source SINQ", *Nucl. Instr. Meth. A.*, **542** pp.264-270 (2005)

[40] Bastürk M, Kardijilov N, Rauch H, Vontobel P, "Neutron imaging of fiber-reinforced materials", *Nucl. Instr. Meth. A.*, **542** pp.106-115 (2005)

[41] Kardijilov N, Loo S W, Lehmann E, Lim I C, Sim C, M, Vontobel P, "Improving the image contrast and resolution in the phase-contrast neutron radiography", *Nucl. Instr. Meth. A.*, **542** pp.100-105 (2005)

[42] Lehmann E, Lorenz K, Steichele E, Vontobel P, "Non-destructive testing with neutron phase contrast imaging", *Nucl. Instr. Meth. A.*, **542** pp.95-99 (2005)

[43] Cowan A R, Brettle D S, Coleman N J, Parkin G J S, "A preliminary investigation of the imaging performance of photostimulable phosphor computed radiography using a new design of mammographic quality control test object", *The British Journal of Radiology*, **65** pp.528-535 (1992)

[44] Underwood A C, Law J, Clayton C, "Reproducibility of Leeds TOR(MAM) mammographic test object plates", *The British Journal of Radiology*, **70** pp.186-191 (1997)

[45] Kotre C J, "Measurements of the frequency distribution of optical density in screening mammography", *The British Journal of Radiology*, **67** pp.856-859 (1994)

[46] European Directive 97/43/Euratom (Medical Exposures Directive) (1997)

[47] Statutory Instrument 2000 No. 1059: The Ionising Radiation (Medical Exposure) Regulations (2000)

[48] Birch I P, Kotre C J, Padgett R, "Trends in image quality in high magnification digital specimen cabinet radiography", *British Journal of Radiology*, **79** pp.239-243

(2006)

Books

[1] Attwood D, *Soft X-rays and extreme ultraviolet radiation: principles and applications*, Cambridge University Press (1999)

[2] Born & Wolf, *Principles of Optics: electromagnetic theory of propagation, interference and diffraction of light*, Oxford: Pergamon (1965)

[3] Bonse U, Graeff W, "X-ray and Neutron Interferometry", *Topics in Applied Physics, Vol 22*, Springer-Verlas (1977)

[4] Bowen D K, Tanner B K, *High resolution X-ray diffractometry and topography*, Taylor & Francis (1998)

[5] Bragg, *X-rays and crystal structure* (4^{th} Edn), G Bell & Sons Ltd (1924)

[6] Cameron J R, Skofronick J G, *Medical Physics*, John Wiley & Sons (1978)

[7] Curry, C, *Wave optics: Interference and diffraction*, Arnold (1957)

[8] Grant R Fowles, *Introduction to Modern Optics*, Holt, Rinehart & Winston (1968)

[9] Hollins M, *Medical Physics*, Macmillan (1990)

[10] Leighton R B, *Principles of Modern Physics* ch.12, McGraw-Hill (1959)

[11] Michette A G, Buckley C J, *X-Ray Science and Technology*, Institute of Physics Publishing (1993)

[12] Steward E G, *Fourier optics an introduction*, Ellis Harwood (1983)

[13] Hecht E, *Optics (3^{rd} Edn)*, Addison-Wesley (1998)

[14] *International Tables for X-ray crystallography Vol. III*, Kynoch Press (1974)

[15] Farr R F, Allisy Roberts P J, *Physics for Medical Imaging*, W. B. Saunders (1997)

[16] Dendy P P, Heaton B, *Physics for Diagnostic Radiology (2^{nd} Edn)*, Institute of Physics Publishing (1999)

[17] Webb S, *The Physics of Medical Imaging, Institute of Physics Publishing (1998)*